Formability and Failure Response of AA5052-H32 Sheets Deformed using a Shock Tube

A Thesis Submitted in Partial Fulfilment of the Requirements for the Award of the Degree of

DOCTOR OF PHILOSOPHY

by

Saibal Kanchan Barik
(Roll No. 146103015)

DEPARTMENT OF MECHANICAL ENGINEERING
INDIAN INSTITUTE OF TECHNOLOGY GUWAHATI
Guwahati – 781039

March, 2022

Department of Mechanical Engineering
Indian Institute of Technology Guwahati
Guwahati-781039, India

CERTIFICATE

It is certified that the work contained in the thesis entitled **"FORMABILITY AND FAILURE RESPONSE OF AA5052-H32 SHEETS DEFORMED USING A SHOCK TUBE"** submitted by **Mr. SAIBAL KANCHAN BARIK** to the Indian Institute of Technology Guwahati for the award of the degree of Doctor of Philosophy has been carried out under our supervision in the Department of Mechanical Engineering, Indian Institute of Technology Guwahati. This work has not been submitted elsewhere for the award of any other degree or diploma.

Date:

Prof. Niranjan Sahoo
Professor
Department of Mechanical Engineering
Indian Institute of Technology Guwahati
Guwahati-781039, Assam, India

Prof. R. Ganesh Narayanan
Professor
Department of Mechanical Engineering
Indian Institute of Technology Guwahati
Guwahati-781039, Assam, India

Dedicated to My Parents

ACKNOWLEDGEMENT

At foremost, I would like to express my deepest gratitude to my supervisor, Prof. R. Ganesh Narayanan and Prof. Niranjan Sahoo, who have relentlessly supported me during the course of my research work with invaluable guidance, motivation and encouragement. Their innovative ideas and advice in doing systematic research work with full freedom have shaped my basic understanding in this domain to a large extent. The professional ethics, smart approach and team work that I have learnt from them, will remain a source of inspiration for the rest of my life. I would also convey my deepest regard to Prof. Vinayak Kulkarni for motivating me and giving his expert opinion during my research work.

I am thankful to my doctoral committee members, Prof. Uday Shanker Dixit, Prof. Swarup Bag, Prof. Ganesh Natarajan (presently at IIT Palakkad) and Prof. Arbind Kumar Singh, for their valuable suggestions, and insightful comments during the progress of my research work, which has constantly encouraged me towards undertaking a meaningful thesis work.

I would like to express my sincere thanks to Prof. K.S.R. Krishna Murthy, Department Head of Mechanical Engineering, for his support and providing full privilege to utilize the experimental facilities in different laboratories of the department.

I am thankful to the administrative staffs of the department of Mechanical Engineering for their valuable support during my research work. My special thanks to Mr. Nandan Kanan Das, Asst, Workshop Superintendent for providing right solutions to any experimental difficulties. I would like to thank technical superintendents of various labs, Mr. Mrinal Sarma, Mr. Dilip Chetri, Mr. Sanjib Sarma, Mr. Monoj Baishya, Mr. Bijoy Choudhury, Mr. Upen Gohain, Mr. Dhaneswar Khaklary, Mr. Saiffuddin Ahmed, Mr. Dipak Deka, Mr. Gakul Das, Mr. Gautam Gogoi, Mr. Joykrishna Saikia, Mr. Minesh Medhi, Mr. Nidul Saikia, Mr. Monuranjan Dowarah, Mr. Porag Saikia, Mr. Santosh Gogoi, Mr. Dulumoni Das, Mr. Ganesh Nath, Mr. Gwmchar Baro, Mr. Jiten Basumatary, Mr. Lakhinath Gogoi, Mr. Nip Borah, and Mr. Ratan Medhi for their assistance during my research work.

I consider myself extremely fortunate to be a member of Gas Dynamics Lab. I am thankful to my lab-mates, Dr. Sumit Agarwal, Dr. Shrutidhara Sarma, Dr. Minelik Walle, Dr. Soumya Ranjan Nanda, Dr. Sangjukta Devi, Mr. Anil Kumar Rout, Mr. Santosh Kumar Hotta, Mr. Abhishek Kamal, Mr. Anand Verma, Mrs. Priyanka Dash, Mr. Ojing Siram, Mrs. Kabita

Naik, Mr. Himanshu Sahoo, Mr. Shashank Kulkarni, Mr. Nikki Rajaura, Mr. Deepak Yadav, Mr. Safeerul Ameen Ek, Mr. Md. Adil, Mr. Anurag Shrivastav, Mr. Ranveer Negi, Mr. Manish Sonkar who have constantly supported me in all the ways.

The moral support and encouragement that I received from my seniors, and fellow mates always boosted me to go forward with positive approach. I am very much grateful to Dr. Rasmi Ranjan Behera, Dr. Arvind Kumar Agrawal, Dr. Pritam Kumar Rana, Dr. Tinu P. Saju, Dr. Avinish Tiwari, Mr. Nitish Bharadwaj, Mr. Priyabrata Nath, Mr. Sukanta Das, Mr. Rishab Saxsena, Mr. Saurav Kumar Dutta, Mr. Saptarshi Dutta, Mr. Sujit Das. Your valuable decisions, team talk, and glory days shall be a part of my good memories.

I am also thankful to Dr. Shuvayan Brahmachary, Dr. Siddesh Desai, Dr. DVN Lakshmi, Dr. Rajeev Anupoju, Dr. Sritam Swapnadarshi Sahu, Dr. Bidhu Bhusan Makut, Dr. Kajwal Patra, Dr. Bhibhuti Bhusan Dash, Dr. Pratap Kumar Behera, Dr. Sibabrata Sahoo, Dr. Abhinash Mahapatro, Dr. Subhasish Behera, Dr. Sanjeev Mishra, Dr. Sudip shyam, Dr. Ajit Kumar Sahu, Dr. Bikash Kumar, Dr. Anupam Alok, Mr. Kelli Durga Prasad, , Mr. Umang Rathore, Mr. Sunil Biswal, Mr. Ankan Mishra, Mr. Pradeep Pankaj, Mr. Saurav Suman, Mr. Sanjay Raj, Mr. Vivekananda Haldar for helping in every possible aspect during the stay at IIT Guwahati.

Last but not the least; I owe my profound gratitude towards my parents Mr. Biswanath Barik, Mrs. Suprava Barik and my sister Mrs. Monalisa Barik for being the constant guiding, and inspiring force in all the difficult times.

Saibal Kanchan Barik

Indian Institute of Technology Guwahati

ABSTRACT

The emerging interest to minimize fuel consumption and carbon emission, lightweight component design has become one of the important goals in the automotive industries. Among the lightweight materials, aluminium alloys are used significantly in automotive body construction because of their acceptable strength to weight ratio, toughness, ductility, and corrosion resistance. However, the limitations include the moderate formability in the conventional sheet forming processes at room temperature and significant springback during stamping of complex geometries. Thus, improving the formability of aluminium alloys receives much attention in the stamping industries. Generally, warm forming and high-velocity forming are preferred to improve the formability of aluminium alloys. However, heating metals during deformation imposes an additional cost to the forming operation. Thus, various high-velocity forming processes are in demand because the inertial effect developed during these processes that delays necking by developing additional tensile stress outside the neck resulting in enhanced formability. In the recent past, various high-energy rate forming (HERF) processes such as electro-magnetic forming (EMF), electro-hydraulic forming (EHF) and explosive forming (EF) have been preferred to fabricate net-shaped products without any defects. Despite several advantages of HERF processes, the major limitations are the higher capital cost, difficulties in machine handling, and requirement of skilled persons.

Recently, the shock tube facility is also introduced in many studies as a dynamic loading device. The shock tube generates a shock wave during the bursting of a diaphragm, which separates the high-pressure driver section and the low-pressure driven section. The high-velocity shock wave creates a dynamic loading environment at the end of the shock tube that helps to deform the material at different strain rates. In the present study, the shock tube has been utilized as a dynamic bulging device to study the forming behaviour of sheets at different strain rates. In addition to this, the high pressure induced gas developed inside the shock tube can be utilized to propel a rigid body at a high velocity, which can deform a material at even higher strain rates. This facilitates the shock tube to serve as a dynamic Erichsen sheet testing device, which allows to study the rate-dependent forming behaviour, as well as the failure mechanism of the sheets.

During such dynamic deformation, to understand the forming behaviour of aluminium alloys, several empirical, semi-empirical, and physical-based flow stress models considering

the effect of strain rate and temperature have been proposed in the past. Various ductile fracture criteria have also been proposed, which can be utilized in conjunction with the finite element (FE) model to predict sheet failure and forming limit. Thus, the influence of different stress-strain relationships and failure models have also been studied in the current work to predict the dynamic forming and failure of sheets deformed using a shock tube.

Generally, in sheet metal forming, the blank is made of one piece. Thus, understanding the forming behaviour of the welded sheet becomes important in many industries. To join aluminium sheets in lap configuration, friction stir spot welding (FSSW) is mostly preferred because of its better mechanical strength and weld quality. Many research activities focus on various joint performance tests such as lap shear test, cross-tension test, peel test and uniaxial tensile test. Scarce attempts are made to understand the effect of welding parameters during dynamic forming of the FSSW sheet. Thus, the shock tube based impact forming can be utilized to understand the dynamic formability and failure response of aluminium sheets with FS spot welds.

The main objectives of the thesis are to analyse the effect of various material processing parameters on the deformation of AA5052-H32 sheets of two different thicknesses 1 mm and 1.5 mm during the shock tube based forming and to predict the dynamic forming behaviour for efficient process design. Thus, the shock tube is first used as a dynamic bulging device to study the effect of pre-strain on the material forming parameters of the sheets. The rate-dependent forming behaviour of the sheets are predicted by a FE code DEFORM-3D. Further, a hemispherical end nylon striker is used in the shock tube to deform sheets both in the safe limit and beyond the safe limit. Deforming beyond the safe limit allowed us to understand the failure response of the sheets. In addition to this, study on the effect of the choice of flow stress models and failure models also gives a thorough understanding about the failure strain, necking location and fracture pattern during the prediction of dynamic forming of sheets. During the study of dynamic forming of the sheets with FS spot welds, the effect of tool rotational speed, plunge speed and plunge depth on the FS spot welding outputs and forming outputs are understood. Furthermore, DEFORM-3D FE code is used to perform FE simulation of both the FS spot welding and forming of the welded sheets interactively. The predicted material flow phenomenon gives an insight about the joint formation during FSSW. Various forming outputs predicted by FE simulation have a fair agreement with the experimental data.

ABBREVIATIONS

DIC	Digital image correlation
EF	Explosive forming
EHF	Electrohydraulic forming
EMF	Electromagnetic forming
FLD	Forming limit diagram
FSW	Friction stir welding
FSSW	Friction stir spot welding
HAZ	Heat affected zone
HERF	High energy rate forming
LDH	Limit dome height
PD	Plunge depth
PS	Plunge speed
RPM	Rotation per minute
SHPB	Split Hopkinson pressure bar
SRS	Strain rate sensitivity
SZ	Stir zone
TMAZ	Thermo-mechanically affected zone
TWB	Tailor welded blank

NOMENCLATURE

A, B	Material constants in Johnson-Cook model and Modified Johnson-Cook model (MPa)
C_1, C_2	Strain rate sensitivity constants
D	Material constants in Cowper-Symonds model (MPa)
D_i	Damage parameter
D_c	Critical damage parameter for different failure models
E	Young's modulus (MPa)
K	Strength Coefficient (MPa)
n	Strain hardening exponent
R	Correlation coefficient
r	Plastic strain ratio
α	Principal stress ratio
β	Material constant in Oyane model
δ	Material constant in Rice & Tracey model
υ	Poisson's ratio
μ	Coulomb's coefficient of friction
ρ	Density of the material, Kg/m^3
$\bar{\varepsilon}_p$	Equivalent plastic strain
$\dot{\bar{\varepsilon}}_p$	Equivalent plastic strain rate (s^{-1})
$\dot{\varepsilon}_0$	Normalized reference strain rate (s^{-1})
ε_f	Failure strain
ε_2	Major strain
ε_1	Minor strain
σ_{ys}	Yield strength (MPa)
σ_u	Ultimate tensile strength (MPa)
$\bar{\sigma}$	Equivalent stress (MPa)
σ^*	Maximum principal stress (MPa)
σ_m	Hydrostatic stress (MPa)

CONTENTS

LIST OF FIGURES

LIST OF TABLES

Chapter 1

State of the art and objective of the work

1.1 Introduction

The increasing regulations on fuel economy, aim to reduce exhaust gas emissions, and potential for material recycling draw the attention of aerospace and automobile sectors towards the production of light-weight sheet structures. It is observed from the review of Joost (2012) that a potential weight saving of 10 % can enhance the fuel efficiency by 6 – 8 %. Thus, among all the sheet metals aluminium alloys are mostly preferable because of their specific engineering properties such as light-weight, good static and dynamic strength, superior corrosion resistance and recycling ability (Fridlyander et al., 2002). Above all, the formability of the sheets is also an important property affecting product design during stamping. In general, the formability of a material refers to the ability of a given work-piece to undergo plastic deformation without failure. The moderate formability of the aluminium sheets at the ambient temperature leads to easy fracture at the round corners of the dies during the stamping process (Hsu et al., 2008). As a result, many manufacturing industries are focused on enhancing the formability of the aluminium alloys.

Though it is well known that a significant increase in the formability of the aluminium alloys can be achieved by carrying out the same operation at a higher temperature (Gu et al., 2019), it adds expense to the conventional stamping process. On the other hand, forming the sheets at higher strain rates also enhance the forming properties (Ahmed et al., 2017). The velocity gradient developed on the material during the deformation is minimized by the inertial forces generated during the high strain rate forming enhancing the stretchability without strain localization. It results in larger deformation than the traditional quasi-static forming. Thus, the alternative approach of stretching the sheet at a high strain rate becomes the most popular in the last two decades.

When the strain rate approaches a certain limit, almost all material exhibit strain sensitive behaviour (Smerd et al., 2006). As a result, determining rate-dependent material properties at various strain rates is crucial. To extract material properties at lower and higher strain rates,

the quasi-static tensile test and Split Hopkinson Pressure Bar (SHPB) test have traditionally been used for sheet metals. However, these tests are limited to deformation in the uniaxial direction. However, in actual forming condition, material deforms biaxially and it is always required to interpolate uniaxial test data with extended range of plastic strain (Koç et al., 2011). Thus, hydraulic bulge test has been used since so long as a convenient method for determining the bi-axial material properties (Mahabunphachai and Koç, 2010). Due to the bi-axial state of stress-induced condition, the maximum achievable strain before the fracture is much higher than the tensile test. Further, the use of hydraulic bulge test is restricted to certain strain rate range. Thus, various high strain rate biaxial forming devices become more popular to obtain the rate-dependent forming behaviour of sheet metals.

In recent past, the demand of various high energy rate forming (HERF) processes increase because of their uniformity in loading during the high strain rate forming of sheet metals (Psyk et al., 2011). Several numerical simulations have also been conducted on the high strain rate deformation to have an insight physics of the problem and to understand the transient nature of the deformation. Despite several advantages of the HERF processes, the major inevitable limitations are higher capital cost, the requirement of skilled personnel, complexity in instrumentation and handling. In order to minimize these limitations and to study the bi-axial dynamic properties of the material, the shock tube has been introduced in various research works (Ray et al., 2015).

The shock tube is a pneumatically controlled device where a high-pressure driver section is separated from a low pressure driven section with the help of a plastic or metallic diaphragm. When the pressure difference reaches a critical limit, the diaphragm ruptures and the rapid release of gas generates a shock wave. The high-velocity shock wave travels down the tube, hits the sheet kept at the end and performs dynamic loading for a short interval of time. Thus, in this present work the shock tube facility is proposed as a good alternative device to study the forming behaviour of the sheet metals at different rate of loading conditions. In many recent works, the high pressure induced air developed in the shock tube has been utilized to provide momentum to a rigid body located inside it (Koohbor et al., 2016a). The same phenomenon is also employed in the present study to propel a hemispherical end nylon striker to deform sheets at high strain rates and the dynamic forming behaviour and the failure mechanism in the material are analysed. FE simulations are also carried out using DEFORM-3D FE code to

understand the forming and fracture responses of the sheet during shock tube based forming at different strain rates.

So far, friction stir spot welding (FSSW), which is derived from friction stir welding (FSW) is generally preferred to join the structures made of aluminium alloys in lap configuration. This solid state welding process becomes a potential candidate for its higher joint efficiency (Rana et al., 2018). During industrial applications, most of the time, the welded sheets are exposed to different loading environment. Thus, identification of rate-dependent material properties of the welded joint and their performance in different strain rate regime are also much important. Most of the studies focus on evaluation of the static strength of the FS welded joint (Rana et al., 2018). There is no attempt to understand the effect of different welding parameters such as tool rotational speed, plunge speed, plunge depth, etc., on the dynamic forming behaviour the FSSW joint. Thus, in the present work, the FS spot welded sheets are exposed to dynamic deformation in biaxial stretch mode using the shock tube. Furthermore, FE simulations are carried out to simulate this phenomenon in three stages – (i) FSSW with plunging and dwelling as first and second stages respectively, and (ii) impact forming as third stage.

In the present thesis work, Chapter 1 represents the literature review, the significance of the work, objectives of the work, and the tasks involved to complete the work. In chapter 2, the effect of bending pre-strain, pressure, and thickness on the material forming behaviour is analysed during the shock wave based impact forming of AA 5052-H32 sheets. In chapter 3, the shock tube facility is utilized to drive a hemispherical end nylon striker at a high velocity using the high-pressure induced air to deform sheets both the safe limit and beyond the safe limit. In Chapter 4, different flow stress models and failure models are used to predict the failure strain and fracture pattern during the shock tube based impact forming. Chapter 5 deals with an investigation to understand the dynamic forming behaviour of FSSW sheets. The effect of tool rotational speed and plunge speed on the FSSW joint is understood and its forming behaviour is analysed. In Chapter 6**,** the effect of tool rotational speed and plunge depth on the FS spot welding outputs are understood and their influence during the impact forming is investigated. DEFORM-3D FE code is also used to perform FE simulations of both the FS spot welding and forming of the welded sheets by establishing an interactive set up. Chapter 7

represents the major findings of the present work and future scope in the field of shock tube based impact forming.

1.2 Literature review

Formability refers to the ability of the sheet material to undergo plastic deformation without fracture. In practice, the formability of the sheet metal is characterized by measuring the fracture strain or by representing a forming limit diagram (FLD). In general, most of the aluminium alloys are rate-dependent and the rate of loading significantly affects their formability. In this context, a detailed literature survey has been performed in this section to understand the static and dynamic behaviour of aluminium alloys. Further, different techniques utilized to study the dynamic forming behaviour of sheets are also analysed with their advantages, disadvantages and application. Later on, the shock tube facility and its application in different dynamic study is discussed in detail. Following this, the formability of welded sheets and the influence of different parameters affecting the static and dynamic strength of the welded sheets are also highlighted.

1.2.1 Static and dynamic behaviour of aluminium alloys

Since the strain rate has an influence on both the plastic flow stresses and the ductility of materials, it also affects various crucial process parameters such as forming forces, energies, and forming limits. Therefore, understanding the rate-dependent deformation behavior of sheet metal is still challenging for many industrial sectors. Although numerical modelling has been shown to be a useful method for solving this problem, its reliability depends strongly on the accurate description of the rate-dependent deformation behavior of the materials. As a result, it is necessary to experimentally illustrate the rate-dependent deformation behavior and related mechanisms in order to accurately predict several forming parameters during the forming processes.

Existing studies show that alnuminum alloys exhibit insignificant and sometimes negative values of strain rate sensitivity (SRS) at quasi-static strain rates, particularly in the strain rates, 10^{-5} s^{-1} $\leq \dot{\varepsilon} \leq 10^{-1}$ s^{-1} (Romhanji et al., 2002), whereas, the flow stress of aluminium alloys increases with the strain rate, indicating a positive nature of SRS at higher strain rates, typically above 10^{3} s^{-1} (Smerd et al., 2006). The alloy composition, working temperature and the

microstructure of aluminium alloys affect SRS significantly Suo et al. (2013) explored the dynamic mechanisms of aluminium processed by equal channel angular processing (ECAP) and found that the SRS was 3 to 6 times larger during high strain rate deformation than under quasi-static conditions. Pothnis et al. (2011) investigated the effect of strain rate on the tensile properties of Al 7075 T651 alloy and observed an increment in yield strength as compared to quasi-static test. From the experimental and numerical investigations on the compression behavior of the AA6061-O at strain rates (10^{-3} – 10^{3} s^{-1}), Jenq and Sheu (1994) found that the yield stress was positively sensitive to strain rates. In a tensile test experiment, Chen et al. (2009) observed that AA6060-T6 and AA6082-T6 are less sensitive (nearly insensitive) whereas AA7003-T6 and AA7108-T6 appeared significantly sensitive to strain rates (0.001–1000 s^{-1}).

At the same time, Al-Mg alloys have negative SRS (i.e. decreased flow stress with strain rate). Yan et al. (2016) obtained two negative SRS zones of 5A06 aluminium alloy, one at strain rate range 0.001 s^{-1} to 1 s^{-1}, and the second zone is at high strain rates above 3000 s^{-1} in both compression and tension tests. Clausen et al. (2004) confirmed that AA 5083-H116 exhibited negative SRS for the strain rates in the range 10^{-4} s^{-1} to 1 s^{-1} due to the effect of dynamic strain ageing which generated serrated stress-strain curves at low strain rates and temperatures. Further, the transition between negative and positive strain rate dependency was observed when the strain rate exceeded 1 s^{-1}, which resulted by the sudden increase in failure strain. Abedrabbo et al. (2007) also demonstrated the insensitive behavior of AA5182-O and AA5754-O to strain rate at room temperature, whilst a significant increase in the SRS was observed with the increase in temperature.

The positive SRS behavior of aluminum alloys at high strain rates increases the mechanical properties of the material significantly. Fig. 1.1 depicts the variation in the tensile properties of 5A06 aluminium alloy at different strain rates as reported by Yan et al. (2016). They obtained 77.1 % increase in maximum yield stress and 27.9 % rise in maximum the ultimate tensile strength of the material within the tested strain rate range. Ma et al. (2014) also reported a significant increase in flow stress and tensile strength with the increasing strain rate for 5A02-O aluminium alloy.

Along with the tensile properties, the formability and the forming limits of the aluminum alloys are also affected by the rate of loading. The increase in the elongation at higher strain

rates is thought to be due to inertial stabilization that delays the onset of necking (Smerd et al., 2006). Hadianfard et al. (2008) correlated such increase in elongation of Al-5754 alloy at high strain rate regime to the decrease in the average size of the damaged second phase particles, thereby accommodating large strains. From the TEM observations, Ma et al. (2014) confirmed that high strain rate deformation gave rise to much denser and homogeneous distribution of dislocations, which led to produce much higher strength and higher plasticity as compared to quasi-static deformation.

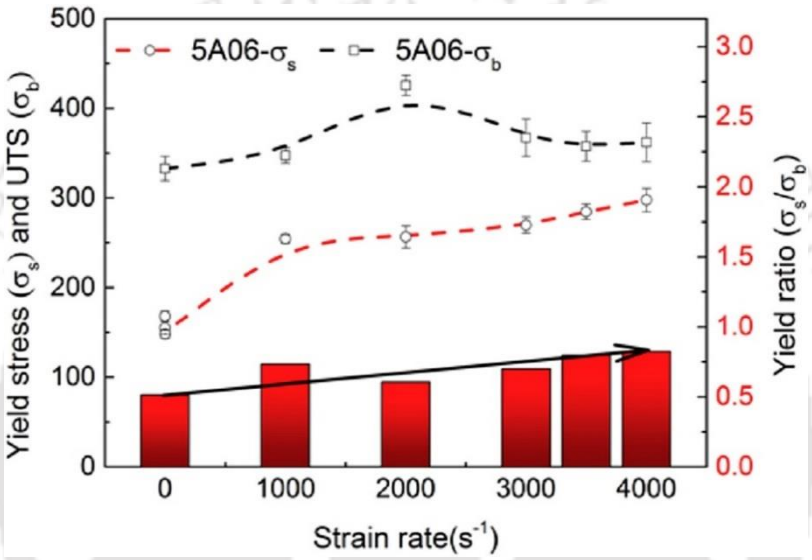

Fig. 1.1: Variation of yield stress, ultimate tensile stress (UTS) and yield ratio of 5A06 alloy at different strain rate (Used with permission from Yan et al. (2016); Elsevier)

1.2.2 Strain rate regime and various testing devices

Because of the limited range of velocity condition in particular machines, it has been impossible to accurately describe the mechanical behavior under a wide range of strain rates using one testing machine. According to the magnitudes of the strains, tensile experiments are divided into quasi-static, static, and dynamic experiments. Based on the strain rate regime, different types of experimental apparatus used now-a-days are reported in Fig. 1.2 (Abd El-Aty et al., 2019).

In quasi-static strain rate regime, generally hydraulic experiments are used to obtained the material properties. Traditionally, hydraulic bulge test has long been recognised as a convenient and practical method for determining the formability of sheet metal, as well as an

effective way for determining the biaxial stress– strain relationships (Mahabunphachai and Koç, 2010). However, because of the use of hydraulic fluid during the experiment, its application is restricted only in the lower ranges of strain rates.

In order to obtain the mechanical performance of the sheet metals in the intermediate to high strain rate loading conditions, SHPB set up is mostly preferred where a pneumatic gas gun is utilized to provide impact loading on the incident bar (Smerd et al., 2006). In many studies, modifications are carried out in some conventional experimental facilities to acquire rate-dependent forming conditions. Various HERF processes, which work in the phenomenon similar to explosive based impact are also used in many research works to study the dynamic forming response as well as the forming limits of different sheets. A detailed literature survey on various dynamic forming devices are presented below.

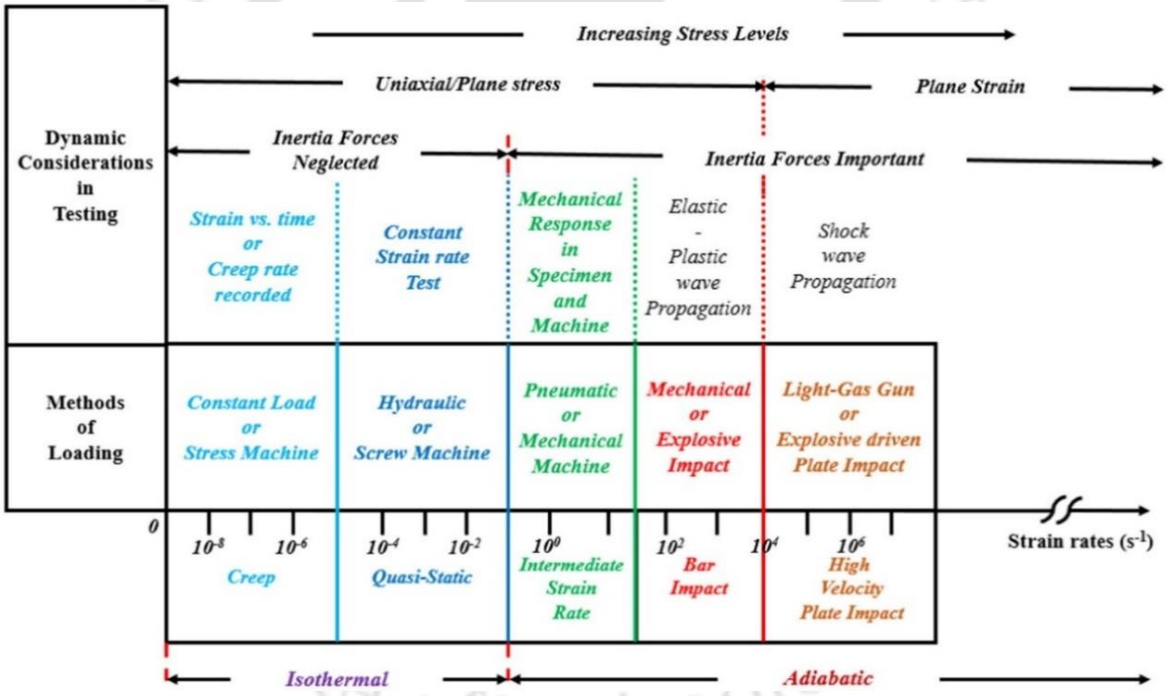

Fig. 1.2: Classification of tensile experiments and loading methods with respect to the value of strain rates (Used with permission from Abd El-Aty et al. (2019); Elsevier)

1.2.3 Drop hammer rig

Broomhead and Grieve (1982) used a drop hammer rig during the bulge test to investigate the effect of strain rate on the strain to fracture of sheets under biaxial tension. With this set up, they determined the forming limit curves of low carbon steel for strain rates of up to 70 s^{-1}. Percy and Lim (1983) identified the forming limit diagram of the steel sheet with the same set

up and reported an enhancement in the formability at the higher forming rate. Further, Pickett et al. (2004) used a similar apparatus to investigate the high strain rate response of high strength steels. However, the use of pressurized oil/water used in this process made the process complicated and its use were restricted to certain range of strain rates.

1.2.4 Modified Split Hopkinson Pressure Bar

Working principle

In the conventional SHPB apparatus, the specimen is placed between the so-called input and output bars, and the dynamic pressure loading is generated by a striker bar (Smerd et al., 2006). In a recent study, Grolleau et al. (2008) modified the conventional SHPB by using a movable bulge cell to perform dynamic bulge testing of aluminium sheets. In this work, the bulge cell was filled with a fluid and when the pressure wave transmitted through the fluid from the input bar, it caused the dynamic bulging of the sheet specimen. They conducted dynamic bulge studies on aluminium sheets for plastic strain rates of up to 500 s^{-1}. They looked into the experimental set up and measurement accuracy in depth and discovered that input bars made of low impedance materials must be required to obtain achievable pressure measurement accuracy. Further, an inverse analysis was utilised to determine the parameters of the rate-dependent material properties using a finite element model of the testing system.

In the further research, in order to eliminate the problem of the filling and removals of the fluid used in the bulge cell, Ramezani et al. (2010) performed the dynamic bulging of the copper sheet by using a polyurethane rubber inside the bulge cell. The use of hyper-elastic rubber as a pressure medium made the bulge test simple to perform. From the dynamic forming analysis of the copper sheet, it was observed that the strength of the sheet increased with the increase in the strain rate. In an another study, Ramezani and Ripin (2010) developed a numerical and theoretical approach to attain pressure-strain curves during this high strain rate bulge forming process. Recently, Simoncini et al. (2021) generated forming limit curves (FLCs) for AA6082-T6 sheet at different strain rates using the SHPB set up. The limit strains were determined on different sample geometries and compared with the results obtained under quasi-static loading condition. It was observed that the formability strongly improved as the strain rate increased from quasi-static to dynamic conditions.

Advantages

The modified SHPB as a dynamic bulge testing device can be easily utilized in lab scale as well as in industries to characterize the material properties at different strain rates.

Limitations

The use of fluid as a pressure medium complicates the process. Further, in the current set up, Digital Image Correlation methods (DIC) would add benefits and eliminate the need for inverse modeling.

1.2.5 High energy rate forming processes

During the high energy rate forming (HERF) operations, a large amount of energy is applied for a short period of time to deform the sheets to the final shape. Various HERF processes such as Electro Magnetic Forming (EMF), Electro-Hydraulic Forming (EHF) and Explosive forming (EF) are utilized to investigate the bi-axial forming behaviour of the material at different strain rates. The HERF processes are not only used to encase safe forming of complex parts but also utilized to identify the limiting strain. All of the HERF processes increase the forming parameters and highlighted three distinct mechanisms that could account for it: (a) the inertial effect generated during the experiment diffuses the neck development and it leads to an increase in ductility, (b) the variation in the material constitutive behaviour leads to increase in the formability, and (c) in closed die forming, the impact of the material with the die wall at high velocity causes the material to spread radially and it suppresses the necking and damage evolution. A detailed literature review on various HERF processes are given below.

1.2.5.1 Electro-magnetic forming

Working Principle

An electromagnetic forming (EMF) is a non-contact technology that uses pure electromagnetic interaction to impart significant forces to any electrically conductive work-piece (Imbert et al., 2005). EMF setup consists of a capacitor bank, a conductive coil, and the metallic sheet to be deformed. The forming coil, which is close to the metallic sheet is connected to the capacitor bank. By charging a large capacitor to a high voltage, it stores a significant amount of energy

(typically between 5 and 200 kJ). The charge is switched over low inductance conductive bus work through a coil or actuator. Large currents run through the coil and the peak current is normally in the range of 10 to 1000 kA. The time to peak current is measured in microseconds. This produces a very strong transient magnetic field in the vicinity of the coil. The magnetic field induces eddy currents in any nearby conductive materials in the similar way the primary circuit of a transformer induces voltage and current in the secondary (Psyk et al., 2011). As a result, currents will be induced in any metallic sheet nearby and these will normally be opposite in direction to the primary current. According to Lenz's law, the currents in the coil and the metallic sheet move in the opposite directions. The Lorentz force governs the electromagnetic repulsion between oppositely flowing currents, which produces the deformation in the metallic sheet. This can eventually lead the sheet to deform plastically at a speed more than 100 m/s. (Oliveira et al., 2005).

Process parameters and their influences

There has been a surge in interest in high-speed forming of light-weight materials in the recent years, which has accelerated the use of the EMF process in many industries. There are several process parameters which have influenced the dynamic forming behaviour of the material during EMF, and some of them are discussed below.

Several types of coil design were suggested with the purpose of better distribution of magnetic forces during EMF. Al-Hassani et al. (1974) investigated the sheet forming by EMF of aluminium sheets using four types of spiral coils on a die having holes. During this analysis, the magnetic pressure distribution was anticipated by measuring the height of the dimples formed. Further, they estimated the magnetic pressure distribution during the process analytically. Ahmed et al. (2011) observed that during the use of the flat spiral coils, the work-piece experienced marginal magnetic force, which led to improper deformation on the sheet. They proposed a new conceptual design of the flat coil, in which the EM forces was intentionally varied by changing the spacing between the turns for the better distribution of the magnetic forces over the work piece. Recently, Soni et al. (2021) studied the effect of various parameters of the coil design on its performance. It was observed that a small change in the diameter and effective number of turns of the coil would significantly change the amplitude of the current pulse and consequently different modes of deformation was also illustrated.

Golovashchenko (2007) performed comparative analysis between the traditional forming limit diagram (FLD) obtained by stretch of aluminium sheet with the hemispherical punch to the results obtained by EMF. They reported a significant increase in the formability of the sheet during the high strain rate forming condition. It was noticed that the forming in a V-shape die or into a conical die further increased the formability of the material. The influence of tool-sheet interaction on the formability was also studied by Imbert et al. (2005). During this study, the sheet was formed freely and by using a conical die. It was observed that employing a conical die increased the sheet's formability, particularly in the locations where the die and sheet come into contact. Chen et al. (2020) performed the die forming of deep-cavity sheet metals by a dual-coil EMF and observed higher accuracy with uniform thickness distribution. Recently, Su et al. (2021) also observed a significant improvement in the limit strains when the sheet was deformed into a conical die during EMF. They concluded that the large contact stress led to a minimum stress triaxiality value, which delayed the occurrence of fracture. Further, the inertial effect associated with the high velocity phenomenon helped to delay the onset of plastic instability during the initiation of necking and enhanced the maximum safe strain.

The inertial effect associated in EMF eliminates the springback and wrinkling phenomenon, which are the major limitations in conventional quasi-static forming processes. Padmanabhan (1997) studied the ways to prevent wrinkling and spring back during EMF of AA 1100-O sheets. The influence of various factors on the spring back and wrinkling were investigated and observed that the increase in the magnetic pressure would reduce the wrinkling. Xiao et al. (2019) used EMF along with the quasi-static stamping process to control the springback of aluminium alloys. They observed that the discharge voltage and number of discharges were the most important process parameters to control springback. The inertial motion developed during this high velocity phenomenon reduced the tangential stresses to a larger extent, which was the main cause of springback. Cui et al. (2019) developed 3D FE model for quasi-static stamping coupled with EMF to analyse the springback during the forming of U-shaped specimen and reported the similar phenomena for the reduction of springback.

To deform lower conductive sheets during EMF, a driver sheet is generally preferred that reduces the discharge energy. Xu et al. (2013a) observed a significant improvement in the

formability of AZ31 Mg alloy sheets during EMF when compared the forming limits with the quasi-static forming results. Aluminium driver sheets were used to accelerate the Mg alloy sheets and the discharge energy was reduced by nearly 50% while forming the sheet to same dome height with no driver sheet. In another study, Xu et al. (2013b) studied the formability of AZ31 Mg alloy sheets by using different thickness of the Al driver sheets. The forming limits of the Mg alloy sheets with 0.5 mm and 1 mm driver sheet were similar to those during the EMF process without driver sheet. However, the forming limits were dramatically increased with the 2 mm driver sheet as compared to the other two cases.

Recently, Yan et al. (2021) compared the deformation uniformity and springback of 7075-T6 sheet deformed by the traditional stamping, EM direct forming, and EM drive forming. AA 1050-O sheet was used as the driver sheet. The EM drive forming resulted in a minimum springback height. The additional part of energy for the deformation by the driver sheet improved the uniformity in deformation with larger forming height as compared to other forming processes.

In much research work, EMF is combined with different quasi-static processes to fabricate complex geometry with better accuracy. Liu et al. (2011) used different configurations of the coils and established a new hybrid method, in which quasi-static hydraulic bulging and EMF experiments were combined to deform AA5052-O sheets. The study demonstrated that the hybrid process significantly improved the material formability as compared to the quasi-static process.

Imbert and Worswick (2012) used EMF to form sharp features in AA 5754 sheets that were difficult to form using the conventional forming. In this work, a two-step forming operation was carried out, in which in the first step a conventional stamping tool was used to form a 20 mm outer radius V-channel. In the second step, a specially designed EM coil was used to sharp the outer radius to 5 mm. The inertial effect associated with the EMF formed the part to the desired shape without failure, which was difficult to achieve using conventional forming process. Further, the experimental data were validated with the FE simulation results performed by LS-DYNA.

Shang and Daehn (2011) developed a new approach, EM assisted sheet metal stamping process, to form a non-symmetric panel from AA 6111-T4 sheet. They observed a significant increase in draw depth and uniform distribution in strain as compared to the conventional

stamping, which helped to produce deeper pans in a single pass operation. Kiliclar et al. (2016) also utilized the similar approach to enhance the formability of AA5083 sheet. They combined the quasi-static deep drawing and EMF and observed an improvement in the forming limit beyond the quasi-static forming limit without damage. Meng et al. (2011) performed warm and electromagnetic hybrid forming on Mg alloy sheets and studied the effects of voltage, capacity, and temperature on the bulge height. A rise in formability was evident during the rise in forming temperature. Moreover, it was noticed that with the constant discharge energy, the bulging height first decreased (< 150°C) and then increased (> 150°C) from room temperature to 230°C.

Noh et al. (2015) developed a two-step EMF process to perform shaped deformation in Al 1100-O sheet. During the single pass EMF, large magnetic force generated a significant wrinkling on the surface of the work-piece. Thus, to achieve the desired shape, a large current was discharged during the second step of the forming. The final fit of the specimen was evaluated by 3D scanning, which revealed good fit with minimal wrinkling. However, it was concluded that the effectiveness of the process seemed to be negative during mass production because of the requirement of large input current.

The microstructural evolution of metallic materials during EMF has also been widely investigated. The mechanical twinning, dislocation slipping and adiabatic shear banding are regarded as the three dominant deformation mechanisms for metals under high strain rate deformation. Li et al. (2009) compared the deformation behaviour of AA5052-O sheets under quasi-static and dynamic tension conditions and concluded that due to the tendency of multi-slip motion of dislocations in dynamic loading conditions, the materials showed much higher plasticity and higher strength over quasi-static deformations. Wang et al. (2017) studied the effect of EM bulging on the fatigue behaviour of the AA 5052 sheets and reported that the bulged specimens exhibited enhanced fatigue strength as compared to the original Al alloy. From the TEM analysis, it was observed that the enhancement in the fatigue strength and increased resistance to fatigue crack propagation was caused due to strain hardening and dislocation shielding effect.

Advantages

EMF has many advantages that make this process an alternative technique of conventional forming processes. Among all the high-speed forming techniques EMF is one of the most suitable techniques of plastic deformation. The major advantages of EMF are listed below:

i. During EMF, the sheet metal experiences improvement in mechanical properties in terms of reduction in spring back and wrinkling. Stretching exceeds conventional process limits thus improving the ductility of the material.

ii. Fabrication of very close tolerances are possible because of the elimination of spring back during such high-velocity forming process.

iii. There is a significant savings in tooling costs as single sided dies are adequate to fabricate the end product.

iv. The process is highly reproducible and the production rate becomes high, as the current passes through the forming coils is the only variable during the forming operation.

v. The process of forming becomes environmental friendly because of the no use of lubricants. This also makes the operation zone out of messy and stinky environment.

Limitations

Besides several advantages, there are some disadvantages of the EMF process:

i. It is restricted to the materials with a high electrical conductivity. However, non-conducting or low conductive material can be formed by the help of a driver sheet. Further, this adds to the operation's complexity.

ii. Very large sheet metal components cannot be formed, because of the design of large coil.

iii. The EMF is relatively inefficient, as only around 20 % of the charging energy is really used for plastic deformation.

iv. Because of the enormous currents and voltages involved in EMF operation, there are many safety risks involved in it.

Applications

The demand of sheet and tubular components in the current automotive, aerospace and nuclear industries require high productive, low-cost and robust forming processes. In such cases, the EMF can produce parts with complex shape with high accuracy.

1.2.5.2 Electro hydraulic forming

Working principle

Electro-hydraulic forming (EHF) is a high-strain rate forming process that uses a high-voltage discharge between two electrodes in a liquid-filled chamber to deform the sheets (Ahmed et al., 2017). During the high voltage discharge, the majority of the energy held in the capacitors is released in a short period of time (usually around 100 µs). As a result, it vaporizes a small volume of the liquid and creates a high-intensity shock wave that travels through the water towards the sheet. The shock wave simultaneously transforms the metal work-piece into a visco-plastic state (rate-dependent plastic behaviour of metals) and accelerates it onto a die, allowing complicated shapes to be formed at high speeds at room temperature (Rohatgi et al. 2012). The entire forming process completes within milliseconds.

The EHF process can be carried out either in free condition, which is represented as electro-hydraulic free forming (EHFF), or with the use of a die, which is called as electro-hydraulic die forming (EHDF) (Rohatgi et al., 2012). During EHFF, the sheet decelerates at the end of the forming and it results in the decrease in the strain rates at the end of the operation. Further, in EHDF process, if the initial energy is insufficient to fully form the part, the blank speed might be affected and there would be no formability improvement. The main limitation in EHF is the lack of the availability of a bank of capacitors that store sufficient energy. The amount of energy required for a discharge highly dependent on the part's size and the material grade of the sheet metal. Most of the time, EHF is best suited for small to medium-sized sheets and tubes with relatively thin wall thickness (Golovashchenko et al., 2013).

Process parameters and their influences

The EHF is more flexible manufacturing process than EMF, because it is more economical and it does not require an expensive machine and complicated dies as in the case of EMF. Several consecutive electrical discharges in EHF can be utilised to completely fill the die of calibrate the spring back without removing the die. There are several process parameters, which affect the forming condition of sheet metal as discussed below.

During EHF, the electrical discharge from the capacitor bank produces a range pressure pulses in the water medium and it results in different magnitude of bulge heights. Rohatgi et

al. (2011) quantified different deformation parameters such as displacement, velocity, strain and strain rate of AA5182-O sheets using EHF under free-forming condition at different discharge voltages and observed a monotonic increase in the deformation parameters. Homberg et al. (2010) successfully achieved the forming of sharp edge contour of high strength steel using EHF process. During this analysis. They formed a smaller radius of 0.8 mm by a discharge energy of less than 6 kJ, whereas the minimum possible radius of curvature could be formed by quasi-static hydroforming was 1.75 mm.

Golovashchenko et al. (2013) deformed DP590 sheets into a V-shaped die and to a conical die by varying the discharge voltage and reported the optimum experimental conditions to fill the dies. Further, they measured the maximum strains at some critical locations and observed a substantial increase in formability as compared to the conventional limit dome height (LDH) results. Shim and Kang (2017) also performed EHF of AA5052-H32 sheets under different charging voltages and could able to deform sharp edges of less than 2 mm radius of curvature.

The high velocity phenomenon in EHF increases the forming limit significantly as compared to the conventional quasi-static processes. Balanethiram and Daehn (1992) reported the increase in the formability of interstitial free steel when deformed at high strain rate using EHF. The forming outputs were compared with the FLD obtained from quasi static punch stretching test and observed a threefold improvement in in-plane failure strain without any substantial change in the material constitutive behaviour. It was argued that the improvement is due to the effect of inertia in stabilizing neck growth and not due to change in material constitutive behaviour.

In another study, Balanethiram et al. (1994) investigated the improvement of formability in EHF as a hyperplastic phenomenon. Using conical dies with an apex angle of 90° in biaxial stretching, the formability of Al 6061-T4, oxygen-free high-conductive (OFHC) copper and interstitial free iron was instigated. The axisymmetric expansion of Al 6061-T4 ring was also investigated in order to observe the material's uniaxial behaviour at high strain rates. Biaxial deformation showed a significant improvement in formability, but uniaxial deformation showed just slight improvement.

The effect of free forming and closed end die forming on the formability of the material during EHF has been investigated in many literatures. Rohatgi et al. (2012) investigated the influence of open (free forming) and conical closed dies in EHF of AA5182-O and DP600

sheets with the help of deformation history. It was discovered that conical closed die produced better results when compared to open die forming. The amplification in forming output was attributed to the focusing action of the conical geometry of the die.

Jenab et al. (2018) also studied the formability of AA5182-O sheet using EHF and compared the results with the forming limit curve (FLC) obtained by quasi-static forming. It was observed that the formability improvement was insignificant when the sheets are formed without a die. However, with the help of a conical die, the effective strain in the safe region was increased by 70 % when it was compared to quasi-static FLC. The combined effect of increased strain rate, negative stress triaxiality, compressive through-thickness stress generated by high-velocity impact attributed to the improvement in the formability of during EHDF. Maris et al. (2016) also investigated the formability of AA5182-O sheet under EHFF condition and observed 8 % increment in the limiting strain as compared to quasi-static FLC.

In a recent study, Woo et al. (2017) eliminated the bouncing effect using EHF which was a major limitation in EMF during the forming of a complex geometry. The water present between the sheet and the chamber helped the sheet to reduce the bouncing did not bounce off the die played an important role as a medium to propagate forming pressure and it helped to make a positive contact with the die at the corners. Additionally, the formability of the sheet is enhanced with no cracks and wrinkles. In another work, Woo et al. (2019) examined theoretical FLD for AA 6061-T6 during EHF using the LS-DYNA program. The tensile test data obtained from SHPB test were incorporated along with Hosford's yield function during the prediction of the theoretical FLD. The obtained FLD showed an improvement in formability at a high strain rate when compared with the quasi-static data. Further, the FLD was compared with the experimental results from EHF free-bulging test, which showed a good correlation between the results.

The improvement in the formability of the material during EHF is correlated with the fracture morphology in many literatures. Ahmed et al. (2017) compared the traditional quasi-static FLD with the EHF results for AA5052 alloys. The limit strains were confirmed to have increased by nearly 45−50 % because of the inertial stabilization. The dimples present in the fractured surface of EHF samples were much bigger and deeper than the quasi-static samples, which indicated that the material had undergone much larger plastic deformation prior to failure in case of EHF. Jenab et al. (2017) investigated the damage mechanisms of AA5182-O

sheets deformed during quasi-static forming and EHF process. The results confirmed that void nucleation, growth and coalescence were the main damage mechanisms in both high and low strain rates. The deformed sheet under quasi-static condition had more voids whereas during EHF, the void formation was supressed due to the high-velocity impact of the sheet against the die and resulted in improvement in the formability.

Advantages

Major advantages of EHF are listed below.

i. Only single-sided dies are required during EHF that significantly reduces the cost of dies as compared to the conventional stamping, which requires mating dies.

ii. During this process, the solid punch is replaced by water. Thus, the friction caused by the contact between the punch and the work-piece is therefore eliminated on one side of the specimen. As a result, the forming force is distributed more evenly throughout the surface of the work-piece, which reduces the stress concentrations and failure initiation.

iii. EHF is a single-step process in comparison to the conventional stamping process, which is usually a multistep progressive process that requires a series of die sets. This simplifies the manufacturing process by lowering the expenses. Further, during the fabrication of complex geometries, several successive discharges can be utilized to fill the die completely to reduce spring back without removing the die.

iv. As pressure pulse developed due to the electrical discharge are mainly utilized during EHF, both the conductive and non-conductive material can be deformed without any special arrangement.

v. The elimination of tooling and fixture design reduces the complexity of the process and it is reliable and well suited for high-volume production.

Limitations

Besides several advantages, there are some disadvantages of the EHF process:

i. The volume of the equipment is too large and it requires large area to keep.

ii. The high speed of the process requires more safety and skilled personnel.

iii. Higher thickness of the work piece is difficult to form.

iv. The sheet profile is usually convex after forming.

Applications

From large body panels to miniature sized and components with complicated profile in automotive and aerospace industries can be easily manufactured by EHF with higher accuracy.

1.2.5.3 Explosive forming

Working principle

Explosive Forming (EF) is one of the conventional high-strain rate forming processes, which has been preferred particularly in the aerospace industries to fabricate large shaped parts (Mynors and Zhang, 2002). The pressure required to shape the work-piece in EF is generated for a short duration by the detonation of explosive charge. The explosion can be performed in contact with the material or positioned at a distance from the material using both air and water as the pressure transferring medium. The EF can be done either in to a die or as a free forming condition. It is widely used in numerous industries to fabricate complex parts from high strength steel and aluminium alloys, due to its excellent repeatability and ability to produce large and geometrically complex parts with good accuracy. The EF experiences a rapid growth in many industries because of less investment in the machine tools and die sets. However, the decline in aerospace activity gradually reduces its usage in recent years.

Process parameters and their influences

The pressure energy developed during EF is mainly decided by the explosive charge used during experiment. Several numerical analyses have been performed along with the experiment to optimize the process parameters used during this process. Mousavi et al. (2007) estimated the explosive charge size necessary to form a blank to a specific depth of draw. With the FE analysis, they predicted the optimum stand-off distance to deform a part with uniform thickness distribution and decrease in spring back. Jacob et al. (2007) studied the effect of stand-off distance and charge mass on the response of fully clamped circular mile steel sheets. Various, theoretical and empirical analyses were also performed to predict the mid-point deflection of the sheets.

Though EF is a traditional forming process, many companies and military establishments still continue to use EF as a regular manufacturing process. Nishiyama and Inoue (1968) performed free forming of a circular steel blank using an air bag during EF and observed a

remarkable improvement in the formability as compared to the conventional forming process. The use of air bag improved the efficiency of energy utilization remarkably during this forming process. Tiesheng et al. (1992) utilized a non-die EF technique to fabricate thin-wall spherical parts, which was difficult to form in conventional forming procedure. The process showed high dimensional accuracy with less wrinkling than conventional punch forming and did not require any special set of dies and forming devices. Fengman et al. (2000) also used similar non-die EF to form thin-wall semi-spherical parts and spherical container with good dimensional accuracy.

In many research works, explosives have been utilized to study the dynamic response of thin metallic sheets. Jones et al. (1970) investigated the dynamic plastic behavior of fully clamped rectangular plates when subjected to uniformly distributed impulsive velocities developed by explosive loading. Nurick and Shave (1996) used similar experimental arrangement to study the deformation and tearing of thin mild steel sheets. Three different modes of deformation such as mode I (large plastic deformation), mode II (tensile tearing and deformation) and mode III (transverse tears) were experimentally identified. Rajendran and Narasimhan (2001) performed underwater contact explosion on HSLA steel sheets and investigated the dynamic response of the sheets. Further, a new damage prediction model was proposed by relating the input shock energy, the contour of deformation, the material properties and the thickness of the sheet, and the predicted dynamic deformation had a good agreement with the experimental observation. Spranghers et al. (2012) analyzed the full field measurements of transient nature deformation of aluminium plates under free air blast loading conditions. 3D high speed DIC system was used for the assessment of the dynamic response of the structure such as surface displacement and deformation accurately at the blast loading condition.

Yasar et al. (2006) deformed cylindrical cups of aluminium alloy sheets by a gas detonation forming system using acetylene (C_2H_2)-oxygen (O_2) mixture at varied volume ratios. Babaei et al. (2015) used similar apparatus to conduct experiments on a clamped circular mild steel sheet. Further, they developed an empirical model to predict the mid-point deflection versus impulsive loading and also the strain-rate sensitive behavior of the sheet during such large deformation at high strain rates. In another work, Mostofi et al. (2017) also used gas mixture detonation loads to study the dynamic response of thin metallic sheets in safe limit and beyond

the safe limit. The developed empirical model also assessed the dynamic plastic response accurately.

In some recent work, EF has been utilized to instigate the forming behavior of sheets at different strain rates. Dariani et al. (2009) experimentally investigated the effect of forming velocity on FLDs for Al 6061-T6 and AISI 1045 sheets. Further, the FLDs obtained at low impact (50/s) as well as explosive free-forming (1000/s) were compared with the conventional FLDs at quasi-static condition. The results showed a substantial improvement in formability at high strain rate for aluminium sheets, whereas it was not considerable for steel sheets.

Advantages

i. The impact nature of the pressure developed during EF deforms the material uniformly with lesser springback. Thus, EF becomes advantageous during the forming of complex geometries.
ii. It is generally preferred to fabricate large parts because of the uniform distribution of pressure during forming in both air as well as water medium.
iii. The lesser investment in the die sets and tools reduces the capital cost.

Limitations

i. EF is not economically viable during mass production of the components.
ii. The complexity in instrumentation and handling restricts the application to some specially equipped industries.

In order to minimize these limitations and to study the dynamic behavior of the materials, the shock tube facility has been used recently in various research laboratories, which works on the same phenomenon (Kumar et al., 2012).

1.2.5.4 Shock tube based forming

Working Principle

A shock tube is a device that creates a gas flow condition that is difficult to achieve with conventional gas flow devices. It is a laboratory apparatus that can produce high velocity, pressure, and temperature conditions for a short interval of time, allowing it to be used in the aerodynamic and thermo-chemical engineering. It is made up of a long rigid cylinder that is split into two sections: a high-pressure driver section and a low pressure driven section. A

diaphragm made of a metal sheet or by the layers of thin Mylar sheets separates the two portions. The diaphragm ruptures when the pressure difference between the driver and driven sections reaches a threshold value, causing a rapid release of gas and it creates a shock wave inside the tube. It propagates with a Mach number greater than one along the driven section. The schematic illustration of the pressure variation inside the shock tube is represented in Fig. 1.3.

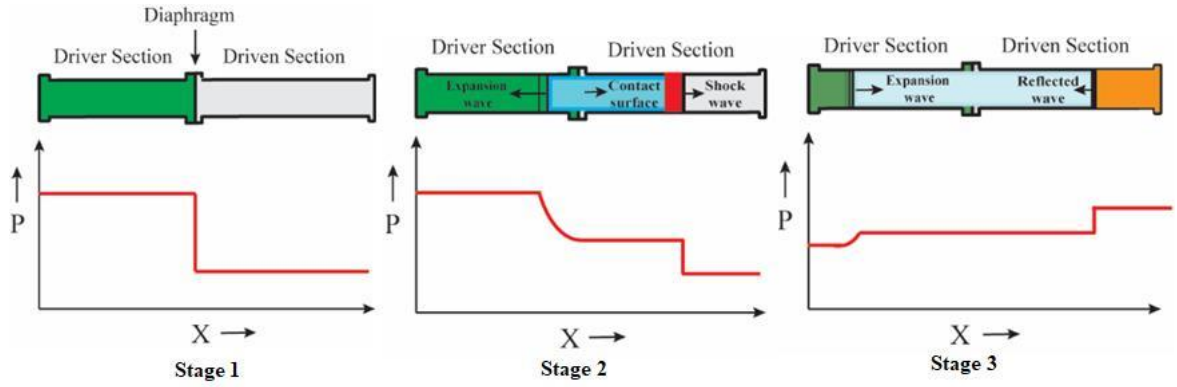

Fig. 1.3: Working principle of shock tube

The magnitude of shock Mach number (M_s) is decided by various factors. The main factor is the thickness of the diaphragm. In most of the studies, constant layers of Mylar sheets have been considered to generate the required magnitude of Mach number repetitively. The speed of the shock wave is also influenced by the gas used in the driver section. For example, during an experiment, for a constant bursting pressure (21.87 bar), the heavier gas such as nitrogen (N_2) travels slowly down the tube resulting in lower Mach number (M_s = 1.86), whereas lighter gas such as helium (He) allows for higher Mach number (M_s = 2.5). Applying vacuum prior to bursting across the driven section also influence the shock wave to travel faster than the normal speed. The propagation of the shock wave generates a high-pressure and high-temperature gas behind it. The equations describing the change in pressure and temperature with respect to the speed of the shock wave are well described in the work of Kumar et al. (2012). When the shock wave travels down the tube and imparts on an end wall, it is reflected back by producing a higher pressure and temperature gas behind the reflected shock wave (Fig. 1.3). In the shock tube, the high pressure field zone is developed for a short interval of time after the incident shock wave is reflected back. The shock tube's end wall can be replaced with sheets or composite metals to study their dynamic behavior and failure mechanism.

Process parameters and their influences

In recent studies, the shock tube facility has been preferred instead of explosive to generate blast loading environment. The major process parameter that affect the pressure induced during the shock tube experiment is bursting pressure of the driver gas. It is mainly decided by the diaphragm thickness. However, the pressure inside the driven section of the shock tube is kept at atmospheric pressure during such shock tube experiment. There are many literature where the shock tube has been utilized to understand the blast response of the composite materials.

LeBlanc et al. (2007) studied the effect of shock loading on three-dimensional woven composite materials using a shock tube. The specimens were exposed to certain range of reflected pressure which was decided by the bursting pressure created by various thickness of Mylar diaphragm. The material's resistance to shock loading was evaluated from the magnitude of permanent deflection, internal damage, and post-mortem compressive strength.

Tekalur et al. (2008) used polyurea in the E-glass vinyl ester composites to improve the blast resistance of the material during shock tube experiment. In another study, Tekalur et al. (2009) used the shock tube to investigate the dynamic damage behavior of E-glass fiber composites, which depicted a progressive pattern of damage during the dynamic loading.

LeBlanc and Shukla (2010) studied the effect of underwater shock loading on an E-Glass/Epoxy composite material using a water filled conical shock tube. Strain gauges were used to measure the in-plane strain generated on the specimen during the experiment. The fluid-structure interaction and the dynamic damage mechanism were realistically modelled using LS-DYNA and the obtained results had a good correlation with the experimental findings. In another investigation, Leblanc and Shukla (2011) used the same shock tube facility to determine the response of E-Glass/Vinyl ester curved composite panels to underwater explosive loading. The transient response of the panels was measured using a three-dimensional Digital Image correlation (DIC) system. The deformation and velocity time histories at several points on the back face of the specimen were used to evaluate the effectiveness of each laminate subjected to shock loading.

Wang et al. (2011) developed a new fluid-structure interaction model using the Rankine-Hugoniot relations to determine the reflected pressure profile from the known incident pressure profile. Further, various physical parameters of the gas such as the shock front velocity, gas

density, local sound velocity, and the impulse transmitted onto the structure were also evaluated through the proposed model and validated with the shock loading experiments.

Pankow et al. (2011) presented the deformation response and development of damage in 3D glass fiber textile when subjected to different magnitude of shock wave based pressure loading. Further, finite element models were developed using ABAQUS to capture matrix micro-cracking, which was responsible for the damage development.

Wright et al. (2014) performed the shock tube based experiments on graded, corrugated steel sandwich panels with high speed digital photography to capture the sequential collapse mode of the sandwich panels. With the same shock tube, Black et al. (2018) conducted an experimental study to evaluate the compressive residual strength of glass fiber/epoxy laminates after exposed to different magnitude of shock wave based loading.

In some recent work, the shock tube has also been used to study the dynamic response and forming behavior of thin metallic sheet. Kosing and Skews (1998) utilized a liquid shock tube to perform high-speed metal forming of circular copper sheet. The better control and increase in safety gave advantages to use it for high-velocity forming of the sheet in comparison to explosive forming. The deformation of the copper sheet was measured and the true stresses and true strains were determined. A theoretical approach was used to predict the midpoint deflection and the energy absorbed by the deformation of the specimen. In another study, Skews et al. (2004) used the same shock tube facility to perform high-velocity forming of sheets and tubes in both free forming condition and forming into an imprinted die. Different projectile materials, driving pressures and impact velocities were used to alter the energy and impulse transmitted. It was observed that the forming method had a potential to fabricate products with better accuracy and repeatability which was difficult in conventional forming methods.

Stoffel et al. (2001) used the conventional shock tube to investigate the dynamic behavior of steel sheets. Further, a material model was developed by considering the elastic-plastic behavior, isotropic and kinematic hardening and strain rate sensitivity of the material and the evolution of deflection, stresses and plastic zones are predicted and validated with the experimental results. In another study, Stoffel (2004) predicted the dynamic response of a steel sheet and a cupper sheet subjected to shock loading using different elastic-viscoplastic laws to obtain their accuracy. Further, the final height of deformation of a shock wave loaded sheet

and quasi-statically deformed sheet with the same loading pressure were compared. It isobserved that impulsive loading condition generated a larger height with conical shape of deformation.

Kumar et al. (2012) conducted both the experimental and numerical investigation on the effect of plate curvature on blast response of aluminium panels using a shock tube. A 3D digital image correlation (DIC) technique coupled with high speed photography was used to instigate out-of plane deformation, velocity and the in-plane strain generated during experiment. The transient response of the panels during impact loading was evaluated by a dynamic computational simulation by incorporating fluid-structure interaction.

The repeatability and reliability in generating shock waves in the diaphragmless shock tube makes it advantageous than the conventional shock tube to be used in industries. Nagaraja et al. (2012) developed a diaphragmless shock tube to perform high-velocity forming of thin metallic sheets. The results obtained from the experimental investigation were repeatable and had a good correlation with the FE simulation results.

Justusson et al. (2013) retrieved the bi-axial rate-dependent mechanical properties of thin aluminium sheets using a shock tube. The DIC technique is used to record the out of plane deflection and strain fields. The rate dependent constitutive properties of the material were determined using an inverse modeling technique in conjunction with the finite element (FE) simulation.

Patil et al. (2018) used a shock tube to investigate the deformation of stacked metallic sheets. The low intermetallic friction among the stacked sheets provided better deformation than a single metallic sheet of the same thickness. In a recent work, Patil et al. (2019) utilized a rapid compression machine (RCM) to study the high-speed deformation behavior of aluminum sheets. The forming behavior and damage predicted by their numerical simulations were in good agreement with their experimental results.

The intra-granular misorientation on aluminium sheet while studying the effect of shock wave based deformation at the microstructural level was observed by Ray et al. (2015). During this study, the improvement in hardness indicated the absence of recovery and strain hardening. Together with this, Bisht et al. (2017) investigated the changes in the crystallographic orientation and microstructure of a thin pure copper sheet subjected to the high strain rate deformation in a shock tube. A significant change in grain orientation was observed with

increasing amount of effective strain without any drastic change in the grain size. Further, the evolved texture was found to be strain-dependent. In another study, Bisht et al. (2019) used the same shock wave assisted deformation process to understand the microstructural response of FCC metals and also elucidated the role of stacking fault energy on the evolution of microstructure and texture.

The shock tube facility can also be used to provide momentum to the rigid body located inside the shock tube by the high-pressure induced air. For instance, Koohbor et al. (2016a) used an aluminium projectile inside the shock tube to impact directly on a polymeric foam to study its energy-absorbing capacity using 3D DIC technique, and also evaluated the inertial stresses developed within the specimen during the deformation. In another study, Koohbor et al. (2016b) utilized the velocity of the projectile to study the dynamic deformation of the polymeric foam by deforming it to a large magnitude of plastic strain. In this study, they computed the total axial stress of the material by superimposing the inertial stresses calculated from the acceleration distribution.

Gupta et al. (2008) used a pneumatic gun to drive different nosed projectiles and investigated the deformation behavior of the layered aluminium plates. Kpenyigba et al. (2013) used a similar pneumatic gas gun and different shaped projectiles to study the perforation process of thin steel sheets. Rusinek et al. (2009) used a Hopkinson tube to understand the failure process of mild steel sheets subjected to impact loading by a hemispherical projectile. The numerical models were also able to describe the physical perforation mechanism accurately. In the similar way, the shock tube facility can also be utilized to study the ballistic limit and the perforation behavior of the material at different loading conditions.

Advantages

The major advantages of the shock tube based forming are listed below.

i. The uniformity in loading and ease of handling make the shock tube facility easy to use to study the dynamic behaviour of the sheet and composite materials at intermediate to high strain rates.

ii. The pressure energy developed because of the rapid motion of the shock wave is responsible for the deformation. Thus, both the conductive and non-conductive materials can be used to study their deformation behaviour at high strain rates.

iii. The inertial effect developed due to the impulsive loading condition stretches the sheet metal significantly without strain localization. It results into higher formability than the conventional forming.

iv. The dynamic loading in the shock tube reduces the Spring-back significantly in comparison to conventional quasi-static forming operations. This simplifies the problem related to the die design significantly.

v. The process is environmental friendly and can be used in laboratory scale as a dynamic loading device by following the required safety and precaution.

Limitations

i. The repeatability of the shock tube experiments is not so accurate because of the use of Mylar diaphragms. However, this error can be eliminated by mounting a quick opening valve between the high pressure driver section and low pressure driven section.

ii. Deforming sheets up to failure by the shock wave based forming can be obtained by increasing the capacity of the shock tube facility. Together with this, this may require huge amount of driver gas and a sophisticated safety chamber.

iii. The bursting of diaphragm creates large noise during the experiment.

Applications

The shock tube facility can be used in lab scale as well as in industries to investigate the dynamic behaviour of sheets and composite materials. Further, addition of a closed end die at the end of the shock tube can be useful to fabricate an end product with low-cost and high accuracy.

1.2.6 Introduction to dynamic forming of friction stir welded sheet

As discussed earlier, the lightweight construction in automotive and aerospace industries increases the usage of aluminium and magnesium alloys significantly. However, joining the structures made from these materials by the conventional welding processes (like fusion welding and/or resistance spot welding) is difficult because of the inconsistent weld quality (Manladan et al., 2017). Therefore, friction stir welding (FSW), which is a solid state welding process, became a potential candidate because of its higher joint efficiency (Cai et al., 2019).

In FSW, a non-consumable rotating tool is gradually plunged into the adjoining edges of the sheets to be welded. Heat is generated due to the friction and it softens the material being

welded. The intensive stirring caused by the rotating tool uniformly mixes the softened material in both the sheets. After a certain dwell time, the tool is withdrawn and a solid state joint is formed between them. This method lies in the direct conversion of mechanical energy to thermal energy to generate weld without the application of heat from any external source. Friction stir spot welding (FSSW), which is derived from FSW, is used mostly to join sheet metals in lap configuration. It has been preferred to join aluminium alloy sheets in lap configuration instead of riveting or resistance spot welding because of advantages such as excellent mechanical properties, less distortion, low cost, higher energy saving, and ease of producing reliable joints consistently (Çam and İpekoğlu, 2017). It has been observed that various process parameters such as tool geometry, tool rotational speed, plunge speed, plunge depth, dwell time and tool tilt angle affect both FSW and FSSW joint formation and it directly influences the mechanical properties of the welded joint. Thus, optimizing the process parameters is vital to generate a good quality weld.

In transportation applications, strain rates in the range of 10^2 to 10^3 are often observed. It is observed that Al alloys are strain rate sensitive when the rate of loading reaches a threshold limit (Smerd et al., 2006). Therefore, it is necessary to study the rate-dependent mechanical behaviour of the welded sheets at different regime of strain rates. Ambriz et al. (2013) studied the tensile properties, fracture behaviour of Aluminium FSW sheets at a constant speed of 10 m/s, and found that like base material, the ductility of the welded joint increased at higher strain rate. Doley and Kore (2017) studied the formability of Tailor Welded Blanks (TWB) made of AA5052-H32 and AA6061-T6 sheets using both quasi-static and EM forming process and a significant improvement in formability was observed during EMF. Recently, Forcellese and Simoncini (2020) investigated the high-speed deformation behaviour of FSW thin sheets of AA 6082-T6 in a SHPB set up. The dome height at the onset of necking under dynamic condition was significantly higher than the height obtained during the quasi-static loading condition.

Though literatures on the dynamic forming of the FSW sheets are limited, forming behaviour analysis at quasi-static regime also gives an insight about the forming limits and failure patterns of the welded sheets. In a research work, Lee et al. (2009) investigated the formability performance of TWB sheets of AA6111-T4 and AA5083-H18 materials using limit dome height (LDH) tests. It was observed that the weld zone of AA6111-T4 sheets had lower

flow stress with slightly reduced ductility, whereas the weld zone of AA5083-H18 had significantly improved ductility with lower flow stress as compared to the base materials. Kim et al. (2010) evaluated the formability of FSW sheet with respect to the different material direction for AA6111-T4 sheets during simple tensile test, hemispherical dome stretching test and cylindrical cup drawing test. Numerical prediction was also performed by using the failure criterion along with anisotropic yield function to capture the onset locations of failure. Kesharwani et al. (2017) performed LDH test on dissimilar aluminium TWBs and observed that the use of a modified conical tractrix die set up enhance the limit drawing ratios by 22 %. The failure was always initiated at the weaker location of the thick sheet and it was propagated across the weld. Habibi et al. (2018) also investigated the FLDs of TWBs produced by FSW of low carbon steel and demonstrated the effect of the welding seam directions on the formability.

In the case of FSSW sheets, several joint performance tests such as lap shear test, cross-tension test, peel test and uniaxial tensile test have been performed in many literatures to understand the mechanical strength of the joint (Rana et al., 2018). Bozzi et al. (2010) studied the influence of tool rotational speed and plunge depth on the FS spot weld strength of AA 5182 sheets and observed that larger size of stir zone (SZ) created at higher rotational speed helps to increase the tensile shear strength of the joint. Rana et al. (2018) also represented similar observation for the FSSW joint of AA 5052 sheets. Further, they mentioned that the cross-tension strength, and the uniaxial tensile strength decrease with the increase in the tool rotational speed. Most of the studies focus on evaluation of the static strength of the FSSW joint. There is no literature available on characterization of the FSSW joint under dynamic loading conditions. However, some research works focus on evaluation of the dynamic strength of resistance spot welds of similar and dissimilar materials. Recently, Sun and Khaleel (2007) evaluated the dynamic strength of self-piercing rivets and resistance spot welds of dissimilar Al sheets using servo-hydraulic test frames with high rate actuators. They observed a decrease in displacement to failure with the increase in the loading rates. Langrand and Markiewicz (2010) studied the mechanical strength of the spot welds under quasi-static and dynamic loading conditions to understand the effect of strain rate and modes of failure under different loading conditions. In the similar way, the dynamic characterization of the FSSW joint can also be performed, which has significant importance in many industrial applications.

1.2.7 Significance of the work

With the emerging interest in light-weight design in the automotive sectors with a continuous attempt to improve the fuel economy, the steel grades are replaced by different aluminium alloys. In many research works, the major limitation, i.e., inferior formability of aluminium alloys at room temperature is eliminated by deforming them at high-velocity. The high-velocity forming processes develop an inertial effect that delays necking by developing additional tensile stress outside the neck resulting in enhanced formability. In the recent past, various HERF processes have been preferred in many industries to fabricate end products at higher accuracy without any defects. Despite several advantages of HERF processes, the major limitations are the higher capital cost, difficulties in machine handling, and requirement of skilled persons.

In some recent work, the shock tube facility has been introduced as a dynamic loading device. The rapid release of gas in the shock tube generates a shock wave, and it creates dynamic loading at the end of the shock tube because of the rapidly induced mass motion. The benefit of the shock tube is utilized in the present study as a dynamic bulging device to investigate the forming behaviour of sheets at different strain rates. In addition to this, the high pressure induced gas developed inside the shock tube can be used to propel a rigid body at a high velocity, which can deform a material at even higher strain rates. This facilitates the shock tube as a dynamic Erichsen sheet testing device, which allows to study the rate-dependent forming behaviour, and the failure mechanism of the sheets.

It has been observed that during such dynamic deformation, most of the materials exhibit distinct loading states (Smerd et al., 2006). To better understand the dynamic behaviour of aluminium alloys, several empirical, semi-empirical, and physics-based flow stress models incorporating the effects of strain rate and temperature have been presented in the past. Various ductile fracture criteria have also been proposed, which can be utilized in conjunction with a FE model to predict sheet failure and forming limit. Thus, in the present work, the influence of different stress-strain constitutive models and failure models have been studied during the prediction of the dynamic forming and failure of sheets deformed using shock tube.

Generally, in sheet metal forming processes, the blank is typically made of one piece. Thus, in the last decade, research on the forming behaviour of the welded sheet increased significantly. To join aluminium sheets in lap configuration, FSSW, which is derived from

FSW is mostly preferable because of its better mechanical strength and good quality of weld. Many research activities focus on several joint performance test such as lap shear test, cross-tension test, peel test and uniaxial tensile test. Scarce attempts are made to understand the effect of welding parameters during dynamic forming of the FSSW sheet. Thus, in the present study, it is aimed to understand the deformation and failure response of Aluminium sheets with FS spot welds under impact loading generated using the shock tube.

1.2.8 Motivation and objective of the work

The main motivation of this thesis is to utilize the advantages of the shock tube facility during the forming of the thin sheets. The uniformity in loading environment during shock wave based deformation analysis encourages to use the shock tube as a dynamic bulge testing device. Apart from that, the shock tube facility can be introduced as a dynamic impact testing device, in which a hemispherical end nylon striker can be moved at a high velocity inside the shock tube to deform thin metallic sheet. It will help to understand the rate-dependent forming behaviour, as well as the failure mechanism of the sheets.

Based on the research opportunity, the present work focuses on the study to understand the forming behaviour and failure response of AA 5052 H-32 sheets of two different thickness 1 mm and 1.5 mm. AA 5052-H32 sheet is chosen in this study because of its diverse application in aircraft and automotive industries. It has a higher strength to weight ratio, better toughness, ductility, and corrosive resistance than the other available light-weight materials.

The main objective of the present work is two-fold- (i) To analyse the effect of various material processing parameters on the deformation of thin metallic sheets during shock tube based forming, and (ii) To predict the material forming behaviour of thin metallic sheets during shock tube based forming for efficient process design.

The important sub-tasks to achieve the objectives are

- Understanding the effect of pre-strain on the forming behaviour of thin sheets during shock wave based deformation analysis.
- Understanding the influence of different striker velocity during impact forming of thin sheets using the shock tube.
- Evaluating the effect of different welding parameters during impact forming of sheets with FS spot welds using the shock tube.

- Comparative assessment of the failure strain and fracture behaviour after shock tube based forming predicted by different flow stress models in conjunction with different failure models.

1.2.9 Organization of thesis

The thesis consists of seven chapters, which are organized as follows:

- **Chapter 1** gives an overview about the dynamic behaviour of aluminium alloys and different experimental facilities that have been utilized to study the forming behaviour of sheets with their merits and demerits. Further, the shock tube facility is introduced and its application as a dynamic loading device is discussed. The forming performance of FSWed sheets is also discussed with different challenging issues. Finally, the significance of the work and detailed objectives of the present thesis are described.
- **Chapter 2** focuses on both the experimental and numerical analysis of the forming behaviour of AA 5052-H32 sheets deformed using a shock tube. During this study, the effect of bending pre-strain, pressure, and thickness on the material forming behaviour is analyzed.
- **Chapter 3** introduces the shock tube facility as a dynamic Erichsen sheet testing device, in which the high-pressure induced air is utilized to propel a hemispherical end nylon striker to deform AA 5052-H32 sheet of 1 mm thickness. the sheet is deformed both in the safe limit and beyond the safe limit for better assessment of the dynamic behaviour of the material.
- **Chapter 4** focuses on a study to understand the effect of the choice of flow stress models and failure models during the prediction of failure strain and fracture pattern during the shock tube based impact forming of 1.5 mm thick AA 5052-H32 sheets. To achieve this, the forming of the sheets is modelled in DEFORM-3D and the results are validated with the experiment performed using the shock tube.
- **Chapter 5** deals with an investigation to understand the dynamic forming behaviour of Friction Stir Spot Welded (FSSW) sheet made of AA 5052-H32 sheets of 1 mm thickness. In this study, the effect of tool rotational speed and plunge speed on the FSSW joint is understood and its forming behaviour is analyzed during shock tube based impact forming experiment.

- In **Chapter 6**, the effect of tool rotational speed and plunge depth on the FS spot welding outputs are analyzed and their influence during shock tube based impact forming is investigated.
- **Chapter 7** represents the major findings of the present work and future scope in the field of shock tube based impact forming. The outcome of the present work is presented in the form of various journal papers and conferences.

Chapter 2

Forming response of sheets deformed through gas loading using a shock tube

Overview

The present study focuses on both the experimental and numerical analysis of the forming behavior of AA 5052-H32 sheets deformed at a high-velocity using a shock tube. The effect of bending pre-strain, pressure, and thickness on the material forming behavior has been analyzed. Various forming parameters such as dome height, strain evolution, effective strain, and stress distribution are predicted by FE simulation using DEFORM-3D FE code and validated by the experimental results. The sharp rise in strain evolution matches quite well with the experimental results obtained by strain rosette. It confirms the rate of stretching of the sheet during the forming process. Circular grids are printed on the sheets, and Hill's 1948 yield criterion is used to calculate the effective strain. Along with this, Hollomon's power law calculates the effective stress on the same location. The experimental effective stress and strain distribution match quite well with the numerical results with slight over prediction. The distribution of the stress and strain confirms the uniform stretching of the material without strain localization. The variation of the forming parameters asserts that the forming behavior is dependent on the degree of pre-strain, and they increase monotonically with the rise in pressure.

2.1 Material details and geometry of the specimen

In the present investigation, the forming behavior of AA 5052-H32 sheets of two different thicknesses, 1 mm and 1.5 mm, has been studied. AA 5052-H32 sheet has wide applications in the automotive and industrial sectors, because of its higher strength to weight ratio, better toughness, ductility, and corrosive resistance than the other available light-weight sheet materials. The chemical compositions of the base materials are obtained by EDX analysis, and the elemental distribution is illustrated in Table 2.1. In order to demonstrate different levels of

bending pre-strain, the sheets are bent to 100 mm (R_{100}) and 150 mm (R_{150}) radius of curvature by sheet rolling machine with an arc length of 180 mm (Fig. 2.1). The flat sheets (R_{∞}) are also considered for a comparative analysis to understand the effect of bending pre-strain on the forming behavior of the material. The sheets are pre-strained along the 0° to the rolling direction, as shown in Fig. 2.1. All the samples have the same free deforming area of dimension 180 mm length × 180 mm wide. In order to characterize the mechanical properties of both the sheets, tensile samples are cut along the 0°, 45° and 90° to the rolling direction (RD) by a Wire-Electro Discharge Machine (Wire-EDM), and the tests are performed according to the standard ASTM E-8 with a cross-head speed of 1 mm/min. The true stress-strain curve for both the thickness sheets is shown in Fig. 2.2. ASTM E-517 is followed to obtain the plastic strain ratio (r) of both the materials along 0°, 45°, and 90° to RD to clarify the effect of anisotropy caused due to cold rolling. The plastic strain ratio (r) is defined by

$$r = \frac{\varepsilon_w}{\varepsilon_t} \tag{2.1}$$

where width strain (ε_w) = $\ln\left(w_f / w_o\right)$, thickness strain ($\varepsilon_t$) = $\ln\left(t_f / t_o\right)$, w_o = initial gauge width, w_f = final gauge width, t_o = initial sheet thickness, t_f = final sheet thickness. The mechanical properties of both the thickness sheets are enlisted in Table 2.2. Though the plastic strain ratio (r) of both the sheets are not varying significantly at different orientations, their effects are noticeable during the variation in elongation, as well as the stress developed in uniaxial testing. Thus, these values are considered during the FE simulation for a better prediction of bi-axial sheet metal forming. The results also depict that the tensile properties of both the thickness sheets are varying in a small range. This confirmation ensures to begin a study to understand the effect of thickness during the sheet metal forming.

Table 2.1: Chemical composition of AA5052-H32 sheets (Weight percentage)

Materials	Mg	Cu	Si	Fe	Mn	Cr	Al
AA5052-H32 (1 mm)	2.68	0.10	0.92	0.31	0.13	0.32	Balance
AA5052-H32 (1.5 mm)	2.82	0.06	0.22	0.39	0.08	0.28	Balance

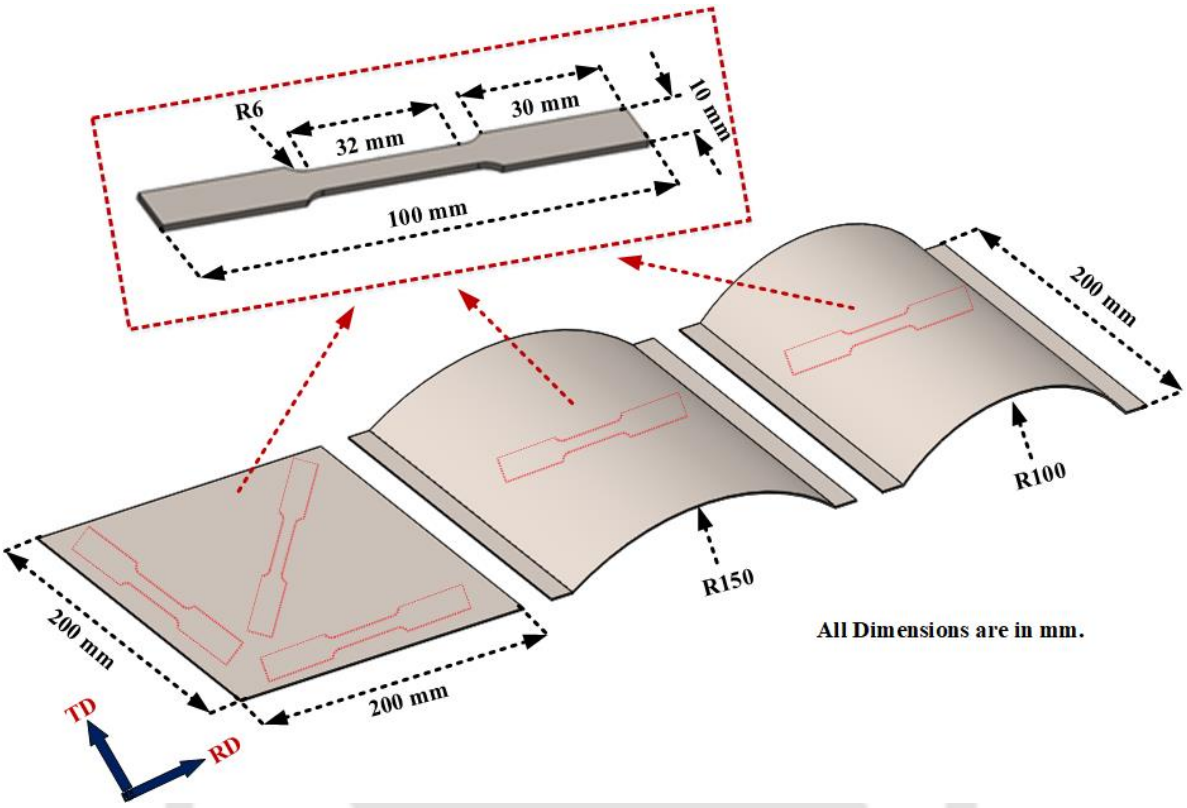

Fig. 2.1: Tensile sample cut from both the flat sheet and pre-strained sheet

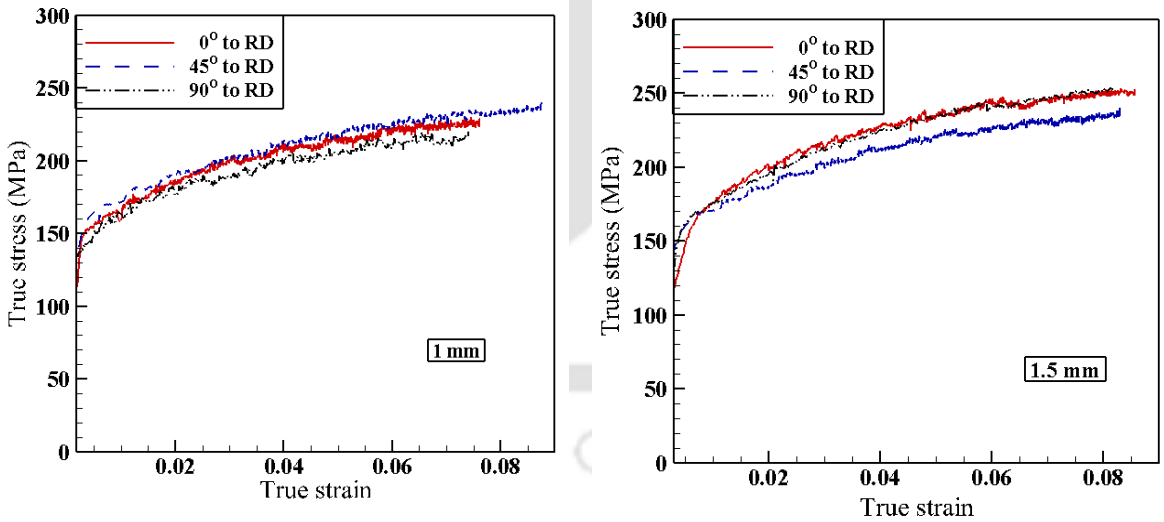

(a) (b)

Fig. 2.2: True stress-strain curve of AA 5052-H32 sheets of thickness (a) 1 mm and (b) 1.5 mm

Table 2.2: Initial mechanical properties of AA5052-H32 sheets

Material	RD	σ_{ys} (MPa)	σ_u (MPa)	n	K (MPa)	ε_u (%)	ε_t (%)	r
AA5052-H32 (1 mm)	0°	158 ± 2	225 ± 3	0.17	350 ± 3	7.8 ± 1.4	8.5 ± 1.2	0.73 (r_{RD})
	45°	168 ± 3	239 ± 3	0.18	376 ± 3	8.6 ± 0.8	9.1 ± 0.9	0.85
	90°	152 ± 2	219 ± 2	0.19	358 ± 4	7.6 ± 1.2	8.4 ± 1.1	0.85 (r_{TD})
AA5052-H32 (1.5 mm)	0°	167 ± 2	246 ± 2	0.18	393 ± 2	8.5 ± 1.3	10.1 ± 1.2	0.73 (r_{RD})
	45°	161 ± 1	237 ± 3	0.19	373 ± 4	8.2 ± 1.2	9.7 ± 1.1	0.73
	90°	168 ± 2	252 ± 3	0.17	398 ± 2	8.1 ± 1.2	9.8 ± 1.2	0.71 (r_{TD})

σ_{ys}: Yield Strength; σ_u: Ultimate Tensile Strength; n: Strain Hardening Coefficient; K: Strength Coefficient; ε_u: Uniform Elongation; ε_t: Total Elongation; r: Plastic Strain Ratio; Gauge length: 25 mm

In order to understand the effect of bending pre-strain on the mechanical properties of the sheets, tensile samples are cut along 0° to the rolling direction of the pre-strained sheets by a Wire-EDM as shown in Fig. 2.1. The pre-strained (bent) tensile samples are tested in a Universal Testing Machine (UTM) without any post-treatment at a crosshead speed of 1 mm/min. The mechanical properties of the pre-strained sheets are shown in Table 2.3 and the tensile test graphs are also illustrated Fig. 2.3. The results indicate that the yield strength (σ_{ys}) and ultimate tensile strength (σ_u) of both the materials increase than the flat sheet because of the bending pre-strain. The mechanical properties of the pre-strained sheets are shown in Table 2.3. Due to the strain hardening effect, the strength coefficient (*K*) of the material increases significantly. However, there is a small variation in the strain hardening exponent (*n*) is observed. The rise in mechanical strength of the material after the bending pre-strain may be attributed due to the twinning induced hardening and dislocation hardening (Li et al., 2009; Liu et al., 2011). The material properties obtained from the tensile tests of the pre-strained sheets are considered during the numerical simulation to predict the other forming parameters.

Table 2.3: Mechanical properties of the pre-strained sheet in comparison to parent sheet (0° to RD)

Tensile Properties	**AA5052-H32 (1 mm)**			**AA5052-H32 (1.5 mm)**		
	Flat	**R_{150}**	**R_{100}**	**Flat**	**R_{150}**	**R_{100}**
σ_{ys} **(MPa)**	158 ± 2	173.34	180 ± 3	167 ± 2	175.63	181 ± 3
σ_u **(MPa)**	225 ± 3	239.75	242 ± 3	250 ± 2	252.58	258 ± 4
n	0.17	0.18	0.18	0.18	0.18	0.19
K	350 ± 3	376 ± 4	381 ± 4	393 ± 2	403 ± 4	412 ± 3
ε_u	7.8 ± 1.4	7.5 ± 1.4	7.4 ± 1.2	8.5 ± 1.3	7.3 ± 1.4	7.5 ± 1.4
ε_t	8.5 ± 1.2	7.9 ± 1.2	8.1 ± 1.2	10.1 ± 1.2	8.9 ± 1.2	9.3 ± 1.2

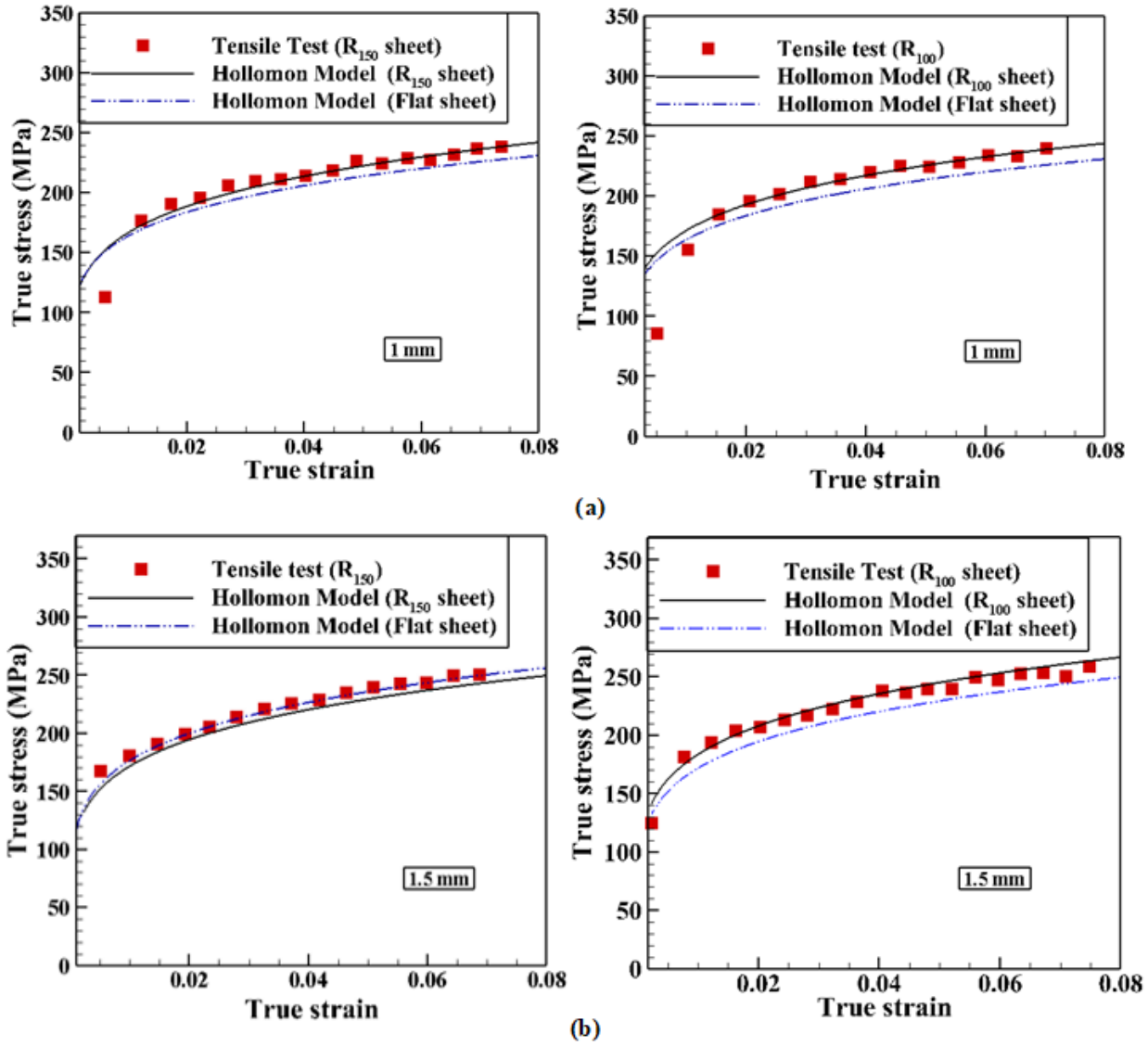

Fig. 2.3: True stress-strain curve of AA 5052-H32 pre-strained sheets of thickness (a) 1 mm and (b) 1.5 mm

2.2 Shock tube experimental facility

The shock tube has been introduced in various studies to conduct sheet metal forming experiments in moderate to high ranges of strain rates ($20 - 850\ s^{-1}$). It is a laboratory device, which is capable of generating high velocity ($400 - 700$ m/s), and pressure ($3 - 30$ bar) conditions simultaneously (Justusson et al., 2013; Kumar et al., 2012). The basic working principle of the shock tube is discussed earlier in Section 1.2.5.4. The shock wave generated inside the shock tube travels down and when it imparts to the end, it reflects and generates a higher pressure and temperature condition than the incident one. The high-pressure field zone

is created for a short duration of time, which induces impact loading at the end of the shock tube. This impulsive environment can be utilized to assess the dynamic behavior of the material. It can replicate the standard bulge testing device to stretch the material bi-axially and understand the variation in forming properties in a moderate to higher range of strain rate by using the pressurized air instead of the hydraulic fluid.

In the current experiment, due to the curvature of the specimens, the end of the shock tube cannot be closed. It enforces the tests to be conducted in the open condition under the atmospheric pressure in the driven section. During the experiment, high-pressure nitrogen (N_2) gas is used as the driver gas because it is cheap and readily available, and the air is used as driven gas for all the set of experiments. Thin layers of Mylar sheets of thickness 0.25 ± 0.01 mm are used as diaphragm to create a pressure difference between the two sections. The experimental set-up used during this study is illustrated in Fig. 2.4.

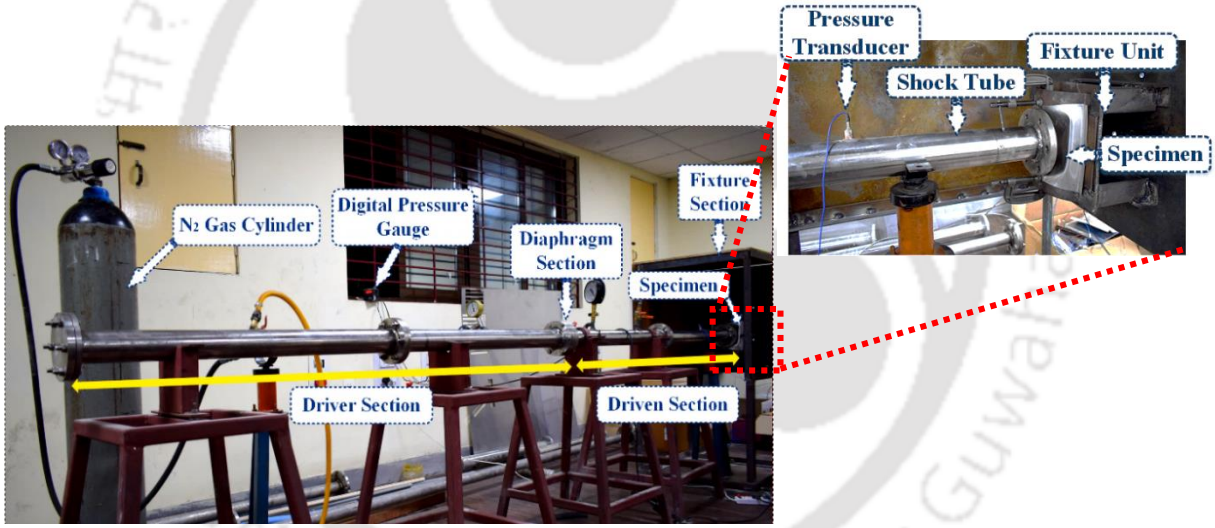

Fig. 2.4: Shock tube facility used during the experiments

The shock tube used during this study has an overall length of 4 m, having a 2 m of driver section and 2 m of driven section, as depicted in Fig. 2.5. The inner diameter of both the driver and the driven section is 55 mm, with a thickness of 10 mm. Two different bursting pressures are attained during the experiment, such as 24.13 ± 1.03 bar and 31.02 ± 0.68 bar by rupturing four and five layers of Mylar sheets, respectively. A digital pressure gauge has been mounted at the driver section to measure the bursting pressure. Two pressure transducers (P_1 and P_2) having sensitivity 14.62 mV/bar are mounted at a distance of 385 mm and 885 mm from the end of the shock tube (Fig. 2.6) to measure the incident pressure, reflected pressure and the

shock Mach number (M_s) generated during the experiments. In order to measure the impulsive pressure experienced by the specimen during shock loading, the third pressure transducer (P_3) having a similar configuration is mounted on a calibration plate. The calibration plate is in contact with the driven section of the shock tube during the calibration of pressure (Fig. 2.6). However, the calibration plate is replaced by the experimental specimens during further experiments. Both the pre-strained sheets and the flat sheets are also in contact with the driven section of the shock tube at the beginning of the experiment. Fig. 2.7 depicts the pressure histories obtained from the three pressure transducers at two different experimental conditions. The signals from the pressure transducers are processed through a signal conditioner (PCB Piezotronics Model 482C) and recorded by the digital oscilloscope (Tektronix MDO 3024) having a maximum sampling rate of 2.5 GS/s. Both the experiments are performed thrice to ensure the repeatability of the obtaining parameters. The average incident, reflected pressure and shock Mach number (M_s) obtained during both the experiments are shown in Table 2.4.

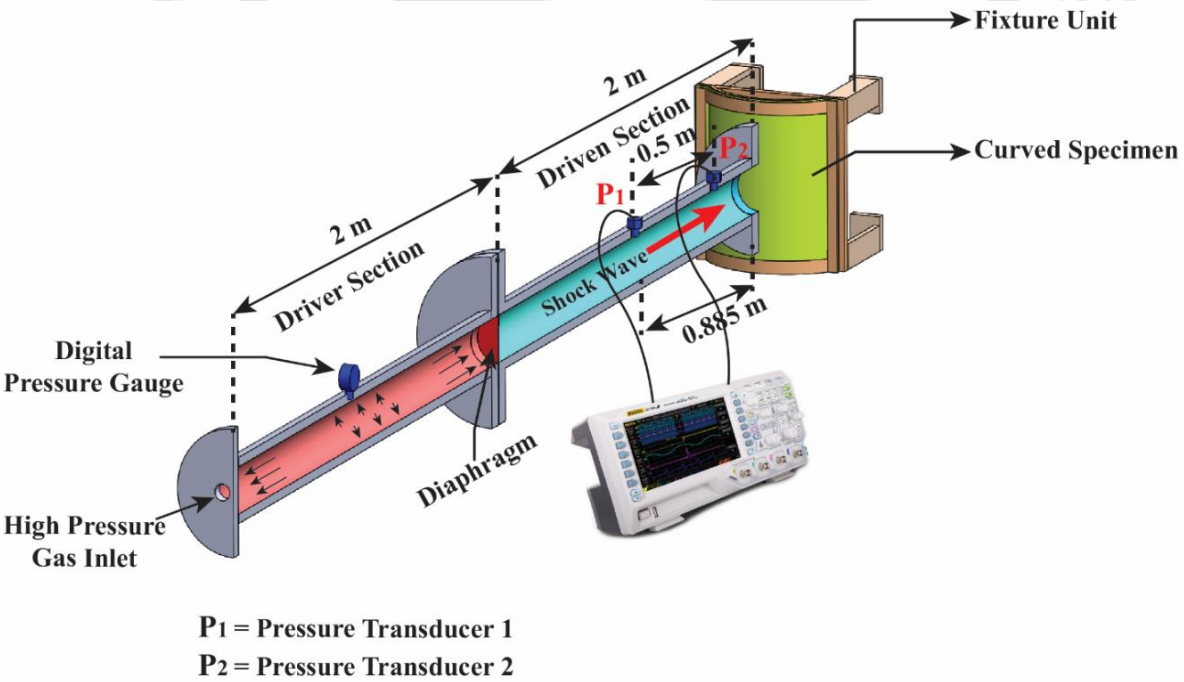

Fig. 2.5: Schematic diagram of the shock tube facility

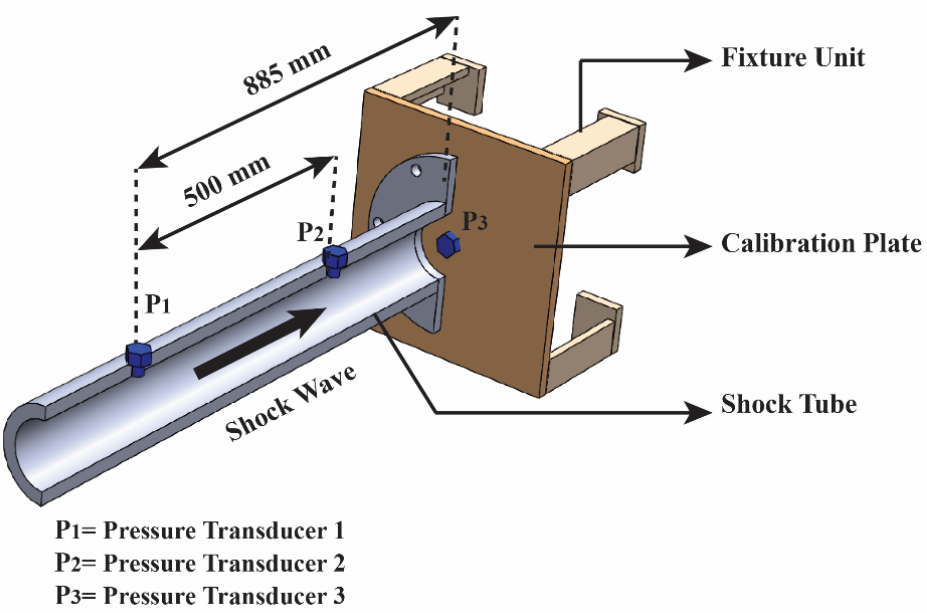

Fig. 2.6: Pressure transducers mounted on the shock tube for the calibration of induced pressure

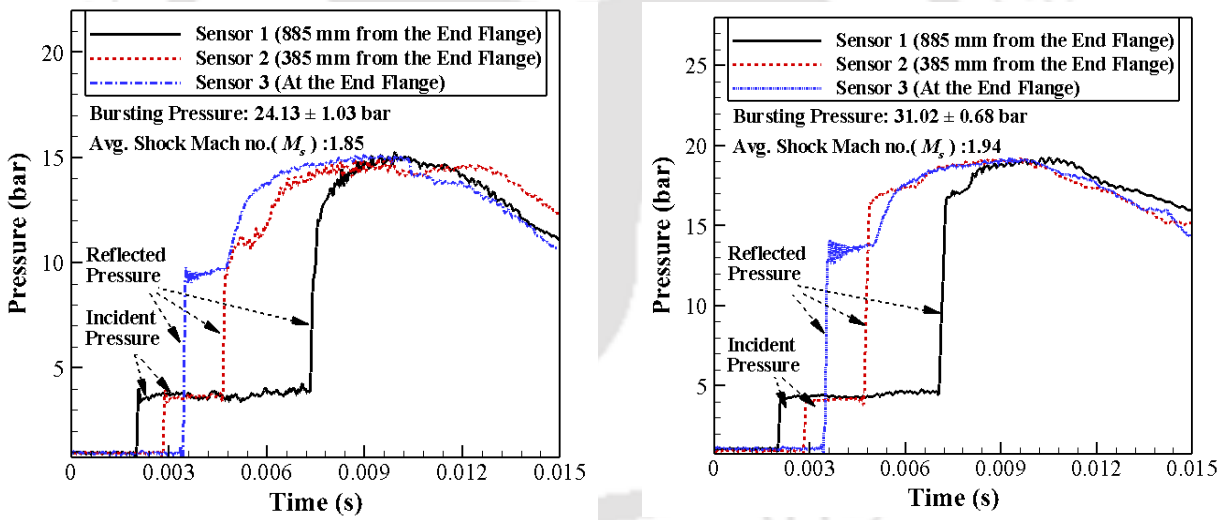

Fig. 2.7: Pressure jump across the shock wave at different bursting pressures (a) 24.13 ± 1.03 bar (b) 31.02 ± 0.68 bar

Table 2.4: Average magnitude of pressure obtained from the experiments

Diaphragm (Mylar sheets)	Avg. Burst pressure, bar	Avg. Incident Shock pressure, bar	Avg. Reflected shock pressure, bar	Avg. Shock Mach number
4 layers	24.13 ± 1.03	3.73 ± 0.48	14.83 ± 0.62	1.85 ± 0.02
5 layers	31.02 ± 0.68	4.32 ± 0.82	19.02 ± 0.55	1.94 ± 0.02

2.3 Shock tube experiments

As the present study is carried out to understand the forming behavior of the pre-strained (bent) sheets in comparison with the flat sheets, the specimens are clamped such that the convex surface of the specimens faces towards the shock tube (Fig. 2.5). In all the curved fixture units, sufficient forming area of dimension 180 mm × 180 mm is provided, such that there should not be any restriction to the free forming of the samples. The final out of plane deflection of the specimens is measured by a vertical height measuring dial gauge having precision ± 0.01 mm. For convenience, the rolling direction of all the samples has been considered as X-axis, whereas perpendicular to it, i.e., transverse direction has been considered as Y-axis. In order to witness the variation in hardness and grain size, the deformed sheets are cut from the three different locations as shown in Fig. 2.8. Vickers's hardness has been measured by applying 500 gmf load for 10 seconds. The deformed samples are perfectly polished and chemically etched by Keller's reagent at ambient conditions to reveal the microstructure of the deformed region. The average grain size has been measured by line intercept method as per ASTM E1382.

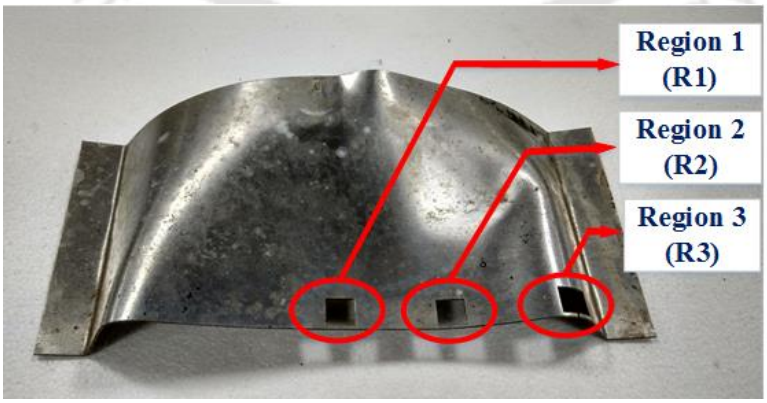

Fig. 2.8: Regions considered for grain size and hardness measurement

2.4 FE simulation of shock wave based deformation of sheets

2.4.1 Finite element formulation

Numerical simulation is not only a design verification tool but also a method to optimize the process parameters of an experimental study. In this present work, the dynamic forming behavior of AA 5052-H32 is predicted under different strain rates using a FE code DEFORM-3D. The impulsive loading environment during the shock tube based deformation process allows to model the problem as a transient, non-linear dynamic three-dimensional analysis which can be solved by Lagrangian incremental method developed for the metal forming processes in DEFORM-3D environment. In order to have an accurate prediction of the material forming, the FE formulation takes into account the flow stress model, yield function and flow rule during the calculation. In the present work, the material is assumed to follow Hill's 1948 yield criterion (Wagoner and Chenot, 1996) and the associated flow rule. Hill's 1948 yield criterion is given by

$$F(\sigma_{22}-\sigma_{33})^2+G(\sigma_{33}-\sigma_{11})^2+H(\sigma_{11}-\sigma_{22})^2+2L\sigma_{23}{}^2+2M\sigma_{31}{}^2+2N\sigma_{12}{}^2=2f\left(\sigma_{ij}\right) \quad (2.2)$$

where f is the yield function; σ_{ij} denotes the stress components; *F*, *G*, *H* ,*L*, *M*, and *N* are the material constants that reflects the anisotropic behavior of the material.

During plastic deformation, the stress and the strain are related by the flow rule and it is given by

$$d\varepsilon_{ij}=d\lambda\frac{\partial f(\sigma_{ij})}{\partial\sigma_{ij}} \quad (2.3)$$

where dλ is an arbitrary constant.

In the principal coordinate system, the principal strains ($d\varepsilon_1, d\varepsilon_2, d\varepsilon_3$) can be obtained by differentiating eq. 2.2 with respect to the three principal stresses and substituting into the flow rule (Wagoner and Chenot, 1996). The principal strains ($d\varepsilon_1, d\varepsilon_2, d\varepsilon_3$) are represented as

$$\begin{aligned} d\varepsilon_1 &= d\lambda\left[G\left(\sigma_1-\sigma_3\right)+H\left(\sigma_1-\sigma_2\right)\right] \\ d\varepsilon_2 &= d\lambda\left[F\left(\sigma_2-\sigma_3\right)+H\left(\sigma_2-\sigma_1\right)\right] \\ d\varepsilon_3 &= d\lambda\left[G\left(\sigma_3-\sigma_1\right)+F\left(\sigma_3-\sigma_2\right)\right] \end{aligned} \quad (2.4)$$

where σ_i represents the principal stress. The arbitrary constant ($d\lambda$) can be obtained by considering the equivalent work definition of effective strain increment, $d\bar{\varepsilon}$. The arbitrary constant ($d\lambda$) is given by

$$d\lambda = \frac{1}{G+H}\frac{d\bar{\varepsilon}}{\bar{\sigma}} \tag{2.5}$$

Effective strain ($\bar{\varepsilon}$) is represented as (Wagoner and Chenot, 1996)

$$\bar{\varepsilon}^2 = \frac{G+H}{(FG+FH+GH)^2}\left[F^2(G+H)\varepsilon_1^2 + G^2(F+H)\varepsilon_2^2 + H^2(F+G)\varepsilon_3^2\right] \tag{2.6}$$

Hill's constant (*F*, *G*, and *H*) can be related to the plastic anisotropy parameters (r_0, r_{90}) by considering the normality condition as $F = r_0; G = r_{90}; H = r_0 r_{90}$.

Effective stress ($\bar{\sigma}$) is given by (Wagoner and Chenot, 1996)

$$\bar{\sigma}^2 = \frac{F}{G+H}(\sigma_2-\sigma_3)^2 + \frac{G}{G+H}(\sigma_1-\sigma_3)^2 + \frac{H}{G+H}(\sigma_1-\sigma_2)^2 \tag{2.7}$$

The effective stress ($\bar{\sigma}$) and effective strain ($\bar{\varepsilon}$) can be related by various flow stress models. The finite element formulation of visco-plastic material is based on the variational approach (Buffa et al., 2006; Pashazadeh et al., 2014). According to this approach, the actual velocity, u_i should satisfy the conditions of compatibility and compressibility and, the velocity boundary conditions. The actual solution gives the following functional a stationary value:

$$\pi = \int_V E_w(\dot{\varepsilon}_{ij})dV - \int_{S_F} F_i u_i dS \tag{2.8}$$

where F_i is the surface tractions, u_i is the velocity component, *V* is the volume of the work piece, S_F is the force surface, and E_w denotes the work function, which gives (Pashazadeh et al., 2014)

$$\sigma'_{ij} = \frac{\partial E_w}{\partial \dot{\varepsilon}_{ij}} \tag{2.9}$$

The solution of the original boundary-value problem is obtained from the solution of the dual variational problem, where the first order variation of the functional vanishes. It is represented as

$$\delta\pi = \int_V \bar{\sigma}\delta\dot{\bar{\varepsilon}}dV - \int_{S_F} F_i \delta u_i dS = 0 \tag{2.10}$$

A penalized form of the incompressibility is added to remove the incompressibility constraint on the admissible velocity fields. The actual velocity filed is determined from the stationary value of the variation as follows (Buffa et al., 2006; Pashazadeh et al., 2014):

$$\delta\pi = \int_V \bar{\sigma}\delta\dot{\bar{\varepsilon}}dV + K_p\int_V \dot{\varepsilon}_v\delta\dot{\varepsilon}_v dV - \int_{S_F} F_i\delta u_i dS = 0 \tag{2.11}$$

where K_p is the penalty constant, which is a large positive constant for volume change, and $\dot{\varepsilon}_v = \dot{\varepsilon}_{ii}$ is the volumetric strain rate, δu_i is arbitrary variation and $\delta\dot{\bar{\varepsilon}}$,and $\delta\dot{\varepsilon}_V$ are the variations of strain rate derived from δu_i .

It is difficult to attain a complete solution that satisfies all the governing equations in a single step. Therefore, FEM uses two different solvers, i.e. conjugate gradient solver and sparse solver during the calculation. The conjugate gradient solver tries to solve a problem iteratively by approximating the solution and it results in to decrease in solving time and memory. However, in certain problems when the work-piece undergoes a rigid motion of deformation or lower contact among the dies, etc., the conjugate solver is prone to non-convergence. In such cases, the sparse solver is advantageous for solving the problem by using the sparseness of the FEM formulation, i.e. it stores only the non-zero terms of the matrix during the calculation to improve the speed of the simulation.

In order to avoid deformation locking under material incompressibility, the penalty method and mixed formulation are employed for the 3D tetrahedral element. When the penalty method is applied to the functional of the metal forming process, the velocity becomes the primary solution variable (Li et al., 2001). After the nodal velocities are solved at a given time step, the deformed configuration is obtained by updating the nodal coordinates. As various material nonlinearities are involved in this process, the stiffness matrix and the solution is obtained iteratively. The iteration control used in the FE solver helps to find out a solution at each step of the simulation and tries to approach towards converged step solution. Two different iterative methods such as direct method and Newton-Raphson method has been used during the numerical simulation to solve a problem iteratively. The convergence of Newton-Raphson method is usually very good if the initial guess velocity is close to the actual solution. However, for complex processes when the initial guess solution is difficult, the use of direct method is more appropriate. In this study, sparse solver + direct method is used as the solver during FE simulation of shock tube-based sheet deformation.

2.4.2 Material constitutive behavior

During the impulsive deformation process, the material undergoes large deformation at a higher strain rate. Therefore, to capture the correct mechanical behavior of the material, it is essential to define the flow stress of the material as a function of temperature, strain, and strain rate. During the study, the work-piece is defined as a rigid visco-plastic material, i.e., the material is rate-dependent, but the elastic deformation of the material is neglected to achieve a better convergence. The characterization of the plastic behavior of the material requires a specific hardening law, a yield function and a flow rule by which the subsequent plastic deformation can be calculated. Neto et al. (2014) referred that the material behavior based on an anisotropic yield function and isotropic hardening is acceptable to get a good result in the numerical simulation of the sheet metal forming. Thus, isotropic hardening behavior is modeled by Hollomon's equation ($\sigma = K\varepsilon^n$), which is the most suitable model for aluminium sheets.

2.4.3 Identification of material parameters

In the present work, the elastic behavior is considered isotropic and constant, and it is defined by Young's modulus and Poisson's ratio as enlisted in Table 2.5. The conventional uniaxial tensile test identifies the material parameters for the work hardening law. The stress-strain data obtained from the tensile test of all the pre-strained sheets are fitted to Hollomon's equation ($\sigma = K\varepsilon^n$), and the material constants are calculated (Table 2.3). The same material properties are used to recalculate the flow stress-strain data and incorporated it into the FE model. Since the materials are deformed at a high-velocity, only the quasi-static flow stress-strain data is not enough to predict the dynamic behavior of the material. Thus, rate-dependent material properties can also be considered during the FE simulation. Generally, in the high-strain rate metal forming simulation, Cowper-Symonds model has been used in most of the studies to consolidate the rate-dependent material properties (Cui et al., 2016; Liu et al., 2009). The Cowper-Symonds model is given by

$$\sigma = \sigma_{qs}\left(1+\left(\frac{\dot{\varepsilon}_{pl}}{C_m}\right)^{\frac{1}{p}}\right) \tag{2.12}$$

where σ is the dynamic flow stress, σ_{qs} represents the quasi-static constitutive behavior of the sheet, $\dot{\varepsilon}_{pl}$ is the strain rate, C_m = 6500 s^{-1}, and the p = 4 are the specific parameters for the aluminium alloys (Cui et al., 2016; Liu et al., 2009). The Cowper-Symonds material model scales the initial quasi-static stress by the strain rate factors (C_m, p) to represent the mechanical behavior of the material at high strain rates.

During this present study, the rate-dependent material parameters are obtained by a new method, i.e., by the tensile testing of the deformed sheet. The tensile sample cut from the mid location of the deformed sheet by the Wire-EDM machine, as shown in Fig. 2.9. There is no additional post-treatment performed on the tensile sample after cutting. The bent tensile samples are tested in UTM at a crosshead speed of 1 mm/min to obtain the rate-dependent properties of the material under the working strain rate condition. The tensile test data obtained from the deformed sheets are fit to the Hollomon's power law, and the material constants are obtained (Table 2.6).

Table 2.5: Parameters considered for numerical simulation

Parameters	**Data**
Mass density, ρ (kg/m^3)	2432
Young's modulus, E (MPa)	68,900
Poisson's ratio, υ	0.33
Stress-strain relation curve	From Table 2.3 and Table 2.6
Plastic strain ratio (r)	From Table 2.2
Coulomb's coefficient of friction (μ)	0.1

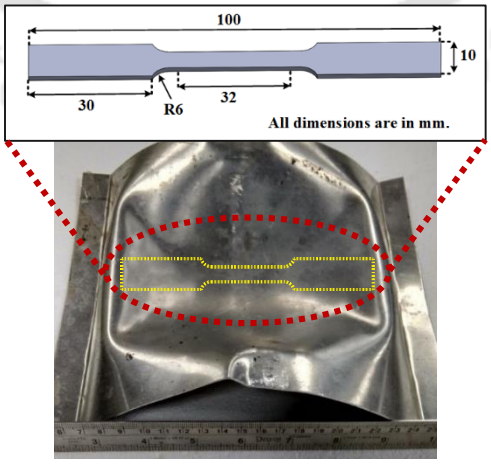

Fig. 2. 9: Tensile sample cut from the deformed sheet

The results illustrate that the yield strength (σ_{ys}) and the ultimate tensile strength (σ_u) of the materials increase as compared to the parent materials in both the thickness sheets. The strain hardening phenomenon further raises the strength coefficient (*K*) of the materials. However, the strain hardening coefficient (*n*) does not change significantly after deformation. Those material constants are again utilized to obtain the rate-dependent flow stress-strain curve for a larger strain value and compared to the Cowper-Symonds relation for the validation. The strain rate of deformation ($\dot{\varepsilon}_{pl}$) required during the calculation of flow stress in Cowper-Symonds relation is obtained experimentally by the help of the strain rosette (Table 2.7), and it is discussed in Section 2.6. A perfect correlation is observed between both the flow stress curves with a slight over prediction. Fig. 2.10 shows a typical comparison between the Hollomon's power law and Cowper-Symonds relation for R_{100} sheet of 1 mm thickness, deformed at a bursting pressure of 31.02 ± 0.68 bar. The results also depict a comparison between the tensile data of R_{100} base sheet and R_{100} deformed sheet at a high strain rate. It illustrates the rate-dependent phenomenon where the mechanical strength of the sheet increases significantly after deformation. This analysis confirms that the method used to obtain the rate-dependent material properties from the deformed sheets is liable and can be considered in the FE simulation instead of Cowper-Symonds relation to incorporate the actual dynamic behavior of the material. The rate-dependent mechanical properties (Table 2.6) are incorporated into the FE simulation for the prediction of the dynamic forming behavior. The flow stress ($\bar{\sigma}$) is defined as the function of strain (ε) and strain rate ($\dot{\varepsilon}$) during the simulation, and the data is fed to the numerical simulation in the form of tabular data. The flow stress is represented as

$$\bar{\sigma} = \bar{\sigma}\left(\varepsilon, \dot{\varepsilon}\right) \tag{2.13}$$

The other parameters considered during the FE simulation are shown in Table 2.5.

Table 2.6: Tensile properties of the sheets after shock tube based deformation

	Tensile Properties	As Received	Bursting pressure, 24.13 ± 1.03 bar			Bursting pressure, 31.02 ± 0.68 bar		
			R_{100}	R_{150}	Flat	R_{100}	R_{150}	Flat
AA5052-H32 (1 mm)	σ_{ys} (MPa)	158 ± 2	189 ± 4	181 ± 4	172 ± 4	216 ± 3	189 ± 4	192 ± 3
	σ_u (MPa)	225 ± 3	249 ± 5	241 ± 5	230 ± 4	274 ± 3	259 ± 3	256 ± 4
	n	0.17	0.17	0.17	0.19	0.17	0.17	0.18
	K (MPa)	350 ± 3	397 ± 4	386 ± 4	379 ± 3	460 ± 3	458 ± 4	438 ± 4
AA5052-H32 (1.5 mm)	σ_{ys} (MPa)	167 ± 2	184 ± 3	178 ± 3	172 ± 4	189 ± 4	186 ± 3	179 ± 3
	σ_u (MPa)	250 ± 2	258 ± 5	259 ± 2	251 ± 4	265 ± 5	260 ± 3	258 ± 5
	n	0.18	0.17	0.17	0.18	0.17	0.17	0.18
	K (MPa)	393 ± 2	432 ± 3	426 ± 3	419 ± 5	452 ± 5	447 ± 3	426 ± 5

Table 2.7: Effective strain rate generated during the forming of the sheets

Material (AA 5052-H32)	Effective strain rate (s^{-1})					
	Bursting pressure, 24.13 ± 1.03 bar			Bursting pressure, 31.02 ± 0.68 bar		
	R_{100}	R_{150}	Flat	R_{100}	R_{150}	Flat
1 mm	110.36 ± 3	105.21 ± 5	88.46 ± 4	152.15 ± 3	128.96 ± 3	106.57 ± 5
1.5 mm	58.33 ± 4	52.31 ± 4	43.36 ± 4	62.95 ± 4	54.85 ± 4	51.57 ± 3

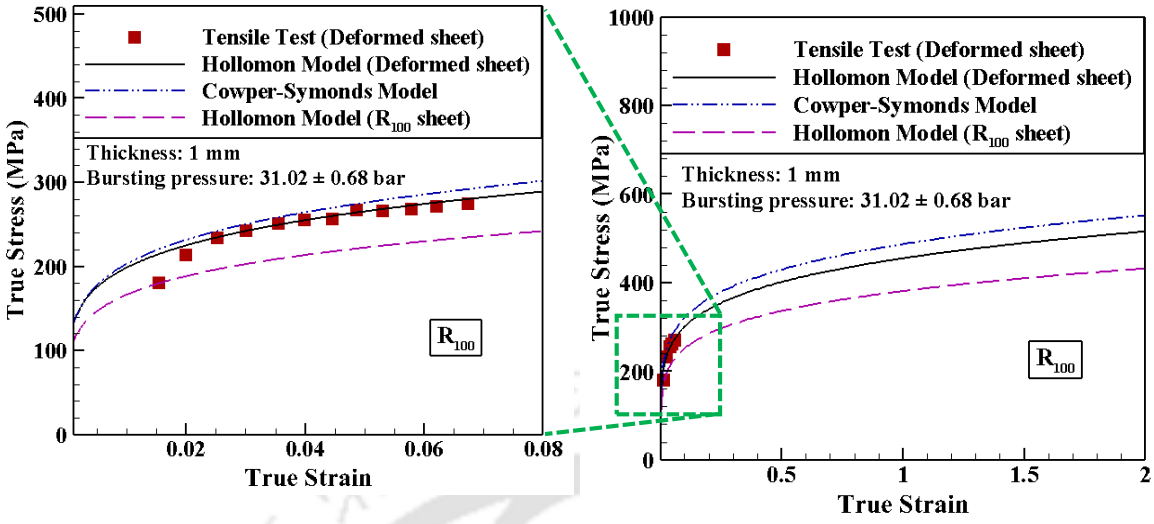

Fig. 2. 10: Comparison between Cowper-Symonds relation and Hollomon's power law for R100 sheet deformed at a bursting pressure of 31.02 ± 0.68 bar

2.4.4 FE Simulation details

Due to the geometric symmetry conditions, only one-quarter of the model is considered for the analysis, as shown in Fig. 2.11. The finite element model has the same dimension as per the specimen used during the experiment. As the material undergoes significant deformation, the work-piece is modeled as a deformable plastic material and meshed with uniform tetrahedral elements (Fig. 2.11). The top and the bottom blank holders are considered as rigid bodies. The nodes of both the sheet and the blank holders that are coinciding with the symmetric planes are constrained with the symmetric boundary conditions. As the impulsive pressure wave generated during the experiment is being used as a tool to deform the sheet uniformly, the pressure-time history obtained at the end of the shock tube, as shown in Fig. 2.7 (pressure experienced by the P_3) is considered as the pressure input boundary condition during the study. A master-slave algorithm is adopted during the simulation by considering the top and bottom blank holder as rigid bodies. The coulomb's classical law models the frictional contact between both the blank holders and the deformable body (sheet). During this study, the coefficient of friction (μ) is varied in the range of 0.01 to 0.2, and the blank holding force (BHF) is also varied from 2 kN to 10 kN. When μ and BHF are smaller in range, the sheet draws inside the blank without deformation, and at higher ranges, the sheet starts rupturing near the blank holders. Thus, an optimum value of the coefficient of friction (μ), i.e., 0.1 and BHF of 8 KN, is considered during all the numerical simulations. Since the sheet is deformed

significantly during the impact loading, the amount of spring back after deformation is minimal, and it is not analyzed in this study.

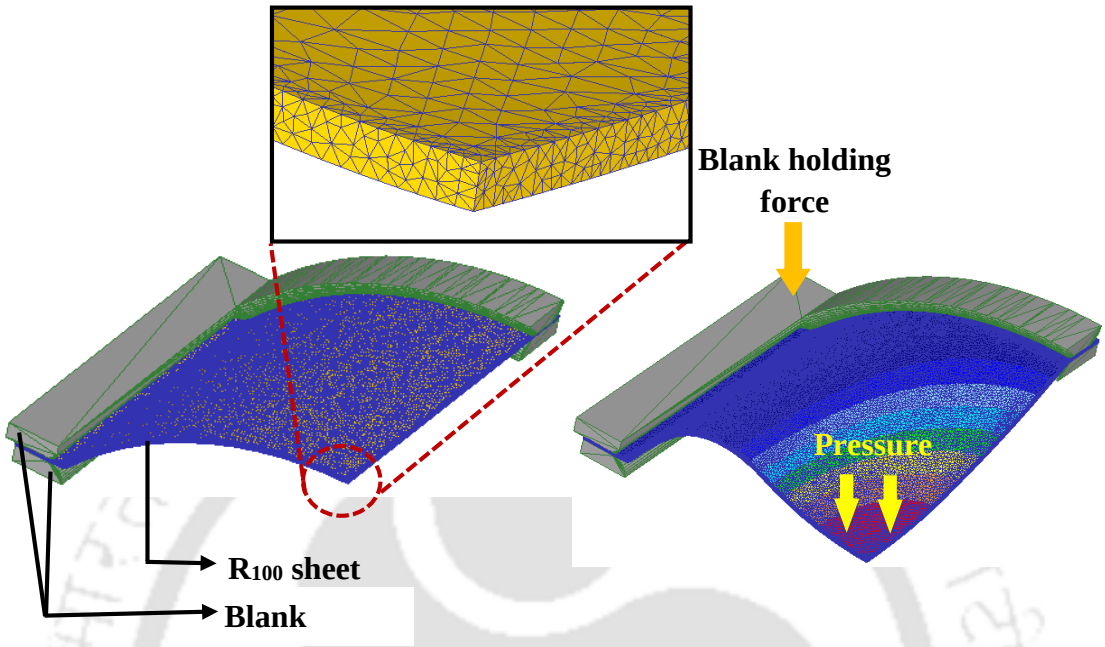

Fig. 2.11: FE model of the R100 sheet (quarter of the specimen)

2.4.5 Mesh sensitivity analysis

The mesh independency analysis has been conducted for the case of flat sheet of 1 mm thickness to obtain the optimum mesh size. The FE simulations are conducted for various mesh sizes, such as 1.5, 1, 0.6, 0.5, 0.25, and 0.2 mm. The maximum displacement, peak effective strain, and computational time have been compared with the experimental result (Table 2.8). Element sizes above 0.5 mm show larger deformation as compared to the other cases. The displacement evolution (Fig. 2.12) also indicates the significance of finer mesh, where the deformation profile of the sheet captures the different modes of deformation during shock loading, which is not captured accurately in coarse meshes. Though the computational time increases tremendously with the reduction in the element size, the computational results match quite well with the experiment. Element size of 0.25 mm generates four layers of tetrahedral mesh element in the thickness direction, as illustrated in Fig. 2.11 and also provides better results with acceptable computational time. Therefore, four layers of mesh elements are generated for all the sheets of 1 mm and 1.5 mm thickness by considering the minimum element size of 0.25 mm and 0.375 mm, respectively.

Table 2.8: Mesh independency analyses

Experimental data and element size (mm)	Number of elements	Height of deformation (mm.)	Maximum effective strain	Computational time (min)
Experimental data	-	10.45	0.044	-
1.2	33576	14.48	0.049	113
1	68382	14.27	0.046	178
0.6	102852	12.29	0.045	193
0.5	132410	12.89	0.044	264
0.25	258743	11.90	0.040	1622
0.2	286658	11.88	0.040	1855

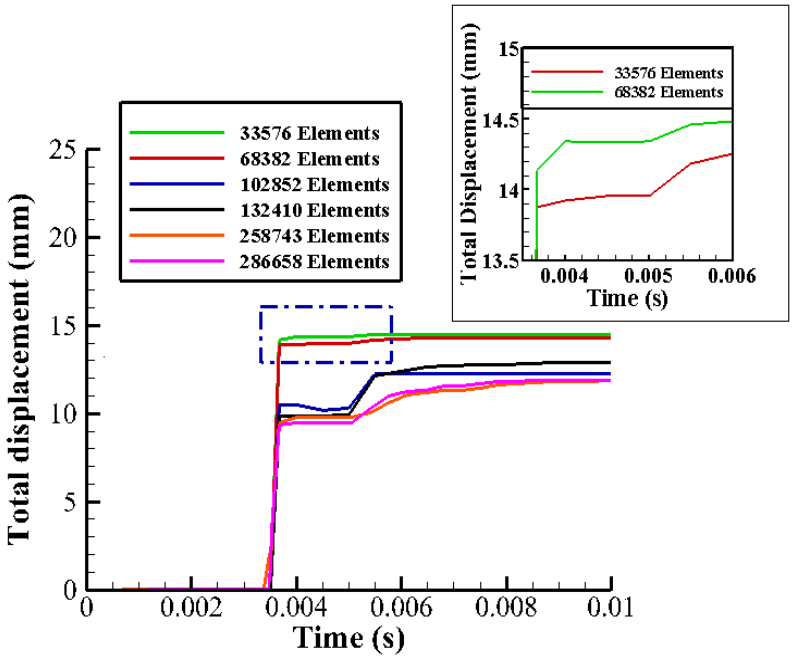

Fig. 2.12: Total displacement vs time graph for different number of elements

2.5 Effective strain and stress distribution analysis

The deformation behavior of the different pre-strained sheets can be obtained by measuring the effective strain and stress generated in the deformed region. Circular grids of diameter 1.924 ± 0.013 mm are printed by the screen printing method on the opposite surface to the loading direction. The diameter of the grids before and after the deformation is measured by a surface profile projector having a precision of ± 0.001 mm. The anisotropic behavior of the sheets is considered during the calculation of the effective strain generated on the deformed

sheet by Hill's 1948 effective strain relation, as shown in eq. 2.6. The effective strain ($\bar{\varepsilon}$) is calculated by measuring the major strain, minor strain, and the thickness strain ($\varepsilon_1, \varepsilon_2, \varepsilon_3$) of each circular grid. The anisotropic coefficients considered during the calculation, such as $F = r_{RD}$ = anisotropic coefficient across rolling direction, $G = r_{TD}$ = anisotropic coefficient across the transverse direction and $H = r_{RD} r_{TD}$ are also evaluated experimentally and reported in Table 2.2. The effective stress ($\bar{\sigma}$) generated on the material can be calculated by Hollomon's power law $\bar{\sigma} = K\bar{\varepsilon}^n$, where *K* and *n* are the strength coefficient and the strain hardening exponent, respectively. The *K* and *n* values of the parent material cannot be used during the effective stress calculation because the mechanical properties of the sheet may change after the shock deformation. Hence, the rate-dependent mechanical properties obtained from the tensile test of the deformed sheets (Table 2.6) are used during the calculation of the effective stress.

2.6 Measurement of strain-time histories

In order to measure the strain rate evolution during the high-velocity forming process, strain rosettes are mounted at the center of the sheets on the opposite surface to the loading direction, as shown in Fig. 2.13. The strain rosette can able to measure the strain along 0°, 45°, and 90° to the rolling direction. Each strain gauge has a length of 6.35 mm and a resistance of 350 ± 2 Ωs. The gauge factor of the strain rosette is 2.01. The three strain gauges of the rosette are connected to three different Wheatstone quarter bridge circuits, as depicted in Fig. 2.14. The semiconductor strain gauge is a passive device that does not generate any voltage or current as an output when it is stressed. Therefore, during strain gauge applications, the Wheatstone bridge circuit is used because of its outstanding sensitivity (Nanda et al., 2017). It is a simple electrical circuit in which four resistances are connected in a series-parallel connection with an input source voltage. Out of four, one resistance is replaced by the strain gauge. However, a variable potentiometer is replaced by one more resistance. Before the start of the experiments, the circuit is balanced, and the residual voltage is considered as a reference. When the specimen is strained by an external load, the resistance of the strain gauge changes, and it causes instability in the Wheatstone bridge.

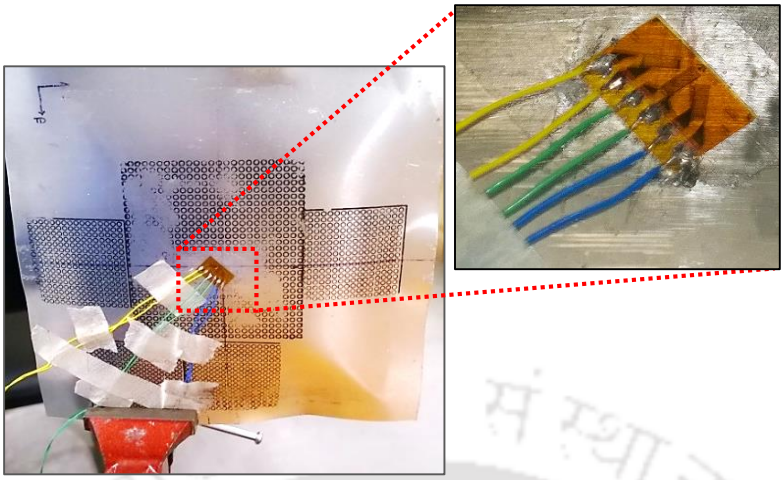

Fig. 2.13: Strain rosette mounted on the surface of a specimen

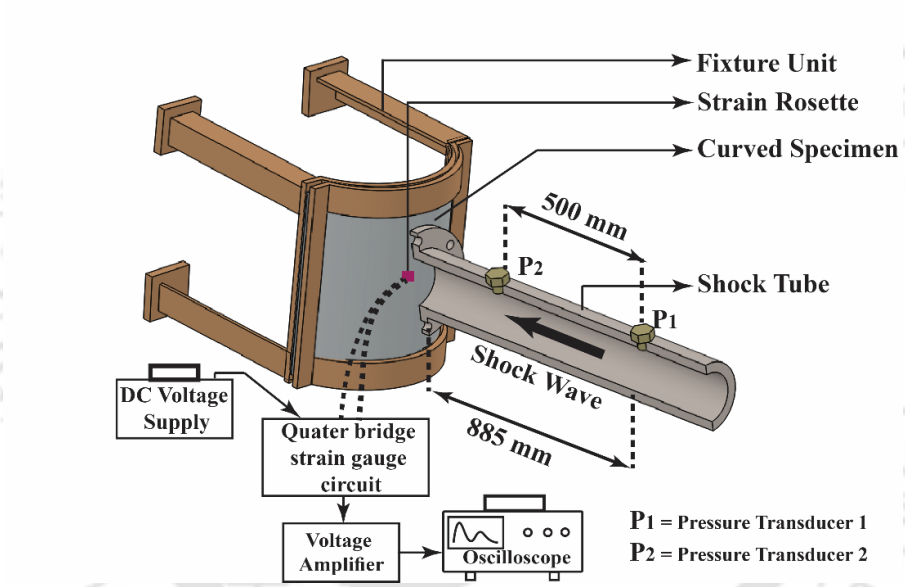

Fig. 2.14: Schematic representation of strain gauge circuit used during the experiment

The output voltage of the circuit is measured in terms of millivolts and very difficult to predict the strain output. Thus, before capturing it in an oscilloscope, the voltage output is amplified by a DC voltage amplifier (INA 128). The experimental set-up with the Wheatstone bridge circuit is shown schematically in Fig. 2.14. The output voltage obtained from the Wheatstone bridge can be converted into strain output by (National Instruments, 1998)

$$\frac{V_{meas}}{V_{in}} = \frac{GF \times \varepsilon}{4}\left(\frac{1}{1+GF\times\frac{\varepsilon}{2}}\right) \qquad (2.14)$$

where V_{meas} represents the measured voltage output from the Wheatstone bridge circuit, V_{in} is the input voltage to the Wheatstone bridge circuit, GF is the gauge factor of the strain gauge, and ε is the in-plane strain generated on the specimen. The strain rate of deformation measured by the strain rosette during the forming of the flat sheet (R_∞) along 0°, 45°, and 90° is illustrated in Fig. 2.15. However, the strain rate data along 0° and 90° are considered during the calculation of effect strain evolution by using Hill's 1948 yield criterion. The effective strain rate from experiments is shown in Table 2.7.

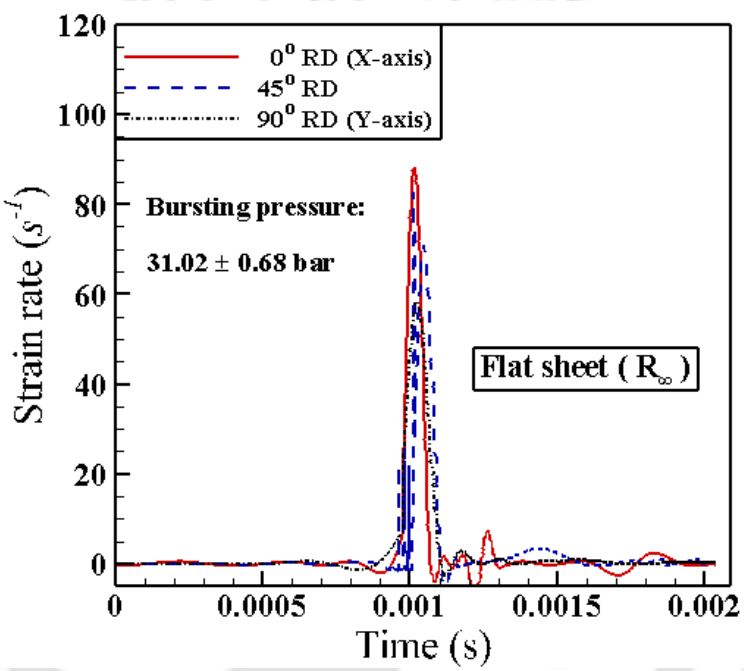

Fig. 2.15: Strain rate during the forming of flat sheet at bursting pressure 31.02 ± 0.68 bar

2.7 Results and Discussion

2.7.1 Effect of bending pre-strain (radius of curvature) on out of plane deformation

In order to demonstrate the effect of bending pre-strain on the sheet metal deformation, the results corresponding to the bursting pressure of 31.02 ± 0.68 bar are illustrated in Fig. 2.16. The FE simulation exhibits two different modes of deformation during the forming process. Due to the impulsive nature of the shock wave, a localized deformation starts at the beginning of the deformation, and with time, the deformation spreads progressively because of the inertial effect caused due to the impulsive action of the shock wave. These two phenomena can be referred to indentation and flexural mode deformation, respectively (Kumar

et al., 2012). The difference between both the deformation mechanisms can be schematically explained in Fig. 2.16 as stage 2 and stage 3 of the deformation.

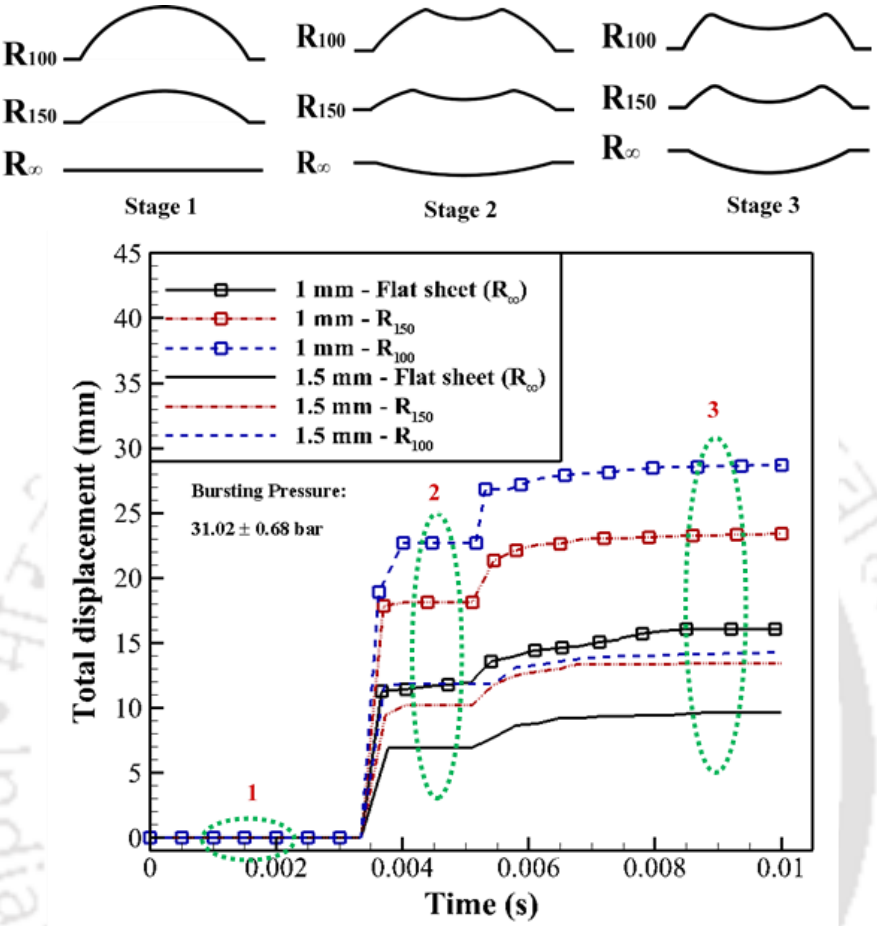

Fig. 2.16: Out of plane deformation evolution of the sheets

The different modes of deformation are dependent on various parameters such as degree of pre-strain, thickness of the sheets, and the pressure-induced during the shock loading. 1.5 mm thick sheets show higher rigidity, and it results in less out of plane deformation than 1 mm thick sheets under the same loading condition. In both the thickness cases, R_{100} sheet shows maximum deformation, whereas least deformation is noticed in the flat sheet (R_∞). It is because of the dominance of the indentation mode of deformation in case of pre-strained sheets, which deforms the sheet locally to a larger extent. With the progress of time, the generated stress wave transmits through the material and expands the localized deformed region and propagates in the freely deforming area, which converts it into flexural deformation. The impulsive wave tries to deform the flat sheet in a similar manner, but the dominance of indentation deformation is not that significant. In this case, the sheet reaches the plateau region without significant

deformation and it results in least out of plane deformation. For the case of R_{150} sheets, because of the influence of both indentation and flexural deformation, the sheet stretches significantly, but the deformation is lesser than R_{100} sample. The two different modes of deformation obtained through FE simulation are depicted in two steps in the displacement vs. time graph (Fig. 2.16). The FE simulation results at different time intervals are illustrated in Fig. 2.17, and Fig. 2.18. Similar modes of deformation are also observed in the experiments.

The deformation due to the flexural mode of deformation is also dependent on the degree of pre-strain and thickness of the sheet. In 1 mm thick sheets, the deformation at the center increases further in R_{100} sheet during the flexural deformation before the sheet reaches the plateau region. Similar observation is also observed in R_{150} sheet case. However, the flat sheet reaches the plateau region after the indentation deformation, and there is no significant deformation observed during flexural deformation. On the other hand, the deformation in 1.5 mm thick sheet is completely indentation dominated. The flexural deformation only expands the deforming region without further stretching the central region. The simulation results also confirm that the rate of deformation is dependent on the degree of pre-strain (Fig. 2.16). The displacement-time graph of R_{100} sheet is steeper than R_{150} and flat sheet cases. It can be explained with the fact that the localized indentation mode of deformation superposes in a small region in the R_{100} sheet and tries to stretch the sheet locally, as shown in Fig. 2.17, and Fig. 2.18, which results in a higher rate of deformation. On the other hand, the flat sheet has a lower deformation rate because it is exposed to a larger region, and it reaches the plateau region without significant deformation. The rigidity of the 1.5 mm thick sheet lowers the deformation rate in case of all the pre-strained sheets.

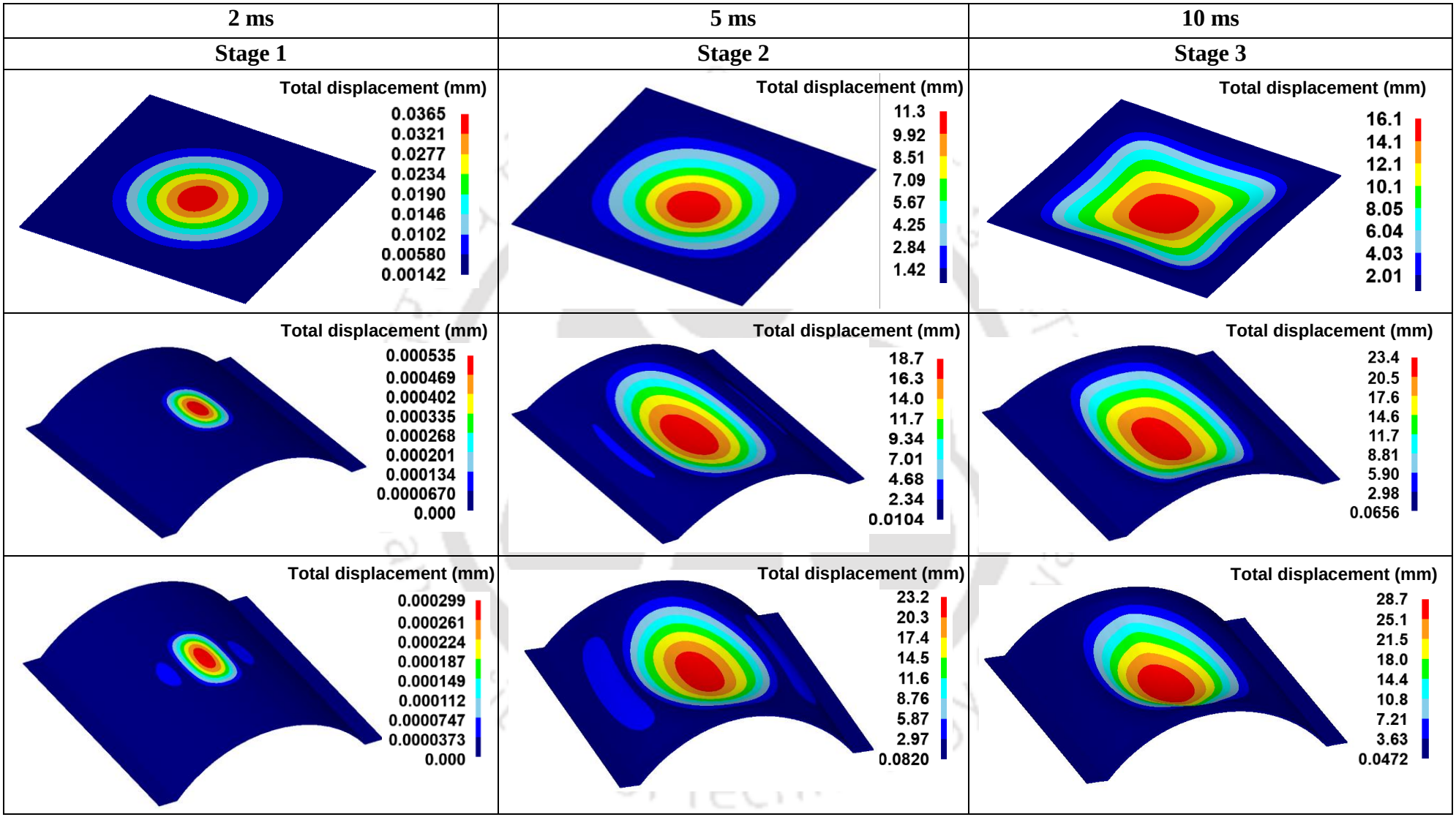

Fig. 2.17: FE simulation results showing deformation of 1 mm thickness sheet at bursting pressure 31.02 ± 0.68 bar

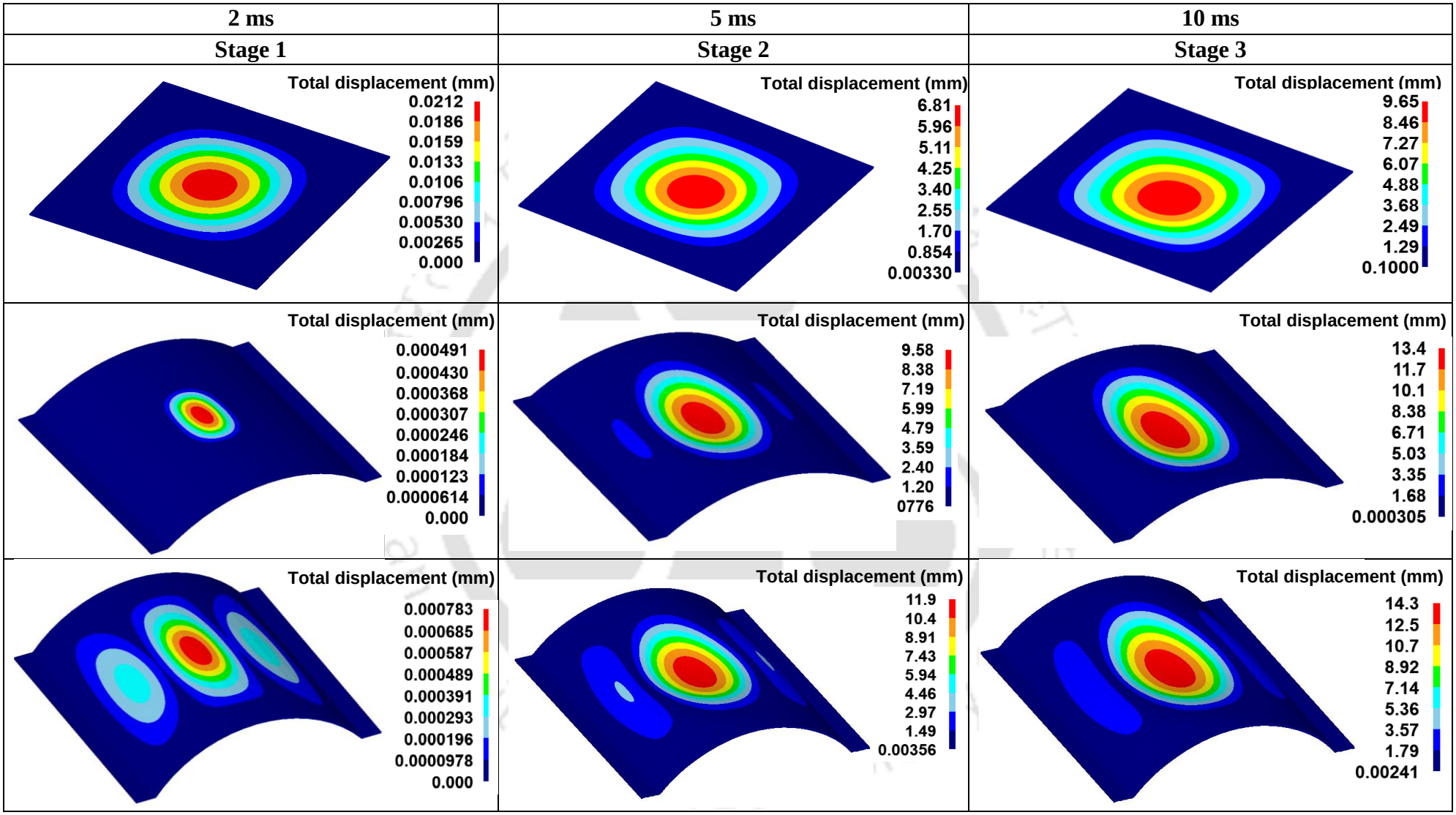

Fig. 2.18: FE simulation results showing deformation of 1.5 mm thickness sheet at bursting pressure 31.02 ± 0.68 bar

2.7.2 Effect of pressure on out of plane deformation

R_{100} sheets deform more than the other two cases of sheets. Thus, only R_{100} sheets are considered for the analysis to understand the effect of pressure. Fig. 2.19 shows the comparison of the experiment to the numerical results at two different pressures. The results depict that the 1 mm thick sheets have undergone significant deformation with the rise in pressure. It is because of the impulsive action of the pressure generated in the shock tube, which develops an inertial effect during the deformation. The inertial forces are stabilized by generating additional tensile stresses in the material which stretch the sheet uniformly. The higher magnitude of pressure not only generates a larger indent at the beginning but also helps to stretch the material significantly in the exposed region during flexural deformation. The deformation mechanism is same for 1.5 mm thick sheets, but the higher rigidity of the material does not make any significant difference in the final deformation.

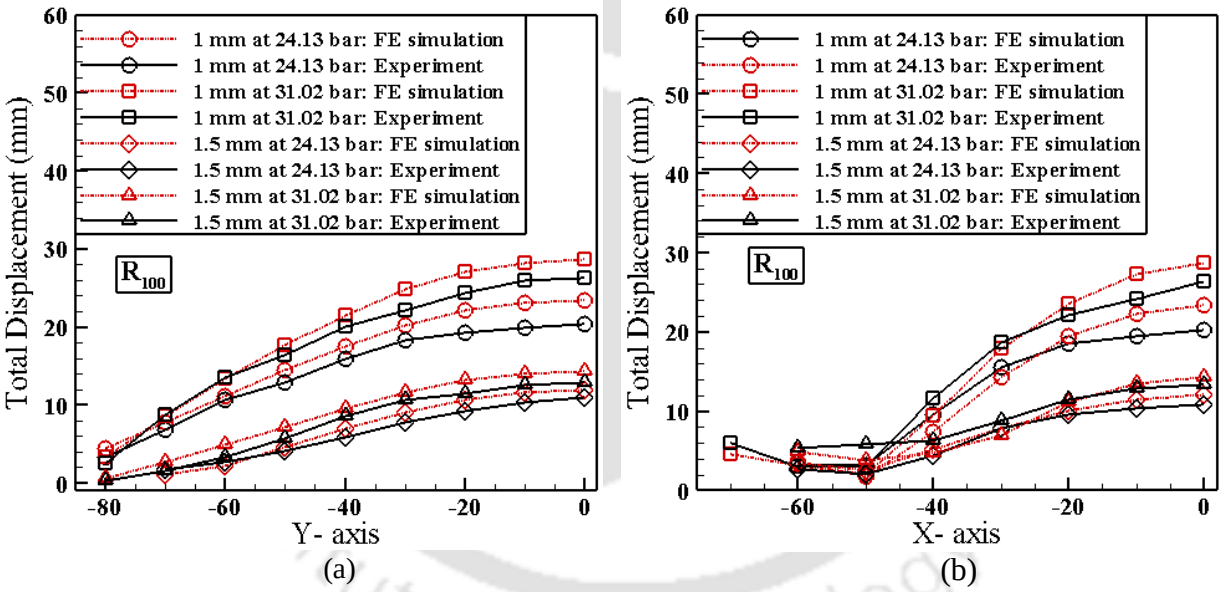

Fig. 2.19: Out of plane displacement of R_{100} sheets at two different bursting pressures along (a) Y-axis and (b) X-axis

The numerically predicted deformation profile matches quite well with the experimental results with a slight over-prediction (Fig. 2.19). It is because of the input pressure condition incorporated in the simulation. During the experiments, the pressure transducer cannot be mounted on the thin sheets because of the risk of damage. Thus, it is mounted on a calibration plate (Fig. 2.6) to obtain the pressure signals for the same experimental conditions as that of the sheet. Those pressure-time histories are given as input during the FE simulations. However,

during the actual deformation of aluminium sheets, part of the impulsive air escapes from the shock tube. Hence, the pressure magnitude cannot be maintained for a long period. It results in lower deformation in experiments as compared to the FE simulations. The existing rise in pressure deforms the 1 mm thick sheet significantly, whereas its effect is not that significant in the 1.5 mm thick sheets due to higher rigidity. Fig. 2.20 and Fig. 2.21 compare the results of the deformed sheets from experiments and FE simulation for two different pressure condition. The FE simulation results are in good agreement with the experimental results.

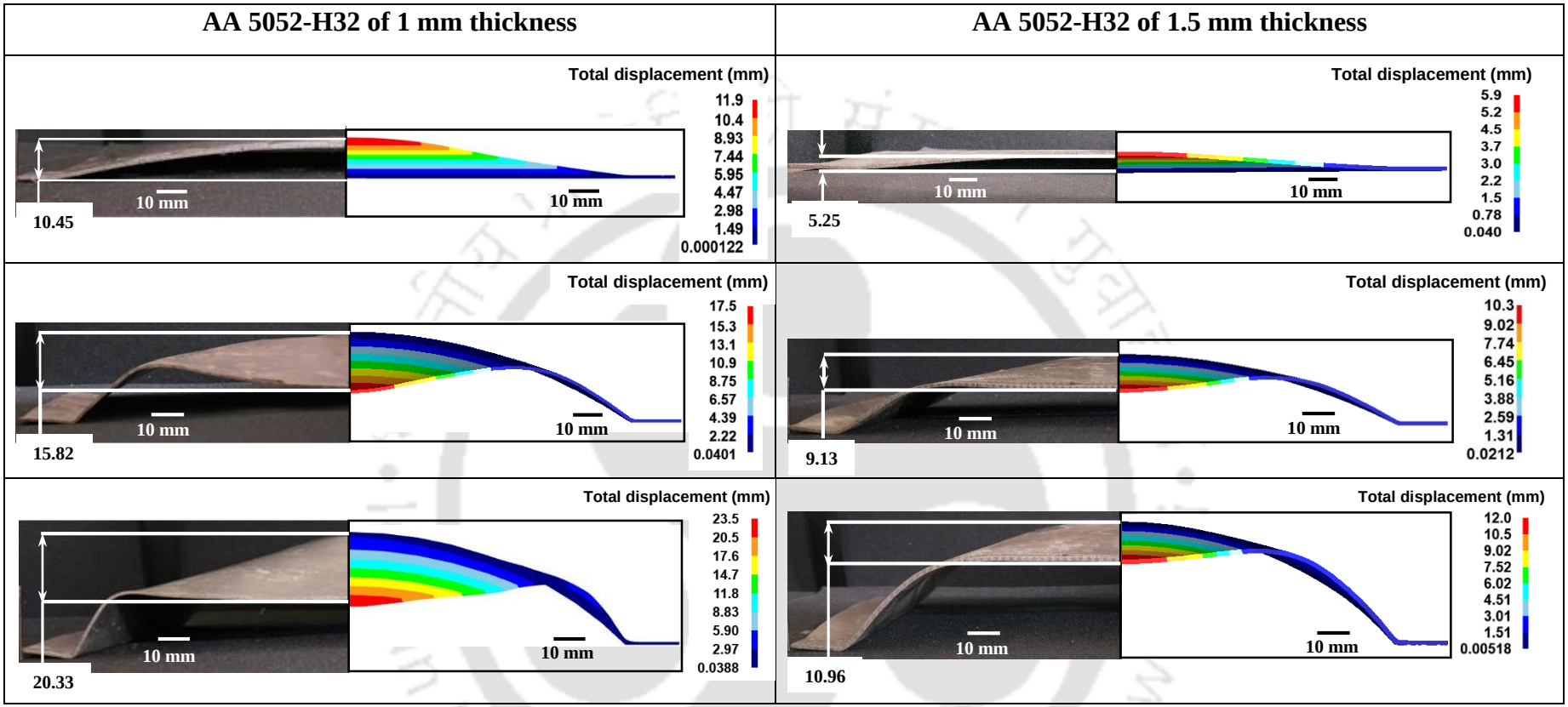

Fig. 2.20: Comparison of experimental and FE simulation results of 1 mm and 1.5 mm thick sheets at 24.13 bar of bursting pressure

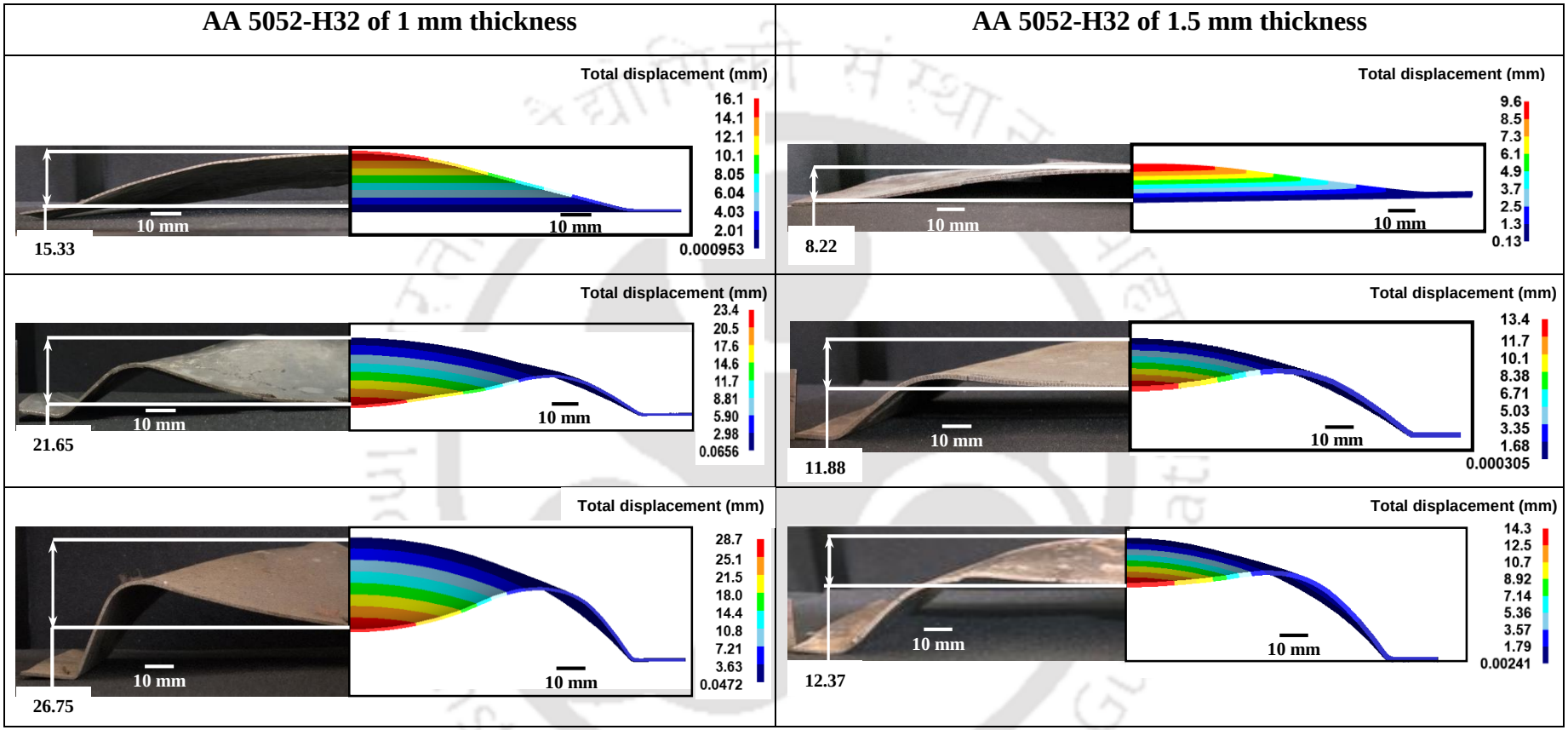

Fig. 2.21: Comparison of experimental and FE simulation results of 1 mm and 1.5 mm thick sheets at 31.02 bar of bursting pressure

2.7.3 Effect of bending pre-strain on strain evolution

In order to demonstrate the effect of bending pre-strain on the strain evolution, all the three cases of sheets are taken into consideration for a bursting pressure of 31.02 ± 0.68 bar. The experimentally obtained effective strain-time histories are compared with FE simulation results (Fig. 2.22). The slope of the experimental effective strain ($\bar{\varepsilon}$) evolution signal matches quite well with the FE simulation results. However, the comparison cannot be performed to large strain values because of the strain limit of the strain gauges. The sharp rise in the effective strain-time curve confirms the sharp rise in the strain rate during the forming process. Table 2.9 compares the strain rate evolved during the experiment, and FE simulation for all the pre-strained sheets.

The different modes of deformation govern the effective strain rate evolution. When the impulsive pressure wave hits the R_{100} sheet, a localized indent starts to form at the beginning due to the indentation deformation. This results in a sharp rise in the strain signal. In case of R_{150} sheet, similar mode of deformation is observed. Under the same loading condition, when the flat sheet is deformed, it is exposed to a larger region. Thus, the generated stress wave tries to expand a larger deforming region during the indentation deformation, and it results in a lower strain rate than the pre-strained sheets (Table 2.9). After that, the deformation continues and stretches the sheet further during the flexural deformation. The strain evolution curves (Fig. 2.22) illustrate that the material stretches even more in the central region during the flexural deformation. In 1 mm thick sheet, the rise in strain in R_{100} sheet during the flexural deformation is quite significant than R_{150} sheet and flat sheet. However, the same variation is not visible in 1.5 mm sheets. The strain evolution is strongly dependent on indentation mode of deformation. The effect of flexural deformation is not that significant because of their higher rigidity.

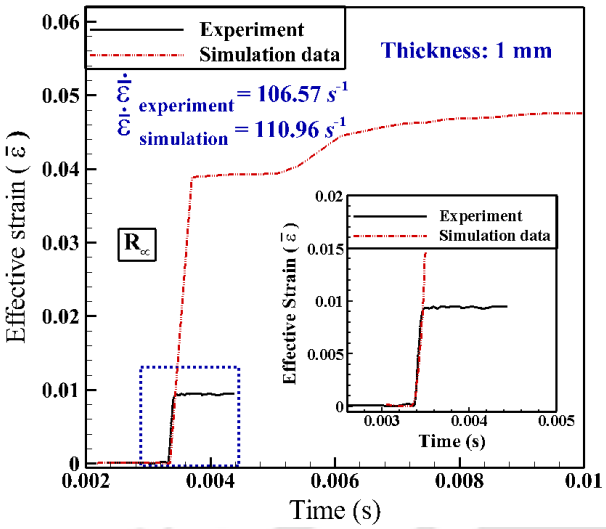

(a) t = 1 mm

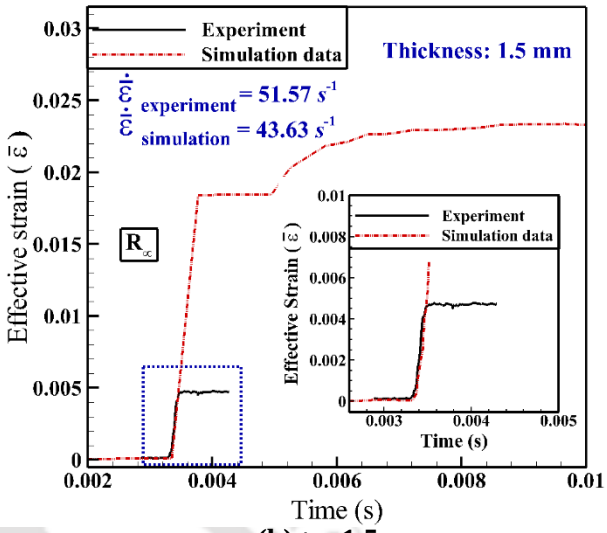

(b) t = 1.5 mm

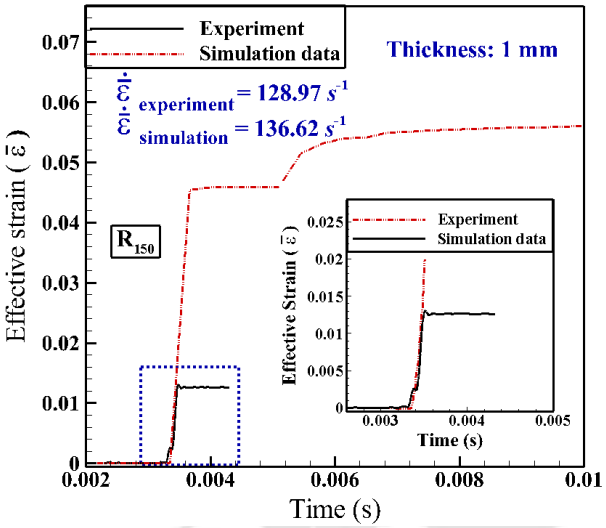

(c) t = 1 mm

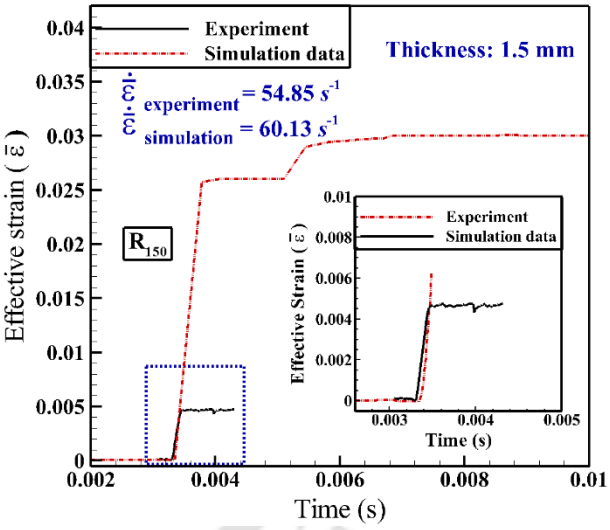

(d) t = 1.5 mm

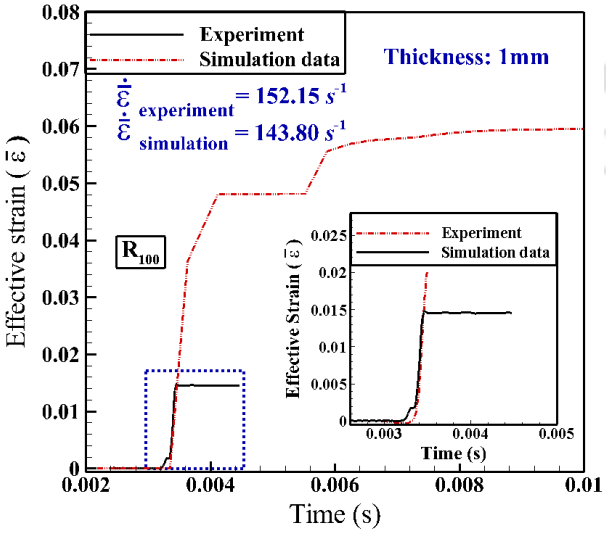

(e) t = 1 mm

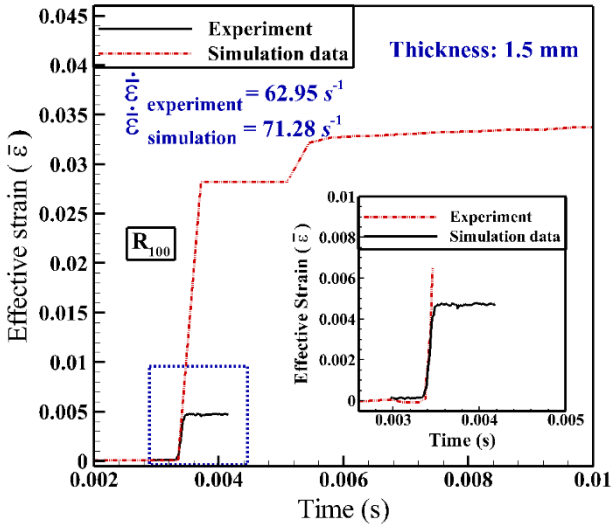

(f) t = 1.5 mm

Fig. 2.22: Comparison of strain evolution of (a, b) flat sheet and (c, d) R150 sheet (e, f) R100 sheet at 31.02 ± 0.68 bar of bursting pressure

Table 2.9 Comparison of strain rate for all the sheets during the experiment and FE simulation

Material	Curvature of the sheet	Effective Strain rate (s^{-1})			
		Bursting pressure, 24.13 ± 1.03 bar		Bursting pressure, 31.02 ± 0.68 bar	
		Experiment	FE simulation	Experiment	FE simulation
AA 5052-H32 (1 mm)	Flat	88.46 ± 4	95.83	106.57 ± 5	110.96
	R_{150}	105.21 ± 3	112.35	128.85 ± 3	136.62
	R_{100}	110.36 ± 3	115.62	152.15 ± 3	143.80
AA 5052-H32 (1.5 mm)	Flat	43.36 ± 4	49.57	51.57 ± 3	53.65
	R_{150}	52.31 ± 3	50.62	54.85 ± 3	60.13
	R_{100}	58.33 ± 4	62.63	62.95 ± 4	71.28

2.7.4 Effect of pressure on the strain evolution

From the deformation analysis, it is observed that all the pre-strained sheets deform significantly with the rise in pressure. However, in order to interpret its effect on the strain evolution, only R_{100} sheets are considered for the analysis. The strain evolution data predicted by FE simulation (Fig. 2.23) confirms that the strain rate of the deformation depends on the pressure developed in the shock tube. Higher impulsive pressure wave stretches the sheet at a higher strain rate. It is because of the impulsive action of the shock wave, which generates an inertial force during the deformation. A higher magnitude of inertial force accelerates the indentation deformation at the beginning and results in a higher strain rate. The effect of pressure on the strain rate of all the sheets is listed in Table 2.9. After the initial indentation, the evolved inertial forces are stabilized by stretching the sheet uniformly in the exposed region during the flexural deformation. Due to lesser rigidity of 1 mm thick sheets, the higher pressure condition stretches the sheet significantly during the flexural deformation, and it results in higher magnitude of evolved strain. The stretching phenomenon in 1.5 mm thick sheets also remains the same, but the rise in strain with the rise in pressure is not significant.

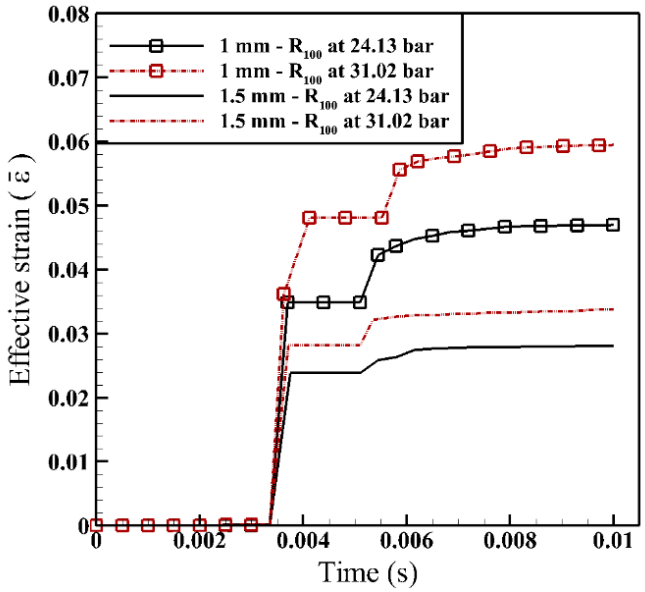

Fig. 2.23: Strain evolution (predicted by FE simulation) for R100 sheets of both 1 mm and 1.5 mm thick sheets at two different bursting pressures.

2.6.5 Effect of bending pre-strain on the effective strain and stress distribution

The effective strain ($\bar{\varepsilon}$) generated on the deformed sheets is measured along both the rolling direction (X-axis) and the transverse direction (Y-axis). Along with this, the effective stress ($\bar{\sigma}$) is also calculated by using Hollomon's power law by considering the mechanical properties such as *n* and *K* obtained from the tensile test of the deformed sheets (Refer Table 2.6). A comparative study has been performed between the experiment and FE simulation by predicting the effective stress and strain on the same location for all the pre-strained sheets at a bursting pressure of 31.02 ± 0.68 bar and depicted in Fig. 2.24, and Fig. 2.25. Though the predicted results are slightly lesser in magnitude than the experiment, the variation of the effective stress and strain are in good agreement with the experimental results.

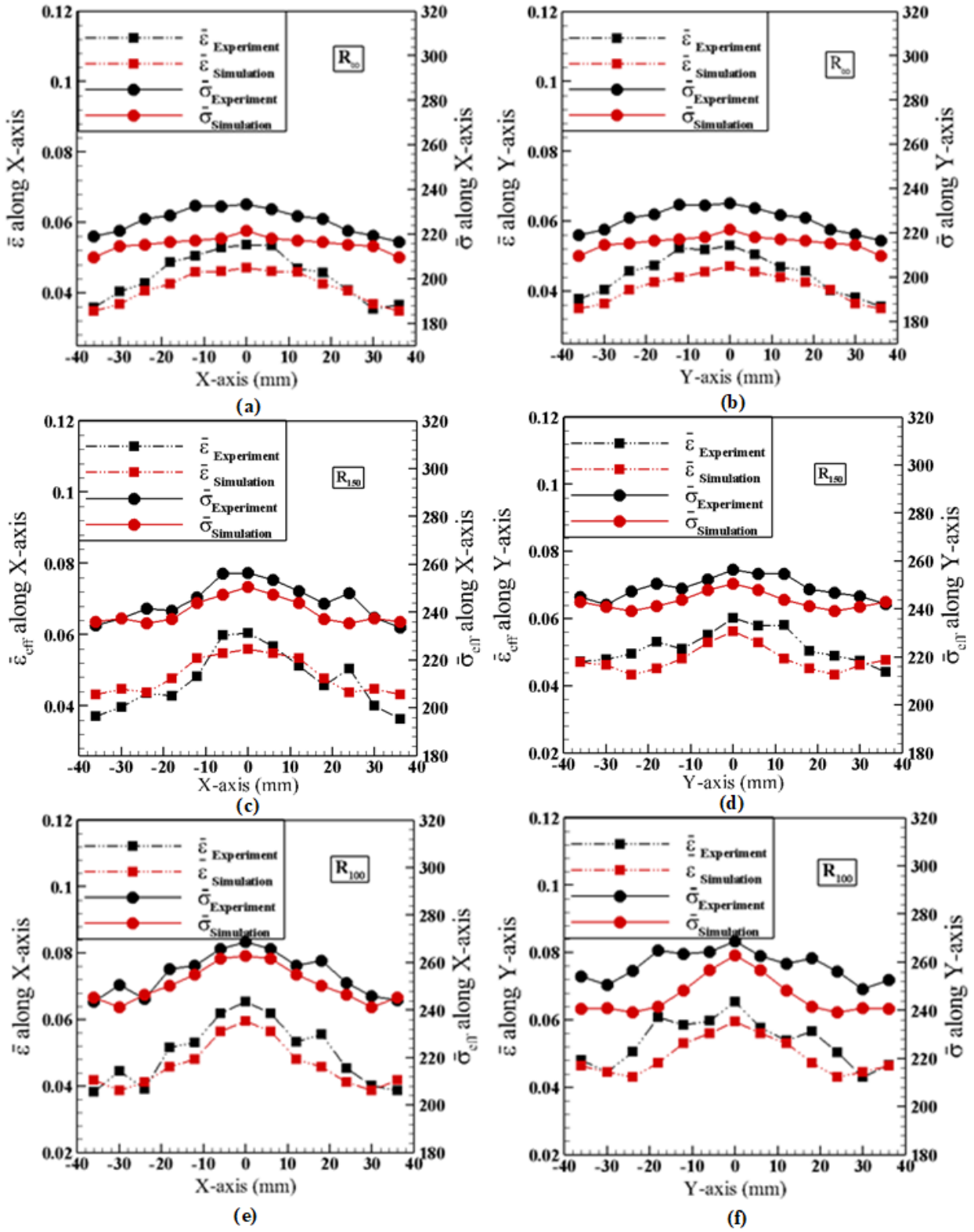

Fig. 2.24: Effective strain and stress distribution of (a,b) flat sheet, (c,d) R150 sheet, and (e,f) R100 sheet of 1 mm thick sheet at 31.02 ± 0.68 bar of bursting pressure

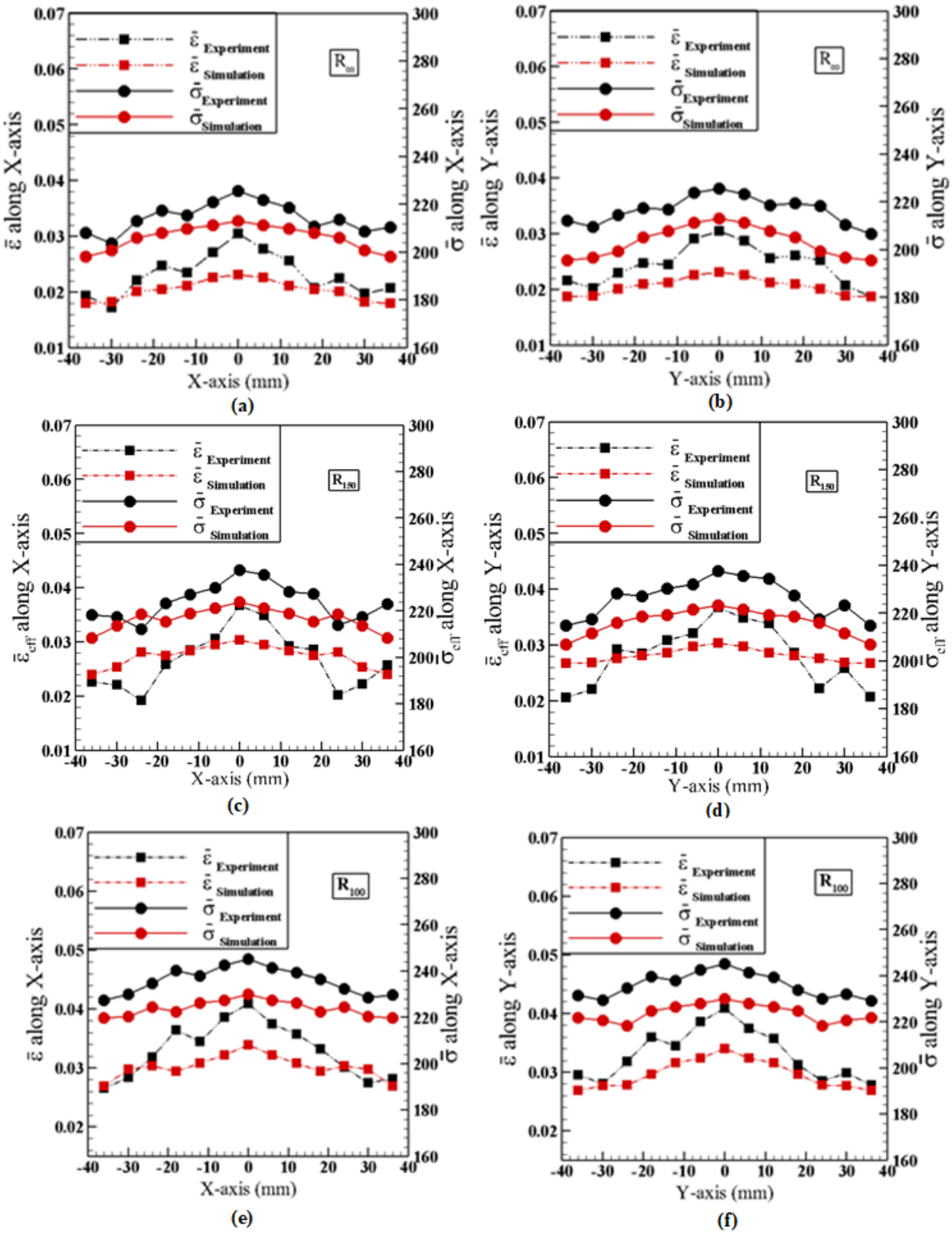

Fig. 2.25: Effective strain and stress distribution of (a,b) flat sheet and (c,d) R100 sheet of 1.5 mm thick sheet at 31.02 ± 0.68 bar of bursting pressure

The effect of bending pre-strain on the sheet deformation is noticed in 1 mm thick sheets. Due to the dominance of flexural deformation in the flat sheet (R_∞), a bi-axial forming is observed where a uniform rise in effective stress and strain is observed in both the X-axis and Y-axis. On the other hand, in R_{100} sheets and R_{150} sheets, the localized indentation deformation stretches the sheets more in the mid-region at the beginning, and it results in a higher magnitude of effective strain, particularly in the mid zone. The sheets deform further until they reach the plateau region during the flexural deformation, and it results in a higher magnitude of effective stress and strain as compared to the flat sheet. The FE simulation also predicts the influence of bending pre-strain on the sheet metal deformation in a similar way as in the experiment (Fig. 2.24 and Fig. 2.25). The 1.5 mm thick sheets also deform in the same manner, but the effect of localized indentation is not observed distinguishably because of less deformation. However, the magnitude of effective stress and strain developed on R_{100} sheet is higher than the R_{150} sheet and flat sheet after deformation (Fig. 2.25). The systematic under-prediction of the effective stress and strain in the FE models suggests better constitutive characterization of both the materials under the working ranges of strain rate. Nevertheless, the tensile properties of the deformed sheets (Table 2.6) used in the FE simulation help to predict the other forming parameters such as dome height and strain evolution acceptably.

2.7.5 Effect of pressure on the effective stress and strain distribution

At higher pressure loading conditions, the sheet is deformed at a high-velocity and it results in a larger magnitude of effective stress and strain after deformation. Only R_{100} sheets are considered during the present comparative analysis. In the case of 1 mm thick sheet, due to the dominance of indentation mode of deformation, strain developed are localized and the magnitude is higher at the central location, as shown in Fig. 2.26. However, the higher magnitude of pressure develops larger inertial force during the flexural deformation, and it tries to stretch the material uniformly in the free to deform region. Thus, the stress and strain developed in the material at higher pressure are more uniform. However, in the 1.5 mm thick sheet, the deformation due to the existing rise in pressure is not that significant. Thus, there is no sufficient rise in stress and strain observed at higher pressure loading conditions (Fig. 2.27). As 1.5 mm sheet is characterized by indentation deformation, the sheet is stretched more in the mid-region only. The numerical results also have a fair agreement with the experimental

results. The numerical model predicts the variation in the material forming behavior at different pressure conditions accurately by considering the different modes of deformation.

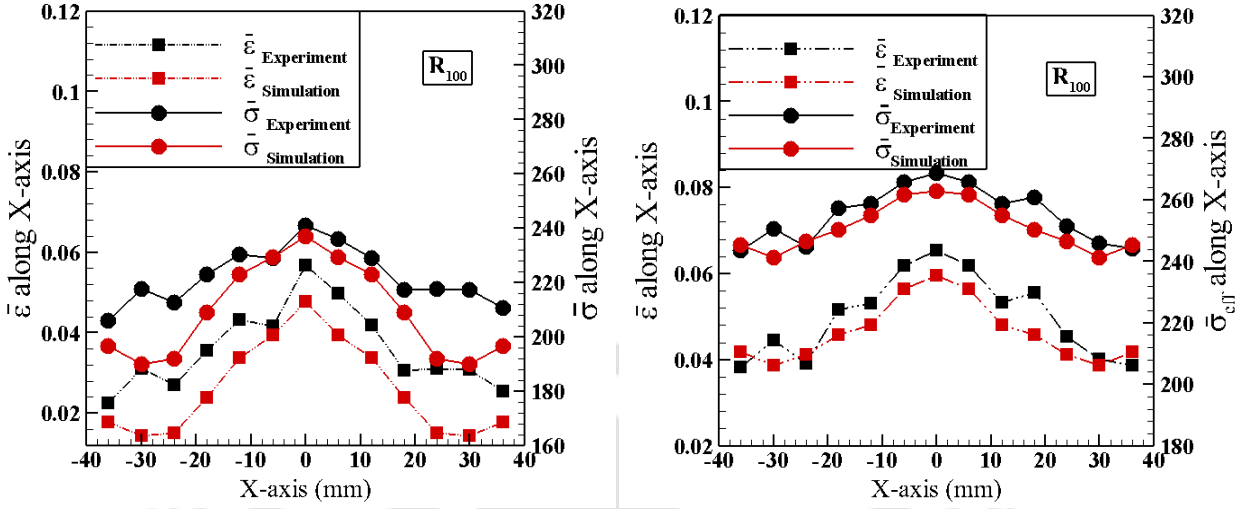

Fig. 2.26: Effective strain and stress distribution of R100 sheet of 1 mm thickness at two different bursting pressures (a) 24.13 ± 1.03 bar and (b) 31.02 ± 0.68 bar

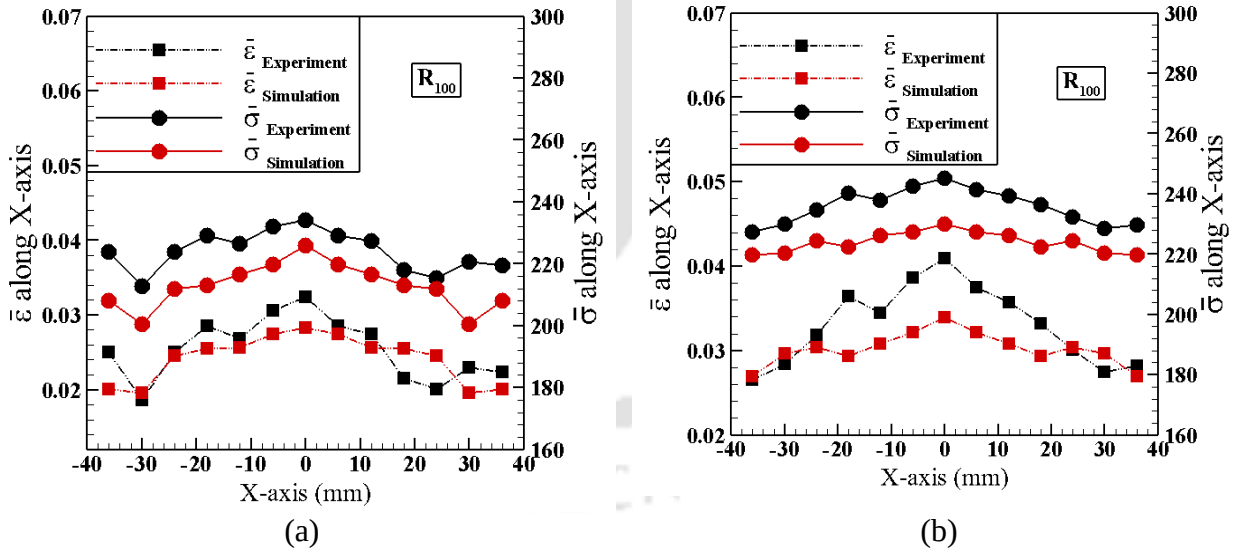

Fig. 2.27: Effective strain and stress distribution of R100 sheet of 1.5 mm thickness at two different bursting pressures (a) 24.13 ± 1.03 bar and (b) 31.02 ± 0.68 bar

2.7.6 Hardness and grain size distribution

The variation of hardness for all the deformed sheets at two different pressure conditions are depicted in Fig. 2.28. The hardness of the deformed sample increases as compared to the parent sheet. This agrees well with Wang et al. (2017) work. This is mainly attributed due to strain hardening of the sheet. Huskins et al. (2010) has quoted dislocation wall strengthening as the dominant mechanism in 5XXX alloys. The 31.02 bar of bursting pressure generates larger hardness at different regions as compared to 24.13 bar, but the difference is not that much significant. The hardness distribution from region R_1 to R_3 is also uniform and the variation is insignificant. The hardness distribution is insensitive to the locations, R_1 to R_3, unlike strain and stress distribution. The effect of bending pre-strain on the hardness variation is also insignificant, though R_{100} shows slightly larger hardness in all the regions as compared to R_{150} and flat sheet (R_∞) (Fig. 2.28). Due to the combine effect of indentation and flexural deformation during forming, the plastic deformation is higher in case of R_{100} sample as compared to the other two cases. This is responsible for higher hardness as well. In case of 1.5 mm thick sheets, similar effect is witnessed as illustrated in Fig. 2.29. The effect of higher bursting pressure on hardness is insignificant. Due to the dominance of indentation mode of deformation, R_{100} sheets have slightly higher hardness value than the other two cases.

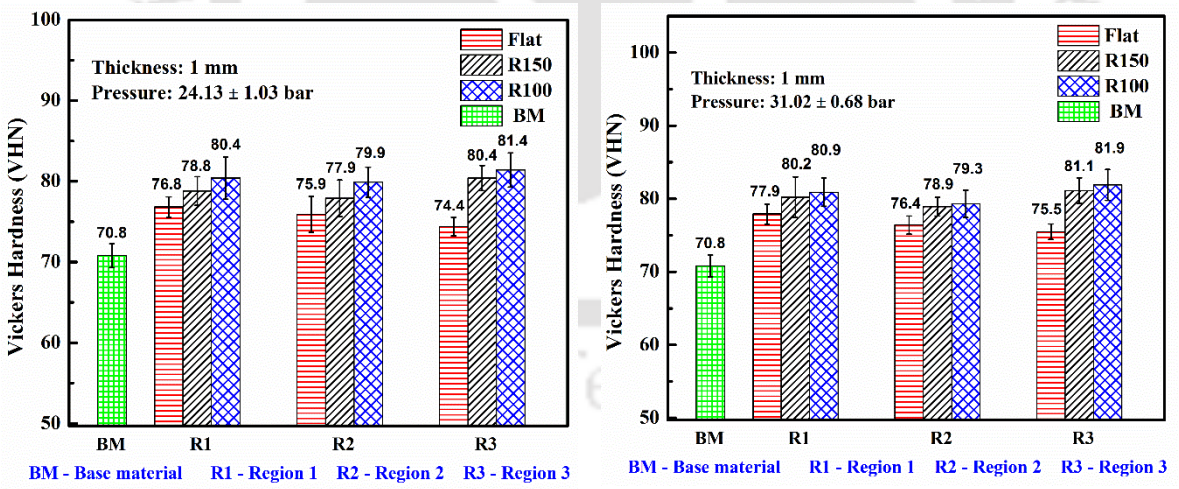

Fig. 2.28: Variation of hardness for 1 mm thick sheet at two different pressures

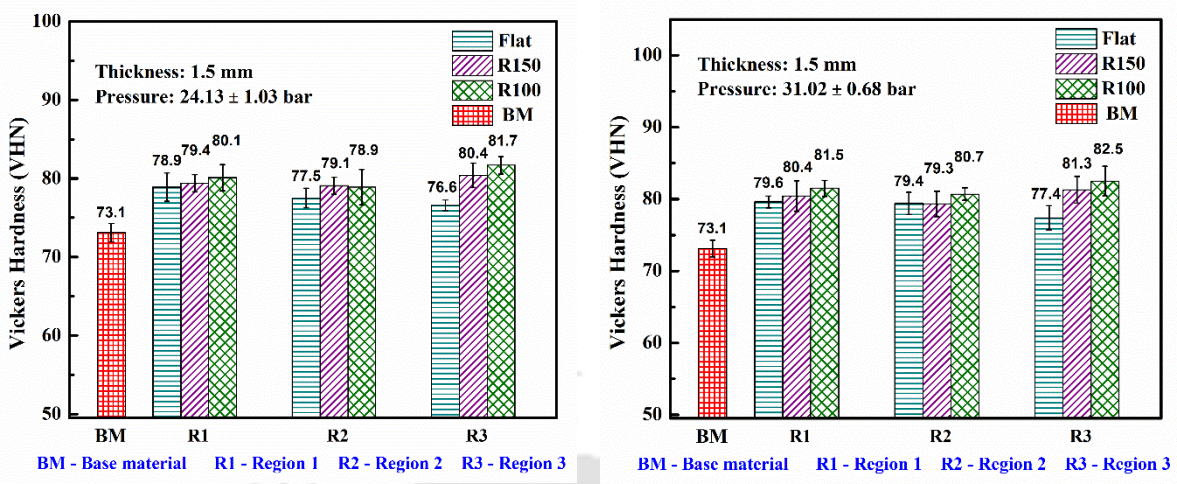

Fig. 2.29: Variation of hardness for 1.5 mm thick sheet at two different pressures

The grain structure after deformation of both 1 mm and 1.5 mm thick sheets is depicted in Fig. 2.30. It is observed that due to shock loading, the equi-axed grains of the base sheets are stretched and form an elongated grain structure. Similar type of observations were made by Li et al. (2009) where the grains were stretched and a number of new grains were generated due to high velocity plastic deformation in EMF process. Since the shock based deformation is conducted at room temperature, instead of grain refinement that is generally seen at elevated temperature, the grains are stretched and elongated. The grain size of 1 mm thick sheets has increased in all the deformed sheets as compared to the base sheet as illustrated in Fig. 2.31. However, the variation of grain size at different locations of the sheet, R_1 to R_3, and with respect to the different bursting pressures is not that much significant. The grain size of the R_{100} sheet is larger than R_{150} and flat sheet. It is mainly because of the combined effect of both indentation and flexural mode of deflection generated in the pre-strained sheet. Moreover, the indentation mode of deformation is prominent in R_{100} sheet which increases the grain size. The variation of grain size for 1.5 mm sheet also follows similar pattern as it is observed for 1 mm sheet (Fig. 2.32). Not much variation is observed in grain size at different locations under different loading conditions.

Curved Sample	Bursting pressure, 24.13 ± 1.03 bar	Bursting pressure, 31.02 ± 0.68 bar	Bursting pressure, 24.13 ± 1.03 bar	Bursting pressure, 31.02 ± 0.68 bar
	AA 5052- H32 (1 mm)		AA 5052- H32 (1.5 mm)	
Parent Sheet	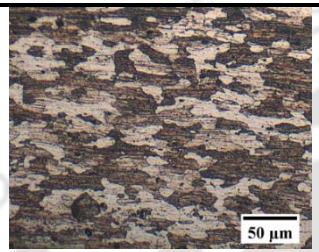		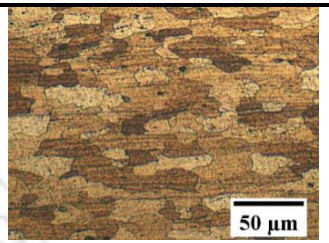	
R_{100}	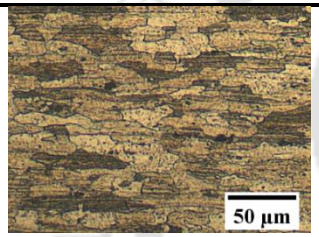	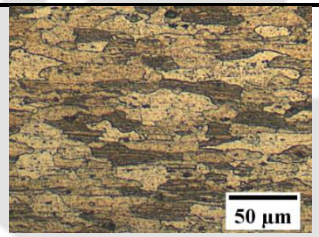	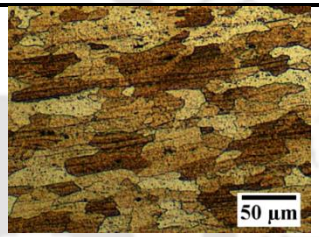	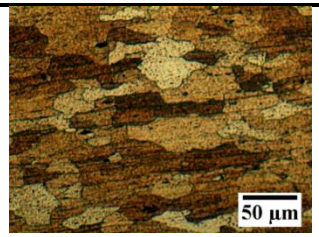
R_{150}	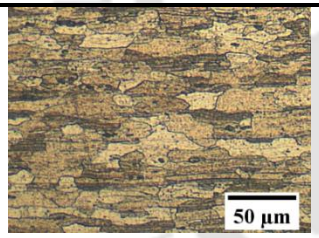	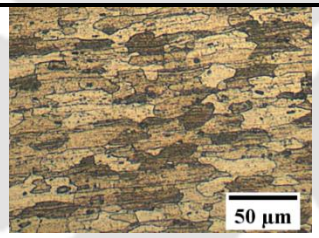	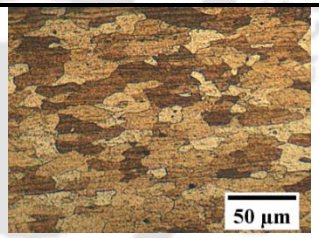	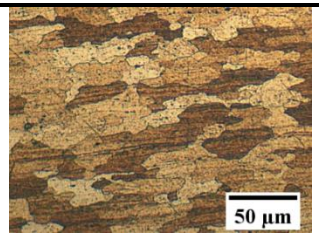
Flat Sheet (R_{∞})	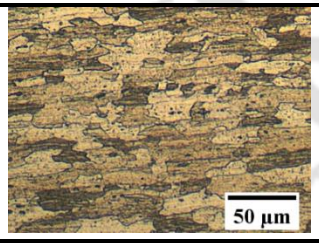	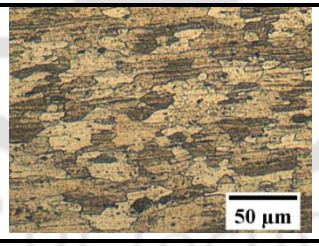	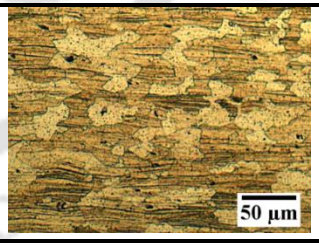	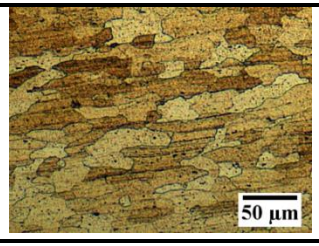

Fig. 2.30: Grain distribution for 1 mm and 1.5 mm thick sheets

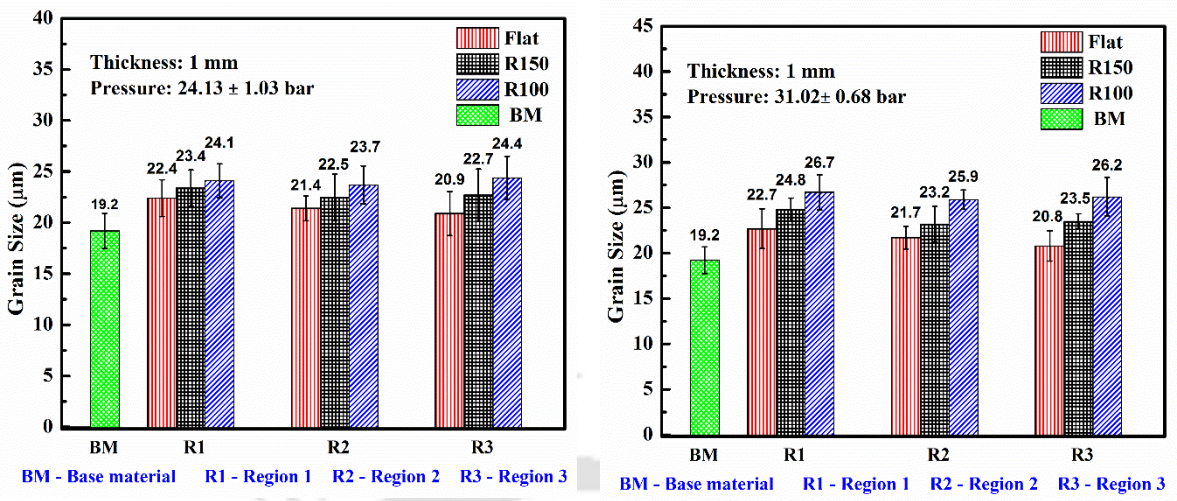

Fig. 2.31: Variation of microstructure for 1 mm thick sheet at two different pressures

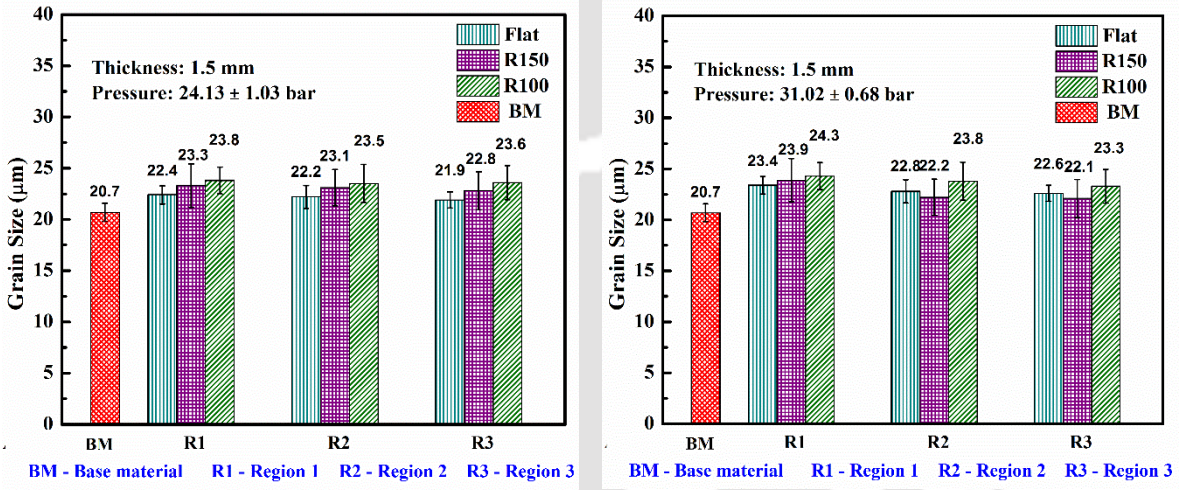

Fig. 2.32: Variation of microstructure for 1.5 mm thick sheet at two different pressures

2.8 Summary

Both the experimental and numerical studies are performed to understand the forming behavior of AA 5052-H32 sheets deformed by a shock tube. The effect of bending pre-strain, sheet thickness, and pressure on the forming behavior is monitored. The following conclusions are derived from the results obtained.

I. The rate-dependent mechanical properties obtained from the tensile test of the deformed sheets are matching reasonably with the Cowper-Symonds relation. Thus, the tensile behavior of the deformed sheets is incorporated during the FE simulation to capture their dynamic behavior is valid and acceptable.

II. The prediction of the sharp rise in the strain evolution by FE simulation matches quite well with the experimental results obtained from the strain rosette. However, the final effective strain value cannot be obtained experimentally because of the maximum limit of the strain rosette. Moreover, the strain-time history confirms the uniform stretching of the material at a higher strain rate without strain localization.

III. The predicted effective stress and strain distribution have a fair agreement with the experimental results. A slight under-prediction in the effective stress and effective strain during FE simulation needs better constitutive characterization of the materials under the working ranges of strain rate.

IV. Under the same loading condition, the R_{100} sheet deforms more than R_{150} sheet and flat sheet. It is because of the indentation mode of deformation which superposes for a longer duration before it changes into flexural deformation. On the other hand, due to the dominance of flexural deformation in the flat sheet, it deforms over a larger exposed region and turns out to be a biaxial deformation. R_{150} sheets shows intermediate state of deformation.

V. With respect to the rise in pressure, the 1 mm thick sheets deform monotonically irrespective of the degree of pre-strain. The significant increase in the deformation is mainly influenced by the inertial effect developed in the material because of the impulsive action of the shock wave. However, the existing rise in pressure does not make any significant change in the deformation of 1.5 mm thick sheets due to its rigidity.

VI. The hardness of the deformed region of the material increases as compared to the parent sheet due to strain hardening for both the thickness sheets. The variation of hardness is insensitive to various locations of the sheets. Similar variation has been observed in the grain size as well. The equi-axed grains of the parent sheets are stretched and elongated due to shock loading and it results in larger grain size.

Chapter 3

Forming response of 1 mm thick sheet deformed through rigid body based impact and gas loading

Overview

The present study focuses on numerical and experimental investigation of the shock tube based forming of AA 5052-H32 sheet of 1 mm thickness using a rigid nylon striker. During the shock tube impact loading, the pressure developed and the velocity of the striker are together responsible for the deformation of sheet. This experimental situation is modelled in two stages, i.e., incorporating pressure in the first stage, and striker displacement in the second stage during finite element simulation using DEFORM 3D. The main aim of this study is to understand the effect of different stress-strain constitutive models and failure models on the forming outputs such as dome height, velocity of the sheet, effective strain rate, effective strain distribution and failure modes. A new strategy is followed to evaluate the rate dependent mechanical properties by the tensile test of the sheet deformed using the shock tube. The forming outputs predicted by incorporating these properties have an acceptable agreement with the experimental data. Out of all stress-strain models, modified Johnson-Cook model shows better flow stress predictability because of the use of nonlinear strain rate sensitivity term in the model. During failure pattern analysis, both the Johnson-Cook model and the Modified Johnson-Cook model have a fair agreement with experimental results. Failure strain and petal formation during failure predicted by Brozzo failure model and Freudenthal failure model match accurately with the experimental results. SEM images confirm deeper and larger parabolic dimples on the fracture surface of shock tube based deformed sheet indicating enhanced formability as compared to sheet formed by quasi-static deformation.

3.1 Experimental Program

3.1.1 Shock tube based impact forming

The details about of the shock tube experimental set up is described in Section 2.2. The impulsive induced gas developed inside the shock tube can be utilized to move a rigid body

and perform impact loading (Fig. 3.1). The pressure energy of the induced gas is transformed as the kinetic energy of the rigid body and it drives the rigid body towards the end of the shock tube at a high-velocity. The rigid body motion can be exploited to deform an experimental specimen mounted at the end flanges of the shock tube (Stage 3, Fig. 3.1). It can be explored as a dynamic Erichsen testing device where a high-velocity hemispherical end striker can be utilized to deform the sheet at different strain rates.

In addition to it, the closed condition of the shock tube benefits to rebuild a high-pressure zone at the end of the shock tube for a short duration because of the rapid motion of the striker (stage 3, Fig. 3.1). The magnitude of high-pressure would be significant enough to deform the sheet uniformly prior to the striker impact. Thus, the shock tube based deformation would be completed in two different steps. First, the high-pressure field would act as a dynamic bulging process, and later on, the further stretching would be completed as a dynamic Erichsen process.

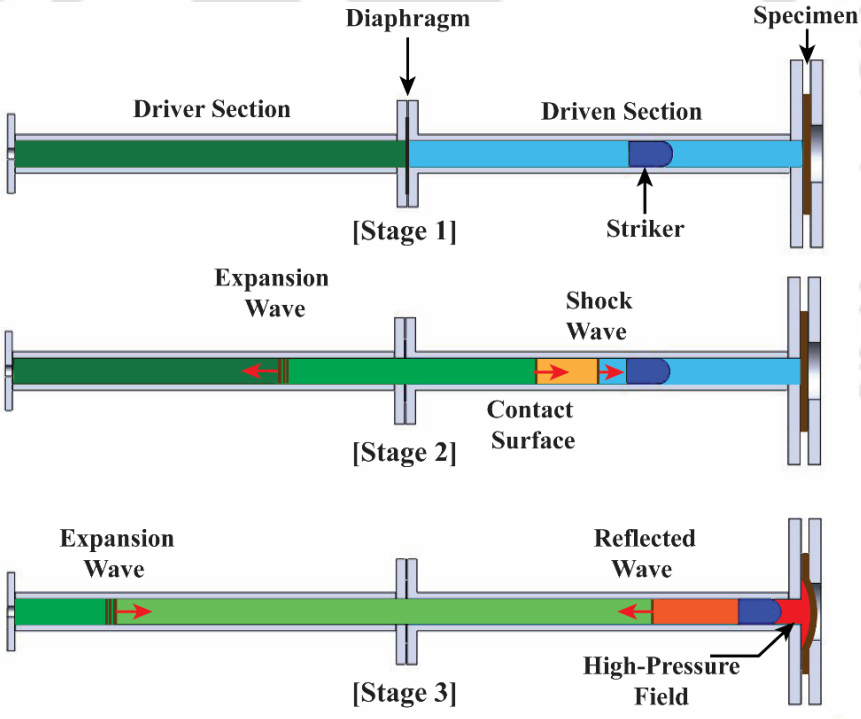

Fig. 3.1: Schematic on working principle of shock tube based deformation

3.1.2 Measurement of pressure and velocity

In this present study, a shock tube facility of overall length 4 m has been used (Fig. 3.2). The dimension of the shock tube facility used during this study can be found in details in Section 2.2. A hemispherical end striker used during this study is made of nylon rod, which

diameter is 54.8 mm and a length of 95 mm. In order to visualize the pressure variation during experiment, two pressure transducers, P_1 and P_2 (PCB Piezotronic; USA; Model 113B22) having sensitivity 14.62 mV/bar are mounted on the shock tube at a distance of 385 mm and 885 mm from the end flanges (Fig. 3.3). In order to obtain the pressure generated at the end of the shock tube because of the rapid motion of the striker, one more pressure transducer (P_3) of same specification is mounted at the end of the shock tube on a rigid flange as it cannot be mounted on a thin sheet (Fig. 3.3). The pressure signals are processed by a signal conditioner, and then connected to an oscilloscope (Tektronix MDO 3024) as depicted in Fig. 3.2.

During experiments, three different input pressure conditions are maintained (Table 3.1) to obtain different velocities of the striker. The pressure-time histories for all the experiments are illustrated in Fig. 3.4. The shock tube experiments are run thrice for each case and the sampling rate is kept constant as 2.5×10^6 S/s. The closed end of the shock tube does not allow the compressed air to escape out and it results in a sharp rise in pressure at the end of the shock tube (P_3). It confirms that when the striker reaches the sheet, it encounters same magnitude of pressure as recorded by pressure transducer 3 (P_3). The pressure magnitude is significant enough for uniform material deformation prior to the striker impact. After this, the further material deformation is happened because of the impact of the striker. The time span of deformation for both the stages i.e., (i) pressure based bulging (stage 1), and (ii) striker based bulging (stage 2) can be estimated from the pressure-time histories (Fig. 3.4).

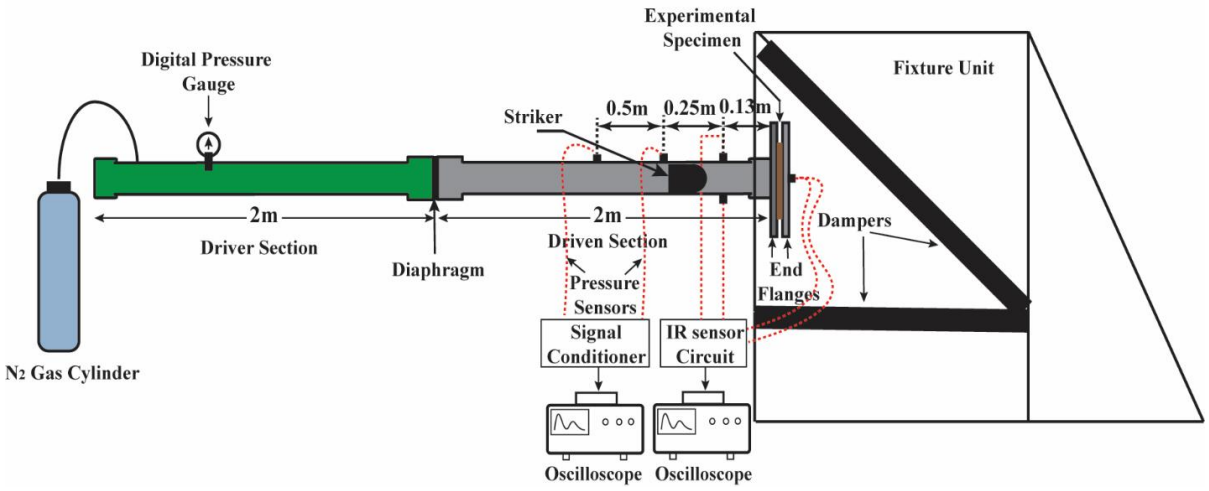

Fig. 3.2: Schematic representation of the shock tube experimental facility

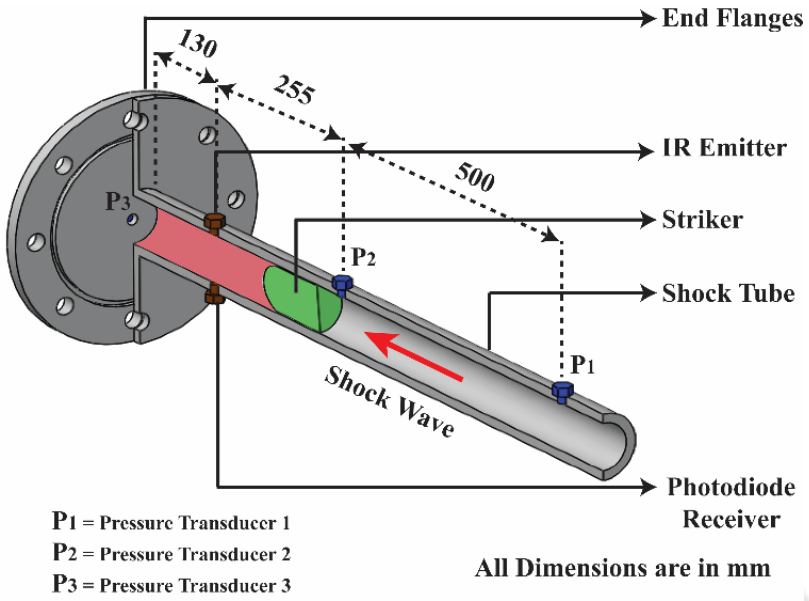

Fig. 3.3: Location of pressure transducers and IR sensors on experimental set up

Table 3.1: Average pressures attained during experiments

Avg. bursting pressure (bar)	Avg. Incident pressure (bar)	Avg. reflected pressure (bar)	Avg. pressure at the end flange (bar)	Avg. Shock Mach number (M_s)
5.68 ± 0.3	2.42 ± 0.1	5.53 ± 0.2	18.35 ± 0.3	1.44 ± 0.02
6.73 ± 0.3	2.50 ± 0.1	5.75 ± 0.1	24.65 ± 0.3	1.49 ± 0.01
7.71 ± 0.3	2.67 ± 0.1	6.30 ± 0.2	29.47 ± 0.3	1.53 ± 0.02

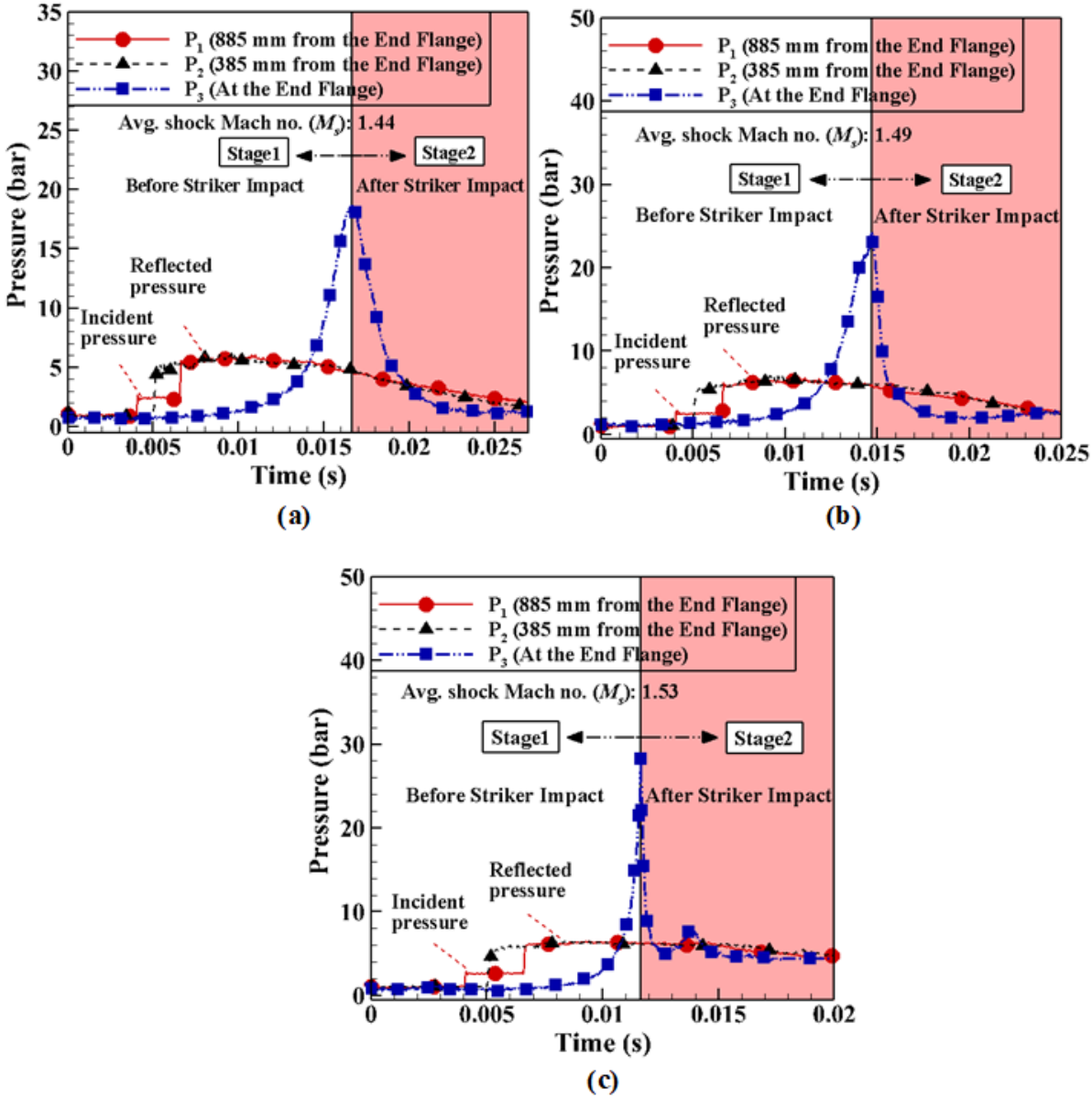

Fig. 3.4: Pressure-time histories for different bursting pressures (a) 5.68 ± 0.3 bar, (b) 6.73 ± 0.3 bar, and (c) 7.71 ± 0.3 bar

The velocity of the striker is measured by the help of an IR emitter and a photo-diode receiver. Both the sensors are mounted on the shock tube at a distance of 130 mm from the end flange (Fig. 3.2 & Fig. 3.5). Two more sets of IR sensors are mounted at the end flange of the shock tube (Fig. 3.5) to identify the velocity of the sheet during the deformation. Both the emitter and receiver are connected to LM 358 (voltage comparator), and a 5V of DC input is supplied in order to power to the sensors (Fig. 3.2). Then, the output voltage of the circuit is visualized in an oscilloscope (Fig. 3.6). The circuit gives a constant voltage output because the

emitted signal from the IR emitter is continuously received by the IR receiver. During experiment, when the striker passes between both the sensors, the emitted signal is interrupted, and it results in a drop in voltage output. When the striker crosses the first sensor (S_1), again the photodiode starts receiving signal, and it results in a sudden rise in output voltage. The time span of drop in voltage illustrates the instance when the striker passes through the IR sensors. This time span can be utilized to obtain the velocity of the striker (Table 3.2). At the same moment, when the sheet reaches 15 mm of height after deformation, and crosses the two IR sensors (S_2 and S_3), the time span of the voltage drop can be used to obtain the velocity of the sheet (Fig. 3.6).

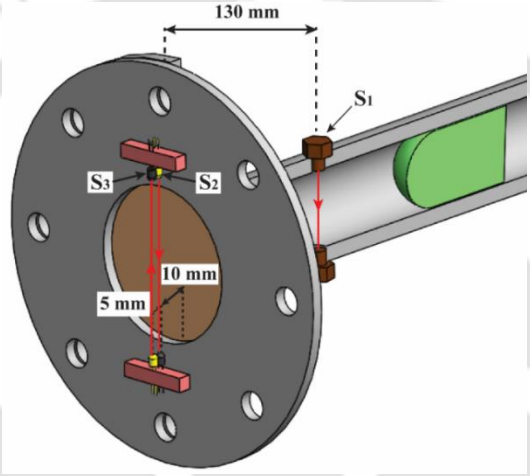

Fig. 3.5: Positioning of IR sensors at the end flange to measure sheet velocity

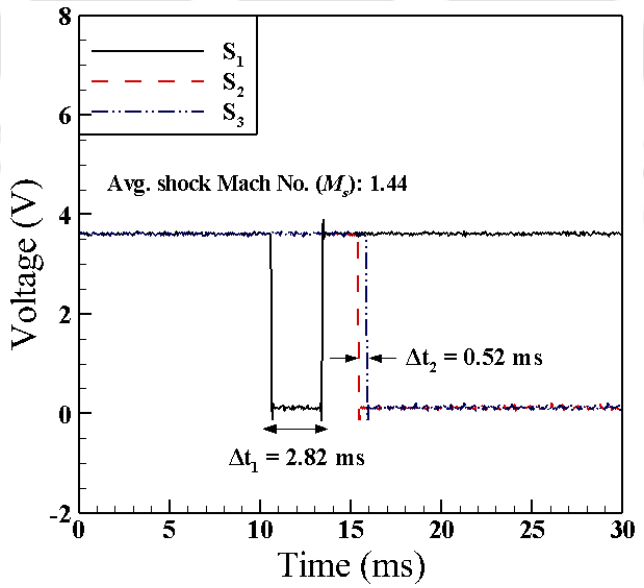

Fig. 3.6: IR sensor signal obtained from an experiment at a bursting pressure 5.68 ± 0.3 bar

Table 3.2: Striker velocities for all the experiments

Bursting pressure (bar)	Mach number (M_s)	Interruption time (ΔT) (ms)	Striker velocity (m/s)
5.68 ± 0.3	1.44 ± 0.02	2.82 ± 0.08	33.62 ± 0.87
6.73 ± 0.3	1.49 ± 0.01	2.29 ± 0.06	41.48 ± 1.06
7.71 ± 0.3	1.53 ± 0.02	1.90 ± 0.06	49.79 ± 1.33

3.1.3 Material specification

The material used in the present work is AA 5052-H32 sheet of 1 mm thickness. The tensile properties of the base sheet, which are obtained according to ASTM E-8 are illustrated in Table 2.2. The tensile results show the anisotropic behavior of the material at different orientations. Thus, ASTM E-517 is followed to obtain the plastic strain ratio (r) along 0°, 45° and 90° to the RD as 0.73, 0.85 and 0.85 respectively. Circular sheets of 185 mm diameter are deformed during the experiment. The effective strain ($\bar{\varepsilon}$) has been measured on the deformed sheet after shock tube based deformation. In experiments, circular grids of average diameter 1.83 ± 0.03 mm are printed on the sheet by chemical etching method. The circular grids deformed into elliptical grids after deformation. The major and minor diameters of the elliptical grids are measured and the effective strain is calculated by using Hill's 1948 yield function (refer Section 2.5). Along with the effective strain, the limit strains ($\varepsilon_1 - \varepsilon_2$ plot) are also quantified with the help of the circular grids method.

3.2 Numerical simulation of shock tube based impact forming

3.2.2 Stress-strain (σ-ε) constitutive models

Several constitutive relations can be implemented, based on the application and requirement of the information to understand the dynamic behavior of AA 5XXX sheet during the high strain rate forming processes (Tian et al., 2014). In the current study, four different stress-strain constitutive relations such as Hollomon model, Cowper-Symonds model, Johnson-Cook model, and modified Johnson-Cook model are used to investigate their importance to predict the high-strain rate forming behavior and the failure mechanism of the sheet.

Generally, the SHPB apparatus is utilized to obtain the dynamic tensile behavior of the material over a wide range of strain rates. In this study, the rate-dependent material properties

of the sheet are identified by the tensile test of a sample cut near to the fracture of the sheet deformed using the shock tube (Fig. 3.7). The tensile test is performed using a UTM at a cross-head speed of 1 mm/min. The true stress-strain curves obtained for different velocities are demonstrated in Fig. 3.8. The variation in the rate-dependent strain hardening properties of the sheet is because of different strain rates of loading. Thus, the strain hardening region of the tensile test data obtained from the deformed sheet are fit to different stress-strain constitutive models and the material constants are evaluated. During the curve fitting, the material parameters are varied in between a certain range under which they generally alter, as per the available literature, and the best fit values are considered for the further calculation. The same procedure is followed for two set of tensile test data for each experimental condition for the repeatability. The material parameters are again utilized to recalculate the flow stress for larger strain and then incorporated during FE simulations. A detailed procedure about the identification of material parameters and input to the software database is explained in Fig. 3.7.

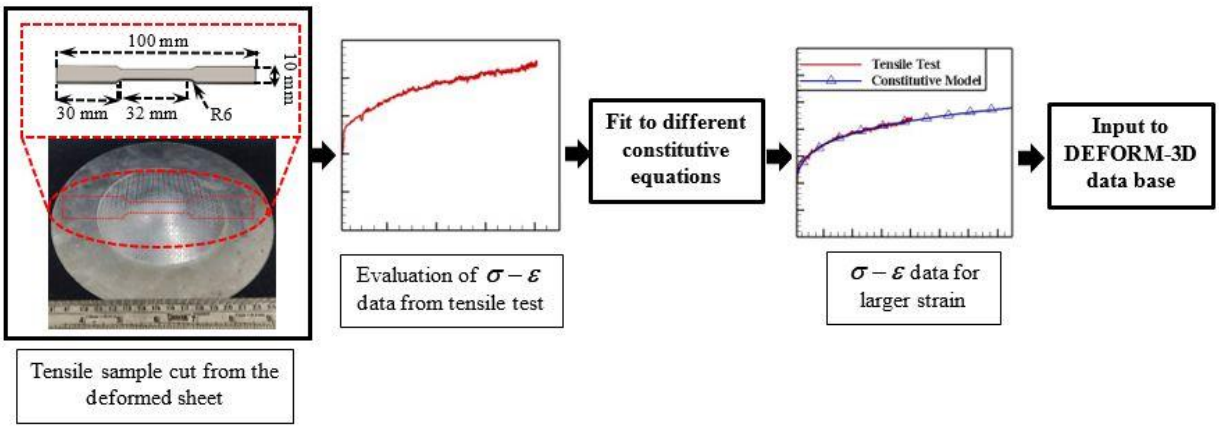

Fig. 3.7: Procedure for identification of material parameter

3.2.2.1 Hollomon model

The first constitutive model used in this work is Hollomon model, which takes into account the strain hardening effect. However, the strain rate sensitivity and the temperature effect are not considered during the analysis. The Hollomon model is given by

$$\bar{\sigma} = K\bar{\varepsilon}_p^{\,n} \tag{3.1}$$

where $\bar{\sigma}$ is the equivalent stress, $\bar{\varepsilon}_p$ is the equivalent plastic strain, K is the strength coefficient, and n is the strain hardening exponent. This model works for a certain range of strain rates, but

it cannot be used for a complete spectrum of strain rates. The tensile test data of the deformed sheet for three different velocity conditions are fit to the Hollomon model and the rate dependent material parameters are identified (Fig. 3.8). The results are compared to the base material properties as shown in Table 3.3. The yield strength (σ_{ys}) and the ultimate tensile strength (σ_u) of the deformed sheets are higher than the undeformed base sheet. The effect of strain hardening is clearly illustrated from the variation of the strain hardening exponent (n) and the strength coefficient (K). The influence of velocity of impact (V_1, V_2 and V_3) are also significant. During the shock tube-based deformation, it is difficult to acquire the strain rate ($\dot{\bar{\varepsilon}}_p$) because of the difficulties in instrumentation. Thus, the predicted effective strain rate ($\dot{\bar{\varepsilon}}_p$) obtained by Hollomon model during FE simulations has been utilized for further calculations. The peak values of $\dot{\bar{\varepsilon}}_p$ for the three velocities 33.62 m/s, 41.48 m/s and 49.79 m/s are 927 s^{-1}, 1440 s^{-1} and 1925 s^{-1}, respectively.

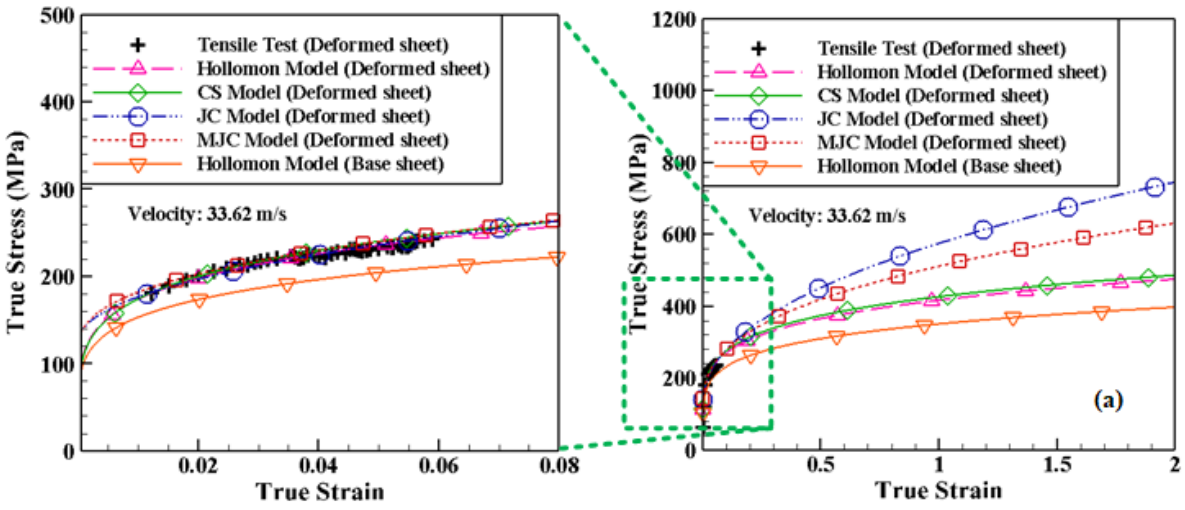

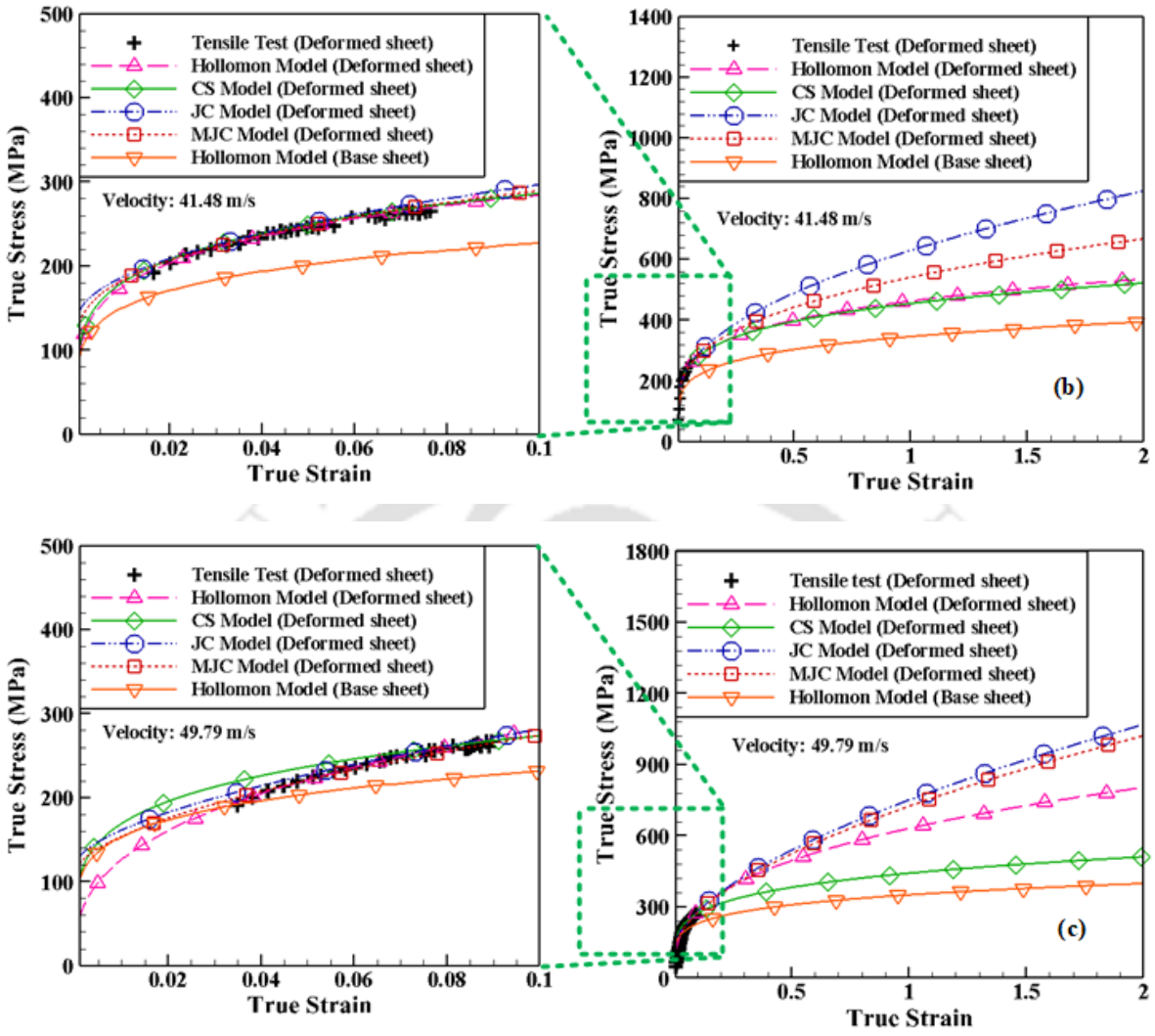

Fig. 3.8: Identification of rate dependent material parameters by curve fitting method for velocity conditions (a) 33.62 m/s (b) 41.48 m/s and (c) 49.79 m/s

Table 3.3: Material parameters obtained for Hollomon model

Material Properties	Undeformed base sheet	Deformed sheet 1 V_1 = 33.62 m/s	Deformed sheet 2 V_2 = 41.48 m/s	Deformed sheet 3 V_3 = 49.79 m/s
σ_{ys}	158 ± 3	183 ± 2	197 ± 2	203 ± 3
σ_u	225 ± 3	242 ± 3	266 ± 2	267 ± 2
K	350 ± 2	416 ± 3	462 ± 3	628 ± 3
n	0.17	0.19	0.21	0.35
σ_{ys} : Yield strength; σ_u : Ultimate tensile strength; n : Strain hardening exponent; K: Strength coefficient; Gauge length: 25 mm.				

3.2.2.2 Cowper-Symonds Model

Among the various dynamic strain hardening models, the Cowper-Symonds (CS) model is widely used as it calculates the dynamic flow stress by multiplying a dynamic hardening factor to the static flow stress of the material. The conventional Cowper-Symonds relation does not take into consideration the thermal softening effect and the constitutive relation is defined as

$$\bar{\sigma} = \bar{\sigma}_{qs}\left[1+\left(\frac{\dot{\bar{\varepsilon}}_p}{D}\right)^p\right] \tag{3.2}$$

where $\bar{\sigma}$ is the dynamic flow stress, $\bar{\sigma}_{qs}$ is the quasi-static flow stress, D and p are the material constants, which are obtained by fitting the dynamic flow stress-strain curve obtained from the tensile test of the deformed sheet. The quasi-static properties of the material are represented by the Hollomon model, where the strain rate sensitivity terms are ignored. The predicted values of $\dot{\bar{\varepsilon}}_p$ from FE simulation is used in eq. 3.2 (described in Section 3.2.2.1). The rate dependent flow stress-strain curve obtained from the tensile test are fit to the CS model (Fig. 3.8) using the material fit constants in Table 3.4. It should be noted that the rate dependent tensile properties defer significantly when compared to the quasi-static properties because of the strain hardening due to the inertial effect. The inertial forces developed during high-velocity dynamic loading condition generates additional tensile stress in the material and it results in significant increase in the strain hardening properties. During this condition, the CS constitutive model (eq. 3.2) scales the quasi-static properties of the material by considering the material constants mentioned in Table 3.4, to adopt it for high-strain rate material deformation.

Noh et al. (2016) demonstrated an inverse parameter estimation method using the nonlinear least square method to identify the material parameters (D and p) for the CS model during the study of the high-strain rate forming behavior of Al 1100-O sheet. They obtained a range of variation in the material parameters with least mean square error between the experimental and simulation results. The material parameters obtained after curve fitting (Table 3.4) is having a good agreement with that ranges. Liu et al. (2011), and Tian et al. (2014) also show a similar variation in the material parameters for AA 5052 sheets.

Table 3.4: Cowper-Symonds model material parameters

Material constants	Deformed sheet 1 V_1 = 33.62 m/s	Deformed sheet 2 V_2 = 41.48 m/s	Deformed sheet 3 V_3 = 49.79 m/s
$\bar{\sigma}_{qs}$	Obtained from tensile test of undeformed base sheet (Table 3)		
D	8500	8500	8700
p	0.63	0.65	0.72

3.2.2.3 Johnson-Cook Model

Johnson-cook (JC) model incorporates the effect of yielding, plastic flow, isotropic strain hardening and strain rate hardening without considering the thermal softening effect during the plastic deformation. Therefore, the terms related to temperature effect are discarded in the conventional JC model. The simplified constitutive relation is defined by

$$\bar{\sigma} = [A + B(\bar{\varepsilon}_p)^n] \times \left[1 + C_1 \ln \frac{\dot{\bar{\varepsilon}}_p}{\dot{\bar{\varepsilon}}_0}\right] \tag{3.3}$$

where *A, B* are the material constants that are determined from the flow stress-strain data of the material at the reference strain rate ($\dot{\bar{\varepsilon}}_0$) (Song et al., 2019). Here, *n* is the strain hardening coefficient, C_1 is the strain rate hardening sensitivity, and $\dot{\bar{\varepsilon}}_p$ is the real strain rate. In the present work, the reference strain rate ($\dot{\bar{\varepsilon}}_0$) equals to 1 s^{-1} is considered. The JC constitutive equation is fit to the dynamic flow stress-strain curve obtained from the deformed sheet and the material constants are obtained (Fig. 3.8). The values $\dot{\bar{\varepsilon}}_p$ are mentioned in Section 3.2.2.1. The lower and upper ranges of the variation of the material parameters are identified from the literature and those values are defined during the curve fitting (Deng et al., 2019; Khodko et al., 2015; Smerd et al., 2006). The best fit values obtained after curve fitting are mentioned in Table 3.5.

Table 3.5: Johnson-Cook model material constants

Material constants	Deformed sheet 1 V_1 = 33.62 m/s	Deformed sheet 2 V_2 = 41.82 m/s	Deformed sheet 3 V_3 = 49.78 m/s
A	121.5	122.7	115.8
B	446.7	456.4	607.3
n	0.42	0.48	0.59
C_1	0.003	0.013	0.006

3.2.2.4 Modified Johnson-Cook Model

Song et al., (2019) demonstrated that the rate-hardening behavior of aluminium alloys are non-linear over a wide range of strain rates and the strain hardening rate decreases with the increase in strain and strain rate. Thus, in the modified Johnson-Cook (MJC) model, the two strain rate sensitivity constants (C_1 and C_2) take care of change in yield strength and hardening rate during deformation. The temperature effect during the plastic deformation is neglected. The modified Johnson-Cook (MJC) model is given by

$$\bar{\sigma}(\bar{\varepsilon}_p, \dot{\bar{\varepsilon}}_p) = [A + B(\bar{\varepsilon}_p)^n] \times \left[1 + C_1 \ln \frac{\dot{\bar{\varepsilon}}_p}{\dot{\bar{\varepsilon}}_0} + C_2 \left(\ln \frac{\dot{\bar{\varepsilon}}_p}{\dot{\bar{\varepsilon}}_0} \right)^2 \right] \tag{3.4}$$

During this analysis, The reference strain rate ($\dot{\bar{\varepsilon}}_0$) remains constant as 1 s^{-1} and $\dot{\bar{\varepsilon}}_p$ is obtained from Fig. 3.10. The material constitutive constants *A*, *B*, *n*, C_1 and C_2 are identified by curve fitting method in the similar procedure obtained for JC model and the best fit values are illustrated in Table 3.6.

Table 3.6: Modified Johnson-Cook model material constants

Material constants	Deformed sheet 1 V_1 = 33.62 m/s	Deformed sheet 2 V_2 = 41.82 m/s	Deformed sheet 3 V_3 = 49.78 m/s
A	123.8	121.6	115.8
B	438.5	510.3	647.3
n	0.38	0.37	0.57
C_1	-0.125	-0.193	-0.09
C_2	0.016	0.024	0.011

3.2.2.5 Selection of yield function

Selecting yield functions like Barlat yield functions and from others would be more suitable for aluminium alloys. However, this is beyond the scope of the present work as it requires incorporating such models in DEFORM by user subroutine. It should be noted that several existing work utilize Hill's 1948 yield function for plasticity analyses and forming prediction of various Aluminium alloys. For example, Talebi-Ghadikolaee et al. (2020) used Hill's yield function to model the ductile damage evolution during U-channel fabrication by

roll forming of AA6061-T6. Pereira et al. (2020) optimized and estimated the work hardening material parameters using Hill's 1948 plasticity model. Failure analyses of AA2024-O sheet during rubber-diaphragm forming was performed using Hill's 1948 yield function (Lee et al., 2018). To understand the effect of post-necking strain hardening models on the FLC estimation of AA5052-O and AA6016-T4 sheets, Pham et al. (2018) assumed Hill's 1948 yield criterion to describe their anisotropy. All the examples show results that have good correlation with experimental data. Thus, in the present analysis, Hill's 1948 yield function is used (as described in Section 2.4.1). The plastic strain ratios required for the yield function are calculated according to ASTM-E517 as listed in Section 3.1.3 and incorporated during FE simulation.

3.2.3 Fracture models and identification of damage parameters

During the high-velocity sheet metal forming, predicting the crack initiation and propagation during material deformation is possible by defining fracture criteria. The ductile fracture occurs under certain conditions influenced by flow stress-strain behavior of the material, strain rate of deformation, and the other process conditions which affect the forming parameters during the deformation. In recent years, numerous attempts have been made to determine the fracture strain during metal forming processes using various fracture criteria. The major mechanism of the initiation of ductile fracture is nucleation of voids, which is caused by the dislocation pile-ups and the cracking of second phase particles. Gurson (1977), developed a mathematical model which involved the void initiation and growth, followed by coalescence associated in ductile fracture. However, according to Hambli (2001), the ductile fracture can be estimated as a function of stress and strain, in which the physical variables of the material can be used to capture the essential microscopic phenomena. Fracture initiates when the integrated product of the equivalent plastic strain, stress and some material parameters exceeds a critical value D_c. The fracture functions are generally written in the following form:

If $\int_0^{\varepsilon_f} f(\sigma,\bar{\varepsilon})d\bar{\varepsilon} - D_c < 0$, there is no failure, and

if $\int_0^{\varepsilon_f} f(\sigma,\bar{\varepsilon})d\bar{\varepsilon} \geq D_c$, failure occurs.

The most generalized failure criteria used in the field of sheet metal forming is based on total plastic work, which is given by Freudenthal as

$$\int_0^{\varepsilon_f} \bar{\sigma} d\bar{\varepsilon} = D_1 \tag{3.5}$$

where $\bar{\sigma}$ and $\bar{\varepsilon}$ are the equivalent stress and strain respectively. The failure strain is represented as ε_f. There are several failure criteria that have been used in many literature to identify the failure strain and fracture behavior (Habibi et al., 2015; Heidari et al., 2020). In this present study, some distinguished failure criteria which have a good correlation with the experimental data are considered and mentioned as follows:

Normalized Cockcroft and Latham model:
$$\int_0^{\varepsilon_f} \frac{\sigma^*}{\bar{\sigma}} d\bar{\varepsilon} = D_2 \tag{3.6}$$

Cockcroft and Latham model:
$$\int_0^{\varepsilon_f} \sigma^* d\bar{\varepsilon} = D_3 \tag{3.7}$$

Rice & Tracey model:
$$\int_0^{\varepsilon_f} e^{\frac{\delta\sigma_m}{\bar{\sigma}}} d\bar{\varepsilon} = D_4 \tag{3.8}$$

Oyane model:
$$\int_0^{\varepsilon_f} \left(1 + \frac{\sigma_m}{\beta\bar{\sigma}}\right) d\bar{\varepsilon} = D_5 \tag{3.9}$$

Ayada model:
$$\int_0^{\varepsilon_f} \frac{\sigma_m}{\bar{\sigma}} d\bar{\varepsilon} = D_6 \tag{3.10}$$

Brozzo model:
$$\int_0^{\varepsilon_f} \frac{2\sigma^*}{3\left(\sigma^* - \sigma_m\right)} d\bar{\varepsilon} = D_7 \tag{3.11}$$

McClintok model:

$$\int_0^{\varepsilon_f}\left[\frac{2}{\sqrt{3}(1-n)}\sinh\left\{\frac{\sqrt{3}(1-n)}{2}\frac{\sigma^*(\alpha+1)}{\bar{\sigma}}\right\}+\frac{\sigma^*(\alpha-1)}{\bar{\sigma}}\right]d\bar{\varepsilon}=D_8 \qquad (3.12)$$

where σ^* is the maximum principal stress, ε_f is the failure strain, σ_m is the hydrostatic stress, α is the stress ratio, n is the strain hardening exponent, δ and β are the material constants, D_1, D_2, D_3, D_4, D_5, D_6, D_7, and D_8 are the critical values of damage.

In order to identify the critical parameters in eq. 3.5 – eq. 3.12, the strain path of deformation must be known. Thus, at the beginning, a numerical study has been carried out to obtain the strain path during failure for the velocity, V_3 = 49.79 m/s, when material fails after deformation. All the four hardening laws mentioned before are used and a single fracture model, i.e. Cockcroft-Latham model (eq. 3.7) is used. During this analysis, the ultimate tensile strength of the material, σ_u = 267 MPa, obtained from the tensile test of the deformed sheet is considered as the maximum principal stress (σ^*). The failure strain, ε_f = 0.38, is measured near the fractured location of the experimental specimen. The critical damage parameter, D_3 = 101.46, which is the product of both the principal stress and the failure strain is used during the preliminary FE simulation. The strain path at the pole of the deformed specimen is obtained for different hardening laws (Fig. 3.9). The result depicts that all the hardening models predict similar strain evolution during deformation. The strain path corresponds to biaxial mode of deformation for certain duration, and then shifts towards the major strain axis (ε_2). In the further analysis, the stage of deformation, when the fracture criterion is satisfied, is identified for all the hardening laws. It is observed that when the damage parameter reaches the critical value (D_3 = 101.46), material starts necking and the material deformation shifts towards plane strain condition as shown in Fig. 3.9. The change of strain path from biaxial to plane strain indicates failure. Thus, by assuming the deformation behavior during necking (failure) as a plane strain condition ($\varepsilon_2 = 0$), the other critical damage parameters (D_1, D_2, D_3, D_4, D_5, D_6, D_7 and D_8) are identified for the current problem.

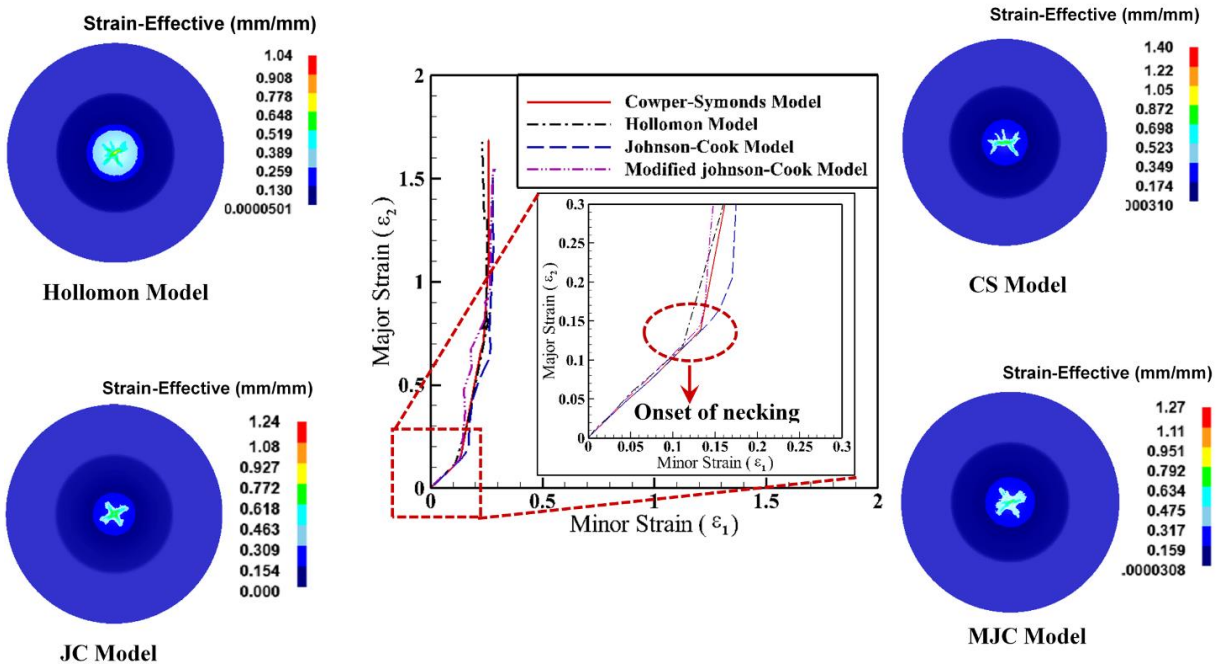

Fig. 3.9: Identification of strain path of deformation and onset of necking

In order to identify the failure strain (ε_f) during the plane strain condition, a sheet specimen with dimensions as shown in Fig. 3.10 is cut from the base sheet and deformed up to failure at the same velocity, V_3 = 49.79 m/s, in the shock tube. Circular grids of average diameter 1.83 ± 0.03 mm are printed on the deforming region by chemical etching method before the shock tube based experiment. The average failure strain (ε_f) is identified by the circular grid method. ε_{1f} = 0.32 is measured near the fractured region along the major axis and that is used during the calculation of critical damage parameter (D_c). All the critical parameters are incorporated during FE simulation for an accurate damage prediction.

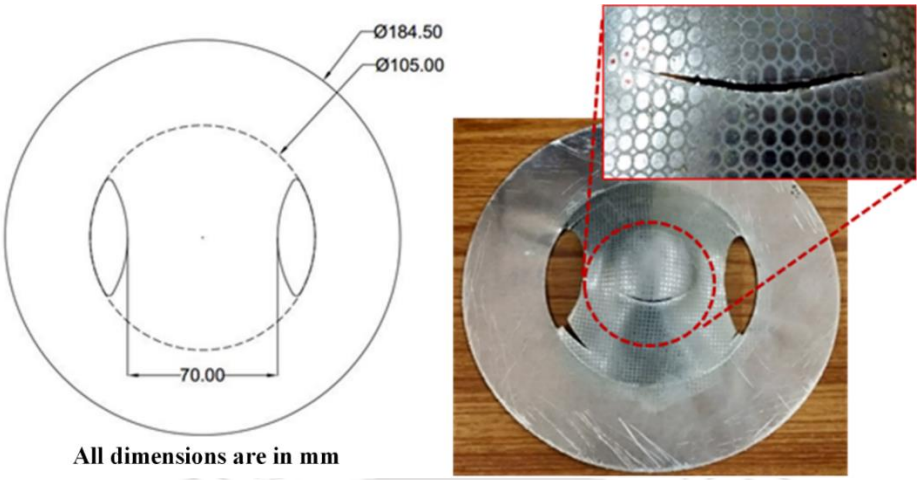

Fig. 3. 10: Dimensions of the plane strain specimen and the deformed sample

Several stress ratios are also obtained for the plane strain condition, in order to incorporate it during critical damage parameter (D_c) calculation. The stress ratios are obtained from Hill's 1948 yield criterion. For anisotropic materials in principal coordinate system, Hill's 1948 yield criterion is expressed as (Takuda et al., 1999)

$$F\left(\sigma_2-\sigma_3\right)^2+G\left(\sigma_3-\sigma_1\right)^2+H\left(\sigma_1-\sigma_2\right)^2=\frac{2}{3}\left(F+G+H\right)\bar{\sigma}^2 \tag{3.13}$$

where F, *G*, and *H* are the anisotropy parameters; σ_i represents the principal stress.

During plastic deformation, the stress and the strain are related by the flow rule and it is given by

$$d\varepsilon_{ij}=d\lambda\frac{\partial f(\sigma_{ij})}{\partial\sigma_{ij}} \tag{3.14}$$

where $d\lambda$ is an arbitrary constant.

The principal strains $(d\varepsilon_1, d\varepsilon_2, d\varepsilon_3)$ for plane stress condition can be obtained by differentiating eq. 3.13 with respect to the principal stresses and substituting into the flow rule. The principal strains $(d\varepsilon_1, d\varepsilon_2, d\varepsilon_3)$ are represented as

$$\begin{aligned} d\varepsilon_1&=d\lambda\left[G\left(\sigma_1-\sigma_3\right)+H\left(\sigma_1-\sigma_2\right)\right]\\ d\varepsilon_2&=d\lambda\left[F\left(\sigma_2-\sigma_3\right)+H\left(\sigma_2-\sigma_1\right)\right]\\ d\varepsilon_3&=d\lambda\left[G\left(\sigma_3-\sigma_1\right)+F\left(\sigma_3-\sigma_2\right)\right] \end{aligned} \tag{3.15}$$

Assuming plane stress condition for thin sheet, Hill's 1948 yield criterion can be demonstrated as

$$F(\sigma_2)^2 + G(\sigma_1)^2 + H(\sigma_1 - \sigma_2)^2 = \frac{2}{3}(F+G+H)\bar{\sigma}^2 \tag{3.16}$$

By substituting principal stress ratio, $\alpha = \sigma_2/\sigma_1$, eq. 3.16 can be derived as

$$F(\alpha)^2 + G + H(1-\alpha)^2 = \frac{2}{3}(F+G+H)\frac{\bar{\sigma}^2}{\sigma_1^2} \tag{3.17}$$

The principal strain ratio, $\beta = d\varepsilon_2/d\varepsilon_1$ for plane stress condition can be expressed as

$$\beta = \frac{F(\alpha) - H(1-\alpha)}{G + H(1-\alpha)} \tag{3.18}$$

Assuming plane strain condition (β = 0), α will be expressed as

$$\alpha = \frac{H}{F+H} \tag{3.19}$$

For no planar anisotropy condition ($r = r_0 = r_{45} = r_{90}$), Hill's anisotropic constants (*F*, *G*, and *H*) can be correlated as *F* = *G* and *H* = *rG*. Substituting *F*, *G*, and *H* into eq. 3.17, the stress ratios can be obtained as

$$\frac{\sigma^*}{\bar{\sigma}} = \sqrt{\frac{2(2+r)(1+r)}{3(1+2r)}} \tag{3.20}$$

$$\frac{\sigma_m}{\sigma^*} = \frac{1+2r}{3(1+r)} \tag{3.21}$$

$$\frac{\sigma_m}{\bar{\sigma}} = \frac{1}{3}\sqrt{\frac{2(2+r)(1+2r)}{3(1+r)}} \tag{3.22}$$

$$\alpha = \frac{\sigma_2}{\sigma_1} = \frac{r}{1+r} \tag{3.23}$$

The principle of equivalent plastic work for plane stress condition is defined as

$$\bar{\sigma} d\bar{\varepsilon} = \sigma_1 d\varepsilon_1 + \sigma_2 d\varepsilon_2 \tag{3.24}$$

The $d\bar{\varepsilon}/d\varepsilon_1$ can be derived as

$$\frac{d\bar{\varepsilon}}{d\varepsilon_1} = \sqrt{\frac{2(2+r)(1+r)}{3(1+2r)}} \tag{3.25}$$

where σ_1, σ_2 are the principal stresses, $\varepsilon_1 = \varepsilon_f$ is the failure strain in the plane-strain deformation obtained as described above. For no planar anisotropy, $r = r_0 = r_{45} = r_{90}$ = 0.85, which is obtained from experiment (refer Section 3.1.3). The ultimate tensile strength of the material (σ_u = 267 MPa) is considered as the maximum principal stress (σ^*). The material constants δ = 1.5 is obtained from the work of Hambli and Reszka (2002) and β = 0.33 is considered for aluminium alloys according to Novella et al. (2015). Table 3.7 shows the values of critical damage parameters calculated for all the fracture models.

Table 3.7 Critical damage parameter for different fracture models

Fracture Models	Critical Damage Parameter
Freudenthal model	D_1 = 85.44 MPa
Normalized Cockcroft-Latham model	D_2 = 0.42
Cockcroft-Latham model	D_3 = 97.41 MPa
Rice & Tracy model	D_4 = 0.83
Oyane model	D_5 = 0.98
Ayada model	D_6 = 0.20
Brozzo model	D_7 = 0.47
McClintok model	D_8 = 0.41

3.2.4 Numerical set up

The complete process of deformation is modeled in two steps because of the feasibility of the multi-operation layout in DEFORM 3D (Fig. 3.11a). In the first stage, the sheet is deformed only by the pressure exerted on the sheet prior to the striker impact. As soon as, the striker

reaches the sheet, pressure attains its peak value at the end of the shock tube. So, the pressure-time data up to the peak pressure (Fig. 3.4) is incorporated as a pressure boundary condition during the first stage of deformation. In the second stage, further material deformation continues because of the high-velocity impact of the striker. The velocity boundary condition is provided to the striker in such a way that it has the velocity given in Table 3.2 at the start of the deformation, and becomes zero at the end of the simulation. The final height of deformation of the specimens measured after experiments are considered as the stopping control in the simulation. An optimized time step of 5×10^{-5} second is provided in the first stage of FE simulation, whereas in the second stage, a constant striker displacement of 0.07 mm is assigned as the step increment.

During FE simulation, the sheet metal is modelled as a deformable plastic body, whereas the two flanges and the hemispherical end nylon striker are considered as the non-deformable rigid bodies (Fig. 3.11a). Selection of a rigid body in DEFORM 3D signifies that the relative positions of the nodes and the elements associated with it remains constant throughout the simulation. The rigid body does not deform but can undergo large body motion. The computational efficiency of FE simulation is also improved by reducing the number of deformable objects. Thus, two flanges and the hemispherical end nylon striker are modelled as rigid bodies and meshed with 21320 and 27632 number of tetrahedral mesh elements, respectively.

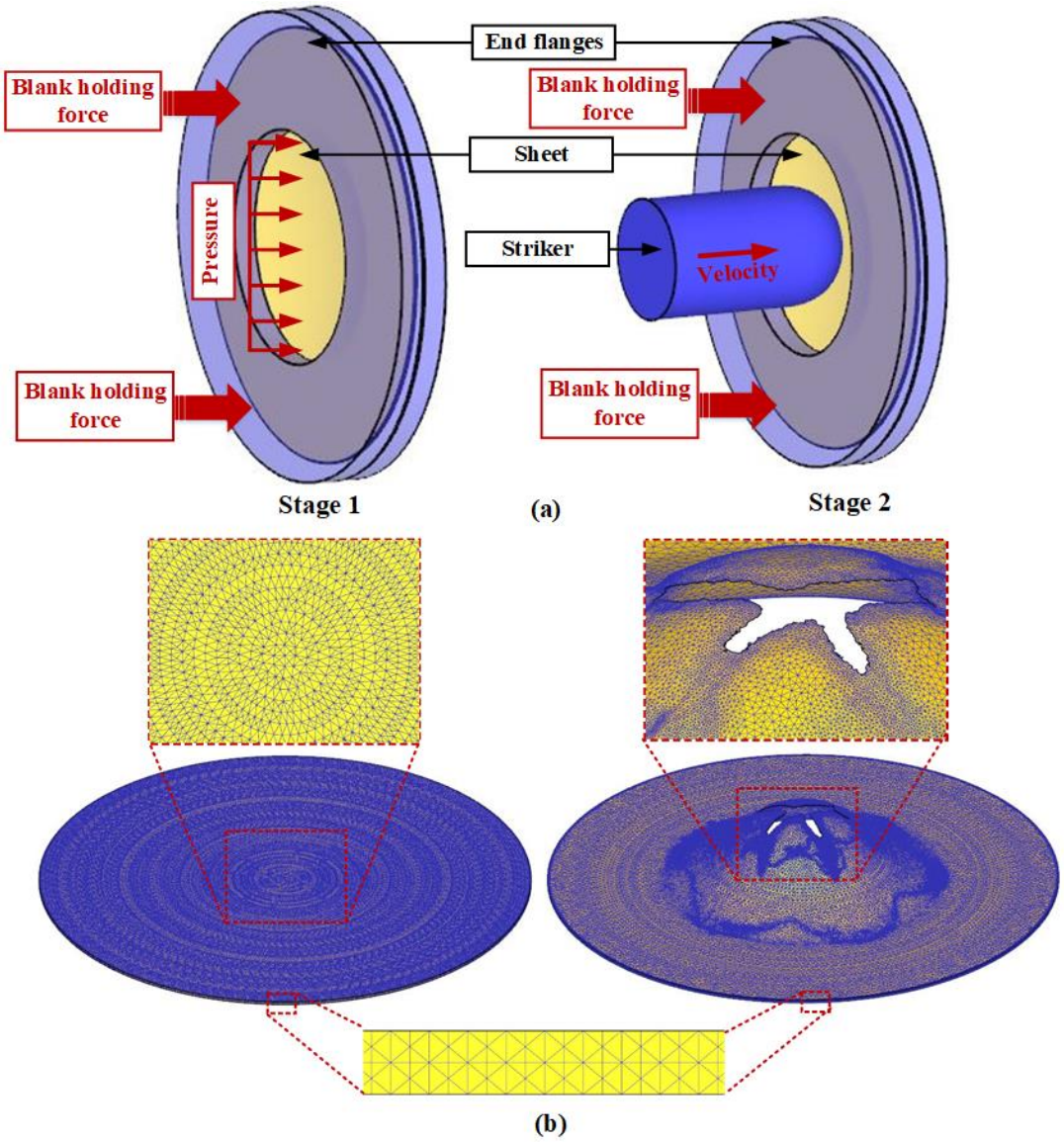

Fig. 3.11: FE simulation of the two stage forming in shock tube based deformation and mesh details

During this analysis, the deformation and failure observed in the material are unsymmetrical, which enforces to consider the complete sheet as the deformable body. To optimize the mesh density and computational time, element size ratio is defined which represents the ratio of the largest element edge to the smallest element edge on the object. During this analysis a constant element size ratio of 6 is considered. A mesh independency analysis has been carried out for velocity, V_1 = 33.62 m/s, to optimize the mesh size. During this analysis, various mesh sizes such as 1, 0.5, 0.33, 0.2, and 0.17 mm have been considered.

All the numerical models are run using Johnson-Cook hardening model and Cockcroft-Latham fracture model. Maximum effective strain for different mesh sizes are compared with the experimental results (Table 3.8). Though 0.2 mm and 0.17 mm element sizes have good agreement with the experimental results, the computational time required to complete FE simulation for 0.17 mm element size is significantly high (Table 3.8). Thus, 0.2 mm minimum element size has been considered for the whole analysis which generates five layers of tetrahedral elements along the thickness direction of the sheet (Fig. 3.11b). The auto remeshing ability of DEFORM-3D generates finer elements at the critical location near to the failure region effectively (Fig. 3.11b).

Table 3.8: Mesh independency analyses

Experimental data and element size (mm)	**Number of elements**	**Maximum effective strain**	**Computational time (min)**
Experimental data	-	0.263	-
1	98653	0.302	245
0.5	124882	0.289	372
0.33	168862	0.276	455
0.2	238783	0.256	725
0.17	296658	0.255	912

The contacts among the striker, end flanges and sheet is modelled by penalty contact algorithm of DEFORM 3D (Iqbal et al., 2019; Jain et al., 2017b). Coulomb's friction coefficient (μ) is considered as a constant parameter to describe the contact boundary condition between the end flanges, sheet and the striker. It is observed from the FE simulation that the damage pattern developed on the sheet after deformation depends on Coulomb's friction coefficient (μ) along with various other parameters such as striker velocity, angle of contact between the sheet and the striker (θ), σ-ε constitutive models and failure models. In order to acquire the actual failure pattern seen in the experiment, the best suited σ-ε constitutive models are considered in conjunction with the failure models during this study. At the same time, μ value is optimized between 0.005 and 0.2 for a single case of FE simulation using Johnson-Cook hardening model and Cockcroft-Latham failure model. At μ = 0.2, plug ejection failure mode is observed, while at μ = 0.005, the results are inaccurate as compared to experiments. As μ decreases, sliding increases between the striker and the sheet. μ = 0.02 predicts a quasi-

petalling failure mode, which has good agreement with the experimental data and hence considered for the whole analysis. The contact condition between the sheet and the end flanges are defined by μ = 0.1. The other material parameters are mentioned in Table 3.9.

Table 3.9: Parameters considered for numerical simulation

Parameters	Data
Mass density of AA 5052-H32, ρ (kg/m^3)	2432
Mass density of Nylon, ρ (kg/m^3)	1140
Young's modulus of AA 5052-H32 , E (MPa)	68,900
Young's modulus of Nylon , E (MPa)	3810
Poisson's ratio of AA 5052-H32, υ	0.33
Poisson's ratio of Nylon, υ	0.39
Stress-strain data of sheet	Fig. 9
Coulomb's coefficient of friction (μ) (between sheet and dies)	0.1
Coulomb's coefficient of friction (μ) (between sheet and striker)	0.02

3.3 Results and Discussion

The forming behavior of AA 5052-H32 sheet has been studied for three different velocities of the striker (Table 3.2) corresponding to three different patterns of deformation. At V_1 = 33.62 m/s, the sheet deforms uniformly without strain localization, whereas at the extreme velocity, V_3 = 49.79 m/, the sheet fails after plastic deformation. As the experiment completes in a small time interval, it is difficult to control the striker movement at an instant when necking occurs on the sheet without failure. Thus, an intermediate velocity, V_2 = 41.48 m/s is achieved by repeating several experiments between the two extreme velocities (33.62 m/s and 49.79 m/s) to achieve the onset of necking on the sheet. Further, during FE simulation, the forming behavior of the sheet is predicted for the two extreme velocities (33.62 m/s and 49.79 m/s) and the effect of different σ-ε constitutive models and failure models are analyzed. The best-suited models are utilized to predict the necking at V_2 = 41.48 m/s.

3.3.1 Comparison of σ-ε constitutive models

The predictability of the four constitutive models for AA 5052-H32 sheet during high-velocity forming can be evaluated by a statistical analysis correlation coefficient (R), expressed as

$$R = \frac{\sum_{i=1}^{N}(E_i - \bar{E})(P_i - \bar{P})}{\sqrt{\sum_{i=1}^{N}(E_i - \bar{E})^2 (P_i - \bar{P})^2}} \tag{3.26}$$

where E_i is the experimental values, P_i is the predicted values by different constitutive models, $\bar{E}$ and $\bar{P}$ are the mean values of E_i and P_i, respectively. The total number of data points considered during the study is represented as N. The correlation coefficient (R) is a statistical parameter, which provides information about the linear relationship between the experimental and predicted values. Fig. 3.12 compares the data points of different constitutive models with the experimental flow stress for three different striker velocities. The correlation coefficient (R) for different constitutive models demonstrate a good predictability, while CS model has slight deviation at higher velocities. Among all, the prediction accuracy of MJC model is highest at all the three velocities because of the consideration of strain rate sensitivity terms during calculation. The predictability of JC model is also in an acceptable range. Though, there is a good correlation of Hollomon model with the experiment, it might not be acceptable for high strain rate experiment because of the absence of strain rate sensitive index.

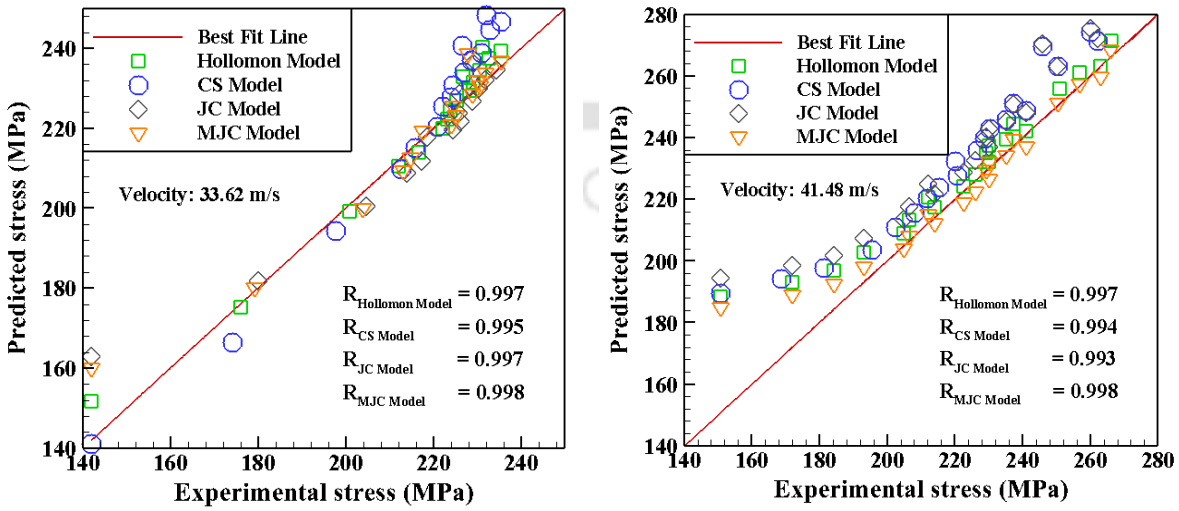

(a) (b)

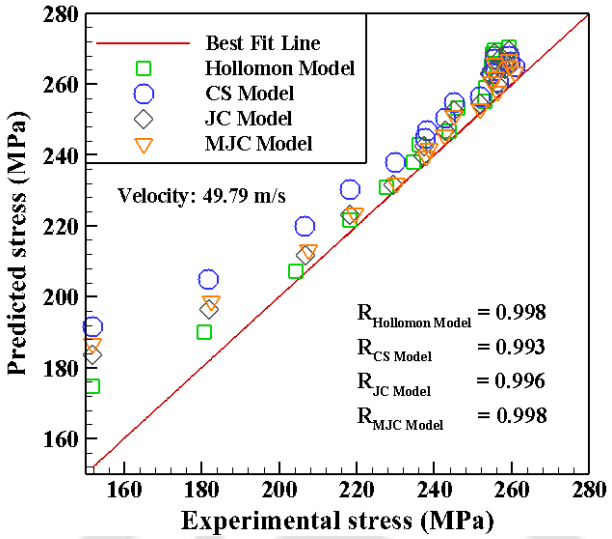

(c)

Fig. 3.12: Comparison between measured and predicted flow stress for four constitutive models for velocities (a) 33.62 m/s, (b) 41.48 m/s, and (c) 49.79 m/s.

3.3.2 Influence of σ-ε constitutive models and failure models

3.3.2.1 Dome height

The predicted dome heights are validated with the experimental results for three different velocities. The numerical simulations are conducted with and without incorporating pressure exerted on the sheet prior to the striker impact (Fig. 3.13). The results depict the importance of input pressure conditions during the FE simulation. The sheet deforms uniformly because of the pressure exerted on the sheet (Fig. 3.4) prior to the striker impact in the exposed region. Along with this, when the striker hits the sheet, deformation continues further and it results in uniform sheet deformation. During FE simulation of no input pressure condition, the sheet deforms only because of the striker impact and it results in more deformation only in the striker hitting region. The results illustrate that the deformation of the sheet is dependent on the flow stress relations. However, all the stress-strain models have a good agreement with the experimental results. The JC model slightly over predicts the dome height at different sheet locations (X-axis).

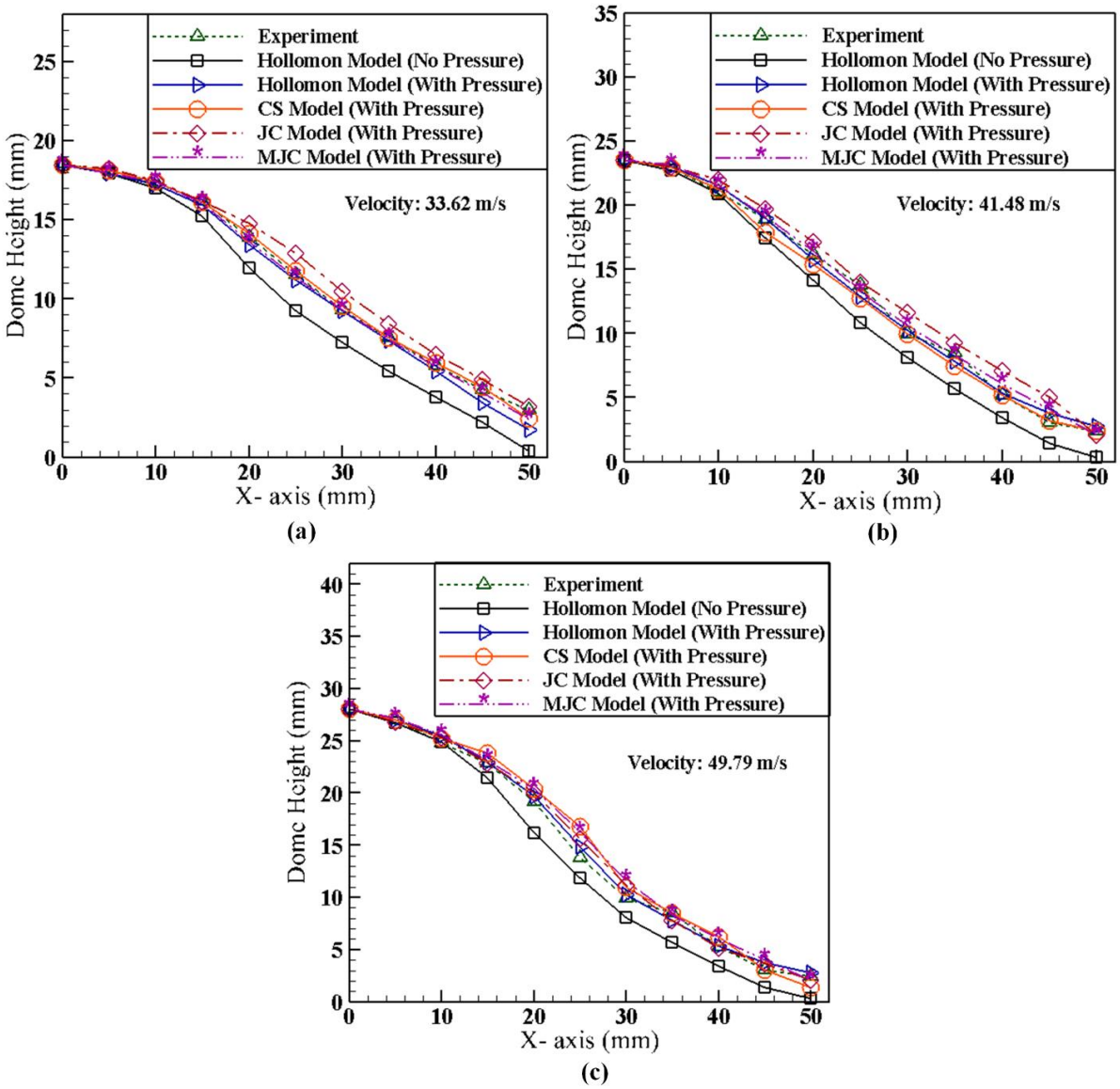

Fig. 3.13: Comparison of dome height of the sheet with experiment for velocities (a) 33.62 m/s (b) 41.48 m/s and (c) 49.79 m/s (0 mm corresponds to pole, and 50 mm corresponds to the end of the deformation)

3.3.2.2 Sheet velocity during forming

During experiments, IR sensors are used to measure the velocity of the sheet (Fig. 3.5), and FE simulation is utilized to predict the velocity of the sheet at the same instance, i.e., when the height of deformation reaches 15 mm. The sheet velocity predicted by different flow stress models is shown in Fig. 3.14. The percentage of variation in the predicted sheet velocity

illustrates that JC model and MJC model, which consider strain rate sensitivity during their calculation have better agreement with the experiment. Besides the strain rate sensitivity term, the CS model has over predicted the sheet velocity. The CS model does not predict the forming behavior of the sheet adequately and its application might be limited in a certain range of strain rate. An under-prediction in results is observed in Hollomon model because of the absence of the strain rate hardening coefficient during the calculation.

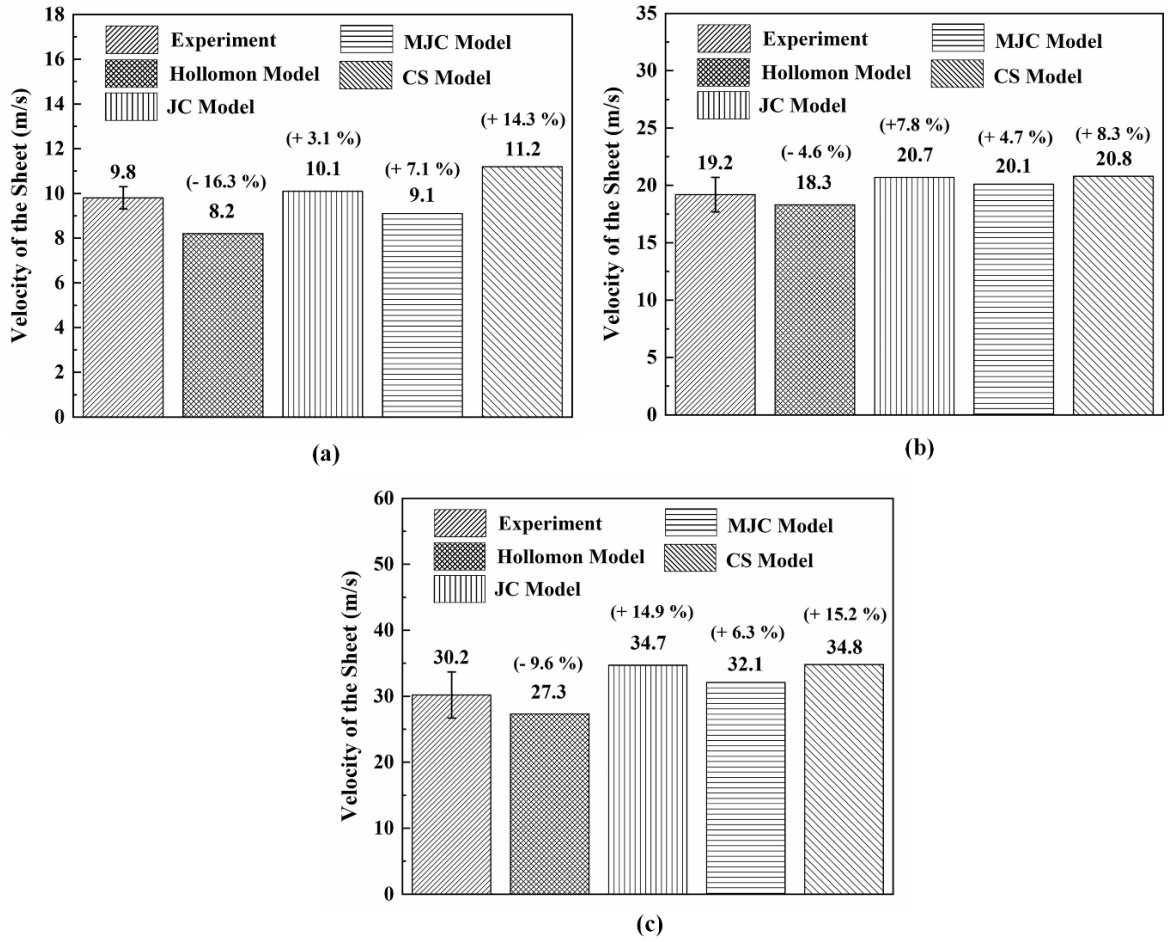

Fig. 3. 14: Comparison of the predicted sheet velocity with experiment for velocities (a) 33.62 m/s (b) 41.48 m/s and (c) 49.79 m/s. (Values in brackets indicate % of variation)

3.3.2.3 Sheet failure

In this study, only one extreme velocity V_3 = 49.79 m/s is achieved, corresponding to sheet deformation beyond its critical limit, and observed to have ruptured. The failure behavior of the material is predicted by FE simulations by using different stress-strain constitutive models, and failure models. The results predicted by FE simulations are shown in Fig. 3.15. During the

analysis, the numerical simulations are continued till the height of deformation observed in experiments. The critical damage parameters (D_c) are incorporated into the FE simulation. Those values are responsible for necking followed by crack initiation and propagation in the material. The predicted results clearly illustrate the importance of different $\sigma - \varepsilon$ constitutive models and the failure models. Out of all, the combination of some models deliver a better result when compared to the experiment. The predicted petalling pattern of the sheet is validated with experiment by visual inspection. Except normalized Cockcroft-Latham model, almost all failure models have well predicted the failure pattern. Out of four hardening models, the results predicted by JC and MJC constitutive models have a fair agreement with the experimental petal formation. The dynamic behavior of the material is well captured by these two constitutive models because of the strain rate sensitive indices, which are incorporated during the calculation of flow stress. This facilitate the usability of both JC model and MJC model in complete spectrum of strain rate. On the other hand, the results predicted by CS model and Hollomon model are in the acceptable range. However, the use of Hollomon model may not be acceptable for higher strain rate application due to the absence of strain rate sensitivity term.

In order to have a better quantitative comparison of the different failure models, the failure strains (ε_f) i.e., the major strain near the failure are obtained for all the models and compared with the shock tube based experiments (Fig. 3.16). The failure strains (ε_f) predicted by different hardening models do not vary significantly. However, a slight variation in ε_f is observed when different failure models are used. Looking in to the failure patterns and the predicted failure strain, it can be concluded that Freudenthal and Brozzo failure models along with JC and MJC constitutive models would have a better failure prediction potential than the other combinations. The Freudenthal damage model has 5-7% deviation, whereas the Brozzo model has 6-8% deviation when compared with the experimental failure strain (ε_f), which is in an acceptable limit. Similar variations are observed in repeated experimental trials.

$\sigma - \varepsilon$ Constitutive Models				
Hollomon Model	**CS Model**	**JC Model**	**MJC Model**	**Experiment**
Failure Model: Cockcroft Latham Model				
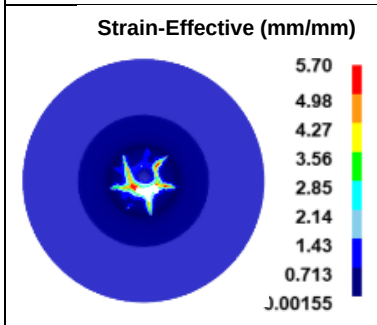	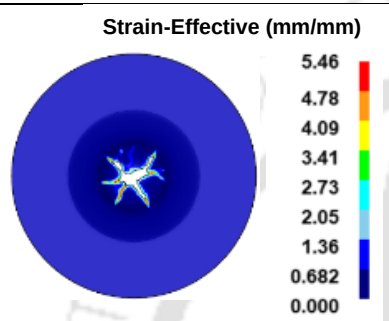	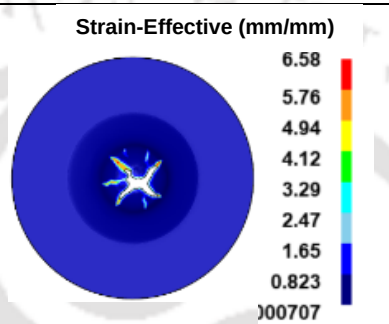	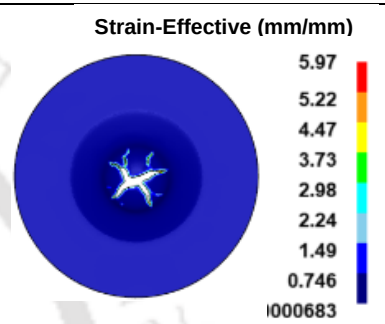	
Failure Model: Normalized Cockcroft Latham Model				
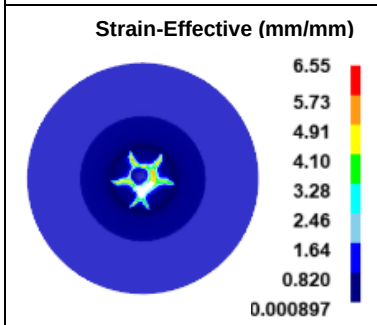	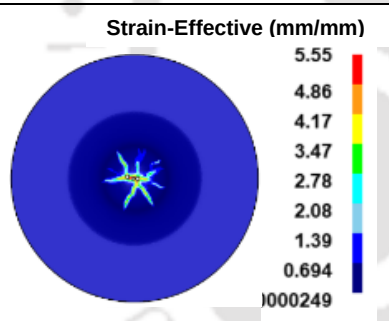	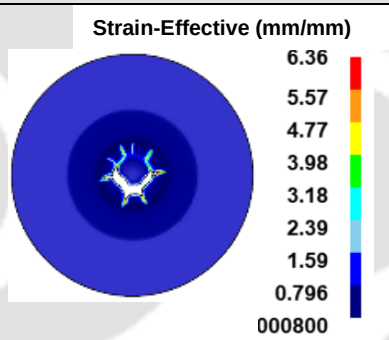	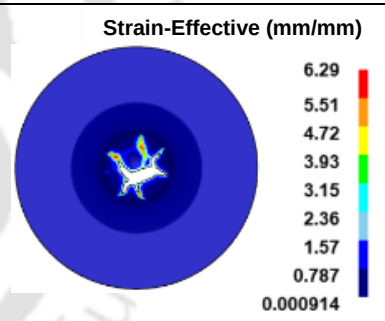	

(a)

$\sigma - \varepsilon$ Constitutive Models				
Hollomon Model	**CS Model**	**JC Model**	**MJC Model**	**Experiment**
Failure Model: Freudenthal Model				
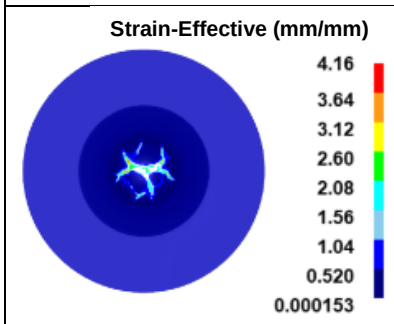	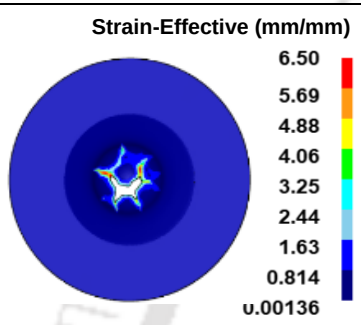	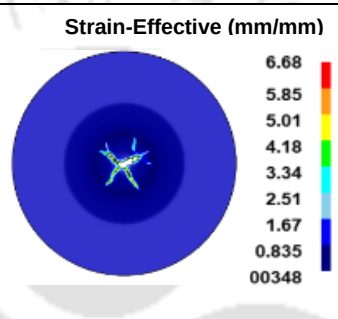	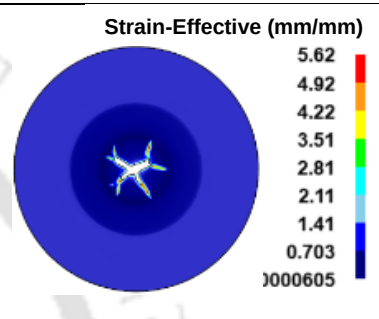	
Failure Model: Oyane Model				
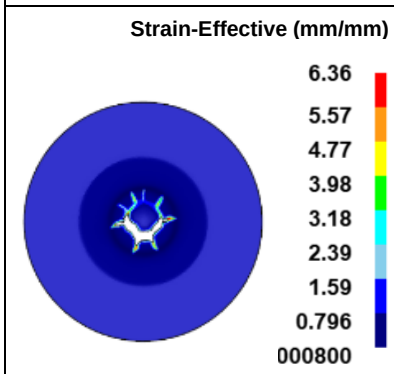	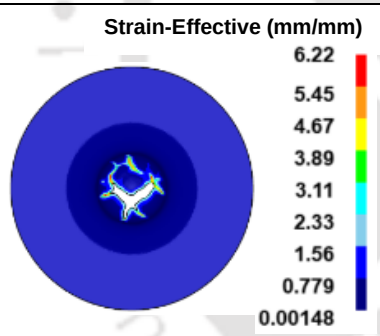	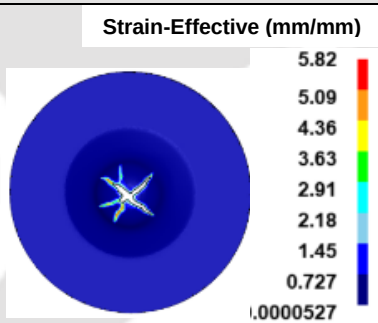	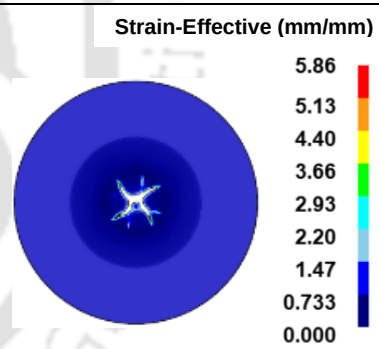	

(b)

$\sigma - \varepsilon$ Constitutive Models				
Hollomon Model	**CS Model**	**JC Model**	**MJC Model**	**Experiment**
Failure Model: Rice & Tracey Model				
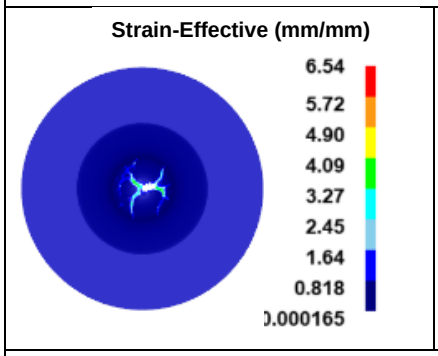	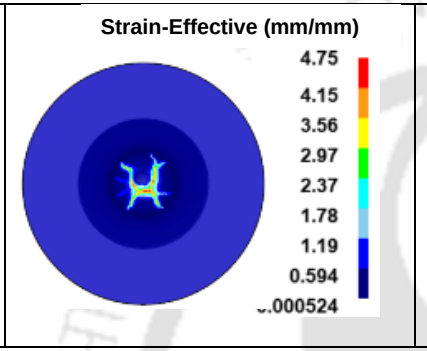	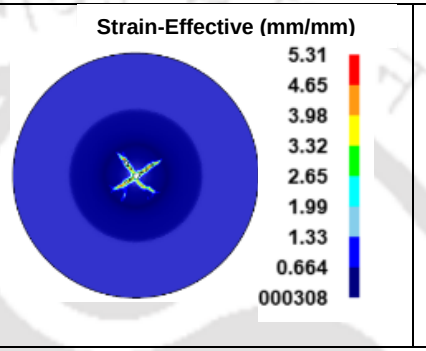	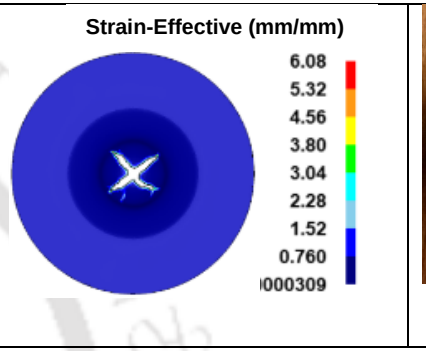	
Failure Model: Brozzo Model				
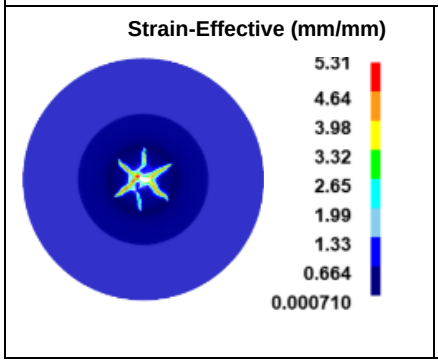	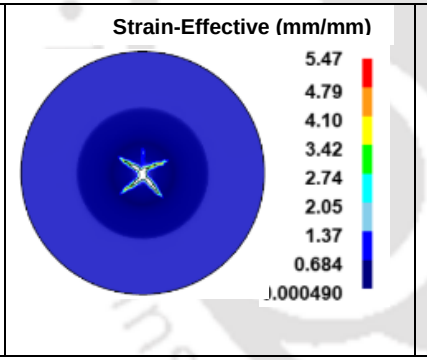	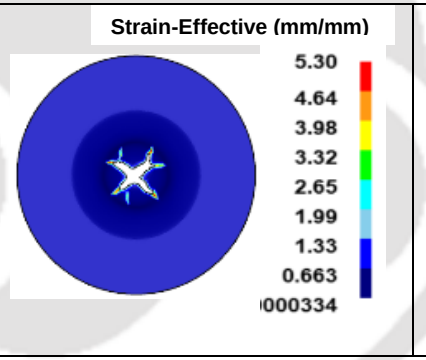	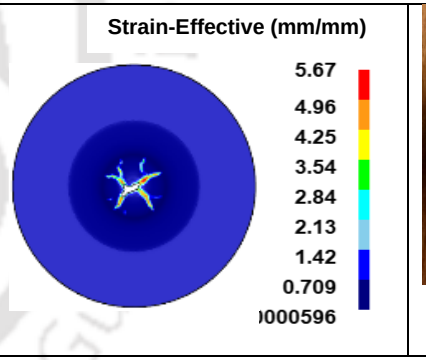	

(c)

$\sigma - \varepsilon$ Constitutive Models				
Hollomon Model	**CS Model**	**JC Model**	**MJC Model**	**Experiment**
Failure Model: Ayada Model				
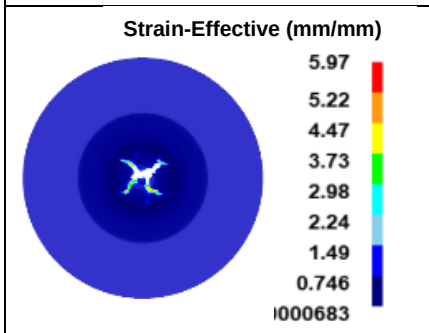	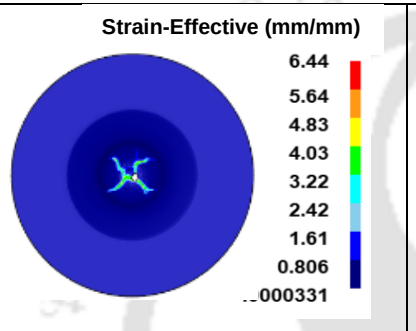	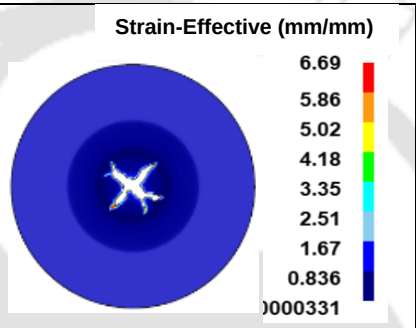	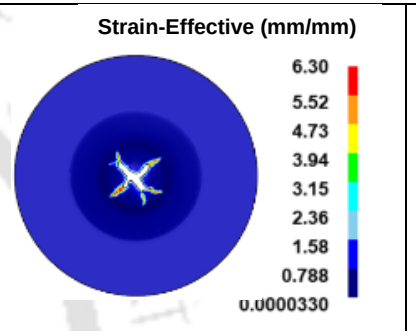	
Failure Model: McClintok Model				
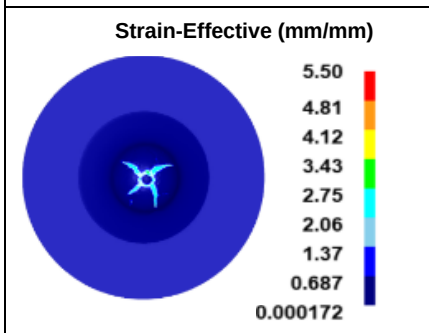	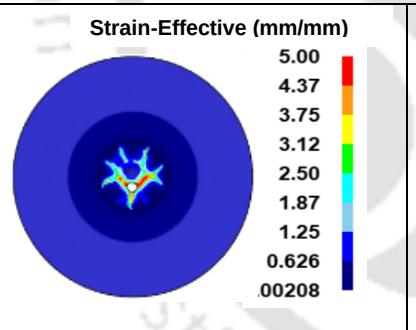	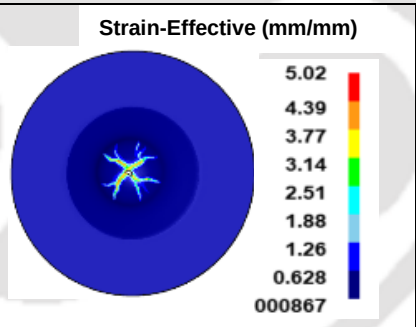	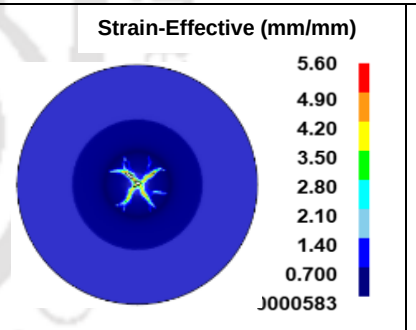	

(d)

Fig. 3.15: Comparison of the failure pattern predicted by different failure models in comparison with the experiment at V3 = 49.79 m/s

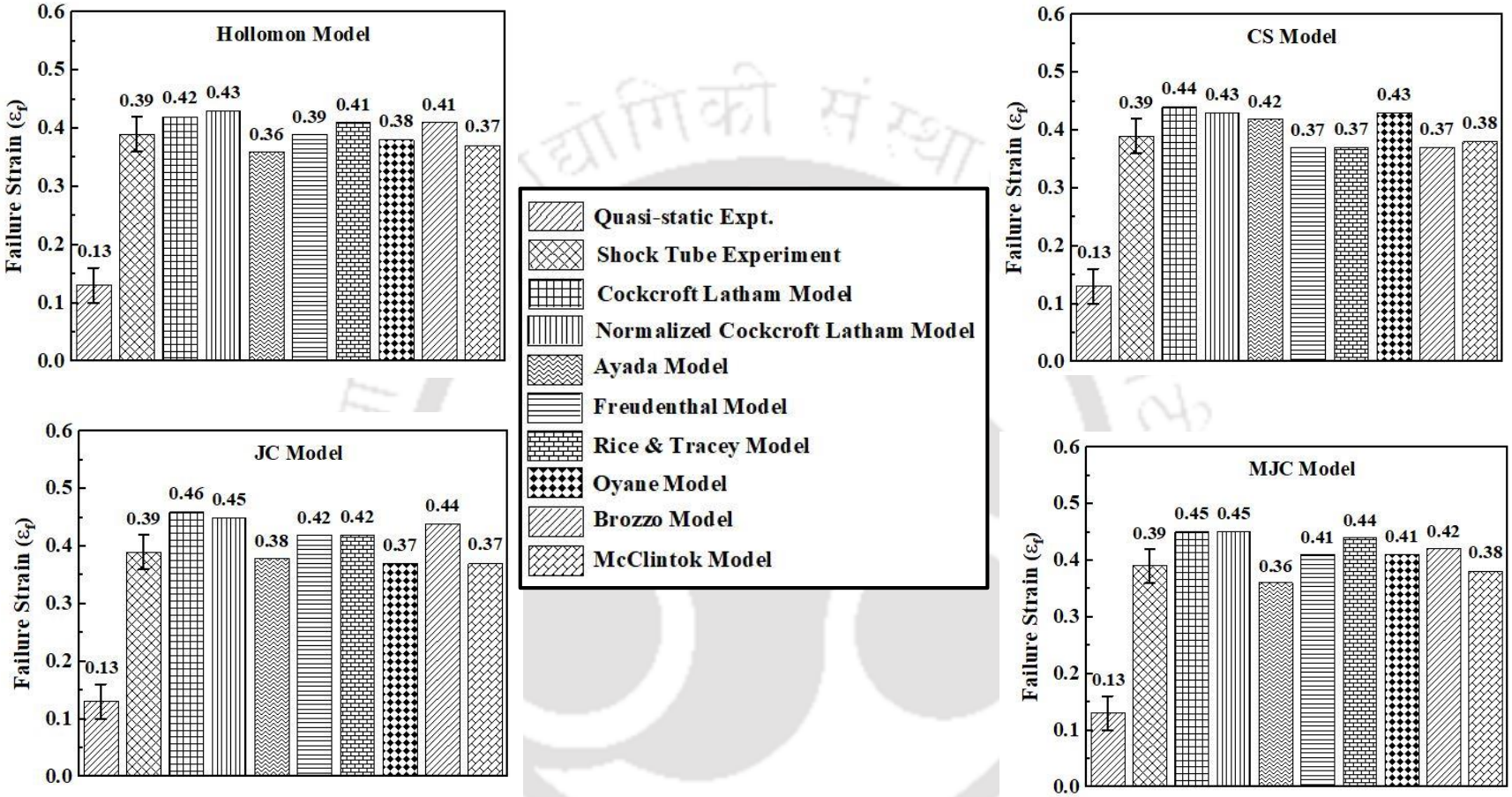

Fig. 3.16: Comparison of the failure strain (ε_f) predicted by different failure models when compared with experiments

3.3.2.4 Forming limit strain

The limiting strain or the failure strain (ε_f) of the material measured near the fractured zone of the failed sample after shock tube based experiment (for V_3 = 49.79 m/s) are compared with the quasi-static biaxial forming results as shown in Fig. 3.16. In order to achieve a quasi-static condition, AA 5052-H32 sheet is deformed until failure by normal hydraulic punch stretching set up at a velocity of 5 mm/min. From the results it is observed that forming limit increases significantly (about 60-70%) when the sheet is deformed at high velocity. Generally, in quasi-static forming, the velocity gradient developed between the two points on the material varies simultaneously. When it reaches a critical value, the necking phenomenon starts and restricts the deformation in the material. While in high-strain rate forming, including shock tube based deformation, a significant improvement in formability is observed because of the inertial effect associated with the process. The inertial force stabilization helps the material to deform more outside the necking zone. This phenomenon minimizes the local velocity gradient developed on the material, and helps to deform the material further without strain localization. In the current study, the FE simulation also captures the material deformation due to the inertial effect, which is taken care by all the constitutive models and the failure models. Out of all, the limiting strain predicted by MJC model along with Brozzo failure model has a deviation of 6-8% (Fig. 3.16) as compared to the experimental data.

3.3.2.5 Effective strain distribution

In order to predict the effective strain distribution, four $\sigma - \varepsilon$ constitutive models are used. The predicted results are compared with the experimental results (Fig. 3.17) for three velocities. At velocity V_1 = 33.62 m/s, the material deforms within the safe limit without strain localization. It results in a biaxial mode of deformation (Fig. 3.17a). At an intermediate velocity, V_2 = 41.48 m/s, the material starts necking with little crack initiation (Fig. 3.17b). At velocity, V_3 = 49.79 m/s material fails severely after deformation. Brozzo failure model is used for failure prediction. The effective strain distribution gives a better visualization of strain change during this state (Fig. 3.17c). It can be concluded that, the material constitutive models considering the non-linear strain rate sensitivity term during flow stress calculation predict the $\bar{\varepsilon}$ distribution accurately. The CS model and JC model have considered the non-linear

sensitivity term. However, it is not possible to define the rate dependent material properties of the material correctly with one set of parameter for a complete spectrum of strain rate. Thus, in MJC model, another strain rate sensitivity parameter has been considered for a better prediction from quasi-static to dynamic loading conditions, and hence it has better correlation with the experiment.

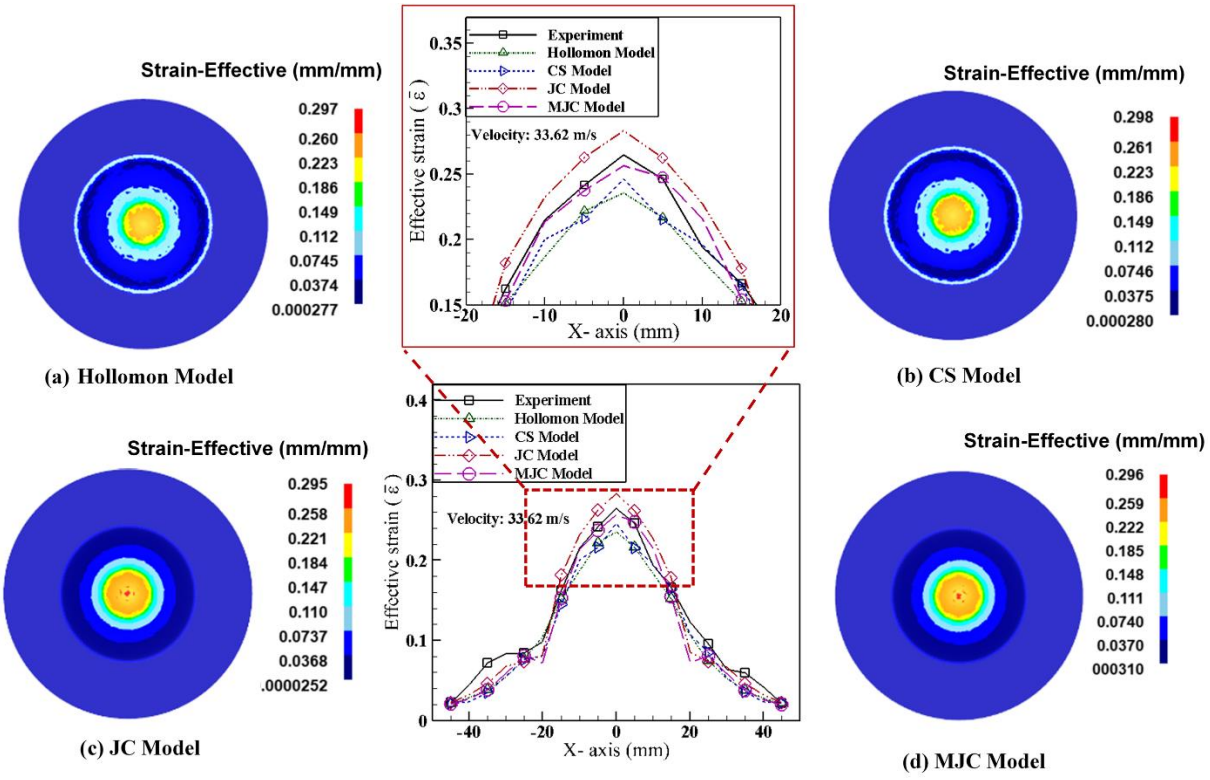

(a)

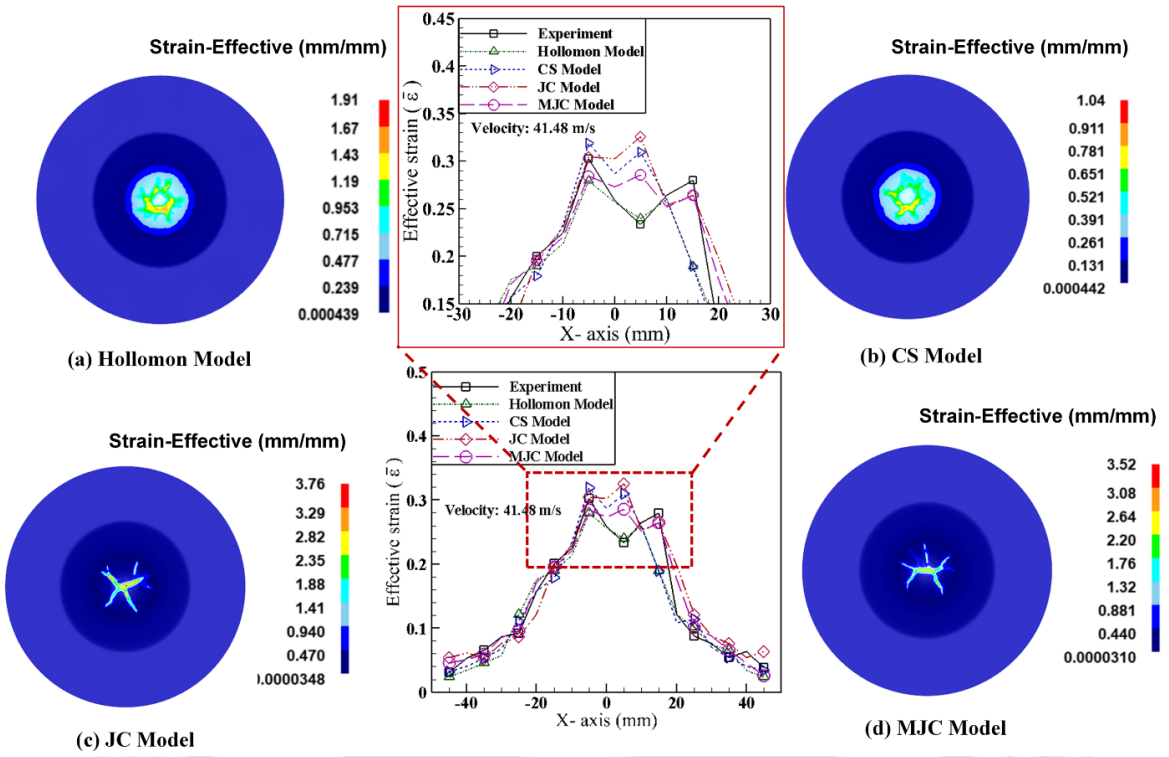

(b)

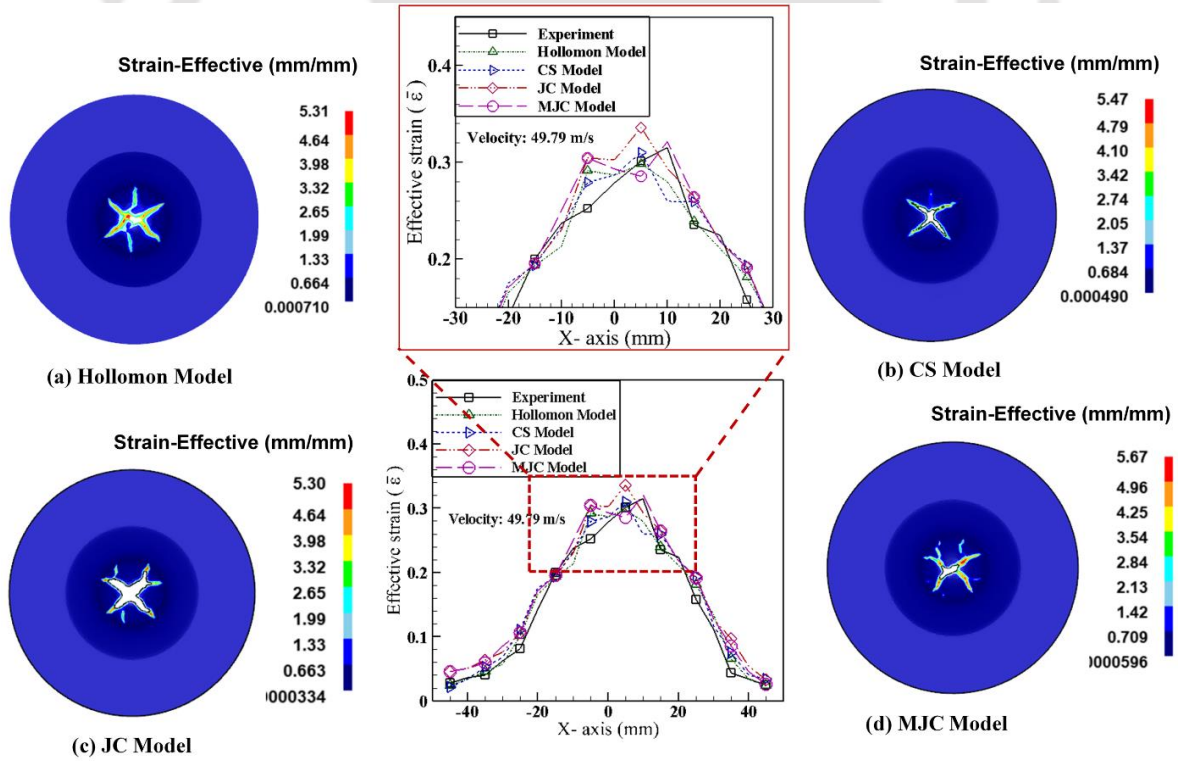

(c)

Fig. 3. 17: Comparison of the predicted effective strain distribution with the experiment for velocities (a) 33.62 m/s (b) 41.48 m/s and (c) 49.79 m/s

3.3.2.6 Strain rate

During the shock tube based forming process, obtaining the strain rate during experiments is difficult because of the practical constraints in instrumentation. Thus, FE simulation has been utilized to identify the range of strain rate at the pole region of the specimen. The average strain rate ($\dot{\bar{\varepsilon}}$) predicted for three different velocities are depicted in Table 3.10. The results show a rate-dependent characteristic. Similar to effective strain ($\bar{\varepsilon}$) distribution, the strain rate ($\dot{\bar{\varepsilon}}$) developed during the deformation is also dependent on the constitutive models. The hardening models that have considered nonlinear strain rate sensitivity during their flow stress calculation such as CS model, JC model and MJC model have lesser variations in $\dot{\bar{\varepsilon}}$ (Table. 3.10). On the other hand, the strain rate ($\dot{\bar{\varepsilon}}$) values predicted by Hollomon model is less in comparison to other hardening models because of the absence of strain rate sensitivity during its calculation. The change in strain rate at different locations of the sheet is also predicted by using the best suited hardening model, i.e., MJC model (Fig. 3. 18). The results illustrate a sharp rise in strain rate ($\dot{\bar{\varepsilon}}$) at the pole region. The material adjacent to the pole region also stretches at high strain rate after striker impact (Fig. 3.18), which is because of the inertial forces. It helps to deform the sheet further without strain localization. This analysis illustrates the rise in forming behavior of high-velocity forming process considering the shock tube based deformation.

Table 3.10: Effective strain rate of deformation predicted by different hardening models

Effective strain rate, $\dot{\bar{\varepsilon}}$ (s^{-1})				
Velocity of striker (m/s)	Hollomon Model	CS Model	JC Model	MJC Model
V_1 = 33.62	927 ± 12	1080 ± 11	1028 ± 8	1045 ± 10
V_2 = 41.48	1440 ± 10	1528 ± 8	1530 ± 12	1535 ± 8
V_3 = 49.79	1926 ± 7	2080 ± 10	2078 ± 10	2055 ± 11

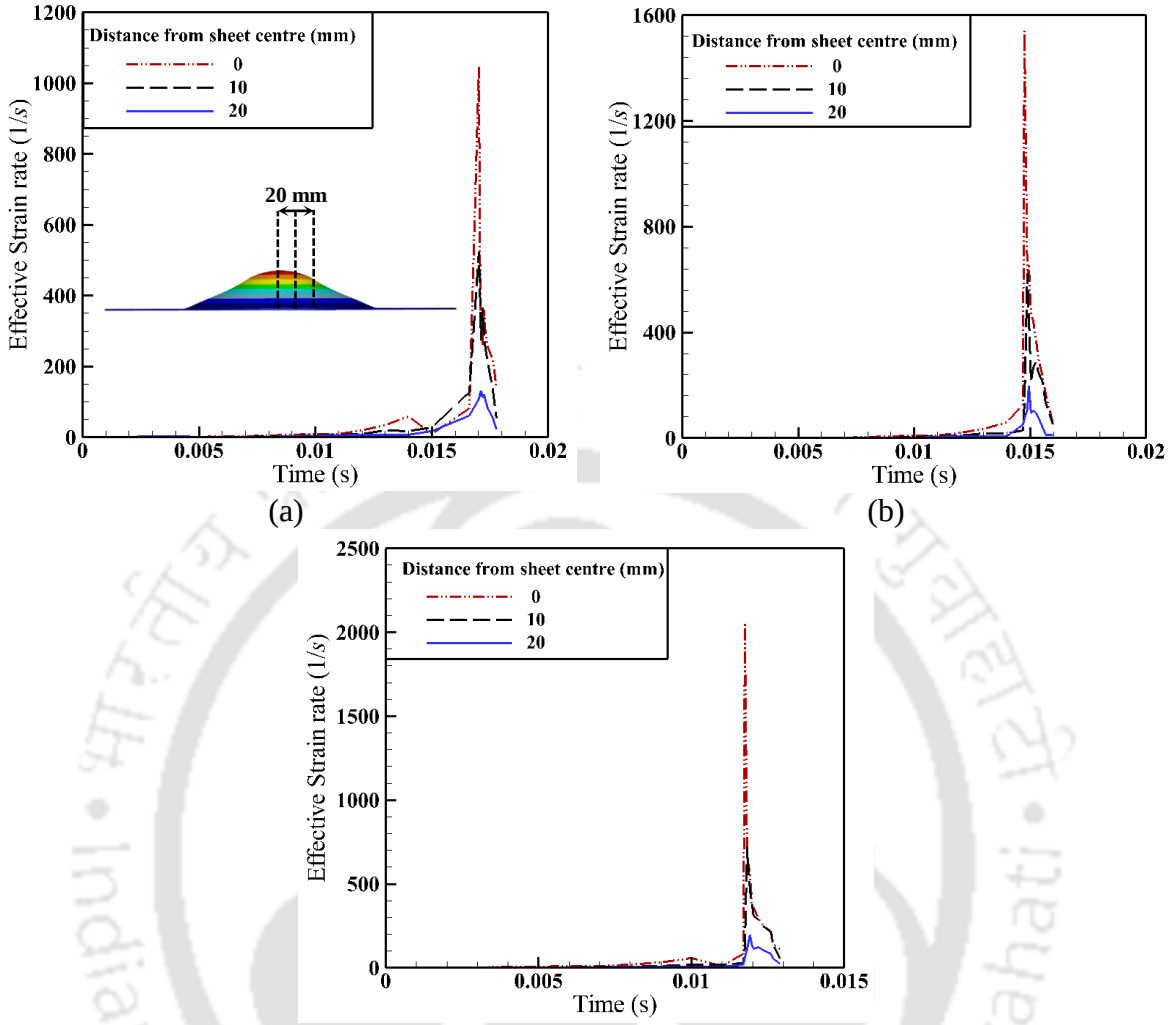

Fig. 3.18: Predicted strain rate at velocities (a) 33.62 m/s, (b) 41.48 m/s, (c) 49.79 m/s at different location

3.3.3 Fractography

The fracture surface along the thickness direction of the specimen formed by quasi-static forming and shock tube-based forming are obtained using scanning electron microscope (SEM) as illustrated in Fig. 3.19. During the shock tube experiment, at a striker velocity, V_3 = 49.79 m/s, the sheet fails after plastic deformation. Thus, a single case is considered during this comparative analysis. Several dimples are observed in both the images indicate that a ductile mode of fracture occurs during the deformation. At the same time, larger plastic deformation because of the impact loading during shock tube-based deformation reveals deeper and larger dimples, which demonstrates the evidence of hyperplasticity. Ahmed et al.

(2017) also represented a similar ductile fracture mode for AA 5052 material during the EHF process. Equiaxed dimples are observed on the fracture surface of the sheet formed by quasi-static forming. On the contrary, parabolic shape dimples are observed in shock tube-based forming, and they are oriented in a certain direction.

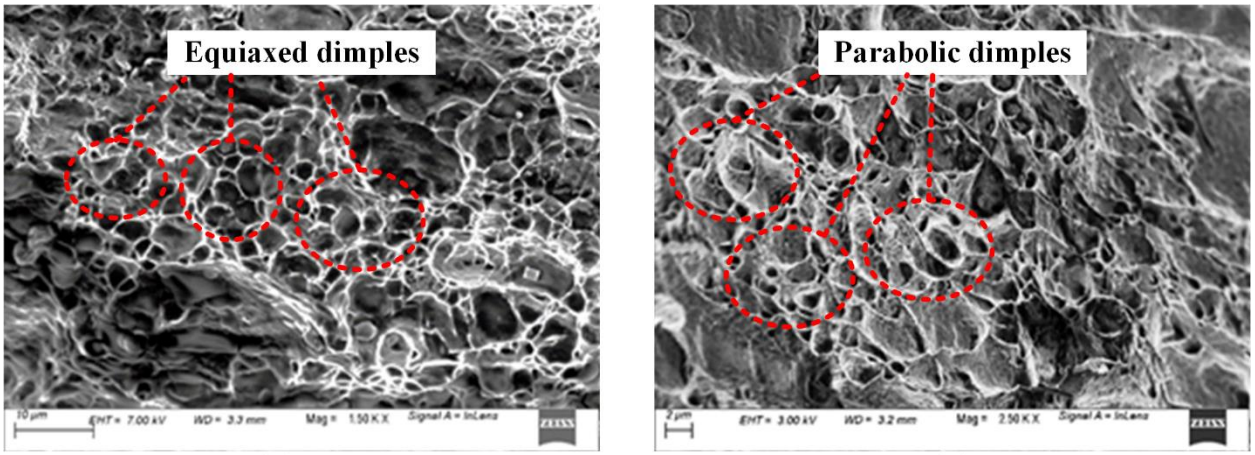

Fig. 3.19: Fractured surface of the specimens tested in (a) quasi-static forming (b) shock tube based forming

3.4 Summary

In the present work, the forming behavior of AA 5052-H32 sheet has been studied during the shock tube based forming. The process analyses have been accomplished by numerical simulations using DEFORM-3D, and the results are validated with experiments. The core objective of the work is to understand the effect of different flow stress models and failure models on the forming behavior. The following conclusions are derived from the results.

I. The rate-dependent flow stress-strain curve obtained from the tensile test of the sheet deformed using the shock tube are fit to different flow stress models and the material constants are identified. The predicted results using these models have a good agreement with the experimental data. This approach is simple to implement and accurate in predicting the formability.

II. Out of four hardening models, MJC model is accurate in predicting the flow stress when compared with experimental data for all the three velocities. This results in better

forming behavior prediction than the other three models. The nonlinear terms of strain rate sensitivity in the model improve the prediction accuracy.

III. The failure strain obtained from both the quasi-static forming and shock tube-based forming process is compared. A significant rise in failure strain, about 60-70% is observed during the shock tube-based forming. It is because of the inertial forces develop during the high-velocity forming, which deforms the material further at a high strain rate without strain localization.

IV. During failure pattern analysis, both JC model and MJC model have a fair agreement with experimental results. The failure strain and the petal formation predicted by Brozzo model and Freudenthal model match accurately with the experimental results. The predicted failure strains differ within 5-8% range when compared with experimental results.

V. The effective strain distribution illustrates a biaxial mode of deformation, where the sheet deforms significantly without sudden strain localization. Out of all flow stress models, MJC model predicts well and the results are reliable for all the three velocities.

VI. SEM analysis shows deeper and larger parabolic dimples on the fracture surface of the shock tube-based deformed specimen, which confirms that material undergoes larger plastic deformation. It attributes to deform the material further and enhance the formability of the material.

Chapter 4

Forming response of 1.5 mm thick sheet deformed through rigid body based impact and gas loading

Overview

The present study deals with both numerical and experimental evaluation of failure strain and fracture pattern during shock tube impact forming of 1.5 mm thick AA 5052-H32 sheet. A hemispherical end nylon striker is propelled to deform the sheet at different velocities. Here the main objective is to understand the effect of flow stress models and fracture models on the forming outputs. The experimental situation is modelled in two stages, i.e., incorporating the pressure in the first stage and displacement of the striker in the second stage in finite element simulation using the finite element (FE) code (DEFORM-3D). A new strategy followed to evaluate the rate-dependent flow stress data from the tensile test of samples sectioned from shock tube-based deformed sheet is acceptable, and finite element simulations incorporating those properties predicted accurate failure strain and fracture pattern. Out of all the flow stress models, the modified Johnson-Cook model has a better flow stress predictability due to the inclusion of the non-linear strain rate sensitivity term in the model. During the prediction of the failure strain and necking location, Cockcroft-Latham failure model, Brozzo failure model, and Freudenthal failure model have a fair agreement with experimental data in combination with the two flow stress models, i.e., Johnson-Cook model and modified Johnson-Cook model.

4.1 Shock tube experiments

The details of the experimental setup are already described in the Section 3.1.1. High-pressure nitrogen (N_2) gas is used as the driver gas, whereas normal atmospheric air is used as the driven gas. The bursting pressure is decided by the thickness of the Mylar diaphragm used in the setup. The incident pressure, reflected pressure, and Mach number of the shock wave (M_s) in the driven section are measured by pressure transducers mounted on the shock tube as illustrated in Fig. 3.3. The pressure-time histories experienced by three pressure transducers (P_1, P_2 and P_3) for three different bursting pressures, 7.67 bar, 9.01 bar, and 10.81 bar, are

demonstrated in Fig. 4.1. The pressure experienced by P_3 confirms that the complete deformation is accomplished in two stages. In stage 1, the sheet deforms because of the pressure developed at the end of the shock tube, and in stage 2, further, deformation occurs because of the impact of the striker. An infra-red (IR) sensor is used to measure the velocity of the striker at a distance 130 mm from the end of the shock tube. The working principle of the IR sensor is described earlier in Section 3.1.2. The average pressures and striker velocity data are provided in Table 4.1.

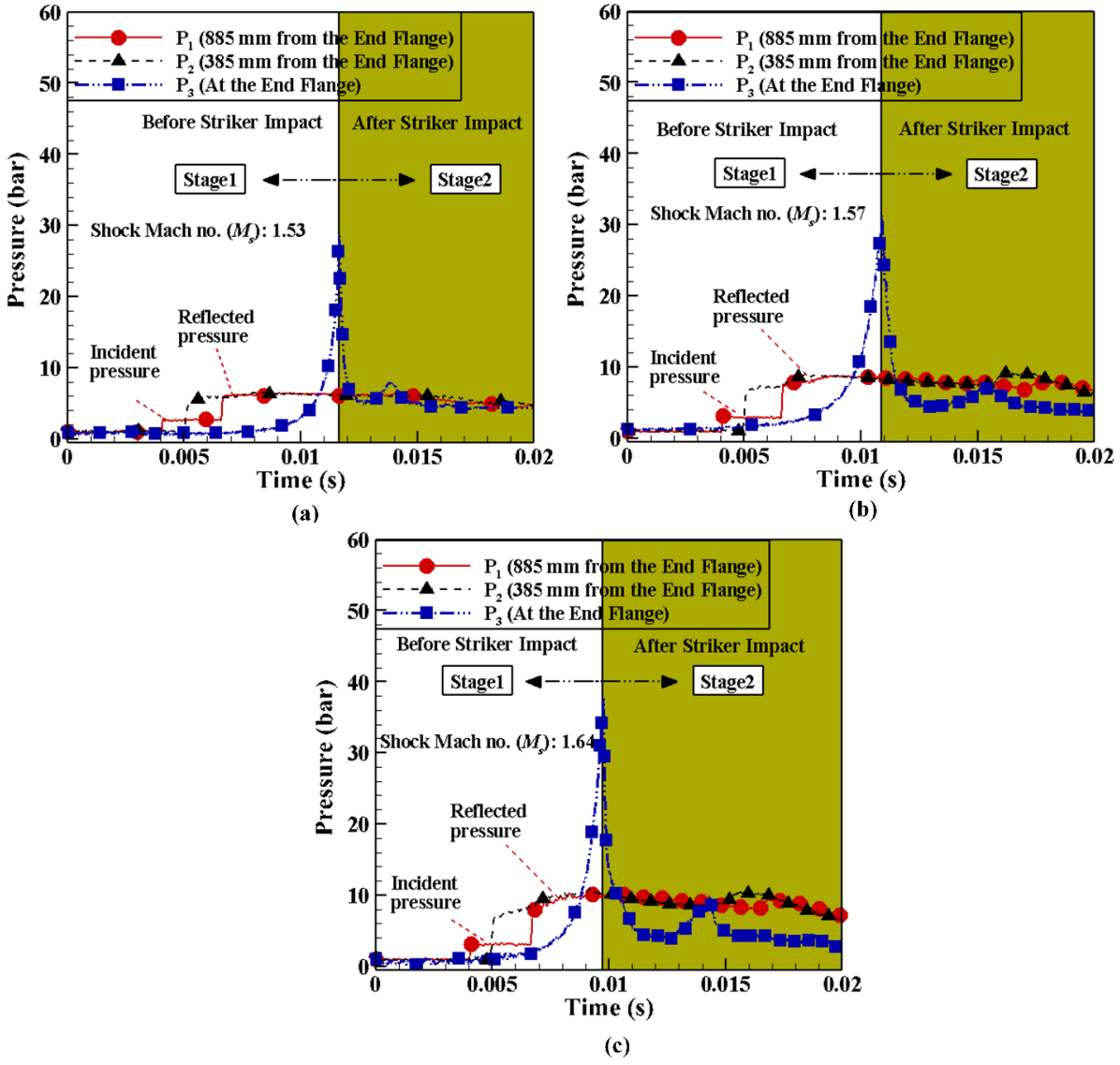

Fig. 4. 1: Pressure histories from shock tube experiments for different bursting pressures: (a) 7.67 ± 0.3 bar; (b) 9.01 ± 0.3 bar; (c) 10.81 ± 0.3 bar

Table 4.1: Average pressures and velocities of the striker during the experiment

Average bursting pressure (bar)	7.67 ± 0.3	9.01 ± 0.3	10.81 ± 0.3
Average Incident pressure (bar)	2.58 ± 0.1	2.75 ± 0.1	3.01 ± 0.1
Average reflected pressure (bar)	7.30 ± 0.2	8.75 ± 0.1	10.03 ± 0.2
Average pressure at the end flange (bar)	27.47 ± 0.3	31.07 ± 0.3	36.45 ± 0.3
Average Shock Mach number (M_s)	1.53 ± 0.02	1.58 ± 0.01	1.64 ± 0.02
Time of interruption (ΔT) (ms)	1.91 ± 0.06	1.67 ± 0.07	1.47 ± 0.06
Striker velocity (m/s)	49.78 ± 1.33	58.78 ± 1.47	67.85 ± 1.36

4.2 Experimental material

During this study, AA5052-H32 sheet of 1.5 mm thickness is considered in this analysis. The tensile properties of the base sheet is illustrated in Table 2.2. Circular sheets of 185 mm diameter are used for shock tube experiments. The plastic strain ratios (r) of the sheet are evaluated along 0°, 45°, and 90° to RD according to ASTM E-517 to identify the effect of anisotropy caused due to cold rolling. r values along 0° (r_0), 45° (r_{45}) and 90° (r_{90}) to the RD are 0.73, 0.73 and 0.71 respectively.

4.3 Numerical Methodology

4.3.1 FE simulation details

FE simulations are performed in DEFORM-3D code. The details about the FE formulation is discussed earlier in Section 2.4.1. The feasibility of the multi-operation layout in the software helps to perform FE simulation in two stages (Fig. 4.2). In the first stage, the pressure exerted on the sheet because of the rapid motion of the striker (experienced by P_3 transducer) is considered for the analysis. The pressure-time history (Fig. 4.2) up to the peak pressure is incorporated during FE simulation as the pressure boundary condition. In the second stage, the velocity boundary condition is provided to the striker such that it has the velocity (given in Table 4.1) at the start of deformation and becomes zero at the end of the simulation. Moreover, the final height of deformation measured in the experiment is considered as the stopping control during FE simulations. Sparse solver + direct method has been used to solve the problem numerically as it involves large deformation at a high strain rate.

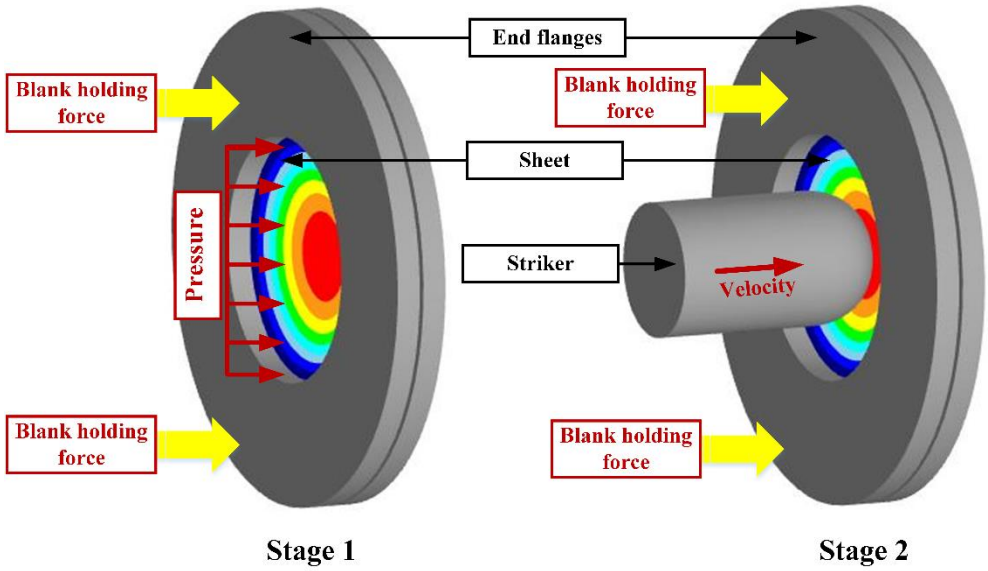

Fig. 4.2: FE simulation stages of shock tube forming using a rigid body striker

During FE simulation, the sheet is considered as a deformable material, whereas the two flanges and the hemispherical striker are modelled as rigid bodies (Fig. 4.2). The part dimensions in the model and the experimental setup are same. The failure pattern of the sheet is unsymmetrical. Therefore, the complete sheet is considered as a deformable body during FE simulations. Coulomb's classical law of friction has been utilized to provide frictional contact between the end flanges, sheet, and the striker. A constant blank holding force (BHF) of 8 kN is provided to the top flange along the loading direction (Fig. 4.2), and the coefficient of friction, μ = 0.1, is defined between the sheet and the end flanges to avoid sliding between them.

It is observed that the failure pattern is dependent on the frictional contact between the sheet and the striker (Kpenyigba et al., 2013; Rusinek et al., 2009). In the existing literature, both coefficient of friction (μ) and friction factor (m) are defined as the contact condition between the die and the workpiece during the plastic deformation (Habibi et al., 2015; Heidari et al., 2020; Sherwood and Durban, 1996). However, in this study, only Coulomb's friction coefficient (μ) is considered as a constant parameter to describe the contact boundary condition between the sheet and the striker. Therefore, μ is varied between 0.005 and 0.2 to obtain an acceptable result as compared to the experiments. At μ = 0.2, the sheet fails with plug ejection, whereas at μ = 0.005, the failure pattern is not accurate as compared to the experiment. After several trials, μ = 0.03 delivers an acceptable failure pattern (quasi-petalling) and has a good

agreement with the experiment. During the actual FE simulation of shock tube forming, a constant μ = 0.03 is considered for all the velocity conditions. The material properties defined during FE simulations are mentioned in Table 4.2.

Table 4.2: Properties incorporated during FE simulations

Properties	Value
Mass density of AA 5052-H32 (kg/m^3)	2432
Mass density of Nylon (kg/m^3)	1140
Young's modulus of AA 5052-H32 (MPa)	68,900
Young's modulus of Nylon (MPa)	3810
Poisson's ratio of AA 5052-H32	0.33
Poisson's ratio of Nylon	0.39
Stress-strain data of AA5052-H32 sheet	Fig. 4.5

The sheet is meshed with the tetrahedral element. The element size ratio defined during meshing controls the mesh density of the sheet. It is the ratio of the largest element edge to the smallest element edge on the object. To optimize the mesh density and computational time, a constant element size ratio of 6 is considered during this analysis. A mesh independency study has been carried out only for striker velocity of V_1 = 49.78 m/s. Various mesh sizes such as 1, 0.75, 0.5, 0.375, 0.3, and 0.25 mm have been considered. The FE simulations are carried out by considering JC flow stress model and Cockcroft-Latham failure model. The maximum effective strain and the corresponding computational time for different mesh sizes are mentioned in Table 4.3. Out of all, 0.3 mm and 0.25 mm mesh sizes have a good correlation with the experiment. However, the computational time for 0.25 mm is larger. Hence, 0.3 mm element size is considered for further analyses that delivered practically acceptable computational time. Moreover, the material deforms at a high strain rate beyond its critical limit, and therefore, it is advisable to define a re-meshing technique. The maximum interference depth (the depth, an element edge of the sheet crosses the surface of the striker) of 0.5 mm is considered as a re-meshing criterion that triggers the start of re-meshing on the sheet. At the beginning of the deformation, the sheet is meshed with uniform tetrahedral element (Fig. 4.3). When the sheet reaches its failure limit, the efficient re-meshing capability

of DEFORM-3D automatically assigns new refined mesh (minimum element size 0.3 mm) to the deforming domain and interpolates the rate-dependent variables from old to the new mesh by calculating them at the new nodes (Fig. 4.3).

Table 4.3: Mesh sensitivity analyses

Experimental data and element size (mm)	Number of elements	Maximum effective strain	Computational time (min)
Experimental data	-	0. 308	-
1	98653	0.402	285
0.75	124882	0.383	432
0.5	168862	0.376	655
0.375	193416	0.343	938
0.3	238783	0.316	1120
0.25	296658	0.315	1445

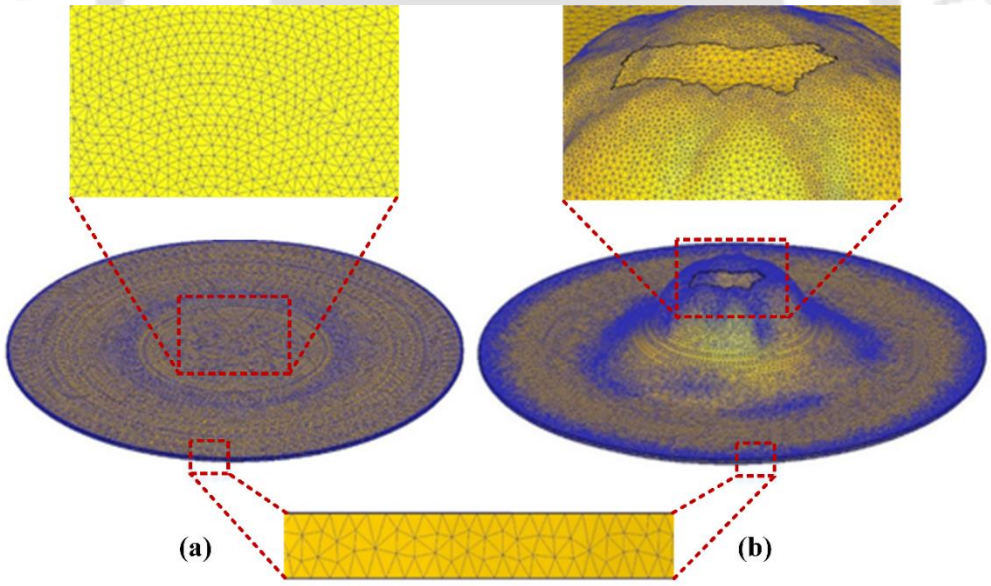

Fig. 4.3: Stages and FE mesh during forming processes: (a) before forming; (b) after forming

4.3.2 Material flow stress models and material constants evaluation

AA 5xxx sheet exhibits rate-dependent characteristics beyond a threshold limit of loading rate (Smerd et al., 2006). Therefore, several flow stress models have been implemented in various studies to understand the dynamic forming behavior of Aluminium alloy (Tian et al.,

2014). In the current work, four different flow stress models, namely Hollomon model, Cowper-Symonds (CS) model, Johnson-Cook (JC) model, and Modified Johnson-Cook (MJC) model (described in Section 3.2.2) are chosen to identify their influence on the forming limit and failure mechanism prediction of AA5052-H32 sheets deformed by a shock tube.

Generally, Split Hopkinson Pressure Bar (SHPB) apparatus is utilized to obtain the stress-strain curves and material constants at high strain rates. In the present study, the rate-dependent flow stress-strain curves are obtained by the tensile test of a sample cut from the sheet deformed using a shock tube (Fig. 4.4). The bent tensile sample is tested in UTM at a cross-head speed of 1 mm/min without any post-treatment. The true stress-strain curve evaluated from the tensile test is fit to different flow stress models, and the material constants are identified (Fig. 4.5).

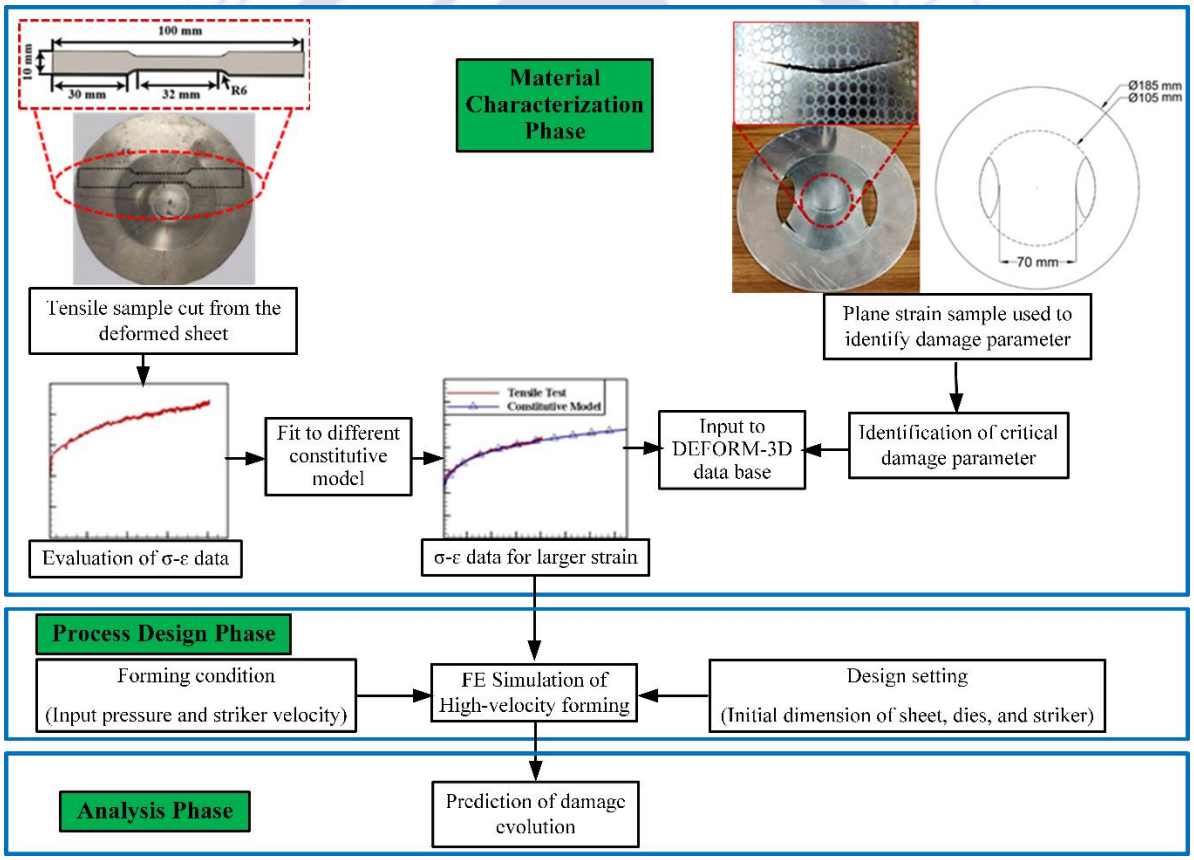

Fig. 4.4: Step by step procedure to evaluate the material constants in flow stress equations

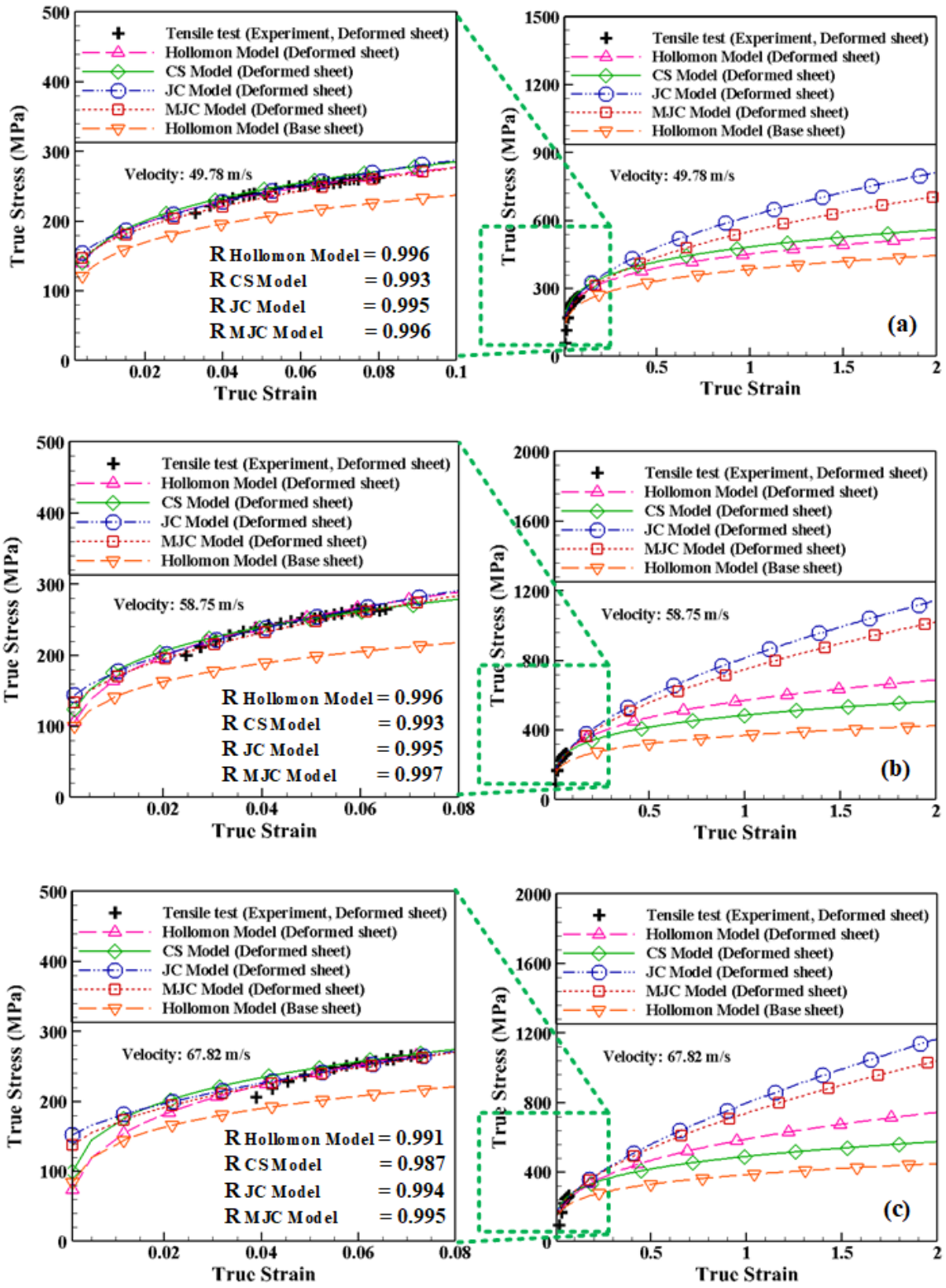

Fig. 4.5: Identification of rate-dependent material parameters by curve fitting method for different striker velocities: (a) 49.78 m/s; (b) 58.75 m/s; (c) 67.82 m/s

During curve fitting to the mentioned flow stress models to experimental data, strain rate becomes an important parameter. Considering the difficulty in instrumentation to identify the strain rate practically, Hollomon model is utilized in this study to predict the average plastic strain rate $\bar{\dot{\varepsilon}}_p$ near the pole region of the sheet from FE simulations for velocities, 49.78 m/s, 58.78 m/s, 67.85 m/s, as 1835 s^{-1}, 2158 s^{-1}, and 2635 s^{-1} respectively. These values are used in CS model, JC model, and MJC model during fitting (Fig. 4.5).

CS model is widely used as it calculates the dynamic flow stress-strain data by multiplying a dynamic hardening factor $(1+\left(\dot{\bar{\varepsilon}} / D\right)^p)$ to the quasi-static flow stress of the material. In this study, the thermal softening effect is not considered during the analysis. The flow stress-strain curve obtained after curve fitting is demonstrated in Fig. 4.5. Noh et al. (2016) imposed an inverse parameter estimation method to identify the material constants (*D* and *p*) for the CS model during the high strain rate forming of Al 1100-O sheet. They obtained the material parameters within a range with the least mean square error between the experiment and simulation results. Here, the material parameters are varied within the same range, and the best fit values are enlisted in Table 4.5.

In both JC model and MJC model, the terms related to thermal effects are discarded. Generally, the material constants *A* and *B* are determined from the flow stress-strain data at the reference strain rate ($\dot{\varepsilon}_0$), which is kept as one (Khodko et al., 2015; Song et al., 2019). During curve fitting, the lower and upper ranges of material parameters, *A, B,* C_1, and C_2, at the reference strain rate are identified from the literature (Deng et al., 2019; Song et al., 2019), and the best fit values within the range are considered for further calculation of the flow stress for larger strain values. The material parameters obtained after curve fitting for JC model and MJC model are listed in Table 4.5. A good description of material anisotropy is essential for the accurate prediction of formability. Out of various anisotropic yield functions, Hill's 1948 yield criterion is utilized in the present work (described in Section 2.4.1). The material parameters of the yield function are calculated from r_0, r_{45} and r_{90} (enlisted in Section 4.2) using available relationships.

Table 4.4: Material constants of the flow stress models

Material constants	Undeformed base sheet	Deformed sheet 1 at V_1 = 49.78 m/s	Deformed sheet 2 at V_2 = 58.75 m/s	Deformed sheet 3 at V_3 = 67.82 m/s
σ_{ys} (MPa)	167 ± 3	198 ± 2	206 ± 2	199 ± 3
σ_u (MPa)	246 ± 3	262 ± 3	265 ± 2	267 ± 3
Hollomon model				
K (MPa)	393 ± 2	452 ± 3	570 ± 3	589 ± 3
n	0.18	0.21	0.27	0.33
CS model				
$\bar{\sigma}_{qs}$	Hollomon model material constants of undeformed base sheet			
D		8500	8500	8500
p		0.75	0.7	0.8
JC model				
A		118.5	120.7	140.8
B		486.6	678.4	627.3
n		0.47	0.56	0.65
C		0.005	0.003	0.005
MJC model				
A		117.8	120.6	141.8
B		501.8	720.3	680.3
n		0.43	0.51	0.57
C_1		−0.197	−0.155	−0.028
C_2		0.026	0.018	0.002

4.3.3 Failure models and evaluation of critical damage parameters

Based on the histories of stress and strain affecting the occurrence of the ductile fracture, various failure criteria have been proposed in the literature (for example, refer (Habibi et al., 2015; Rao et al., 2003)). The failure models considered in the present work for the fracture prediction of AA5052-H32 sheet are Cockcroft-Latham model, Normalized Cockcroft-Latham model, Freudenthal model, Rice & Tracy model, Oyane model, Ayada model, Brozzo model, and McClintok model (enlisted in Section 3.2.3). The accuracy of the failure models during the impact-based forming of aluminium alloys have not been understood yet. Hence, the mentioned failure models are considered in this study.

The critical damage parameters (D_1, D_2, D_3, D_4, D_5, D_6, D_7, and D_8) are also identified for 1.5 mm thick AA5052-H32 sheets from experiments. To understand the strain path of deformation, a numerical study has been carried out for the velocity V_1 = 49.78 m/s until necking occurs. All the four flow stress laws referred before are utilized along with Cockcroft-Latham failure model (listed in Section 3.2.3). The ultimate tensile strength of the un-deformed sheet, σ_u = 246 MPa (from Table 4.5), is considered as the maximum principal stress (σ^*). The failure strain, ε_f = 0.42, is measured near the necked region of the sheet. The critical damage parameter, D_1 = 116.88, is obtained from the product of σ^* and ε_f, and it is used during preliminary FE simulation. The strain path at a location near the neck of the deformed sheet is obtained, as shown in Fig. 4.6. The predicted strain paths demonstrate a biaxial mode of deformation for a specific duration and then shift towards the major strain axis (ε_2) with no significant difference among the hardening laws. When the damage parameter reaches the critical value, necking initiates, and at the moment, the strain path shifts towards the plane strain condition (Fig. 4.6). Thus, by assuming the deformation behavior during failure as a plane strain condition ($\varepsilon_2 = 0$), the other critical damage parameters (D_1, D_2, D_3, D_4, D_5, D_6, D_7, and D_8) are obtained.

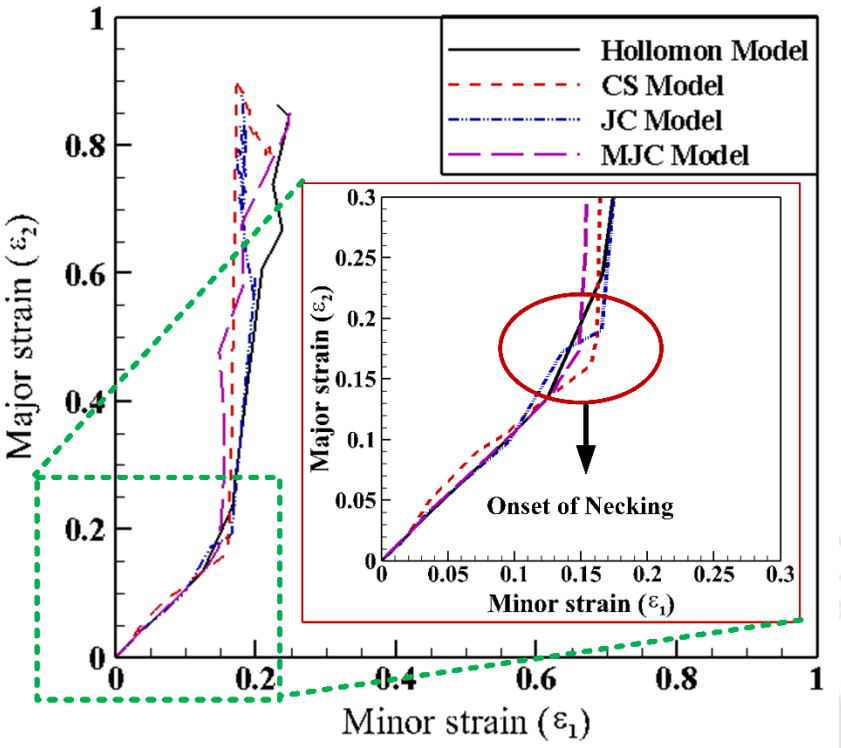

Fig. 4.6: Strain path evolution during shock tube forming of AA5052-H32 sheet

The stress ratios required for the calculation of critical damage parameters for the plane strain condition with no planar anisotropy condition, i.e., $r = r_0 = r_{45} = r_{90}$ = 0.73 can be obtained from Hill's 1948 yield criterion (Refer Section 3.2.3). To evaluate the failure strain (ε_f) in plane strain condition, which is confirmed by FE simulations, a sample having 184 mm outer diameter and 70 mm minimum width (Fig. 4.4) is deformed at a velocity, V_1 = 49.78 m/s, in the shock tube. The average failure strain, ε_{1f} = 0.34, is measured from the deformed circular grids. The ultimate tensile strength of the AA5052-H32 sheet, σ_u = 246 MPa, is considered as maximum principal stress (σ^*). The material constant δ = 1.5 is assumed from the work of Hambli and Reszka (2002), and β =0.33 is assumed for aluminium alloys as per Novella et al. (2015). The strain hardening exponent (*n*) of the undeformed sheet (Table 4.5) is considered during this analysis. All the evaluated critical damage parameters are listed in Table 4.7.

Table 4.5: Critical damage parameters for failure models

Fracture models	Critical damage Parameters
Cockcroft-Latham model	D_1 = 94.51 MPa
Normalized Cockcroft-Latham model	D_2 = 0.43
Freudenthal model	D_3 = 83.64 MPa
Rice & Tracy model	D_4 = 0.86
Oyane model	D_5 = 0.99
Ayada model	D_6 = 0.21
Brozzo model	D_7 = 0.48
McClintok model	D_8 = 0.49

4.4 Results and Discussion

4.4.1 Performance of flow stress models

The accuracy of flow stress prediction from four different hardening models for AA 5052-H32 sheet is quantified by correlation coefficient (*R*), and average absolute relative error (*AARE*) expressed as

$$R = \frac{\sum_{i=1}^{N}(E_i - \bar{E})(P_i - \bar{P})}{\sqrt{\sum_{i=1}^{N}(E_i - \bar{E})^2 \sum_{i=1}^{N}(P_i - \bar{P})^2}} \tag{4.1}$$

$$AARE = \frac{1}{N}\sum_{i=1}^{N}\left|\frac{E_i - P_i}{E_i}\right| \times 100\% \tag{4.2}$$

where E_i denotes the experimental flow stress, P_i denotes the predicted values by different flow stress models, $\bar{E}$ and $\bar{P}$ are the mean values of E_i and P_i, respectively. The total number of data considered during the study is represented as *N*. The correlation coefficient (*R*) is a commonly used statistical parameter that reflects the strength of the linear relationship between the experimental and predicted flow stress, while *AARE* is an unbiased statistical tool for estimating the predictability of a model (Chen et al., 2015; Tian et al., 2014). All the experimental and predicted flow stresses shown in Fig. 4.5 are selected to calculate the values of *R* and *AARE*, and the results are listed in Table 4.8. The data demonstrate that the predicted

flow stress values developed by different flow stress models have a good correlation with the experimental results, though CS model shows deviation at higher velocities. Moreover, the accuracy of MJC model is better at all three velocities because of the incorporation of strain rate sensitivity terms in a non-linear fashion in the model.

Table 4.6: Calculated *R* and *AARE* for different flow stress models

	Hollomon Model			CS Model			JC Model			MJC Model		
Velocity	V_1	V_2	V_3	V_1	V_2	V_3	V_1	V_2	V_3	V_1	V_2	V_3
R	0.996	0.996	0.994	0.993	0.993	0.991	0.995	0.995	0.995	0.996	0.997	0.997
AARE (%)	2.86	2.86	3.35	3.83	3.83	4.22	3.17	3.17	3.17	2.86	2.58	2.58
Here, V_1 = 49.78 m/s; V_1 = 58.75 m/s; V_1 = 67.82 m/s												

4.4.2 Height of deformation

The deformation of the sheet is predicted with (pressure force from the gas and momentum of striker), and without incorporating, the pressure force (only momentum of striker) exerted on the sheet. The deformation profile predicted by different flow stress models is compared to that from experiments (Fig. 4.7). The predicted deformation with pressure and striker velocity shows a fair agreement with the experimental results. It shows the importance of input pressure that helps to deform the sheet uniformly in the exposed region before the striker impact. The material stretches further with the help of the striker moving with high-velocity. Thus, the deformation in shock tube-based forming is completed in two stages. On the other hand, in the case with striker velocity (without pressure force), the sheet deforms largely in the striker hitting zone only (Fig. 4.7). Moreover, sheet deformation is dependent on the stress-strain relations as well. Though all the flow stress models have a fair agreement with experimental data, the results predicted by the JC model and the MJC model are quite accurate.

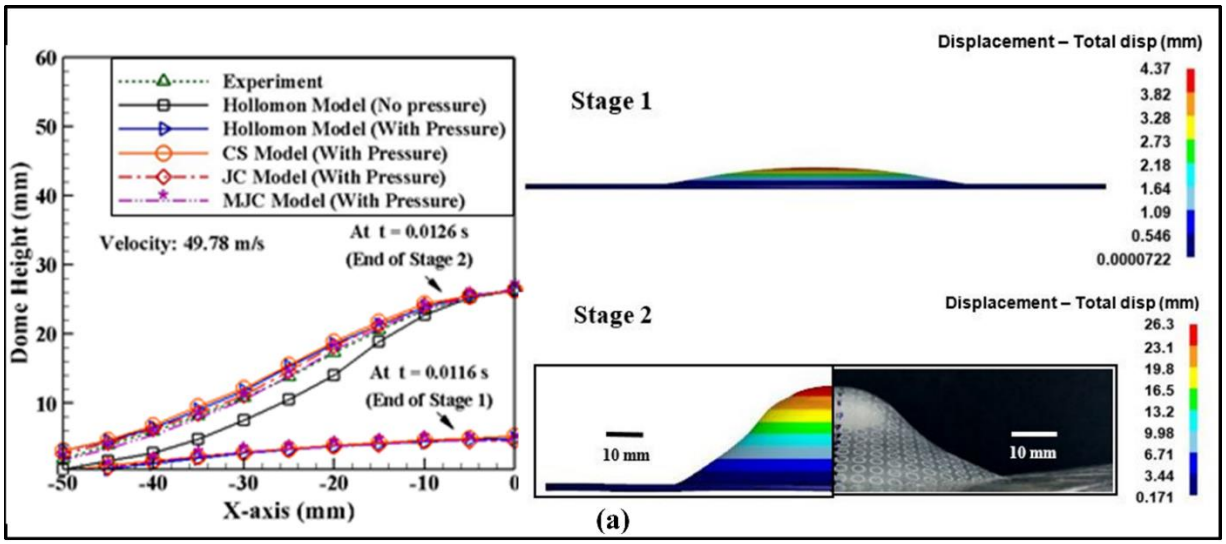

(a)

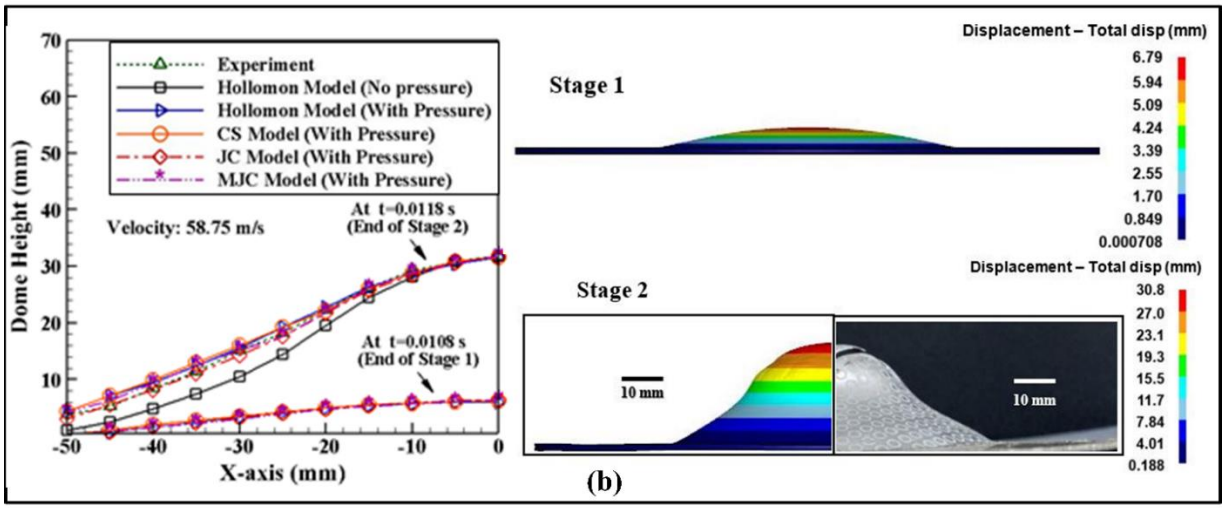

(b)

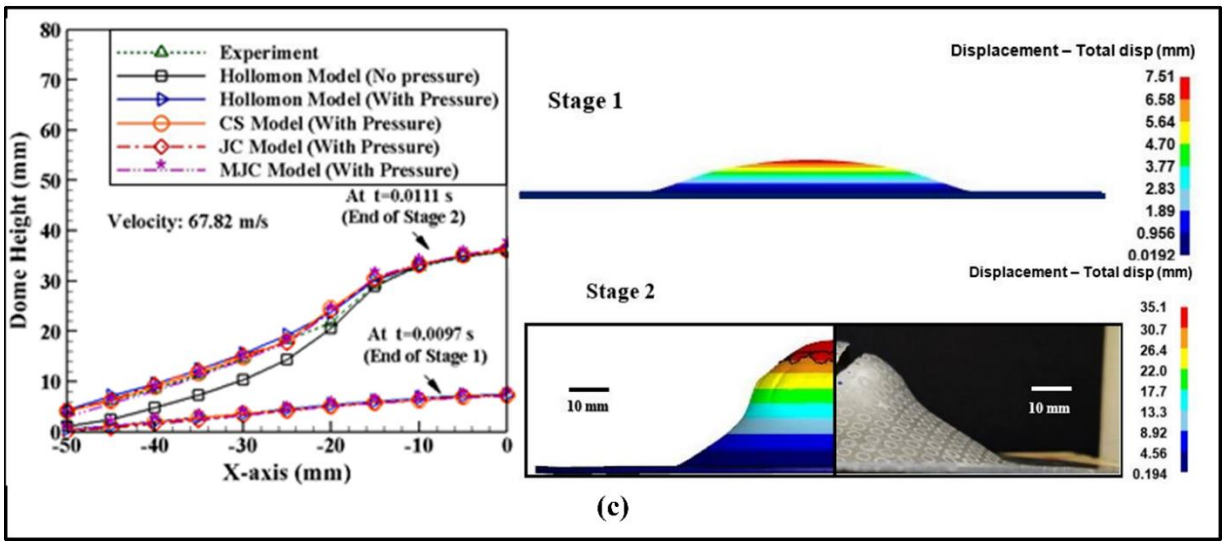

(c)

Fig. 4.7: Prediction of dome height and validation with experiments for different striker velocities: (a) 49.78 m/s; (b) 58.75 m/s; (c) 67.82 m/s

4.4.3 Failure prediction and validation

4.4.3.1 Necking prediction

At velocity V_1 = 49.78 m/s, only necking is witnessed in the parent sheet. During necking, the velocity gradient between the two adjacent points on the material deviates suddenly, and it leads to strain localization. The influence of flow stress models and failure models during necking is analyzed here. A "damage parameter, (C_i)" has been monitored and is defined as the ratio of the damage value at a location in the sheet to the critical damage parameter (D_1 to D_8), as mentioned in Table 4.7. The variation of C_i is tracked from the center to the radial distance along the rolling direction (Fig. 4.8). When C_i = 1, the material undergoes critical damage, and necking occurs. Although the variation of C_i with radial distance depends on the flow stress models, the necking location predicted by different failure models matches acceptably with the experimental data (Fig. 4.8). All the flow stress models have good potential to identify the necking location. Out of all failure models, the Brozzo model and Freudenthal model have a good agreement with the experimental results.

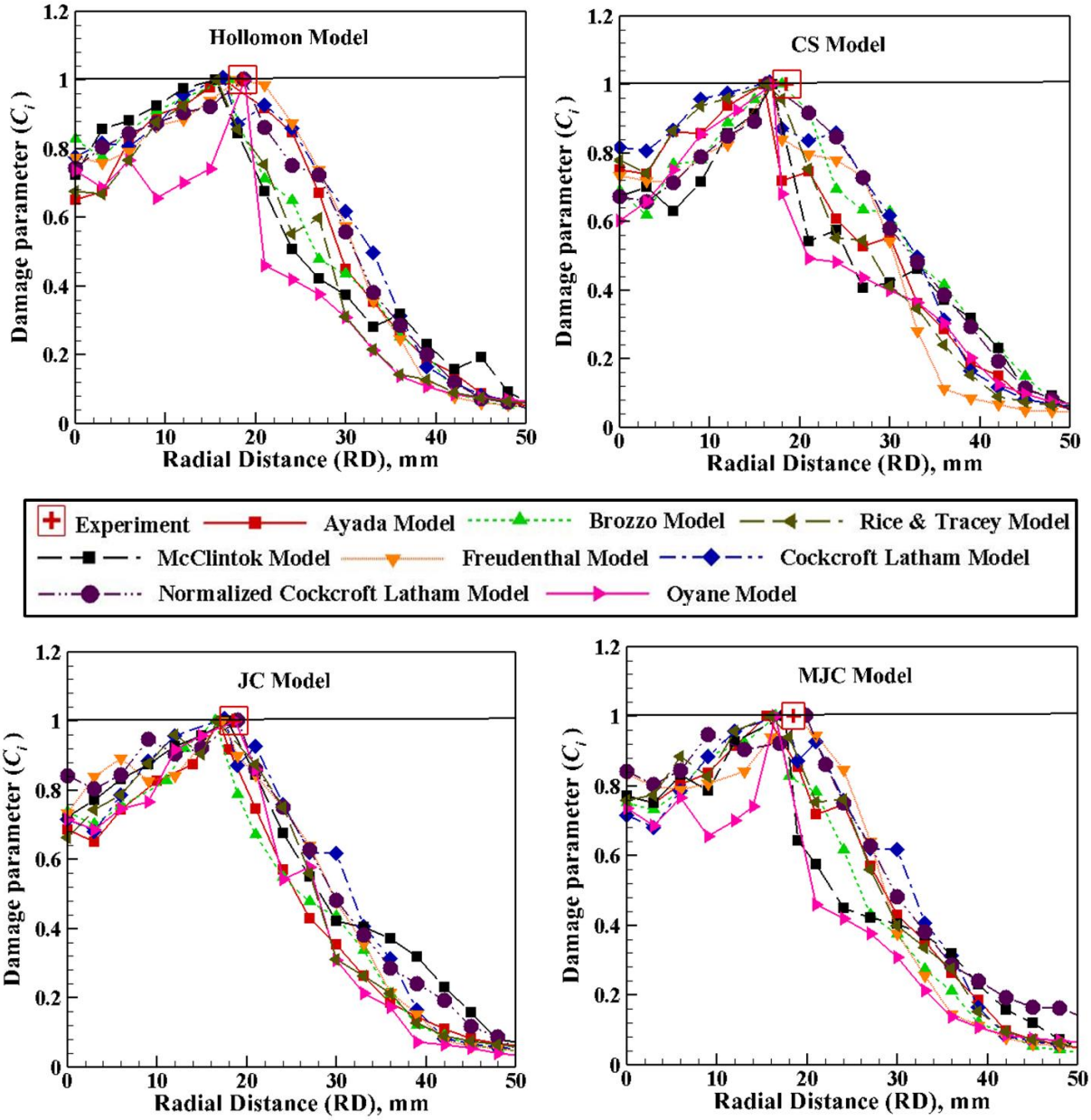

Fig. 4.8: Distribution of damage parameter (*Ci*) along the radial distance in rolling direction

The evolution of the major strain at the necked zone is predicted, as shown in Fig. 4.9. It is observed that when the sheet reaches its critical damage parameter (D_1 to D_8 in Table 4.7), the curve reaches an inflection point indicating the occurrence of necking. FE simulations are continued until the dome height (i.e. 26.35 mm) as observed in experiments, is reached. The dome height at the inflection point is predicted using various failure models and flow stress models (inset figures in Fig. 4.9). All the failure models under-predict the dome height at necking when compared to experimental data, and there is an insignificant difference in the

predictions – a variation of 1-2 mm in dome height at failure is observed. However, accurate data analyses (percentage difference) show that Ayada model, Oyane model and Cockcroft Latham model predictions are closer to experimental data. Moreover, the flow stress models, Hollomon model, CS model, JC model, and MJC model, perform equal, as seen from the standard deviation of the failure strain data.

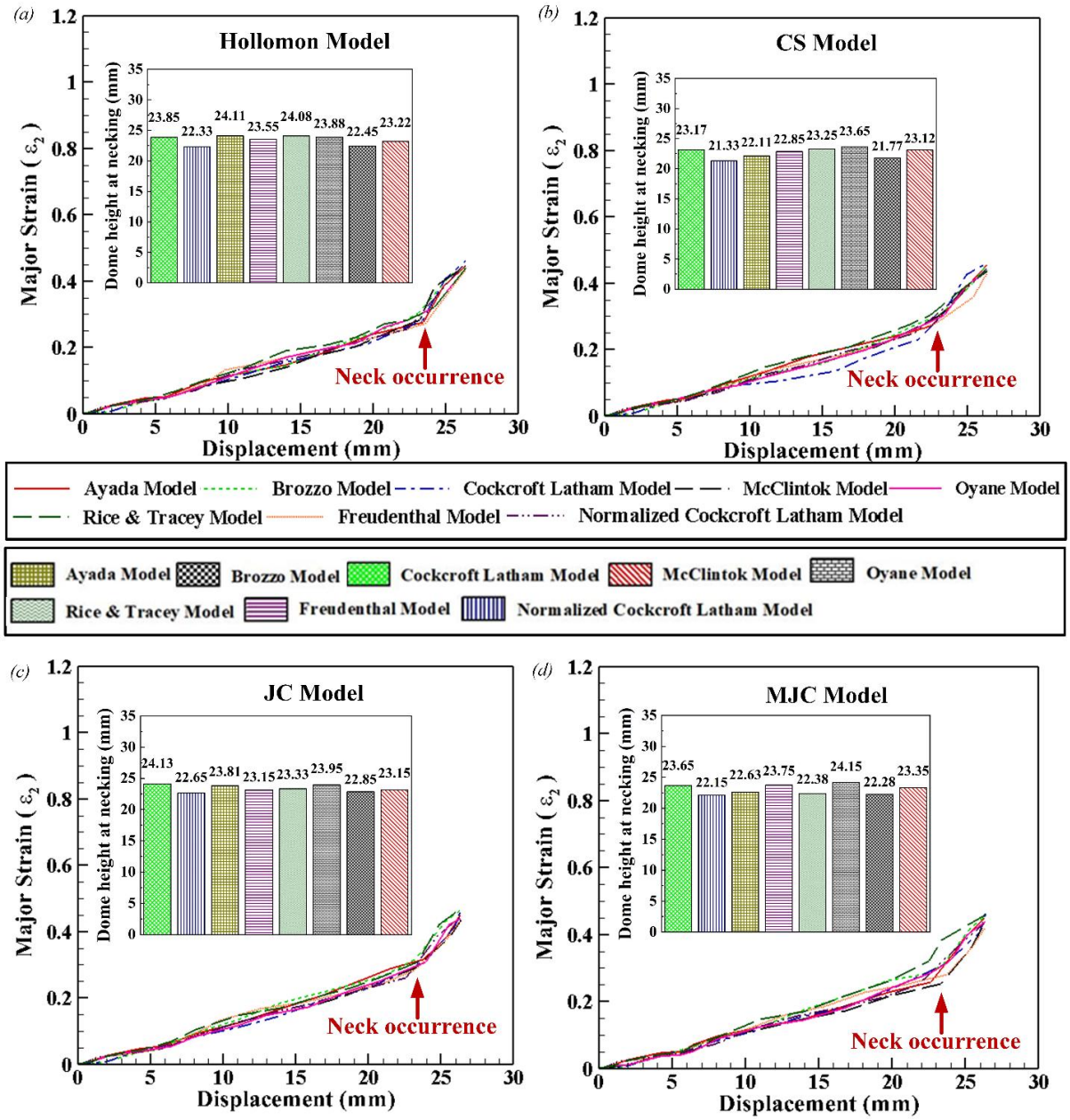

Fig. 4.9: Major strain evolution with striker displacement at the necked location: (a) Hollomon model; (b) CS model; (c) JC model; (d) MJC model

4.4.3.2 Sheet failure prediction

The sheet is observed to fracture characterized by a typical failure pattern when deformed at velocities V_2 = 58.75 m/s and V_3 = 67.82 m/s. The results are discussed here in terms of failure strain and fracture pattern. The fracture pattern prediction is sensitive to the striker velocity, coefficient of friction (μ), contact angle (θ) between the sheet and the striker, flow stress models, and fracture models.

To predict an acceptable fracture pattern in FE simulations, μ is varied between 0.005 to 0.2. The results obtained at μ = 0.03 have a better agreement with experimental observation, and hence, it is considered for further analyses. The fracture pattern predicted by various flow stress models is depicted in Fig. 4.10. During FE simulations, necking initiates when the critical damage parameter (D_1 to D_8) in Table 4.7 is reached, and cracks propagate radially with further deformation. FE simulations are performed until dome height observed in experiments. The failure patterns are inspected visually and compared, as shown in Fig. 4.10. The results demonstrate that both JC model and MJC model have predicted the failure pattern acceptably in combination with failure models, which is due to the inclusion of strain rate-sensitive indices during flow stress calculation. While using Hollomon model and CS model in FE simulations, the material plugs out from the central region instead of petal formation in most of the failure models (Fig. 4.10). Thus, the usability of Hollomon model and CS model is restricted to a specific strain rate range only in applications such as shock tube forming.

Failure strain (ε_f) predicted for V_2 = 58.75 m/s by the procedure elaborated earlier is shown in Fig. 4.11. The predictions from various flow stress models and fracture models have an acceptable agreement with the experimental results. Overall, by referring ε_f and the failure patterns together, Cockroft-Latham model, Freudental model and Brozzo model have a fair agreement with the experimental results. All the three failure models have about 8% deviation from the experimental failure strain.

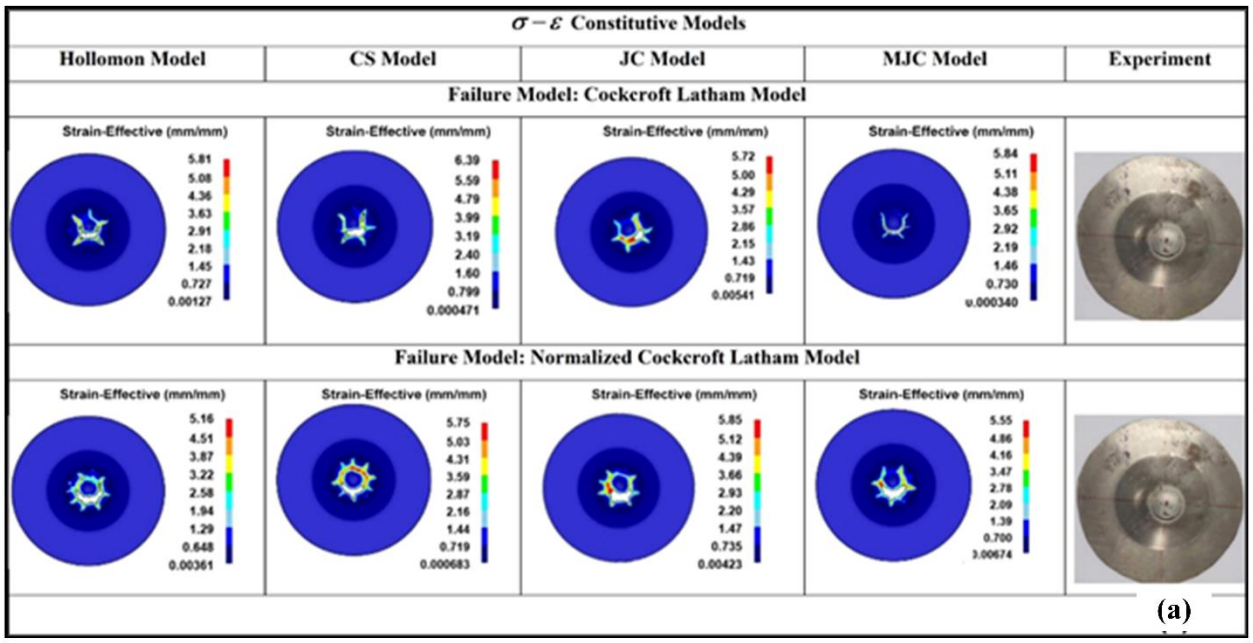

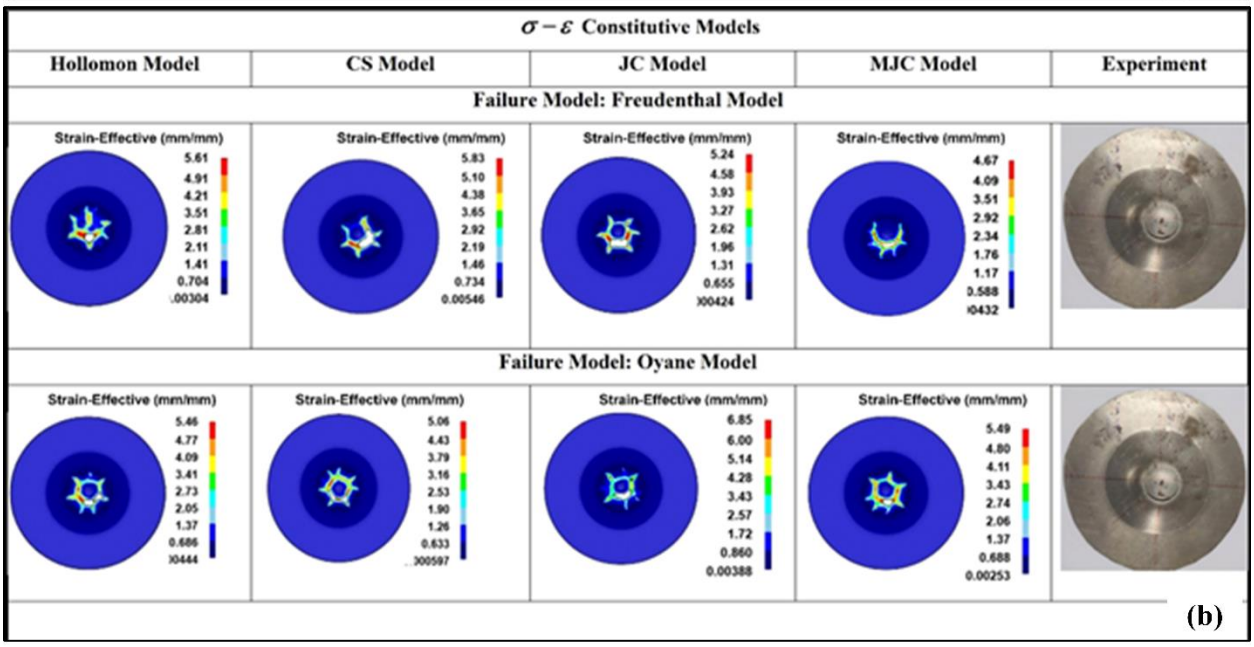

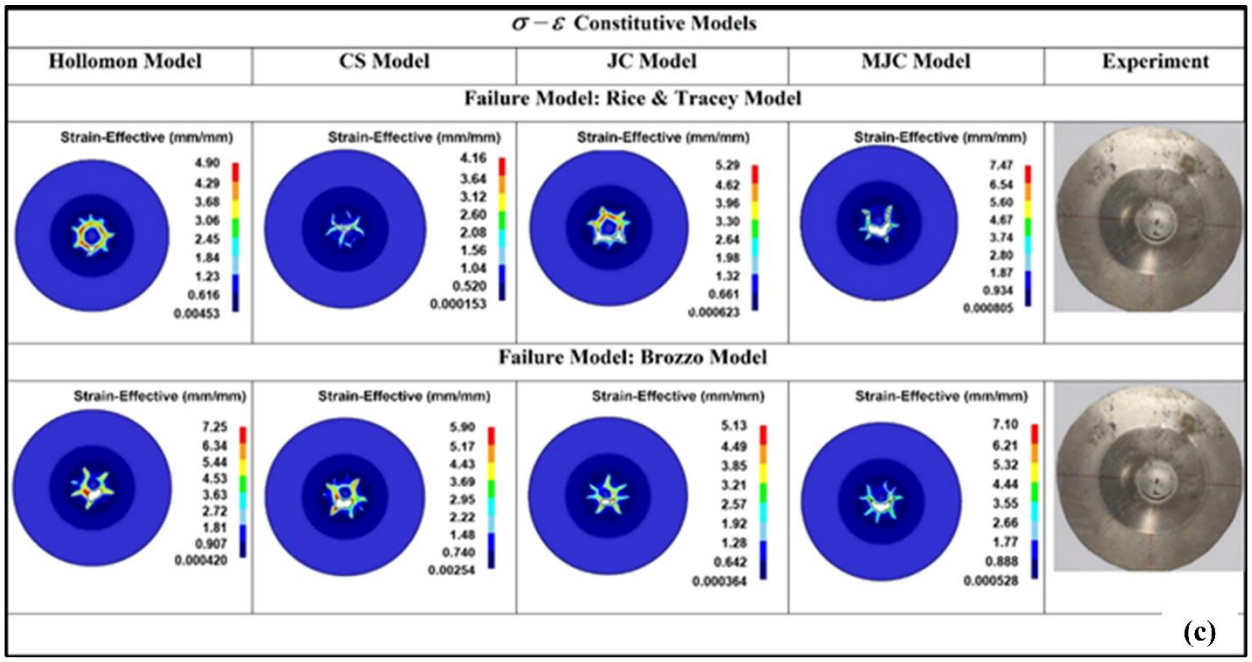

Fig. 4.10: Comparison of the failure pattern predicted by flow stress models in comparison to the experimental observation at V3 = 67.82 m/s

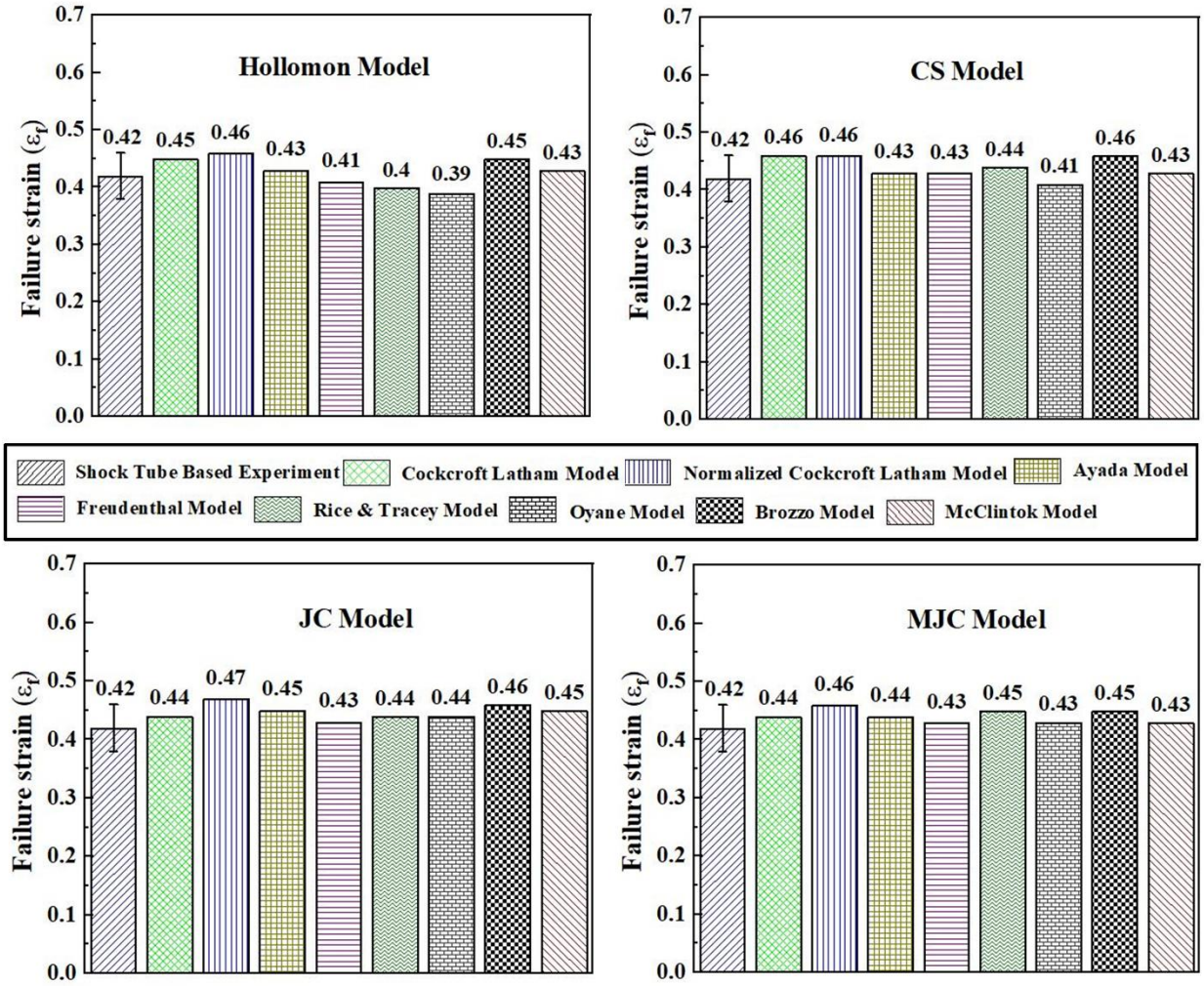

Fig. 4.11: Comparison of epsilon f predicted by flow stress models at velocity V_3 = 67.82 m/s

In order to evaluate the fracture and crack propagation further, the sheet is deformed at a larger velocity, V_3 = 67.82 m/s. Here, only Freudenthal damage model is used for prediction as it is one of the three failure models that showed accurate prediction at V_2 = 58.75 m/s. FE simulations are performed until dome height (35.13 mm) seen in experiments, is reached. The failure pattern predicted by different flow stress models is demonstrated in Fig. 4.12. The results show different number of radial cracks, which are dependent on the flow stress relations used. ε_f is also quantified and compared to the experimental results (Fig. 4.13). Apart from the Hollomon model, all the three flow stress models have predicted both the fracture pattern and failure strain accurately. The differences in ε_f are in an acceptable range. It is because of strain rate sensitivity terms accounted for in the stress-strain relationship. However, MJC

model is preferred to reproduce the material strain hardening behavior over a wide range of strain rates because of the presence of non-linear strain rate sensitive term in the model.

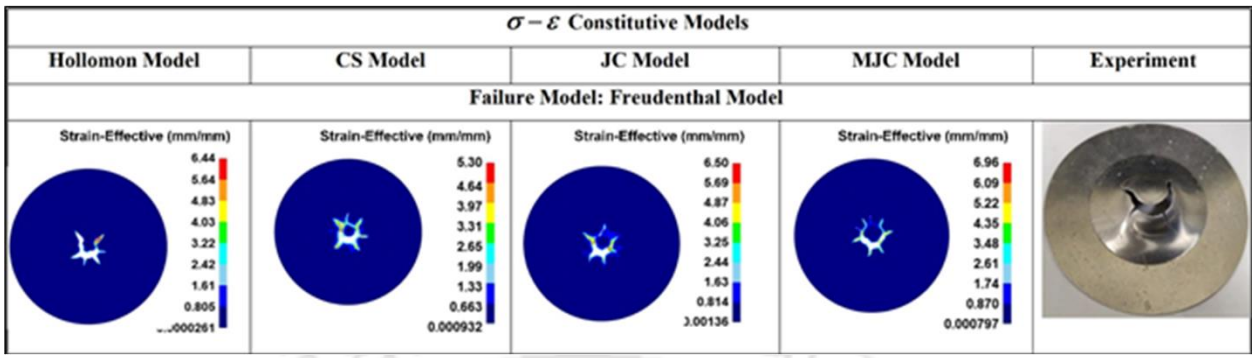

Fig. 4.12: Comparison of the failure pattern predicted by flow stress models in comparison the experimental observation at V_3 = 67.82 m/s

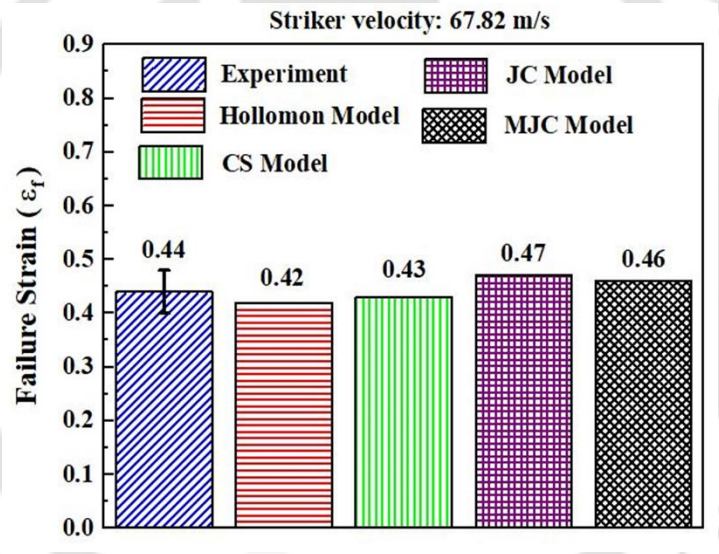

Fig. 4. 13: Comparison of ε_f predicted by flow stress models at velocity V3 = 67.82 m/s

4.5 Summary

In the present study, the failure strain and fracture pattern during shock tube forming of 1.5 mm thick AA 5052-H32 sheet are predicted. Numerical simulations are conducted for the purpose in DEFORM-3D, FE code. The predicted results are validated with experimental data obtained from lab-scale shock tube experiments. Here the main aim is to study the effect of various flow stress models and fracture models. The following conclusions are drawn.

I. The rate-dependent flow stress-strain curves obtained from the tensile test of the sheet deformed by shock tube are fit to different flow stress models, and the material

constants are obtained. The same material constants are reutilized to obtain the flow stress for larger strain and incorporated during FE simulations. The predicted forming outputs have an acceptable agreement with the experimental data.

II. Out of four flow stress models, the predictability of the MJC model is better because of the inclusion non-linear strain rate sensitivity term during the flow stress calculation.

III. Both the JC model and the MJC model have better predictability on the failure pattern. The application of the Hollomon model and the CS model is restricted to a certain strain rate range.

IV. The failure strain and the location of necking are well predicted by different failure models in combination with different flow stress models. Out of all, the Cockroft-Latham model, Freudental model and Brozzo model have a good agreement with the experimental results. The failure strain predicted by these failure models has about 8% deviation from the experimental results.

V. The two-stage (pressure force from the gas and momentum of striker) shock tube-based deformation process is well predicted by the flow stress models that incorporate strain rate sensitivity during the flow stress calculation. Out of all, MJC model predictions are accurate, and the results are reliable for all the striker velocities considered.

Chapter 5

Forming response of 1 mm thick sheets with friction stir spot weld

Overview

In the present study, both the experimental and numerical investigations are carried out to understand the dynamic forming behavior of Friction Stir Spot Welded (FSSW) sheet made of AA 5052-H32 sheets of 1 mm thickness using a shock tube. A hemispherical end nylon striker is propelled at high velocity to deform the FSSW sheet in biaxial mode of deformation. Furthermore, the effect of tool rotational speed and plunge speed on the FSSW joint is studied. During this analysis, a new strategy is followed to evaluate the rate-dependent flow stress-strain properties, which are incorporated during FE simulation using FE code, DEFORM-3D. Tensile test data obtained from the unwelded section of the deformed FSSW sheet is fit to Modified Johnson-Cook (MJC) model, and the rate-dependent properties are identified. In the case of the spot welded region, a hardness based multiplying factor is generated to evaluate the stress-strain data by fitting to MJC model. The effect of tool rotational speed and plunge speed on the welding and forming outputs are presented. Temperature evolution during FSSW is validated with the experimental data, and good correlation is obtained. The predicted material flow visualization during FSSW gives insight into the mixing of the material during the joint formation. The results agree with available findings. Various forming outputs such as effective strain distribution, necking height, and the failure pattern are predicted using MJC model in combination with Freudenthal damage model, and the results have good agreement with the experimental data.

5.1 Experimental details

5.1.1 FSSW experiments

FSSW experiments are performed on a pair of 1 mm thick AA 5052-H32 sheets. The mechanical properties of the sheet along the 0° to the rolling direction (RD) are identified by uniaxial tensile tests at room temperature and at elevated temperatures in UTM at a crosshead

speed of 1 mm/min. The true stress-strain data at elevated temperatures are fit to Hollomon flow model and the material constants are identified (Table. 5.1). The true stress-strain curves at different temperatures are illustrated in Fig. 5.1. The plastic strain ratios (*r*) of the material are obtained at room temperature as per ASTM E-517 and enlisted in Table 2.2.

Table 5. 1: Tensile properties of AA 5052-H32 base sheet

Temperature (°C)	**RT**	**100**	**200**	**300**	**400**
σ_{ys} **(MPa)**	171	167	168	161	158
σ_u **(MPa)**	238	235	221	203	173
n	0.143	0.126	0.115	0.095	0.049
***K* (MPa)**	348	321	292	257.3	212
ε_u **(%)**	8.7	10.1	9.8	6.3	3.6
ε_t **(%)**	9.6	12.3	10.4	11.3	11.9
σ_{ys}: Yield strength; σ_u: Ultimate Tensile Strength; *n*: Strain Hardening Coefficient; *K*: Strength Coefficient; ε_u: Uniform Elongation; ε_t: Total Elongation; Gauge length: 50 mm; RT: room temperature					

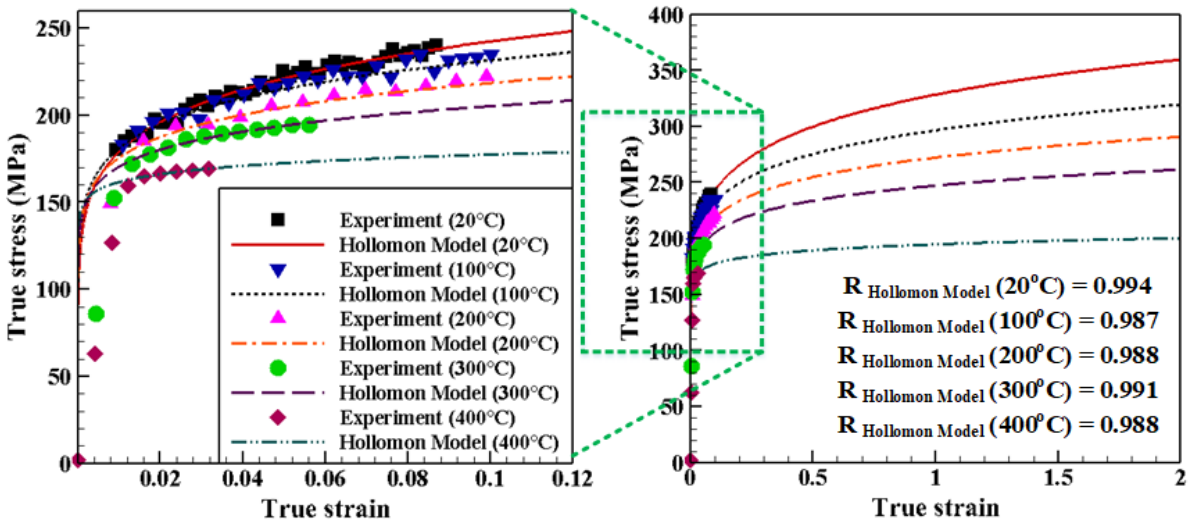

Fig. 5.1: True stress-strain curves obtained from Hollomon flow stress model at different elevated temperatures

In this study, a tool made of H13 tool steel with a flat shoulder and a straight cylindrical pin is selected to fabricate FSSW joints. The tool shoulder diameter, pin diameter, and pin height are 18 mm, 6 mm, and 1.2 mm respectively. FSSW experiments are performed at three different rotational speeds, 750 rpm, 900 rpm, and 1200 rpm, and two different plunge speeds, 7.5 mm/min and 10 mm/min, to understand their effect on the weld strength during high-velocity shock tube-based forming experiments. The plunge depth is kept constant as 1.6 mm. The dwell time of 10 seconds is maintained based on the existing literature (Zhang et al., 2011) to have better welding properties. All the experiments are carried out thrice for repeatability. Out of these, two welded samples are considered for shock tube-based forming experiments, and one sample is kept for weld characterization.

During FSSW experiments, the evolution of temperature is measured by mounting K- type thermocouple on the surface of the specimen at a distance of 10 mm from the shoulder edge (Fig. 5.2). The head of the thermocouple is properly adhered to the specimen by a thermal insulator to avoid heat loss to the environment during the experiment. The output from the thermocouple is connected to a DAQ unit (Make: Agilent; Model: 34970a) for data recording and visualization.

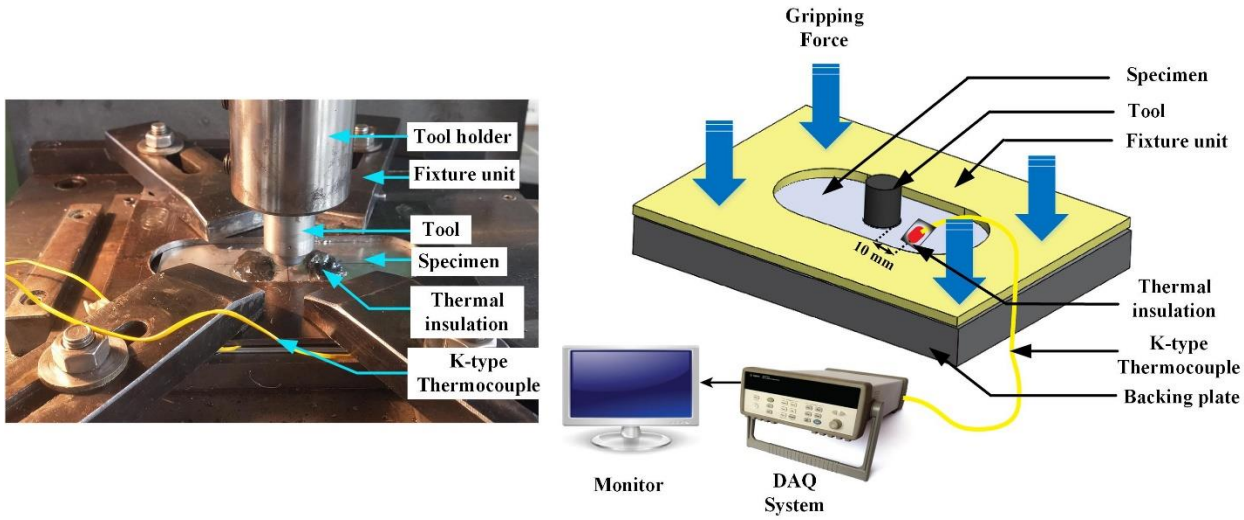

Fig. 5.2: Thermocouple mounted on the specimen to measure temperature evolution during FSSW experiments

5.1.2 Shock tube-based forming experiment

In the present study, a shock tube facility has been utilized to deform the FSS welded sheet at high strain rates (Fig. 5.3). The details of the experimental setup are described in Section 3.1.2. A nylon striker of diameter 54.8 mm and 95 mm overall length with a hemispherical end is kept at a distance of 300 mm from the end of the shock tube (Fig. 3.2). A set of IR sensors are mounted at a distance of 130 mm from the end of the shock tube to measure the velocity of the striker (Fig. 3.2). During the analysis, bursting pressure in the driver section is kept constant at 15.05 ± 0.35 bar for all the cases of forming. The pressure-time graph recorded by two pressure transducers (P_1 and P_2) during the experiment is shown in Fig. 5.3. The experimental condition generates an average incident pressure of 3.41 ± 0.17 bar, reflected pressure of 11.63 ± 0.21 bar, and striker velocity of 68.76 ± 0.55 m/s.

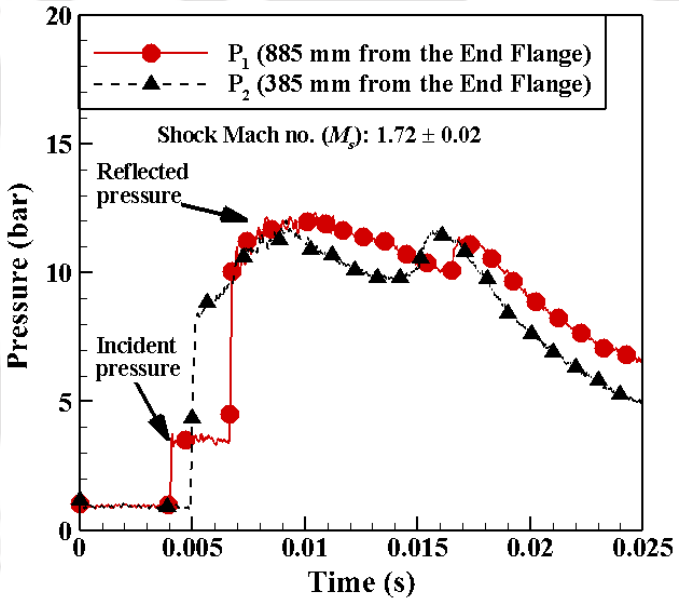

Fig. 5.3: Pressure-time graph obtained for bursting pressure 15.05 ± 0.35 bar

5.2 Numerical simulation of shock tube-based forming of FSSW sheet

The complete process (FSSW + Forming) is modelled in three stages in the multi-operation layout of DEFORM-3D FE code (Fig. 5.4). The plunging and dwelling operation in FSSW is modelled in two stages as a thermo-mechanical problem, and the welded sheet is redirected for high-velocity biaxial forming in the third stage. The multi-operation layout establishes an interactive setup among all the stages of simulation in such a way that the material properties and boundary conditions of an object can be easily passed between two successive operations.

Therefore, the material properties of the sheets after welding is easily retrieved before the start of the FE simulation of the forming process. The dimensions of all the parts of the model are same as per the experiments. The work-piece is modelled as a deformable plastic body, whereas the welding tool, end flanges, and the striker is modelled as a rigid body (Fig. 5.4). The detailed procedures of the FE simulation are discussed below.

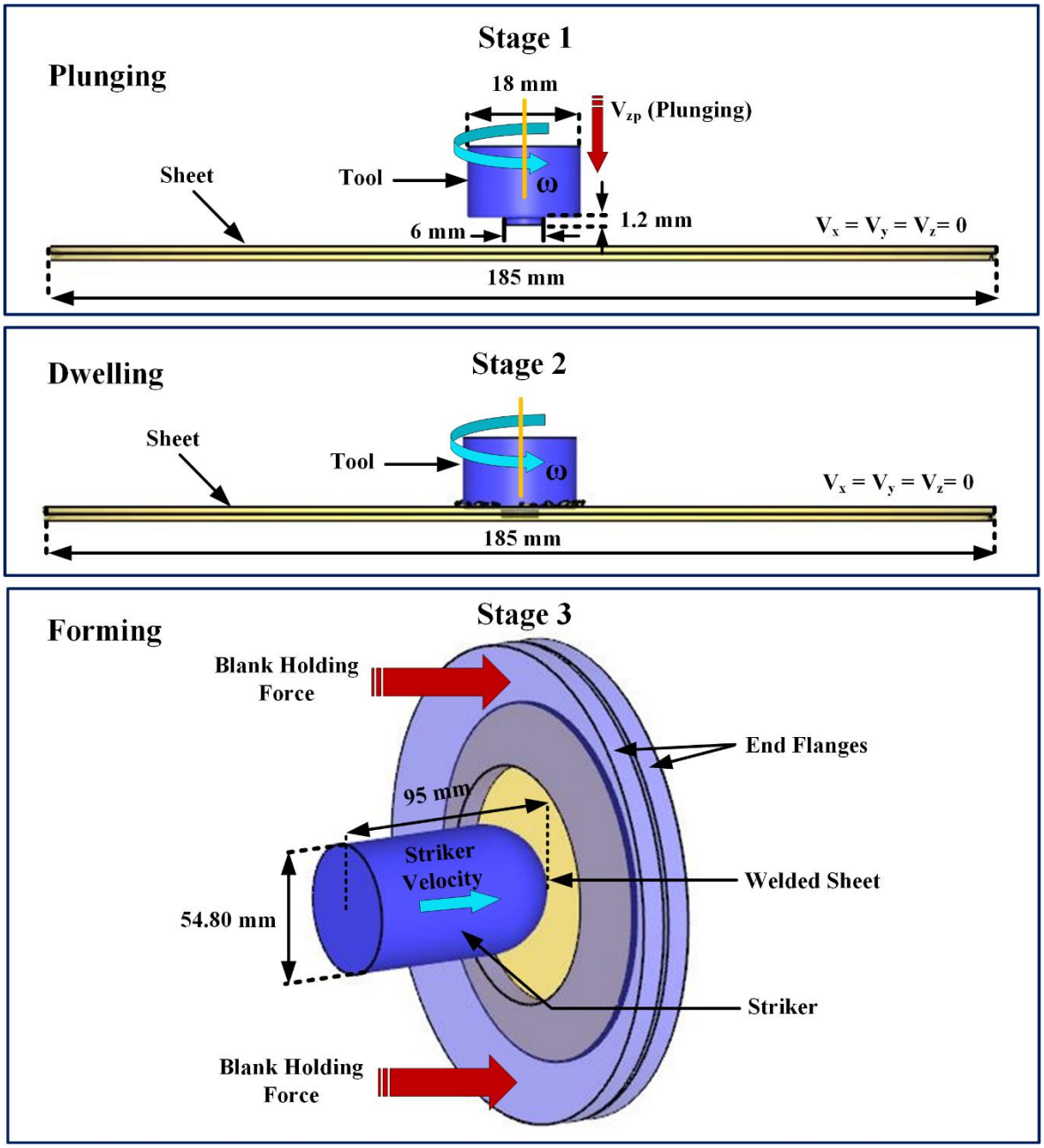

Fig. 5.4: Stages of FE simulation for shock tube-based forming of FSS welded sheet

5.2.1 FE simulation of FSSW

5.2.1.1 Geometric modelling and mesh generation

The complete FSSW operation is solved in two stages as a fully coupled 3-dimensional thermo-mechanical problem, which is solved by Lagrangian implicit method. The work-piece is considered as a deformable plastic material, and it is modeled as a single block, i.e., the two sheets are modelled as a unique simulation object for which the zone corresponding to the shoulder position during welding is presented with material continuity (Fig. 5.5). This choice was made in order to avoid contact instabilities during material bonding, and at the same time, taking to account the thermal barrier between the interface of the sheets (Zhao et al., 2016).

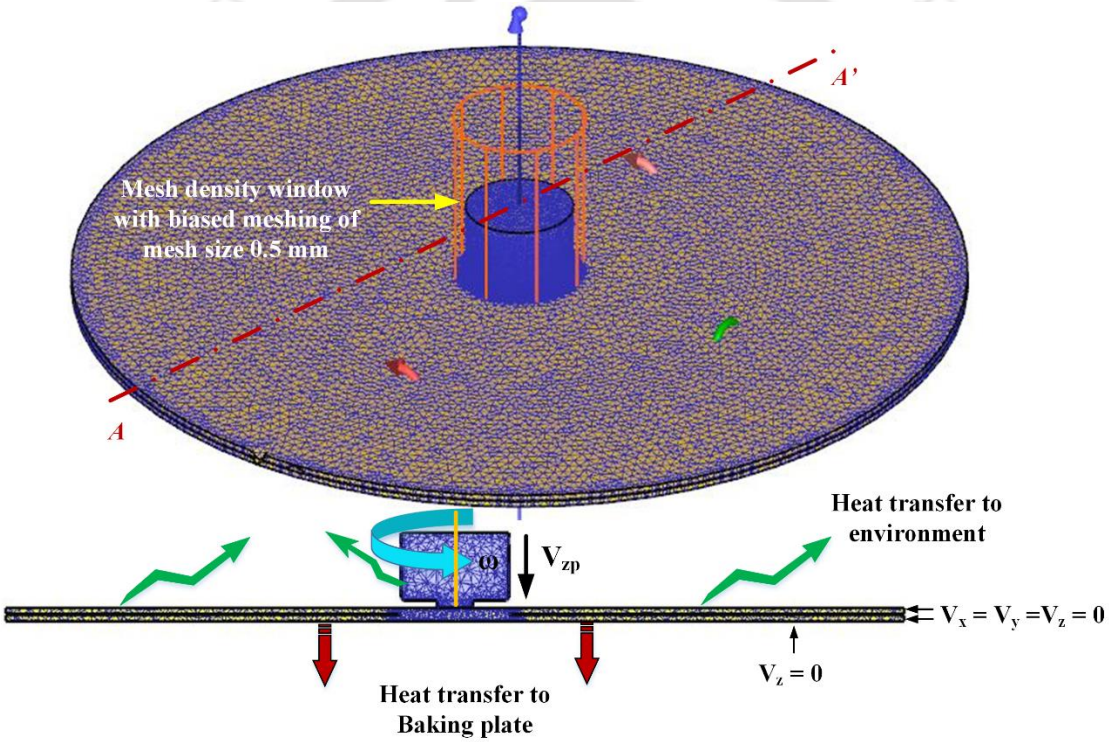

Fig. 5.5: Meshed assembly of the model with boundary conditions

During this analysis, coupled tetrahedral meshing has been defined for the work-piece. To improve the computational efficiency of the model, biased meshing is used at the interaction zone of the work-piece and the tool using mesh density window (Fig. 5.5). To understand the effect of element size, several mesh sizes such as 0.7 mm, 0.5mm, and 0.3 mm are selected, whereas the rest of the work piece domain is meshed with minimum element size of 1 mm with a size ratio of 2. The mesh independency analysis is performed for a welding condition with

rotational speed 750 rpm, and plunge speed 7.5 mm/min. The peak temperature recorded by a thermocouple at a distance 10 mm from the shoulder edge is compared with the FE simulation results. Though the results obtained for element sizes 0.5 mm and 0.3 mm do not vary much and have a good agreement with the experiment, the computational time for 0.3 mm element size increases significantly. Thus, 0.5 mm element size inside the mesh density window is considered for simulating FSSW. Along with this, the maximum effective strain and effective strain rate are also compared for various element sizes (Table 5.2). The elements corresponding to 0.5 mm and 0.3 mm predict almost the same values. Hence selecting 0.5 mm element size is justified. Since the yield strength of tool material (H13 tool steel) is much higher than AA 5052-H32 work-piece, the assumption of choosing the tool as a rigid body is valid. In the analysis, the tool is also meshed with tetrahedral element of 0.5 mm size to define a precise geometry, which generates 37160 number of elements.

Table 5.2: Mesh sensitive analysis for FSSW stage

Element size (Mesh density window)	**Number of elements**	**Peak Temperature (10 offset to shoulder) (°C)**	**Maximum effective strain**	**Maximum effective strain rate (s^{-1})**	**Computational time (*min*)**
Experiment	--	257.26	--	--	--
0.7 mm	63852	277.36	148	68.36	3120
0.5 mm	132914	268.42	104	52.34	4745
0.3 mm	218652	267.12	101	52.92	9023

5.2.1.2 Material model for FSSW simulation

During FSSW process, the material undergoes large plastic deformation at high temperature. Thus, the high-temperature tensile test data of AA 5052-H32 sheet (Fig. 5.1) are fit to Hollomon equation $\left(\sigma = K\varepsilon^{n}\right)$, and the material constants are identified (Table 5.1). Those material constants are again utilized to extrapolate the flow stress for larger strain value and incorporated during FE simulation as tabular data. The other temperature-dependent material properties considered during FE simulation are obtained from literature (Bajpei et al.,

2017), and also mentioned in Table 5.3. The thermo-mechanical properties of H13 tool steel are obtained from the material library database of DEFORM-3D (Fluhrer, 2007).

Table 5.3: Temperature dependent mechanical properties of AA5052 and H13 tool steel

AA5052-H32						
Temp. (°C)	ρ **(Kg/m^3)**	E **(GPa)**	K_p **(W/m °C)**	α **(µ/ °C)**	**C (N/mm^2/°C)**	υ
20	2781.25	72	162.5	21	2.43	0.33
80	2756.25	68	168.75	24	2.43	0.33
180	2695	64	193.75	25	2.43	0.33
280	2650.5	56	206.25	26	2.43	0.33
380	2610.66	40	225	27	2.43	0.33
480	2605	22	237.5	28.5	2.43	0.33
H13 tool steel						
20	7780	210.29	24.57	11.7	2.78	0.3

ρ : Density; C: Heat capacity; K_p: Thermal conductivity; α : Coefficient of thermal expansion; E : Young's Modulus; υ : Poisson's ratio

5.2.1.3 Boundary and frictional contact conditions

The tool and the work-piece are defined with boundary conditions in such a way that the actual physical phenomenon during FSSW can be accurately simulated. The boundary conditions defined during modelling are depicted in Fig. 5.5. The motion of the side faces of the work-piece is constrained in X, Y, and Z directions, while the motion of the bottom face of the work-piece is only restricted in Z-direction. The plunge speed and the rotational speed of the tool are defined along the negative Z-axis as per the experiment.

The initial temperature of the work-piece and the tool are set as 25°C. The heat transfer between the work-piece/tool surface and the environment can be expressed as

$$-K_p \frac{\partial T}{\partial n} = \sigma_b \varepsilon_b \left(T^4 - T_b^4\right) + h_a \left(T - T_b\right) \quad (n \text{ is the direction vector}) \tag{5.1}$$

Furthermore, the heat exchange at the interaction region between the tool, sheet, and baking plate can be defined by

$$-K_p \frac{\partial T}{\partial Z} = h_b \left(T - T_b\right) \tag{5.2}$$

where σ_b is the Stefan-Boltzmann constant, ε_b is the emissivity of the material, K_p is the thermal conductivity of the material, T_b is the ambient temperature, h_a is convective heat transfer between work-piece/tool and the environment, and h_b is the convective heat transfer coefficient between the work-piece and the backing plate. To improve the computational efficiency of the FE simulation, the backing plate is replaced by a local heat exchange window to define the heat transfer between the bottom face of the sheet and the environment with the convention coefficient (h_b) as 500 W/m^2°C (Fluhrer, 2007) as shown in Fig. 5.5. The heat exchange from the other faces of the work-piece and the tool to the environment are also defined by generating heat exchange local windows with convection coefficient (h_a) as 20 W/m^2°C. The emissivity for AA 5052- H32 sheets and H13 tool is considered as 0.03 and 0.7, respectively (Fluhrer, 2007). It has been observed that the heat transfer between the tool and the work-piece is higher than the work-piece and the environment. Thus, the heat transfer coefficient between them is considered as 11000 W/m^2°C (Zhao et al., 2016).

The contact condition between the work-piece and the tool during FE simulation of FSW is complex. In few studies, sliding frictional condition is defined, while in most of the studies, sticking friction model is best suited during simulation of the material state during FSW and it is given by

$$\tau = mk \tag{5.3}$$

where τ and k are the frictional stress, and the shear yield stress of the material, respectively. m represents the shear friction factor. In order to calibrate the correct magnitude of m, several numerical simulations were performed with different m values for a weld condition with 750 rpm and 7.5 mm/min plunge speed, and the peak temperature at a distance of 10 mm from the shoulder edge are compared with the experimental result (Fig. 5.6). For simulation, the optimum element size of 0.5 mm in the weld spot was considered. The result represents a good correlation of FE simulation with the experiment for m = 0.4, with 6.7 % deviation. Thus, the value of m = 4 is considered as a constant for other cases of FE simulation.

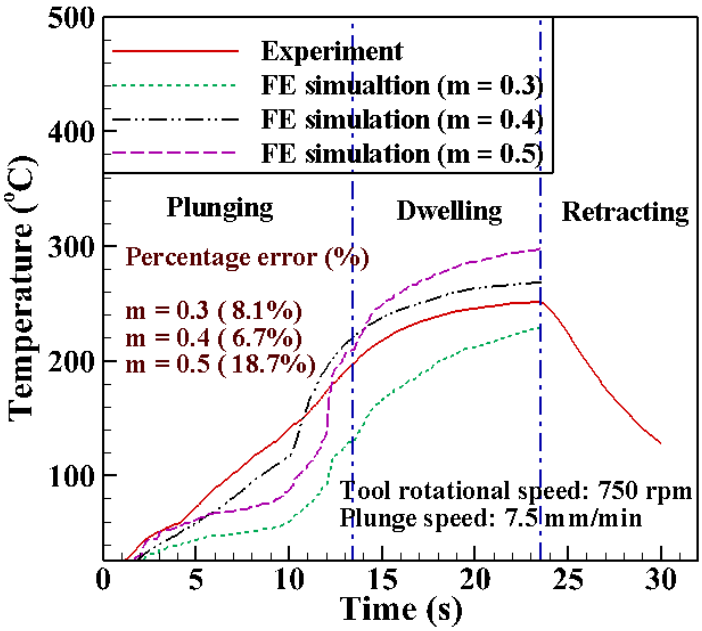

Fig. 5.6: Comparison of temperature evolution during FE simulation with experiment for various *m* values

5.2.2 FE simulation of shock tube-based forming

5.2.2.1 Material model for forming operation

After completion of FSSW simulation, the work-piece is redirected for high strain rate forming in DEFORM-3D. The multi-operation environment allows to transfer object data between two successive operations, which helps to retrieve all the welding properties of the work-piece before the start of the forming simulation. The shock tube-based forming takes place at the atmospheric temperature under high strain rate condition. Thus, incorporation of the rate-dependent mechanical properties to the sheet with FSSW is crucial. For an accurate prediction of the forming behavior of the welded sheet, it is unfair to assign the mechanical properties of the base material to both the spot weld and unwelded sections of the sheet. Therefore, a new strategy is followed during this analysis, in which the single block welded work-piece is separated into two zones such as spot weld zone and unwelded zone (Fig. 5.7). Both the zones are assigned with the rate-dependent mechanical properties separately obtained from experiments.

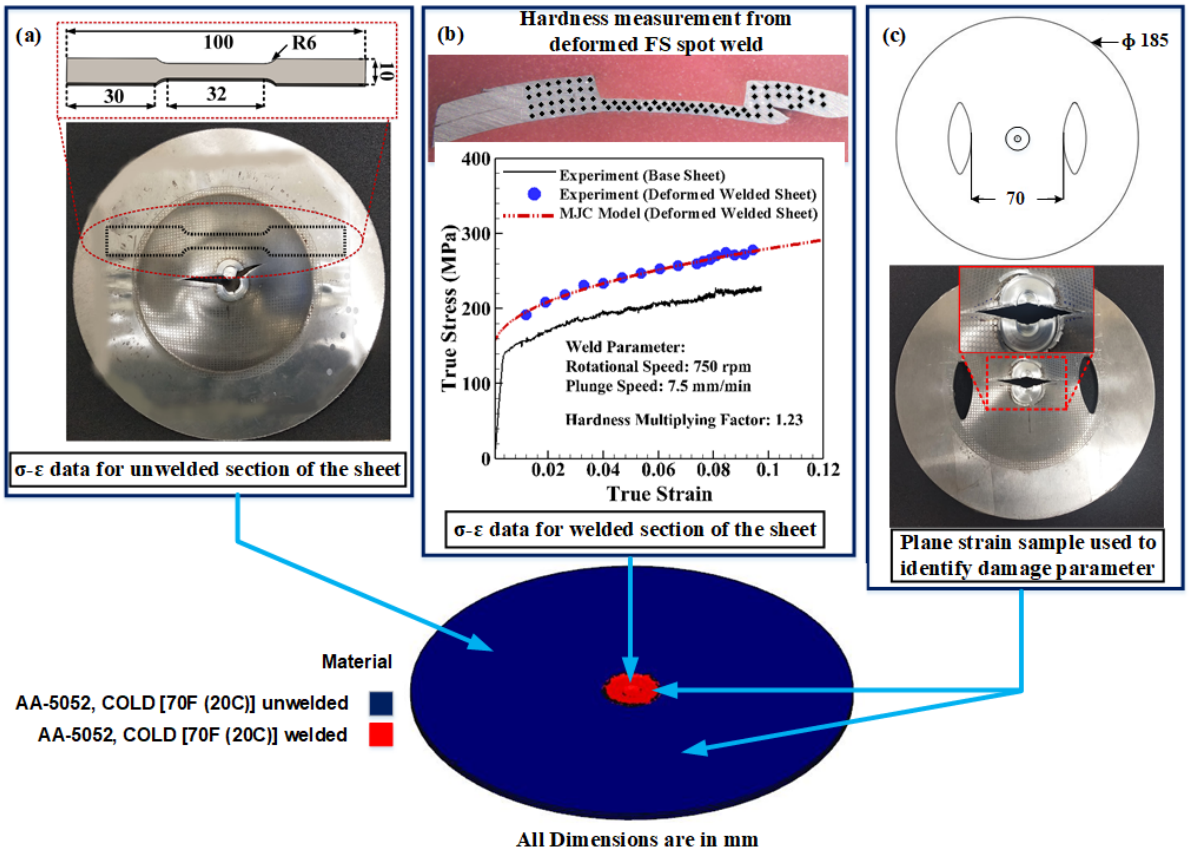

Fig. 5.7: Procedure to define material constants during FE simulation of shock tube-based forming of FSSW sheets

In most of the research work, Split Hopkinson Pressure Bar (SHPB) is utilized to conduct tensile test at high strain rate. In this current work, a new method is followed to identify the rate-dependent mechanical properties of the spot weld and unwelded region. For the unwelded section, a tensile sample is cut in a safe location of the deformed sheet near to the fracture after the shock tube-based forming experiment (Fig. 5.7a). The tensile test is performed on the bent tensile sample without any post-treatment at a crosshead speed of 1 mm/min in UTM. On the other hand, sectioning the tensile sample from the FS spot weld of the deformed sheet is impossible because of the presence of fracture. Thus, the rate-dependent plastic behavior of the spot weld of the sheet is correlated with the hardness variation in the weld spot after forming. A hardness increment factor has been identified between the average hardness value of the welded joint after forming to the undeformed base sheet, and that factor is multiplied to the true stress-strain data of the undeformed base sheet to obtain the rate-dependent stress-

strain curve for the FS spot weld (Fig. 5.7b). The experimentally identified stress-strain data of the spot weld and unwelded sections of the sheet is fit to modified Johnson-Cook (MJC) model given in eq. 3.4, and the material constants are identified. The material constants *A*, *B*, and *n* are identified at a reference strain rate ($\dot{\bar{\varepsilon}}_0$), which is kept as one (Khodko et al., 2015; Song et al., 2019), C_1 and C_2 are the strain rate sensitivity constants, $\dot{\bar{\varepsilon}}$ is the real strain rate. During high-velocity shock tube experiment, it is practically difficult to identify the real strain rate because of the restrictions in instrumentation. However, it is required while using eq. 3.4. Thus, FE simulation is carried out to obtain the average strain rate near the pole region of the welded sheet. For this modelling, the rate-dependent true stress-strain data of both the welded and unwelded section are fit to Hollomon hardening model ($\bar{\sigma} = K\bar{\varepsilon}^n$), and the material constants (*K* and *n*) are identified (Table 5.4). The material constants are further utilized to calculate flow stress for larger strain (Fig. 5.8), and the stress-strain data are incorporated in a tabular form during FE simulation. The average strain rates during the forming of different welded sheets are mentioned in Table 5.4. Further, the identified strain rates are again utilized in MJC model to calculate the rate-dependent material constants mentioned above for FSSW and unwelded sections of the sheet by the curve fitting method (Fig. 5.8). During the curve fitting, the lower range and the upper range of the MJC model material constants are identified from the literature (Deng et al., 2019; Khodko et al., 2015; Song et al., 2019), and the best fit values as mentioned in Table 5.4 are further utilized for the calculation of the flow stress for larger strain (Fig. 5.8).

Defining material anisotropy is essential for an accurate prediction of formability. In this study, it is assumed that AA 5052-H32 sheet would follow Hill's 1948 yield criterion and the associated flow rule. The details about Hill's 1948 yield criterion are discussed earlier in Section 2.4.1. It is observed that the failure pattern is sensitive to the flow stress model, fracture model, coefficient of friction (μ), and angle of contact (θ) between the sheet and the striker. Along with the best feasible material models, the Coulomb's coefficient of friction (μ) is also optimized, which is defined as the contact condition between the striker and the work-piece during plastic deformation. μ is varied between 0.005 to 0.2 to obtain an acceptable failure pattern similar to the experiment. At μ = 0.2, the material fails, and complete plug ejection was observed, whereas the failure pattern is unreal at μ = 0.005. After several trials, μ = 0.05 resulted in an acceptable failure pattern and has a good agreement with the experiment. Thus,

μ = 0.05 is kept constant for further cases of forming simulation. In order to avoid sliding between the end flanges and the sheet, μ = 0.1 has been assumed.

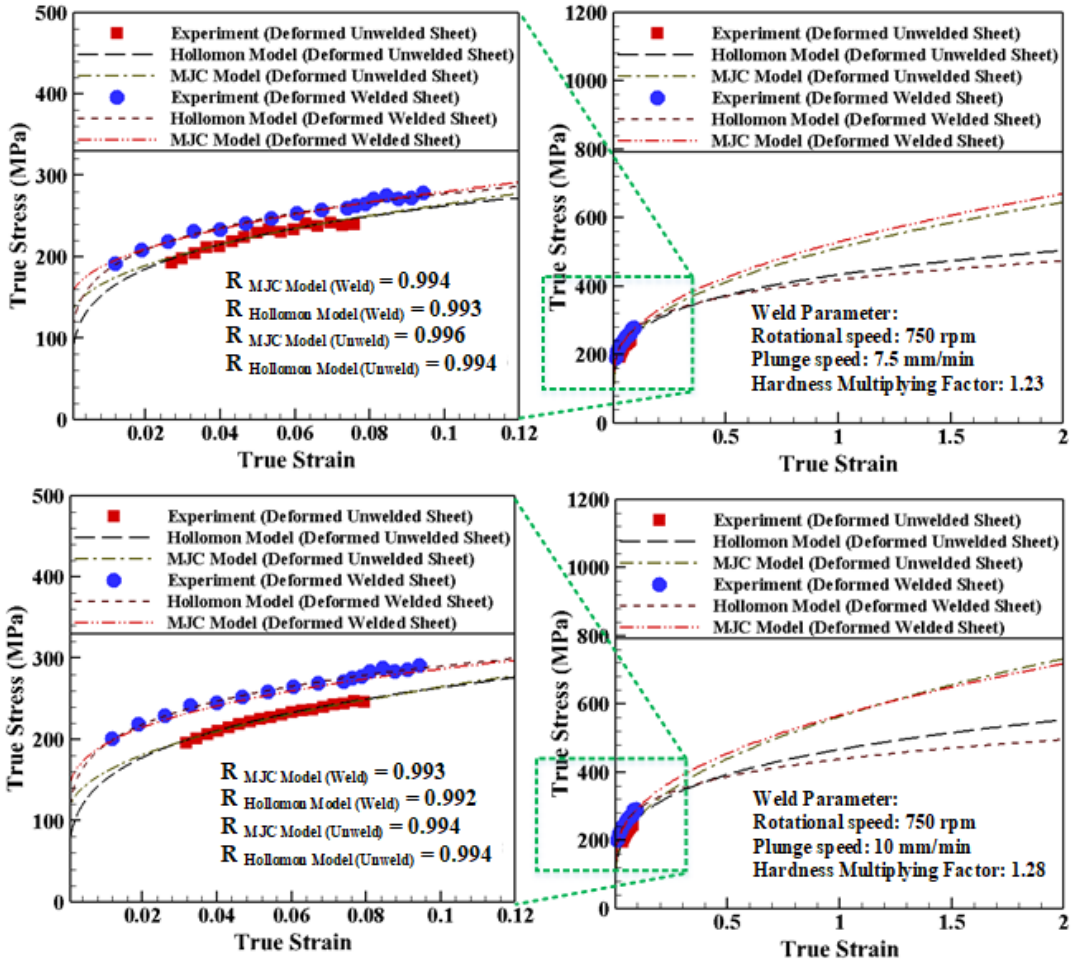

(a)

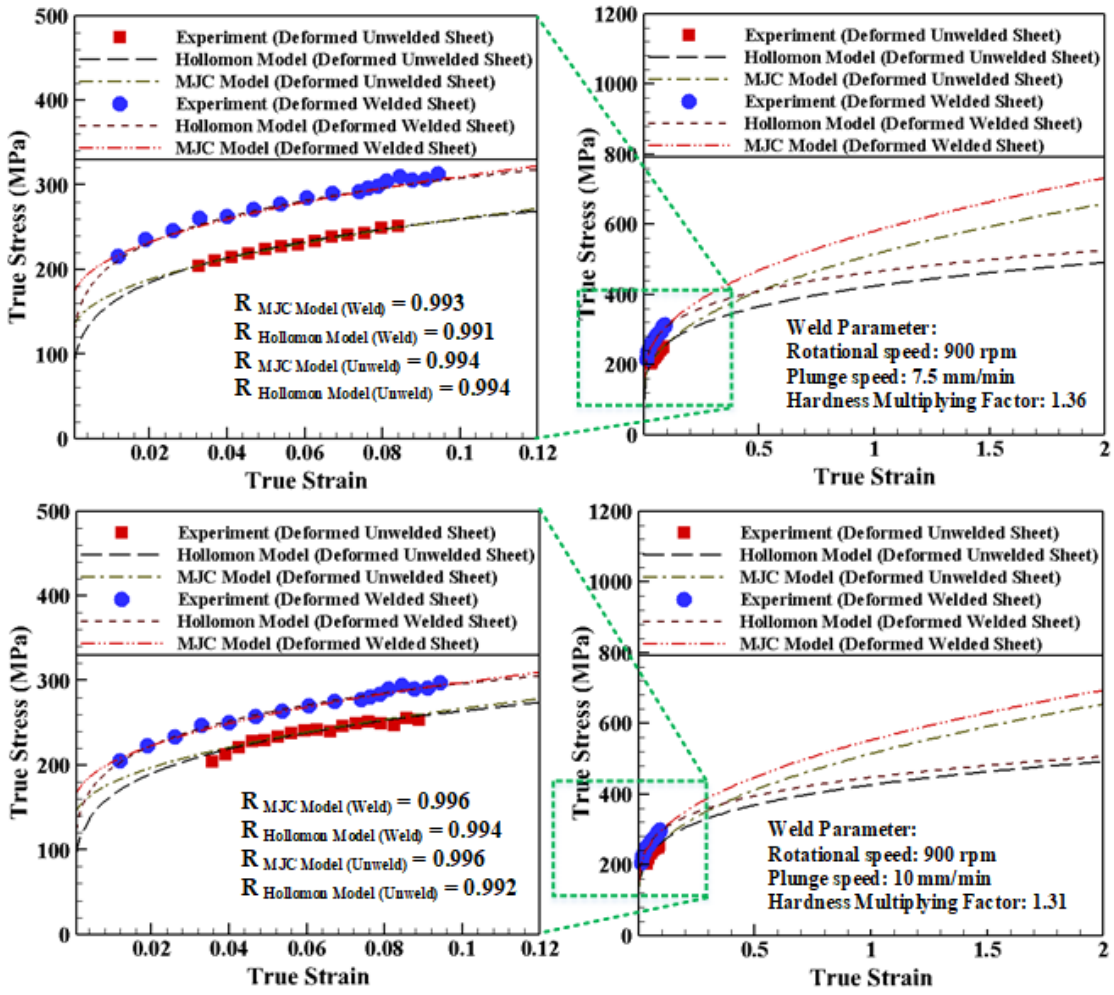

(b)

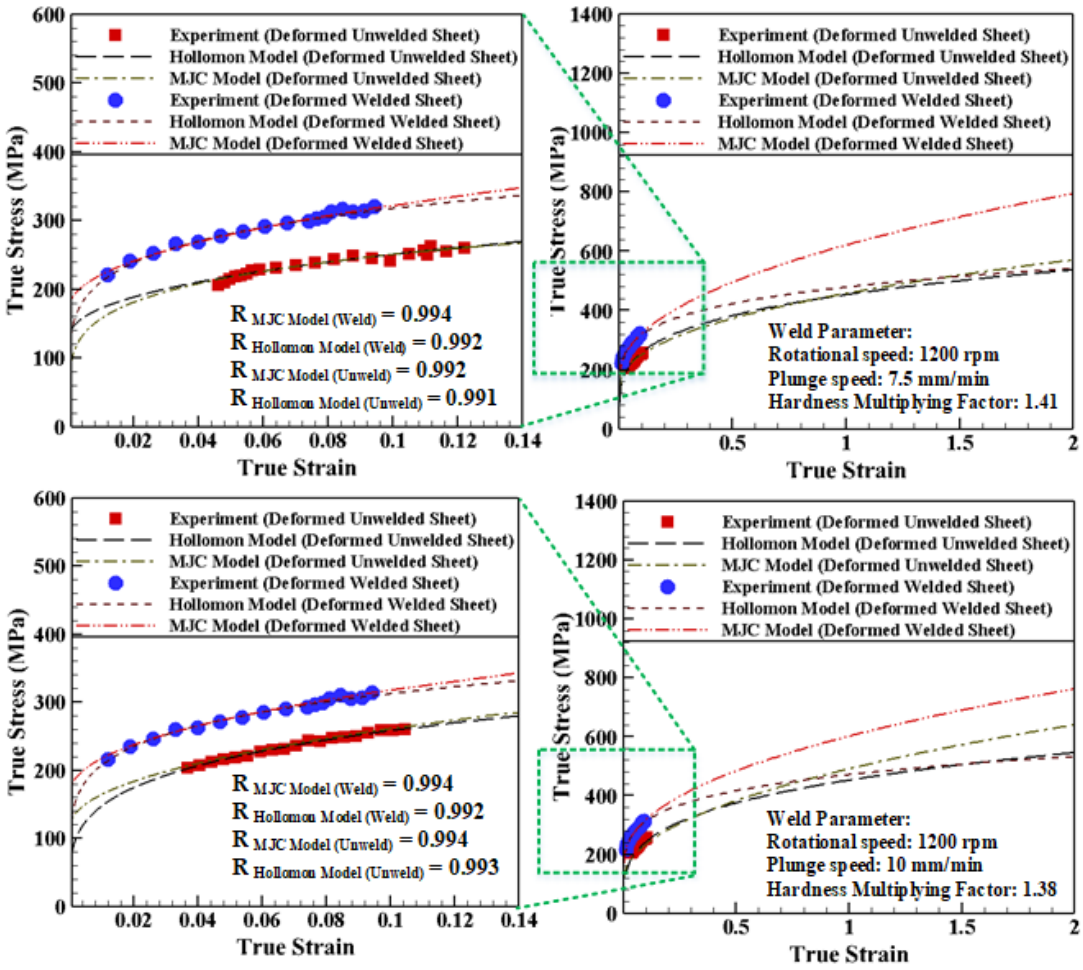

(c)

Fig. 5.8: Identification of rate-dependent material parameters by curve fitting method for FS spot weld and unwelded section of the sheets

Table 5.4: Identification of material constants for Hollomon model and MJC model

Hardening Model		**Strain rate (s^{-1})**	**Hardness Multiplying Factor in case of FSSW**	**Hollomon Model**		**MJC Model**				
Material Constants				***K* (MPa)**	***n_1***	***A* (MPa)**	***B* (MPa)**	***n_2***	***C_1***	***C_2***
FS spot Weld	**R.S: 750 rpm P.S: 7.5 mm/min**	2356	1.23	417.76	0.18	151.2	408.4	0.45	-0.0793	0.0094
	R.S: 750 rpm P.S: 10 mm/min	2373	1.28	437.38	0.18	145.3	475.5	0.43	-0.0845	0.0095
	R.S: 900 rpm P.S: 7.5 mm/min	2288	1.36	463.77	0.18	148.8	404.7	0.44	-0.0704	0.0102
	R.S: 900 rpm P.S: 10 mm/min	2315	1.31	446.75	0.18	141.2	388.7	0.43	-0.0895	0.0122
	R.S: 1200 rpm P.S: 7.5 mm/min	2415	1.41	478.18	0.18	153.3	409.9	0.47	-0.0471	0.0078
	R.S: 1200 rpm P.S: 10 mm/min	2386	1.38	470.61	0.18	146.5	398.5	0.45	-0.0662	0.0103
Unwelded region	**R.S: 750 rpm P.S: 7.5 mm/min**	2356	--	438.98	0.22	132.7	462.9	0.47	-0.1621	0.0196
	R.S: 750 rpm P.S: 10 mm/min	2373	--	465.87	0.25	136.2	616.9	0.45	-0.0961	0.0082
	R.S: 900 rpm P.S: 7.5 mm/min	2288	--	423.13	0.21	138.6	457.5	0.45	-0.0912	0.0095
	R.S: 900 rpm P.S: 10 mm/min	2315	--	425.47	0.21	146.6	429.8	0.45	-0.0824	0.0088
	R.S: 1200 rpm P.S: 7.5 mm/min	2415	--	419.81	0.22	143.3	386.6	0.42	-0.0868	0.0088
	R.S: 1200 rpm P.S: 10 mm/min	2386	--	451.63	0.24	136.6	519.5	0.44	-0.0912	0.0087
R.S: Rotational speed; P.S: Plunge speed										

5.2.2.2 Identification of damage parameter during forming

Severe plastic deformation above a critical limit leads to the onset of necking and initiation of crack. During this study, Freudenthal failure model (eq. 3.5) as mentioned earlier in Section 3.2.3 is utilized to understand the occurrence of ductile fracture and propagation of crack on AA 5052-H32 sheets with FS spot welds during shock tube-based impact forming. Several failure models are available in DEFORM-3D data base (Fluhrer, 2007). However, Freudenthal model is chosen in this study because of its better accuracy in predicting the failure pattern and fracture strain during sheet forming as observed elsewhere (Dizaji et al., 2016; Pereira et al., 2020). In the current work, circle grids of grid diameter 1.5 mm are generated on the surface of the work-piece before the start of the forming simulation (Fig. 5.9a). The strain paths at a location near to the failure of the deformed FS spot welded sheets are predicted (Fig. 5.9b). It is observed that the sheet stretches biaxially at the initial stage, and when the critical damage parameter is reached, necking initiates, and the strain path shifts towards the plane strain condition (Fig. 5.9b). Thus, by assuming plane strain condition ($\varepsilon_2 = 0$) during the deformation the critical damage parameter for Freudenthal model is calculated. The stress ratio and strain ratio required for the calculation of critical damage parameter (D_1) can be derived from Hill's 1948 yield criterion assuming no planar anisotropy condition, i.e. $r = r_0 = r_{45} = r_{90} = 0.73$, and plane strain condition (mentioned in Section 3.2.3). The failure strain, ε_f = 0.34 is identified by deforming a plane strain sample of diameter 185 mm in the shock tube experiment (Fig. 5.7c). The critical damage parameter for Freudenthal damage model is calculated for both the FS spot weld and unwelded sections of the sheet as listed in Table 5.5 and incorporated during FE simulation during the forming stage. Other material properties are enlisted in Table 5.6.

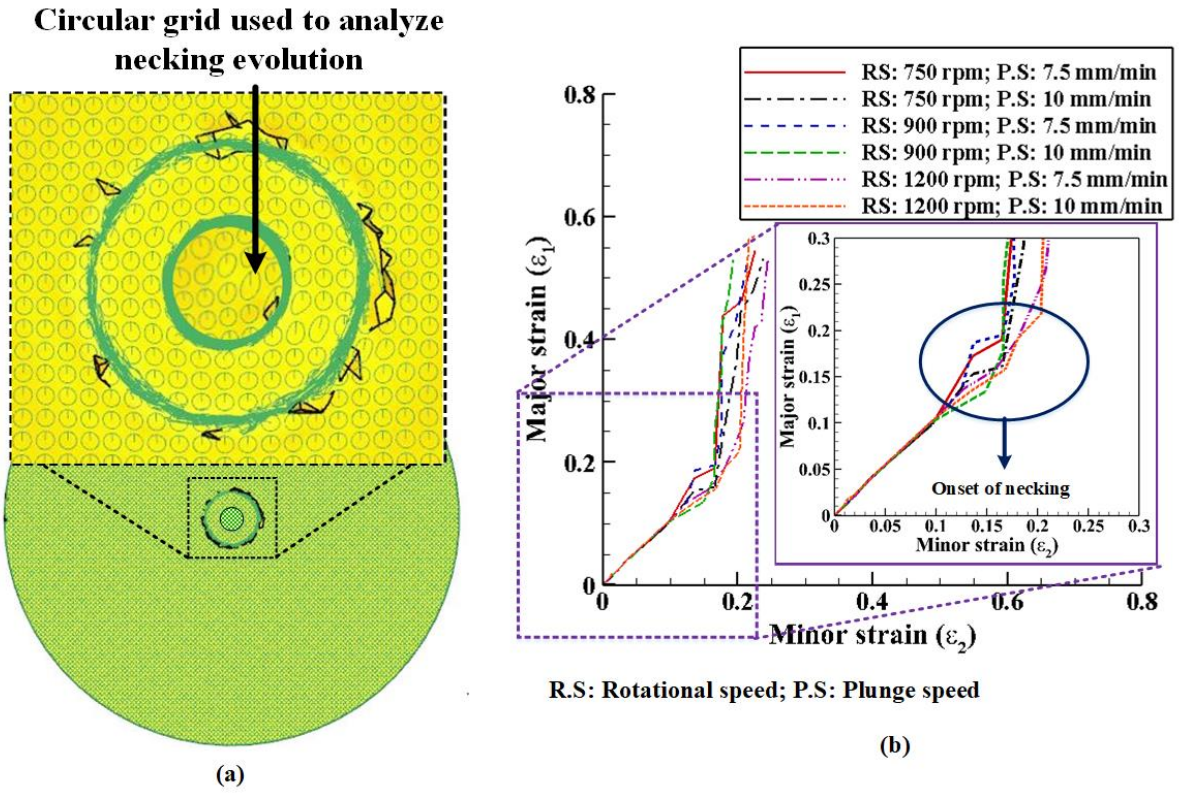

Fig. 5.9: Strain path evolution during shock tube based forming of sheets with FSSW

Table 5.5: Critical damage parameter for Freudenthal failure model

Welding Condition		Critical Damage Parameter (MPa)
FS spot weld region	R.S: 750 rpm P.S: 7.5 mm/min	98.51
	R.S: 750 rpm P.S: 10 mm/min	103.12
	R.S: 900 rpm P.S: 7.5 mm/min	107.68
	R.S: 900 rpm P.S: 10 mm/min	105.34
	R.S: 1200 rpm P.S: 7.5 mm/min	115.33
	R.S: 1200 rpm P.S: 10 mm/min	111.36
Unwelded region	R.S: 750 rpm P.S: 7.5 mm/min	86.68
	R.S: 750 rpm P.S: 10 mm/min	87.54

	R.S: 900 rpm P.S: 7.5 mm/min	88.76
	R.S: 900 rpm P.S: 10 mm/min	89.42
	R.S: 1200 rpm P.S: 7.5 mm/min	87.66
	R.S: 1200 rpm P.S: 10 mm/min	87.12

Table 5.6: Properties incorporated during FE simulations of forming

Properties	Value
Mass density of AA 5052-H32 sheet (kg/m^3) at room temperature	Refer Table 5.3
Mass density of Nylon (kg/m^3)	1140
Young's modulus of AA 5052-H32 sheet (MPa)	Refer Table 5.3
Young's modulus of Nylon (MPa)	3810
Coulomb's coefficient of friction between striker and sheet	0.05
Coulomb's coefficient of friction between end flanges and sheet	0.1
Rate-dependent $\sigma-\varepsilon$ data of AA5052-H32 unwelded sheet	Refer Fig. 5.8
Rate-dependent $\sigma-\varepsilon$ data of AA5052-H32 FS spot welded sheet	Refer Fig. 5.8

5.2.2.3 Mesh details and mesh sensitive analysis for forming of sheets with FS spot welds

A new mesh window is generated on the deforming zone of the welded sheet. To optimize the mesh density and computational time, the welded sheet has meshed with a constant element size ratio of 6, which represents the ratio of the largest element edge to the smallest element edge. The largest element size inside the mesh window is decided as 1. However, the minimum element size for this analysis is finalized by mesh sensitivity analysis. Various element sizes such as 1 mm, 0.5 mm, 0.33 mm, 0.25 mm, and 0.2 mm are considered for the analysis. The mesh independency analysis is carried out for forming the sheet with spot weld at the welding condition, 750 rpm, and 7.5 mm/min plunge speed. During this analysis, Hollomon hardening model is used along with Freudenthal failure model. The material constants for the models can be found in Table 5.4 and Table 5.5. The effective strain ($\bar{\varepsilon}$) distribution obtained from FE simulations using different element sizes are compared with experimental data as depicted in Fig. 5.10. The results illustrate a good agreement between experiments and simulation results with element sizes, 0.25 mm and

0.2 mm. However, due to the significant increase in computational time for 0.2 mm element size, the FE simulations of all the forming cases are carried out with the minimum element size 0.25 mm.

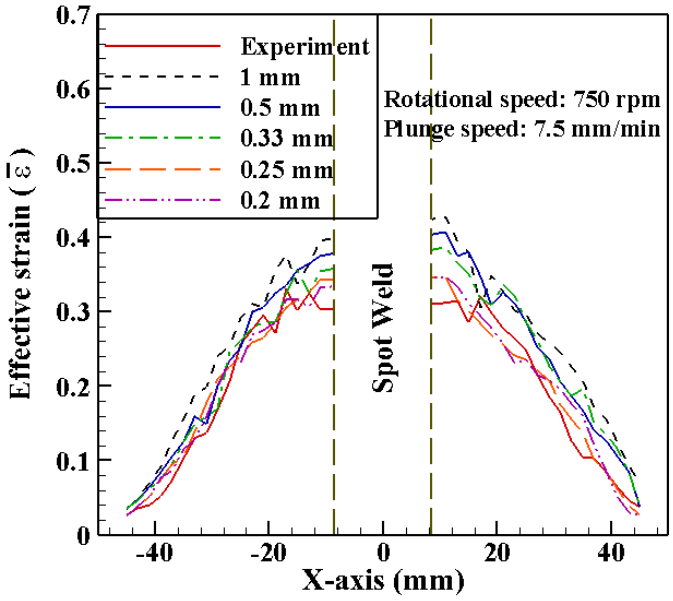

Fig. 5.10: Comparison of effective strain ($\bar{\varepsilon}$) distribution predicted for different mesh element sizes to experimental data

5.3 Results & discussion

5.3.1 Temperature evolution during FSSW experiments

The temperature signals measured at a distance of 10 mm from the shoulder edge during FSSW experiments are compared with FE simulation, and the results have a good agreement in all the welding conditions (Fig. 5.11). The rise in temperature is directly proportional to the rotational speeds, and the effect is predicted correctly by FE simulations. The effect of plunge speed during FSSW is also analyzed by FE simulation. It is observed that the decrease in plunge speed increases the temperature. However, the effect is insignificant. A maximum deviation of about 8.67 % is observed between simulation and experimental data for the case with 1200 rpm and 7.5 mm/min. For all other cases, the predictions are acceptable.

The temperature evolution during plunging and dwelling stages is well captured by FE simulation. During plunging, the temperature increases monotonically because of the increase in contact between the tool and the work-piece. The temperature rise during plunging is largely

dependent on the plunge speed. The temperature rise is faster in the case of 1200 rpm (Fig. 5.11). The temperature rise continues further during the dwelling period, and the rate at which temperature increases is directly proportional to the rotational speed (Fig. 5.11). The rate of temperature rise with the increase in plunge speed is not so significant. The peak temperature during welding is always captured just before the tool retraction. The temperature distribution along the transverse direction of the weld spot at the interference of two sheets (z = 1 mm) is illustrated in Fig. 5.12. The temperature distribution profile matches well with the results available in the existing literature (Buffa et al., 2006).

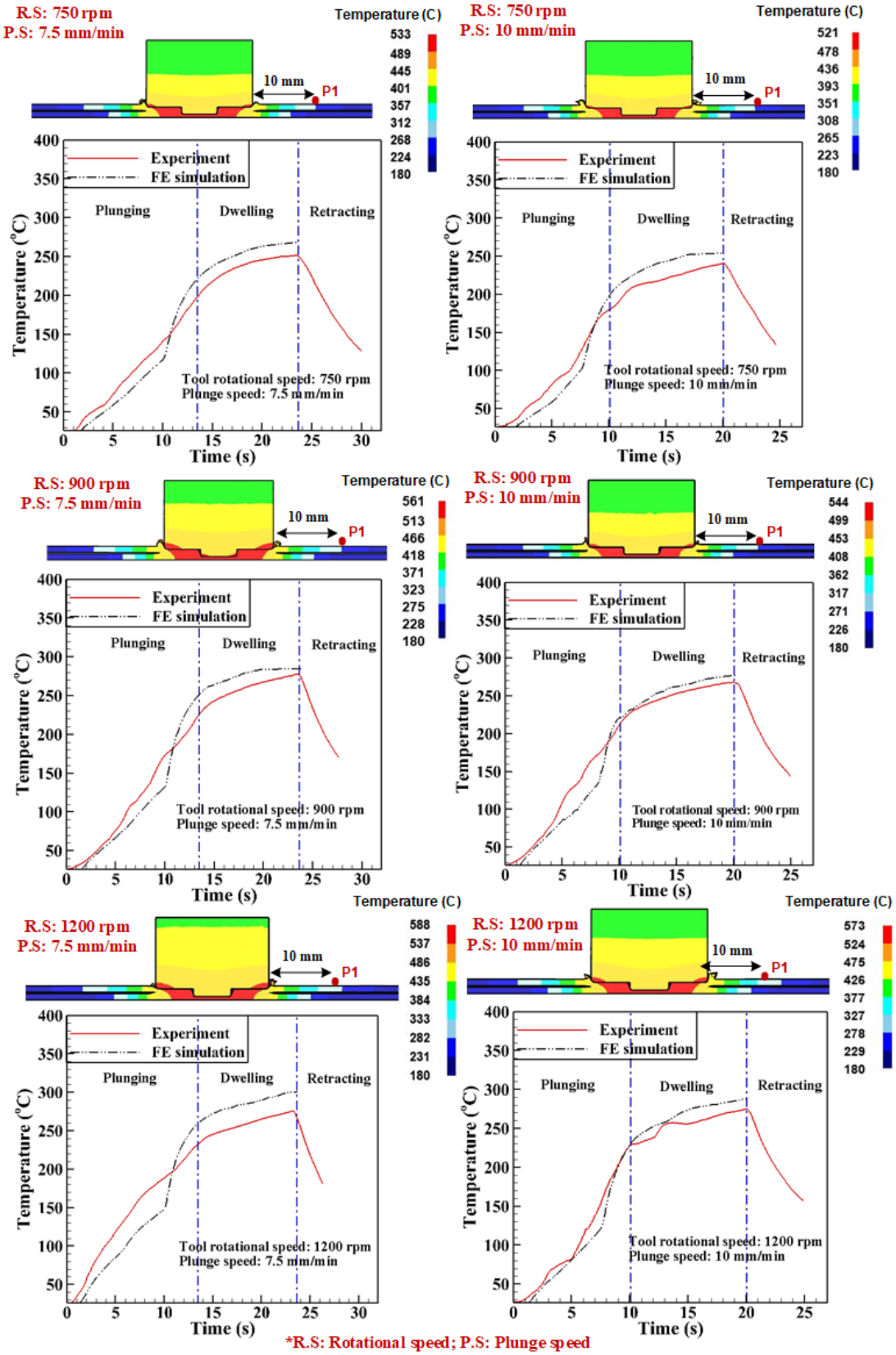

Fig. 5.11: Comparison of temperature evolution during experiments with that from FE simulations

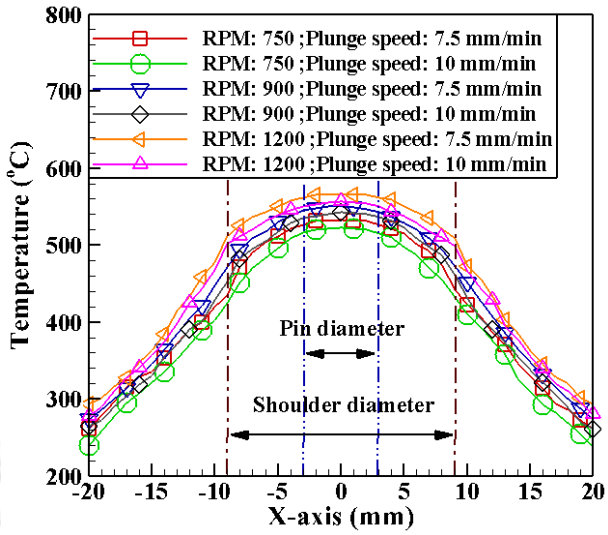

Fig. 5.12: Temperature distribution along the transverse section of the spot weld

5.3.2 FSSW joint characterization: stir zone prediction and hook morphology evaluation

After FSSW, the joint is divided into three zones namely stir zone (SZ), thermo-mechanically affected zone (TMAZ), and heat-affected zone (HAZ) based on microstructure. The severe plastic deformation at elevated temperature in SZ develops finer grains due to dynamic recrystallization. The SZ is surrounded by TMAZ, which experiences less heat input and plastic deformation than SZ, whereas the HAZ experiences a thermal cycle without plastic deformation. The microstructure evolved at different zones is illustrated in Fig. 5.13.

The shape and size of the stir zone significantly affect the mechanical properties of the joint. During FE simulation of the FSSW, the metallurgical aspect of the material is not considered. Thus, the evolved microstructures during the experiment cannot be compared with FE simulation. However, the point tracking method in DEFORM-3D can be utilized to predict the shape of SZ. During the analysis, total 133 number of points are defined with 0.5 mm horizontal spacing and 0.33 mm vertical spacing on the welded spot (Fig. 5.13). Due to the symmetry of welding, only half of the weld spot is defined for the purpose. After FSSW, the points are displaced from their initial position because of the plastic deformation caused by the tool. It results in the displacement of points from SZ, and the points away from the SZ remain undisturbed. By connecting line to the position of the border points, SZ can be identified. The results are verified with SZ obtained from the macrostructure (Fig. 5.13), and a good correlation has been observed. FE simulation results also depict the material deformation mechanism. The position of the points after completion of FSSW clearly elucidates that the material below the center of the tool pin experiences compression,

whereas the rest of the material inside SZ experiences both compression and shear deformation (Fig. 5.13).

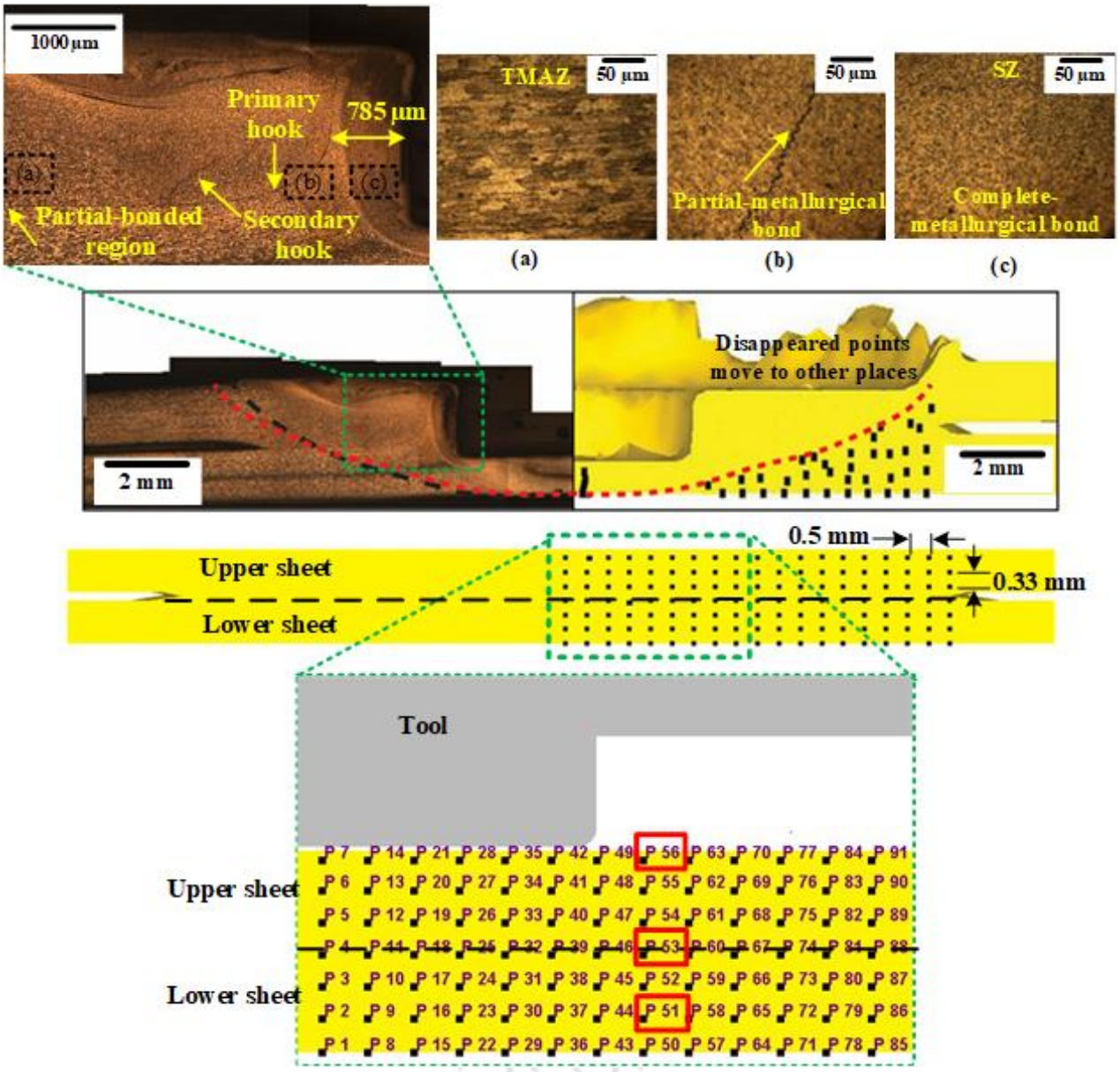

Fig. 5.13: Characterization of the weld spot for welding condition, tool rotational speed: 750 rpm, plunge speed: 7.5 mm/min, and SZ size comparison with FE simulation

FSSW joint morphology can be understood from the macrostructure illustrated in Fig. 5.14. Badarinarayan et al. (2009) reported that out of various characteristics, the combination of larger hook width (horizontal distance from the primary hook to the pinhole periphery) and smaller hook height (vertical distance from the primary hook to hook initiation point) can produce higher joint

strength. Thus, in the present study, the effect of rotational speeds and plunge speeds on the hook geometries are quantified (Fig. 5.14). The hook width increases significantly with the increase in rotational speed. However, the hook height shows an inverse relation with rotational speed. Bozzi et al. (2010) also reported similar observation and indicated that higher rotational speed generates more frictional heat and performs extensive stirring of the material. The severe plastic deformation at higher rotational speed merges a portion of the hook with the extruded material zone, and it results in an increase in bonding width and reduction in hook height. The effect of tool plunge speed is also analyzed, and it is observed that lower plunge speed results in larger hook width. However, the hook height increases with the increase in tool plunge speed. The larger processing time promotes more heat generation and plastic deformation, which leads to increase in the hook width and decrease in hook height.

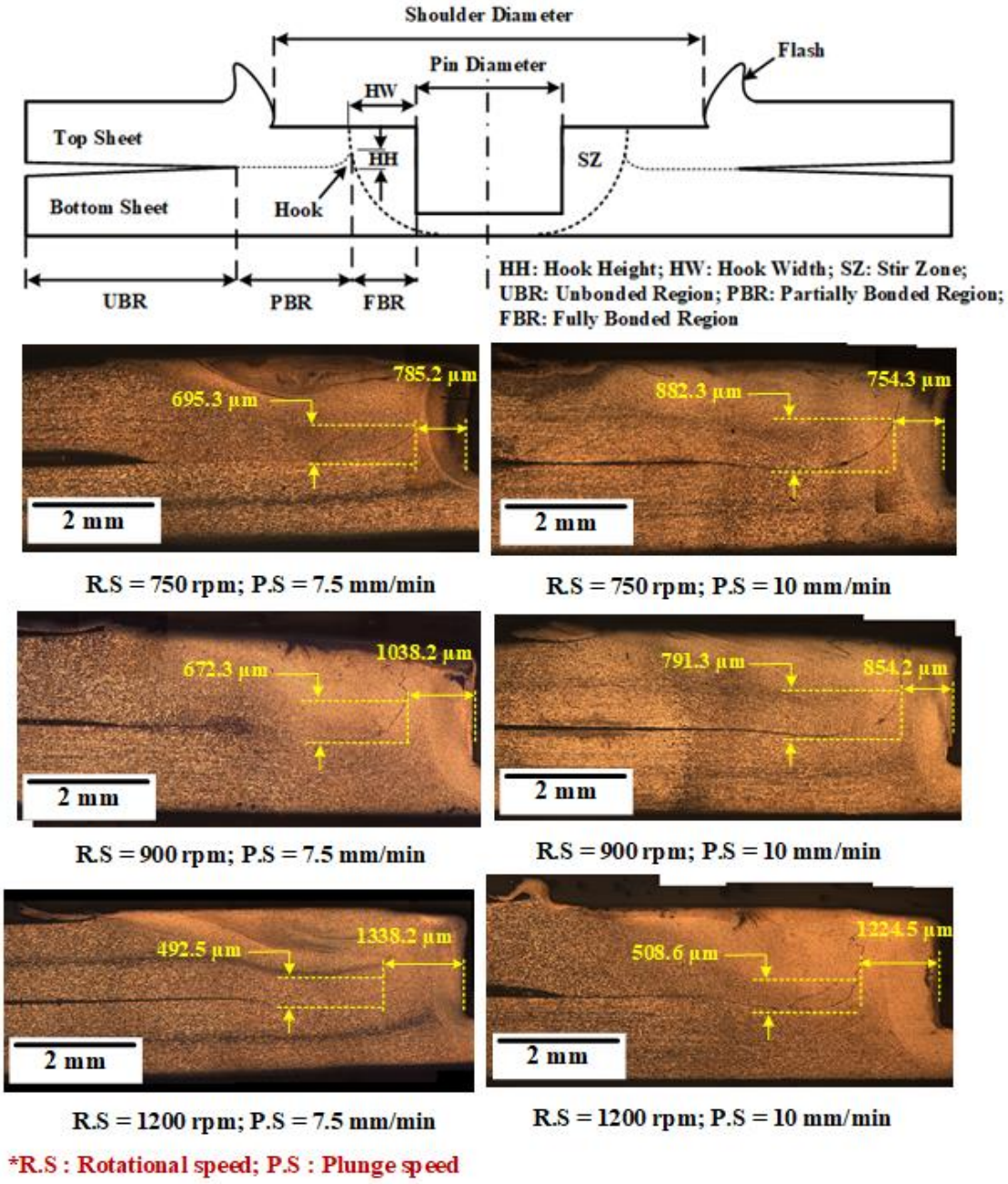

Fig. 5.14: Hook morphology of the welded joints at different welding conditions

To visualize the material flow, the point tracking method is utilized during FE simulation of FSSW. Three points, i.e., point 51, point 53, and point 56 (Fig. 5.13), which are available at the bottom, middle, and top regions of the sheet before the start of the welding are considered. The points are tracked throughout the FSSW operation, and the coordinates of the points are presented in Fig. 5.15. The choice of assuming single block geometry in the welded section helps to understand the material flow behavior during FSSW without any contact instability. From the

results, it is understood that when the rotating tool plunges the upper sheet, the material adjoining to immediately underneath the pin extruded upward (point 56), and it continues until the shoulder contacts the upper surface of the work-piece. Further stirring pushes the material on the upper sheet (point 56) downward and mixes with the middle layer material (point 53). At the same time, the bottom sheet material (point 51) is stirred and lifted upward. The material mixing is more intensive at higher rotational speed, as depicted in Fig. 5.15. Yang et al. (2010) traced the material flow during FSS welding of AZ31 Mg alloy sheets and reported a similar phenomenon for the cause of material mixing during FSSW. The effect of plunge speed on the material mixing during FSSW process is also illustrated in Fig. 5.15. Larger processing time at lower plunge speed helps in uniform mixing of the material. The increase in plasticization of the material at high temperature expands the bonding region width, as visible in Fig. 5.14, which leads to the increase in the welding joint strength.

The hardness variation across FSSW at the mid-thickness of the top sheet and bottom sheet is measured (Fig. 5.16). The hardness in the periphery of the pinhole is maximum because of the finer grains in SZ (Fig. 5.13). On the other hand, the hardness across the periphery of the shoulder is lower on the top sheet. A slight decrement in hardness is also visible below the shoulder region in the bottom sheet. The localized decrement in the hardness is because of the softening of the material due to metallurgical recovery after the thermal cycle (Rana et al., 2018). The intensive stirring of the material at the higher rotational speed leads to dynamic recrystallization, and it results in an increase in hardness. Huskins et al. (2010) reported that apart from grain boundary strengthening, precipitation hardening and increase in dislocation density at the higher rotational speed increase the hardness of AA 5XXX alloys during FSW process. Though the material mixing is uniform at lower plunge speed (Fig. 5.15), its effect is less significant in hardness variation.

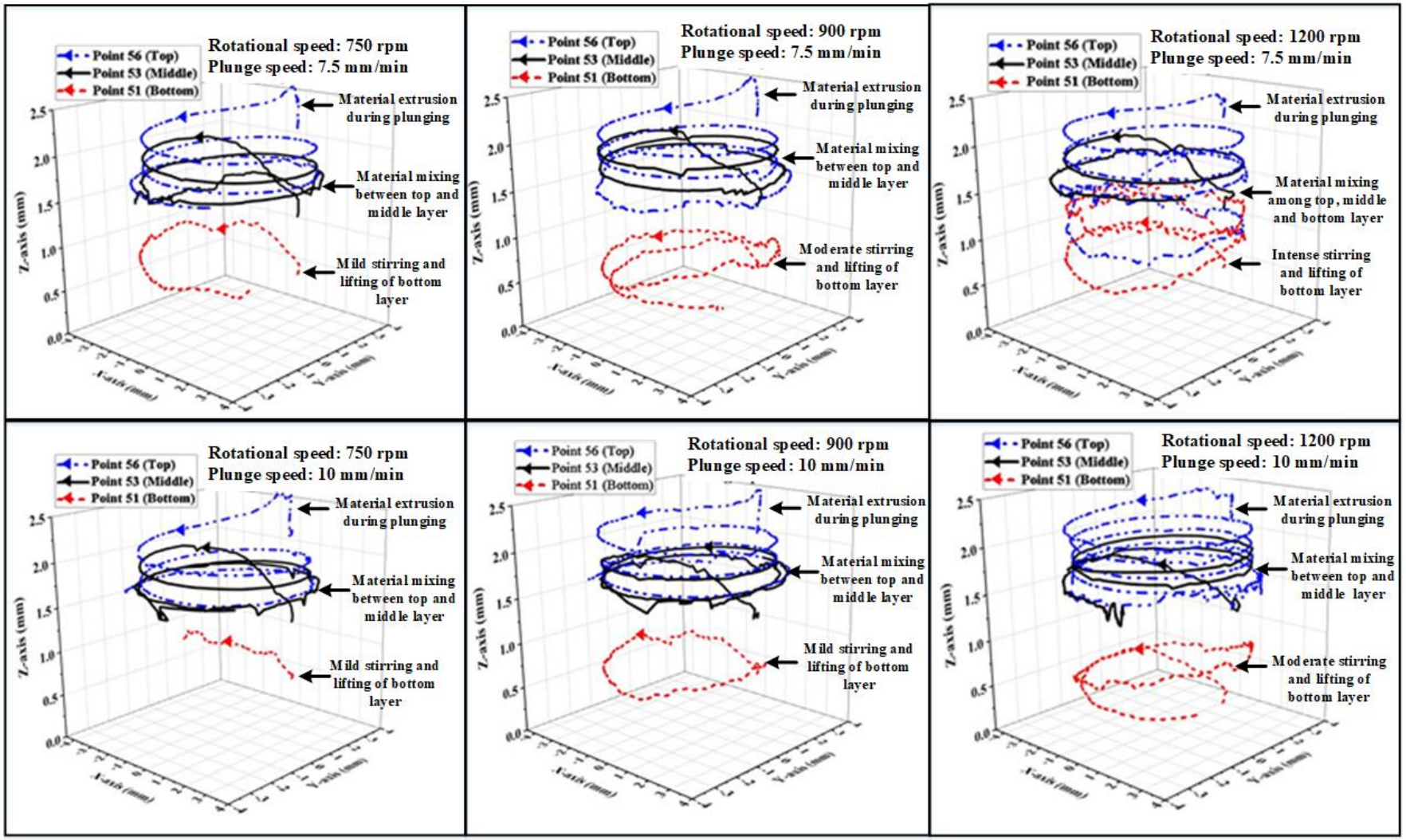

Fig. 5.15: Material flow visualization at different FSSW cases

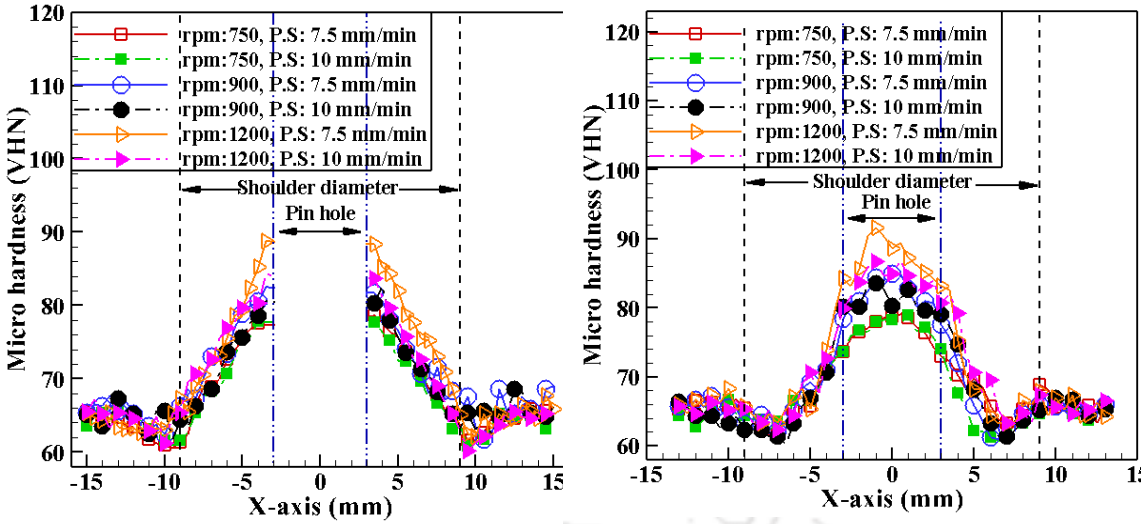

*rpm: Rotation per minute; P.S: Plunge speed

Fig. 5.16: Hardness distribution at the mid thickness of (a) top sheet (b) bottom sheet

5.3.3 Deformation profile prediction

The sheets with FS spot welds are deformed at high strain rate until fracture in a shock tube and the same phenomenon has been modelled using FE simulation. All the FSSW sheets are deformed at a striker velocity of 68.55 m/s, and the final height of deformation is defined as the stopping control for the simulation. The final height is the height observed in shock tube-based forming experiments. The deformation profiles predicted by MJC model in combination with the Freudenthal damage model are compared with the experiment, and a good correlation is observed (Fig. 5.17). The final height of deformation is strongly dependent on the weld strength. Larger hook width and increase in hardness in the welded joint clearly indicate the rise in welding strength (Badarinarayan et al., 2009; Rana et al., 2018). Its effect can be directly related to the final height of deformation. FSSW sheet made at 900 rpm has lower height of deformation than 750 rpm case. In both the cases, failure starts from the welded region. On the other hand, in 1200 rpm, the sheet fails outside the welded region, in the base material. The detailed failure behavior of the welded sheets is described in Section 5.3.5.

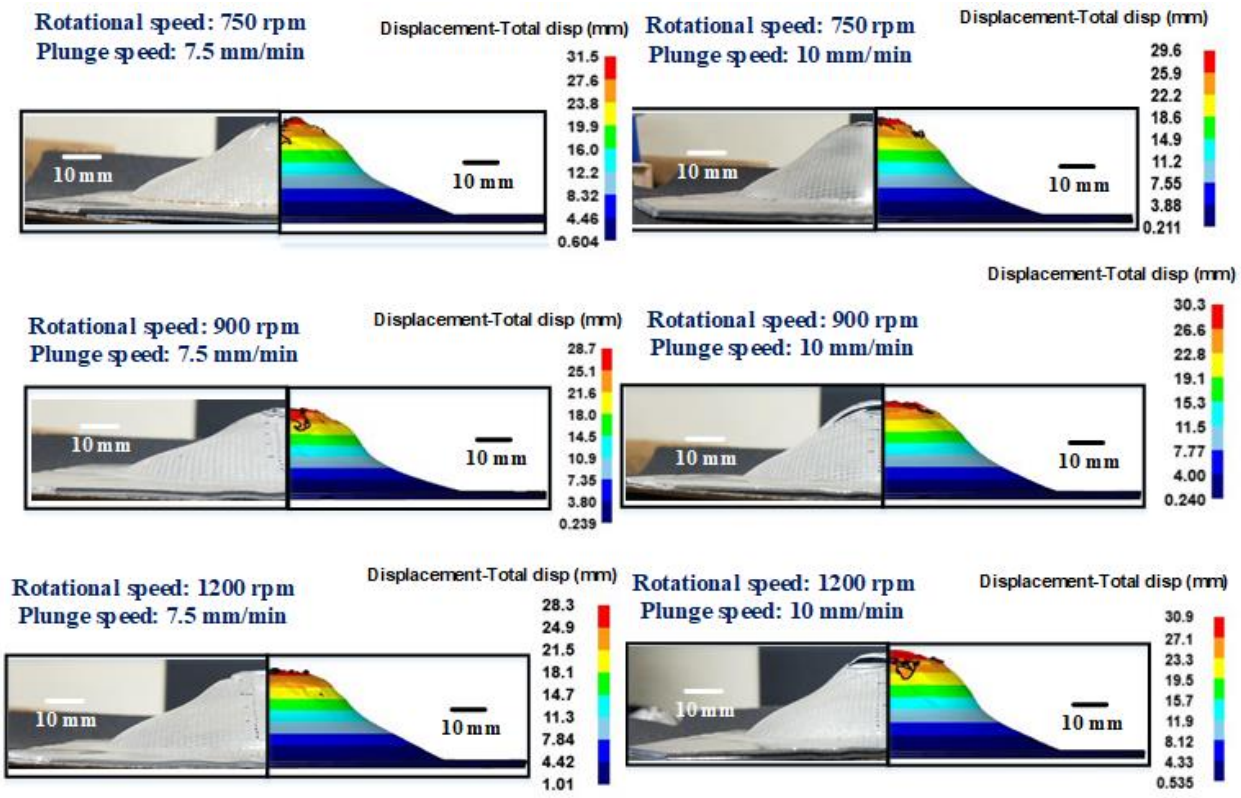

Fig. 5.17: Prediction of the deformation profile of the FSSW sheet

5.3.4 Prediction of necking height

During high-velocity forming in the shock tube, it is difficult to capture the necking phenomenon experimentally. Thus, the dome height at necking is predicted from FE simulation. Circular grid flow pattern is generated on the surface of the sheet before the start of the forming simulation (Fig. 5.9a). When the damage value reaches the critical limit, necking initiates. The dome height at the onset of necking is obtained from FE simulation and elucidated in Fig. 5.18. For all the welded sheets, necking initiates from the pinhole. However, the welding strength significantly affects the dome height at necking. FSSW sheet made at 1200 rpm starts necking at larger height than 750 rpm and 900 rpm weld cases. However, the effect of plunge speed on the height at necking is insignificant.

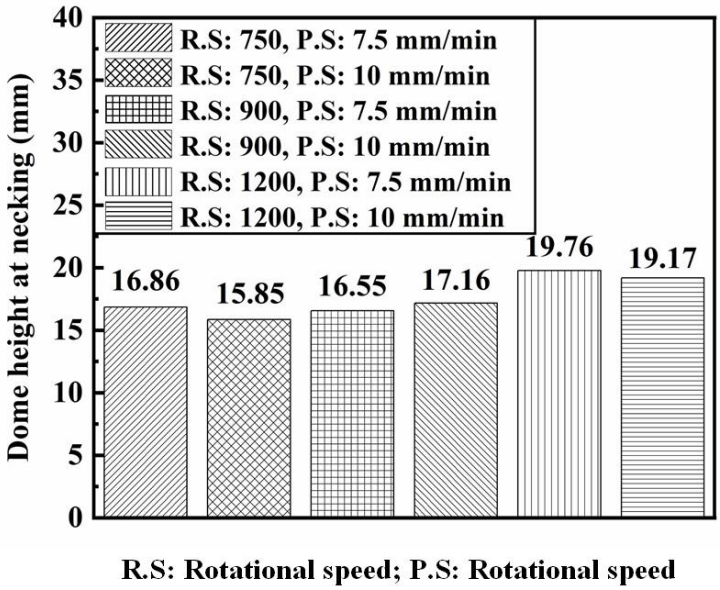

Fig. 5.18: Prediction of dome height at necking of sheets with FSSW

5.3.5 Effective Strain distribution and failure pattern

During forming experiments, all the FSSW sheets fail after deformation. However, the changes in crack pattern, crack propagation length, and height of deformation directly depend on the weld strength. The predicted crack pattern developed on the welded sheets after reaching the final height of deformation matches quite well with the experimental data (Fig. 5.19). The results elucidate that the necking initiates from the pinhole. However, the increase in weld strength at 1200 rpm restricts the further propagation of the crack, and the sheets fail from the base material (Fig. 5.19). For the other two rotational speeds, 750 rpm and 900 rpm, the crack initiates and propagates from the pinhole. The variation in tool plunge speed does not affect the crack pattern on the FSSW sheets significantly (Fig. 5.19). However, lower crack propagation length (confirmed by visual inspection in Fig. 5.19) and dome height (Fig. 5.17) of the FSSW sheets generated at lower plunge speed directly signifies the increase in weld strength.

Effective strain distribution predicted during FE simulation are also compared with the experimental results, and an acceptable correlation has been observed (Fig. 5.20). The effective strain developed on the welded sheets during forming confirms the uniform stretching of the material. The inertial effect developed during this dynamic forming environment restricts the strain localization in the material, which helps to increase in formability of the deformed sheet (Ahmed et al., 2017). The results ensure the better predictability of the Freudenthal damage model in combination with the MJC model for all the welded sheets.

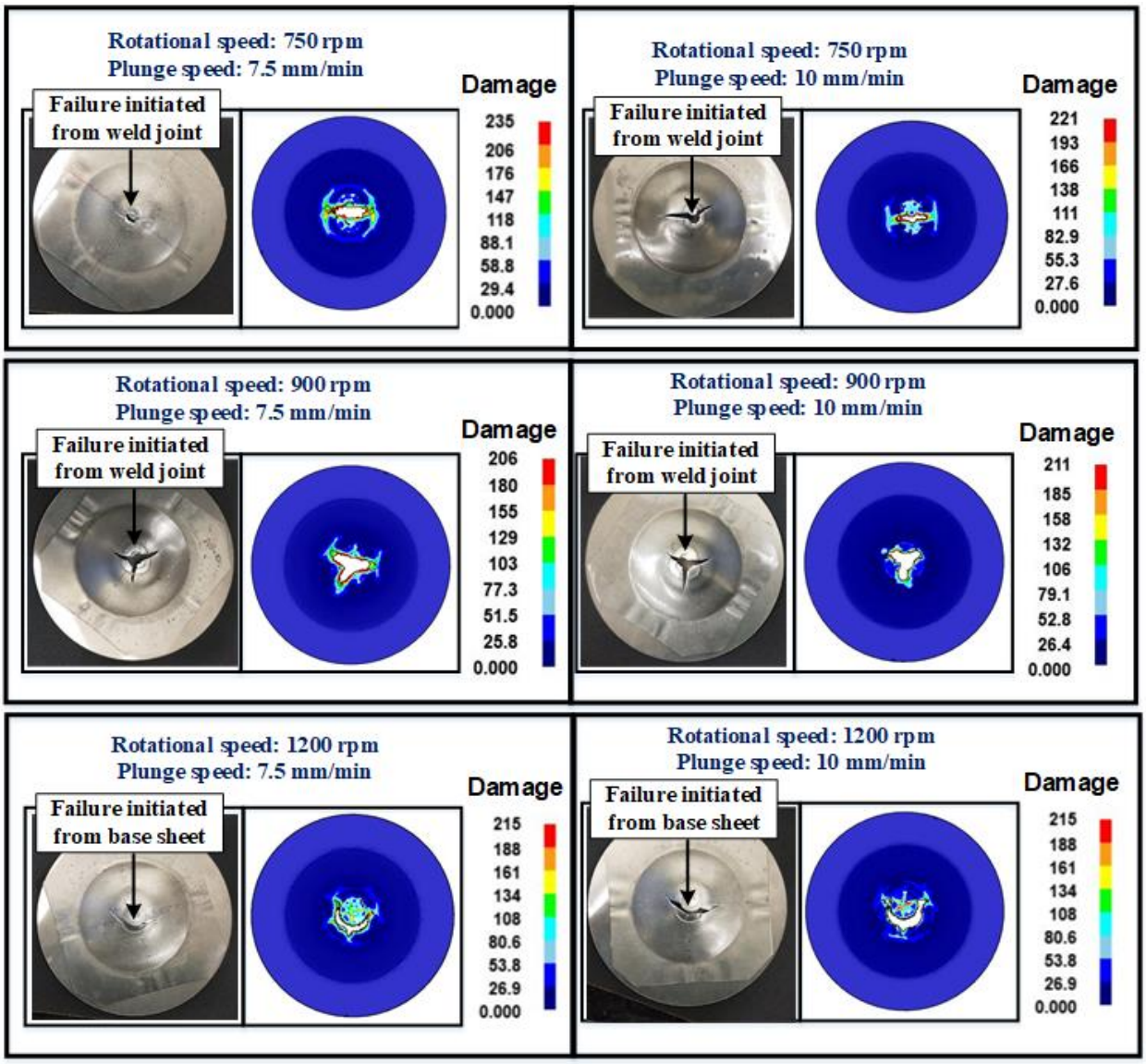

Fig. 5.19: Failure pattern prediction and comparison with experimental observation

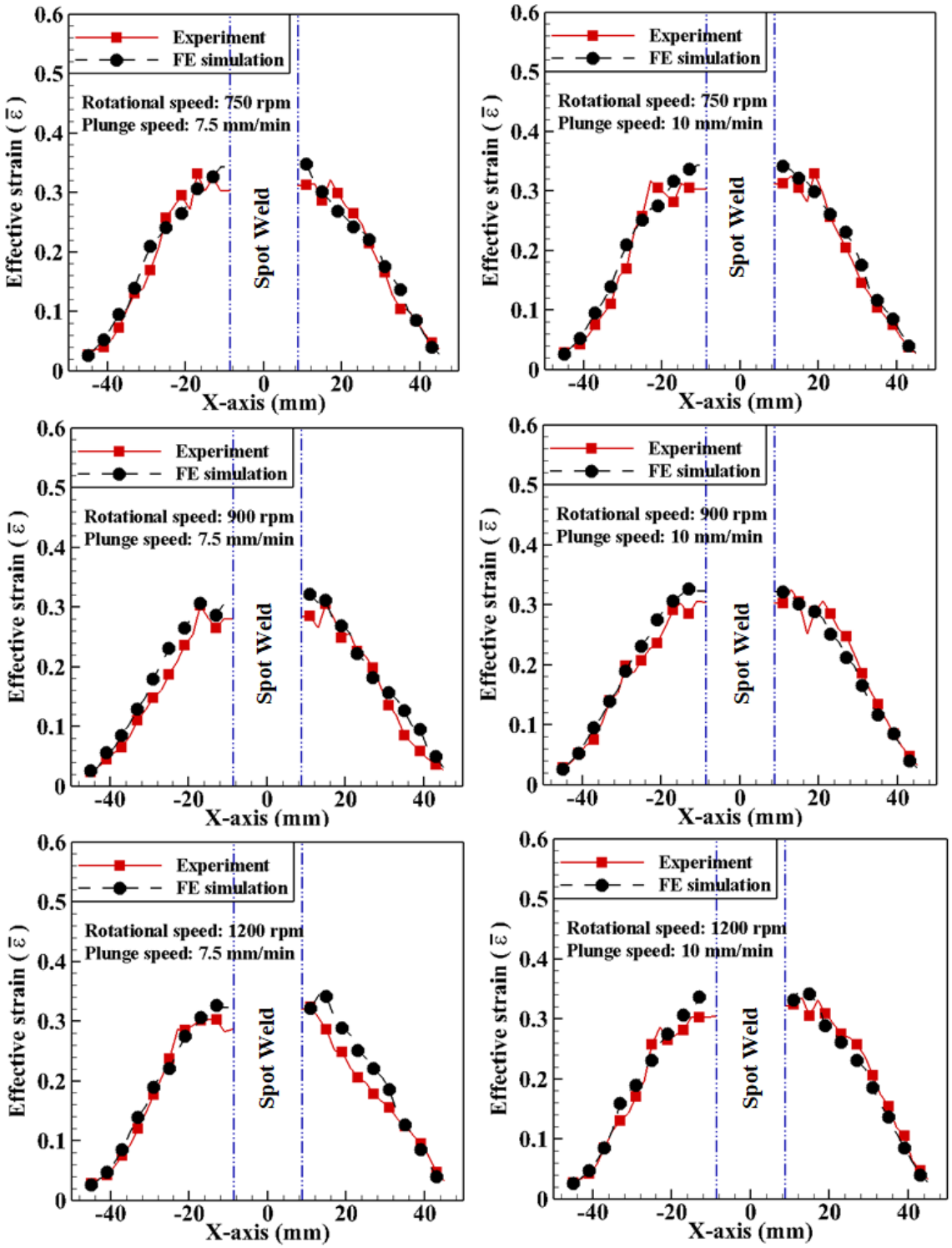

Fig. 5.20: Comparison of predicted effective strain with experimental data for FSSW sheets

5.4 Summary

The present work aims to understand the formability of AA 5052-H32 sheets with friction stir spot welds at high strain rates using a shock tube. Effect of tool rotational speed and plunge speed on the FSSW outputs and forming outputs are evaluated. Numerical

simulations of FSSW and forming with FSS welds are carried out at experimental conditions using DEFORM-3D to understand the rate-dependent formability. The following conclusions are drawn from the results.

I. A two-stage manufacturing process constituting FSSW of sheet as first stage and impact forming as second stage has been implemented at lab scale, and the same has been predicted by FE simulations. The overall results are encouraging. Through this work, a validated experimental-modelling strategy has been presented to design the two-stage manufacturing process.

II. During FE simulation of impact forming, the rate-dependent flow stress-strain data for the unwelded section of the FSSW sheet are identified from the tensile test of the sheet deformed by shock tube, and for the spot weld region, a hardness multiplying factor is identified for the purpose. The approaches are simple to implement in laboratory and sufficiently accurate in predicting the formability of sheets with spot welds.

III. The temperature evolution during FSSW clearly signifies that the temperature rise is directly proportional to the tool rotational speed. However, the rate of temperature rise with the increase in plunge speed is insignificant.

IV. The material flow visualization during FSSW elucidates the intensive material mixing phenomenon at higher rotational speed. Furthermore, larger processing time at lower plunge speed promotes more uniform plastic deformation that leads to an increase in bonding width.

V. Larger weld strength at higher rotational speed delays the necking phenomenon during forming of FSSW sheet. It results in larger dome height at necking. Though necking initiates from the pinhole for all the weld cases, increase in strength at 1200 rpm restricts further crack propagation, and the sheet fails from the base material. Same phenomenon is also captured during FE simulation. The variation of tool plunge speed has insignificant effect on the dome height and the failure pattern.

VI. FSSW joint morphology confirms that the hook width increases significantly with the increase in the tool rotational speed. However, the hook height shows an inverse relation with the rotational speed. At the same time, lower plunge speed results in larger hook width and smaller hook height because of larger heat generation and plastic deformation

VII. Deformation profile, failure pattern, and effective strain distribution predicted by MJC flow stress model in combination with Freudenthal damage model has a fair agreement with the experimental results.

Chapter 6

Forming response of 1.5 mm thick sheets with friction stir spot weld

Overview

In this present study, both the experimental and numerical investigations are carried out to understand the formability of AA 5052-H32 sheets of 1.5 mm thickness with friction stir spot weld (FSSW). A shock tube experimental facility is utilized in which a rigid hemispherical striker is propelled at a high velocity and deforms the FSSW sheets at high strain rates. In this analysis, the effect of different tool rotational speed and plunge depth on the FS spot welding outputs and forming outputs are understood. Furthermore, DEFORM-3D FE code is used to perform FE simulation of both the FS spot welding and forming of the welded sheets interactively. During the forming analysis, a new strategy is followed to identify the rate-dependent mechanical properties that are incorporated during FE simulation. The tensile data obtained from the unwelded section of the sheet deformed using the shock tube is fit to modified Johnson-Cook (MJC) model. In the case of the FS spot welded region, a hardness based multiplying factor is identified and used to obtain stress-strain data by fitting to MJC model. The predicted temperature evolution during the FSSW is validated with the experimental data and a good correlation has been observed. The predicted material flow phenomenon gives an insight about the joint formation during FSSW. Various forming outputs such as deformation profile, crack pattern and effective strain distribution predicted by MJC model in combination with Freudenthal damage model is compared with the experimental data and the results have a fair agreement.

6.1 FE modelling of FSSW and dynamic forming

6.1.1 FE formulation

As described earlier in Section 5.2, the complete FSSW process (plunging + dwelling) is simulated in two stages, and in the third stage, the welded sheet is further redirected for high-velocity shock tube based forming using the multi-operation (MO) layout in DEFORM-3D FE code (Fig. 6.1). Further details about the FE formulation used in DEFORM-3D is highlighted in the previous Section 2.4.1. The effective auto-remeshing technique used in DEFORM-3D helps to simulate the FSSW operation quite efficiently.

The material undergoes severe plastic deformation during both the welding and forming process. Thus, the work-piece is modelled as a deformable plastic object. On the other hand, the FSSW tool used during welding, and the end flanges along with the striker used during impact forming are defined as a rigid body due to negligible wear (Fig. 6.1). During this present analysis, sparse solver + direct method is used to simulate both the FSSW and impact forming process.

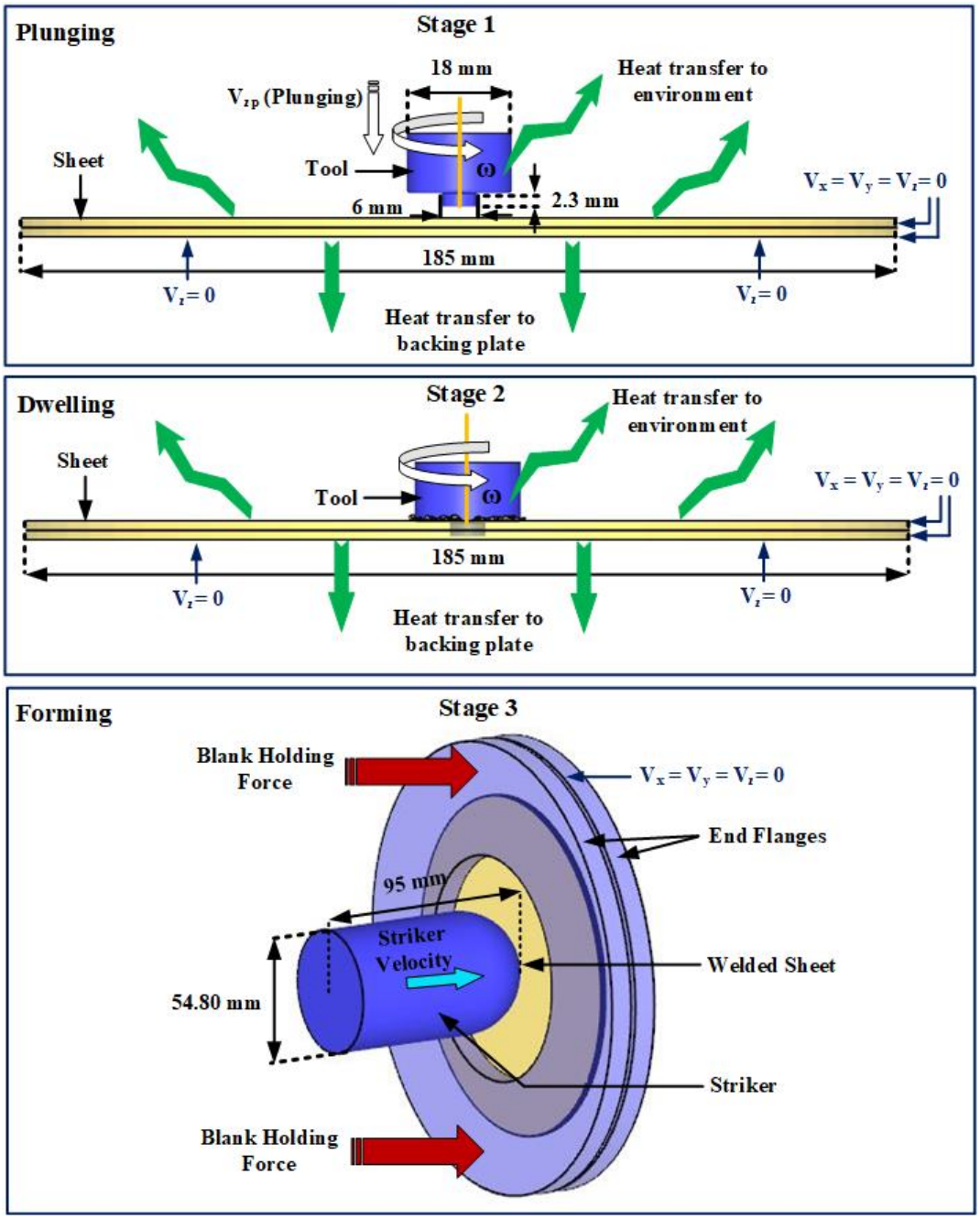

Fig. 6.1: Steps followed to perform FE simulation of impact forming of FSSW sheets

6.1.2 FSSW simulation details

6.1.2.1 Geometrical features and welding parameter details

During this analysis, two sheets are modelled as a unique simulation object, in which the welded region (the region below the tool shoulder) at the center of the two sheets is designed as a single block model (Fig. 6.2). The choice becomes advantageous over numerical instabilities observed while defining the contact condition at the interface of sheets. The rigid tool has a flat shoulder of 18 mm diameter, and it has a straight cylindrical pin of 6 mm diameter and 2.3 mm height. The diameter of the welded section, regarded as a continuum model is 18 mm, which is same as the tool shoulder diameter. The thickness of both the upper and lower sheets are 1.5 mm and a small gap is provided in the unwelded section (Fig. 6.2).

To understand the effect of different welding parameters, specifically tool rotational speed and plunge depth, on the formability, FE simulations are carried out for three different tool rotational speeds viz., 750 rpm, 900 rpm, and 1200 rpm for two different plunge depths, 2.5 mm and 2.8 mm. The plunge speed of the tool is kept constant as 10 mm/min. The dwell time is kept constant as 5 seconds to attain good quality spot weld (Zhang et al., 2011).

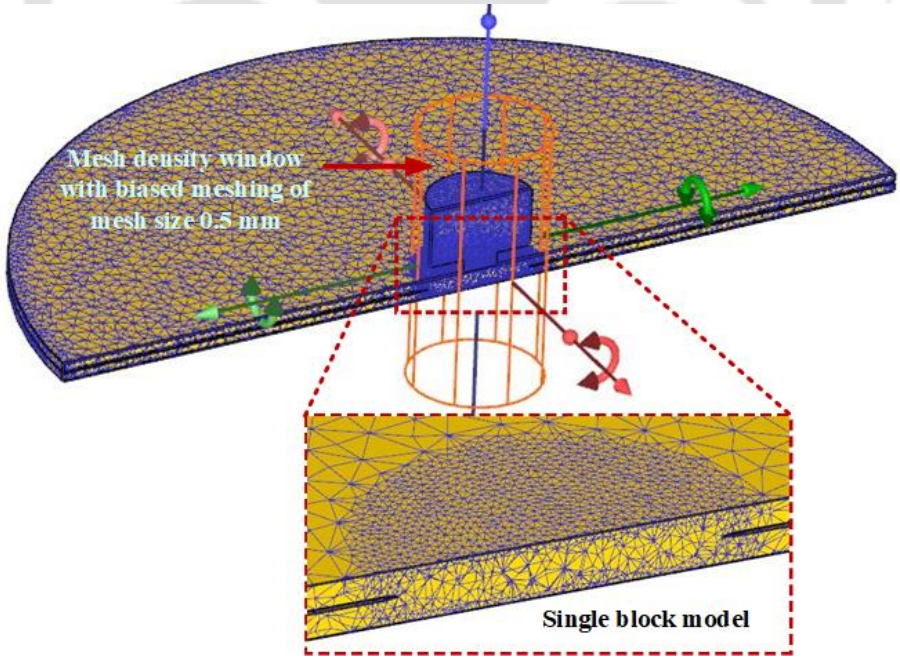

Fig. 6.2: Numerical model utilized for FE simulation of FSSW process

6.1.2.2 Material constitutive model

During FSSW, the material undergoes severe plastic deformation at high temperature. Thus, in the present study, the temperature dependent plastic properties of AA5052-H32 sheet of 1.5 mm thickness are incorporated during FE simulation. The high-temperature tensile tests are performed at elevated temperature range of 20°C to 425°C in universal testing machine (UTM) at a cross-head speed of 1 mm/min. The tensile test data are fit to Hollomon flow stress model, $\sigma = K\varepsilon^n$, and the material constants, *K* and *n*, are identified (Table 6.1). Here, *K* is the strength coefficient, and *n* is the strain-hardening exponent. The material constants are further utilized to identify the flow stress (σ) for larger strain (ε) as depicted in Fig. 6.3, and incorporated in tabulated form during FE simulation. Other material properties such as yield strength, tensile strength, elongation are also evaluated as per established procedures (Table 6.1). The other temperature dependent mechanical and thermal properties for AA 5052-H32 sheet and H13 tool (Fig. 6.4) are obtained from literature (Bajpei et al., 2016; Fluhrer, 2007) and provided as input to FE simulation to predict accurate results. The anisotropic characteristic of the material during plastic deformation is expressed by Hill's 1948 yield criterion as mentioned earlier in Section 2.4.1.

Table 6.1: Hollomon model material constants for AA5052-H32 base sheet

Temperature (°C)	σ_{ys} **(MPa)**	σ_u **(MPa)**	***n***	***K*** **(MPa)**	ε_u **(%)**	ε_u **(%)**
20	167.85	255.91	0.173	404.65	8.4	10.3
125	161.19	248.04	0.195	375.09	10.6	12.8
240	158.30	222.85	0.186	296.93	8.7	11.6
360	152.05	191.81	0.093	253.51	7.3	12.6
425	150.37	178.04	0.048	218.61	3.9	12.7
σ_{ys}: Yield strength; σ_u: Ultimate tensile strength; *n*: Strain hardening coefficient; *K*: Strength coefficient; ε_u: Uniform elongation; ε_t: Uniform elongation; Gauge length: 50 mm						

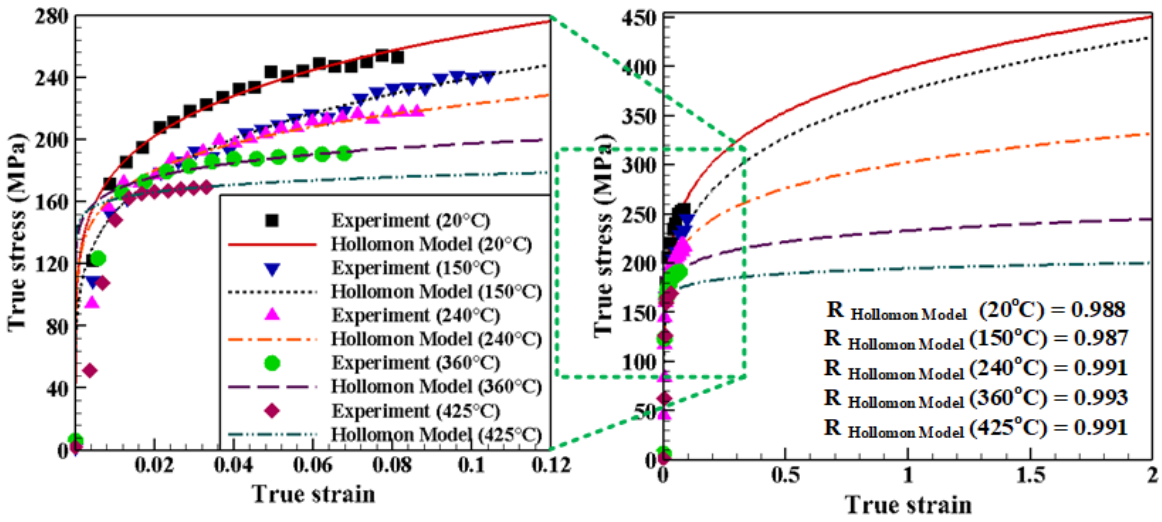

Fig. 6.3: True stress-strain curve of AA 5052-H32 sheet at different elevated temperatures

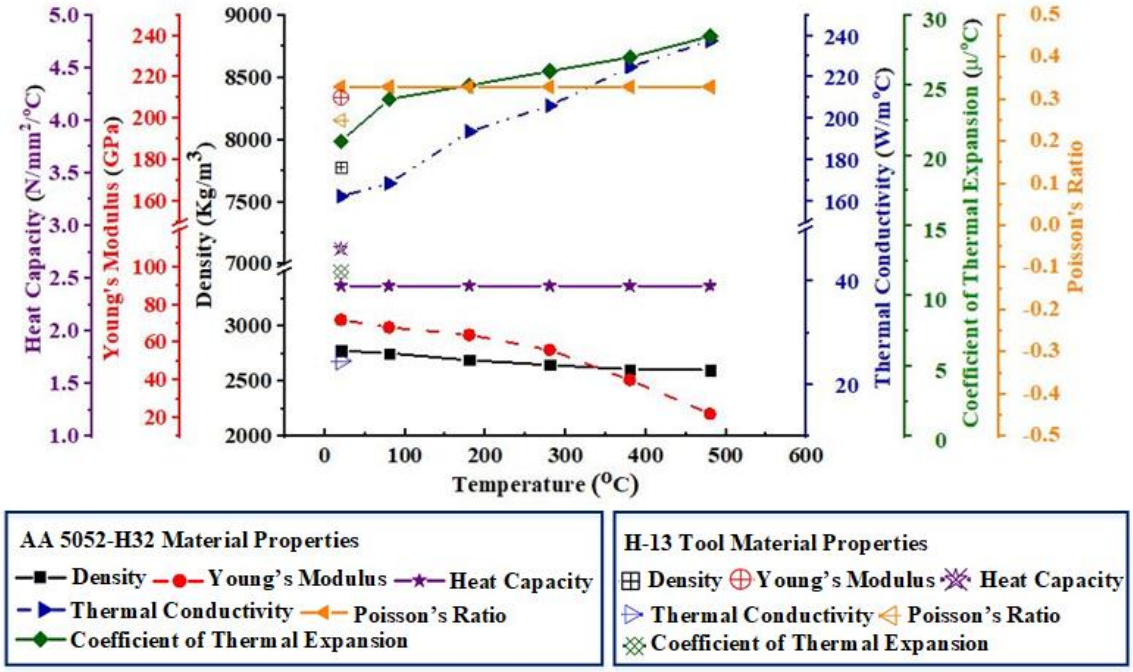

Fig. 6.4: Temperature dependent material properties of AA5052-H32 sheet and H13 tool incorporated during FE simulation.

6.1.2.3 Friction model and boundary conditions

In the present work, sticking friction model (eq. 5.3) as described earlier has been used to define the contact conditions at the interaction region between the tool and the sheet. It is observed that sticking frictional condition is adequate while modelling bulk forming processes and it is mostly preferred to simulate the severe deformation in FSW process (Buffa et al.,2006). The shear factor (m) is decided by calibration, in which the peak

temperature obtained after plunging and dwelling for different shear factors are compared to experimental data from the present work at a 10 mm offset distance from the shoulder edge for 750 rpm tool rotational speed and 2.5 mm plunge depth (Table 6.2). The temperature predicted for m = 0.4 matches quite well with the experimental data, and the same value has been considered as a constant for other cases of FE simulation of FSSW.

Table 6.2: Peak temperature predicted by FE simulation for different shear factors (m) and comparison with experiment

		Peak temperature after plunging (°C)	Percentage error (%)	Peak temperature after dwelling (°C)	Percentage error (%)
Experimental data from present work		201.85	--	239.83	--
FE simulation	m = 0.3	160.63	20.31	214.68	10.48
	m = 0.4	216.81	7.41	255.51	6.53
	m = 0.5	233.93	15.91	275.34	14.80

During FE simulation of FSSW, in order to provide rigid motion to the work piece, the side faces of the work-piece are constrained along three directions, i.e., $V_x = V_y = V_z = 0$, as illustrated in Fig. 6.1. Backing plate is not considered in this analysis to improve computational efficiency, and instead of that the downward movement of the work-piece is restricted by defining $V_z = 0$ at the bottom face of the work piece. The tool is defined with rotational speed and plunge speed in every stages of FSSW. Heat transfer due to convection and radiation from the free surface of sheet and the tool are described in Section 5.2.1.3. Here, the backing plate is replaced by a local heat exchange window to define the heat transfer between the bottom face of the work piece and the environment with convection coefficient (h_b) as 500 W/m^2°C (Fluhrer, 2007). Furthermore, heat exchange windows are also defined for both the tool and other faces of the work piece to demonstrate heat transfer with the environment. The convective heat transfer coefficient (h_a) is kept as 20 W/m^2°C (Buffa et al., 2006) and the emissivity for AA 5052-H32 sheet and H13 tool is considered as 0.03 and 0.7 respectively (Fluhrer, 2007). The heat transfer at the interaction region between the tool and the work piece is higher than the work piece and environment. Thus,

the convection coefficient (h_b) between the tool and the work piece is defined as 11000 W/m^2°C (Buffa et al.,2006).

6.1.2.4 Mesh sensitive analysis

The work-piece and the tool are meshed with tetrahedral elements. Mesh density window is used to define finer mesh at the tool-work piece interaction zone (Fig. 6.2). It significantly improves the computational efficiency of the FE simulation without affecting the final results. The finer element size inside the mesh density window is confirmed after mesh sensitive analysis. Various mesh element sizes such as 1 mm, 0.75 mm, 0.5 mm, and 0.3 mm are defined inside the mesh density window to perform mesh sensitive analysis, whereas rest of the work piece domain is meshed with 1 mm element size and size ratio is kept as 2. The temperature evolution at a distance of 10 mm from the tool shoulder edge on the top sheet is validated with the experimental data of FSSW with 750 rpm tool rotational speed and 2.5 mm plunge depth (Fig. 6.5). The shear friction factor m = 0.4 is considered as a constant during this analysis. The temperature evolution predicted by element sizes, 1 mm and 0.75 mm, have poor agreement with the experimental result (Fig. 6.5). However, the results predicted by element sizes, 0.5 mm and 0.3 mm, have a fair agreement with experimental data. The average computational time required in case of 0.5 mm element size is 2665 minutes, whereas 0.3 mm element size needs 3864 minutes of computational time, which is significantly high. Thus, 0.5 mm element size is defined inside the mesh density window for all the cases of FE simulations of FSSW. The tool is meshed with minimum element size of 0.25 mm with size ratio 4, which generates total 42224 number of elements. The adaptive re-meshing technique in DEFORM-3D helps to avoid mesh distortion that generates because of large plastic deformation during FSSW simulation. The maximum interference depth (the depth, an element edge of the work piece crosses the surface of the tool) of 0.3 mm is defined in the re-meshing criteria window. When it triggers, re-meshing starts in the work-piece and a new mesh is generated. The solution information from the old mesh is interpolated into the new mesh and the simulation continues further.

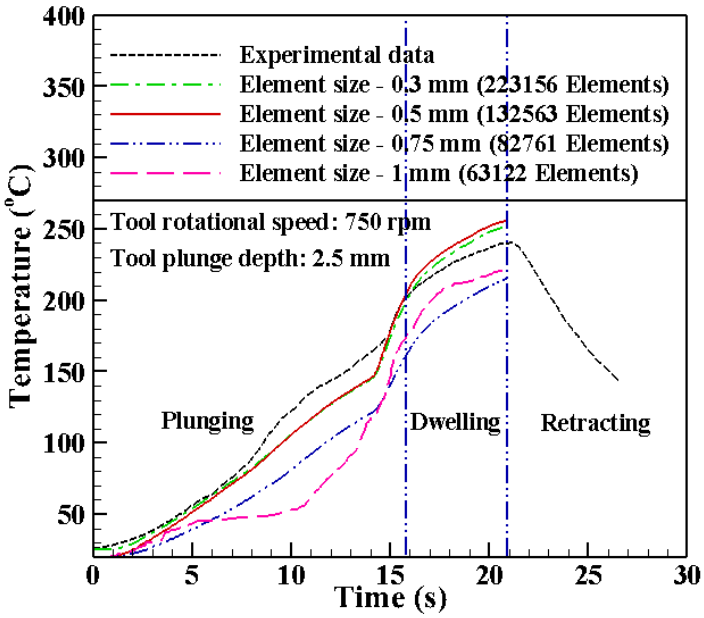

Fig. 6.5: Mesh sensitivity analysis during temperature prediction and comparison with the experimental data

6.1.3 FE simulation of impact forming of FSSW sheet by shock tube

6.1.3.1 Identification of flow stress model material properties

In this current work, a shock tube facility is utilized to deform the FSSW sheet at high strain rates. The details about the shock tube facility is described earlier in Section 3.1.1. During FE simulation, the multi operation layout in DEFORM-3D helps to retrieve all the FSSW welding properties at the start of the forming operation by establishing an interactive set up. The dynamic forming environment created during the shock tube experiment helps to deform the sheet at high strain rate under room temperature condition. Thus, it is mandatory to define the rate-dependent mechanical properties of the material during the forming analysis. Furthermore, the rate-dependent mechanical properties of both the FS spot weld and unwelded section cannot be same. Therefore, the single block FSSW work-piece model is divided in to two regions as illustrated in Fig. 6.6 and the mechanical properties are assigned to the respective domains.

The new strategy followed to obtain the rate-dependent material properties for both FS spot weld and unwelded section of the sheet are discussed earlier in Section 5.2.2.1. After shock tube forming experiment, a tensile sample is cut from the deformed unwelded section of the FSSW sheet closer to the fracture (Fig. 6.6), and the tensile sample is tested in UTM at a cross-head speed of 1 mm/min without any post treatment. The tensile test data are fit to Modified Johnson-Cook (MJC) model (eq. 3.4) as illustrated in Fig. 6.7, and the rate-

dependent material constants for the unwelded section are identified (Table 6.3). On the other hand, the rate-dependent properties for FS spot weld are correlated to the hardness variation in the weld spot after deformation. A hardness multiplying factor is identified, which is the ratio of average hardness of the welded joint after deformation to the average hardness of the base material and that factor is multiplied to the true stress of the base material (Fig. 6.7). The newly obtained true stress-strain data are again fit to MJC model (eq. 3.4) and the rate-dependent material constants for the FS spot weld are identified (Table 6.3). During curve fitting, it is mandatory to know the magnitude of $\dot{\bar{\varepsilon}}$, and during shock tube experiments, identification of strain rate ($\dot{\bar{\varepsilon}}$) is complex. Thus, it is identified by FE simulation in the present analyses. The true stress-strain curves obtained from both the FSSW joint and unwelded section are fit to Hollomon model ($\bar{\sigma} = K\bar{\varepsilon}^n$), and the material constants (K and n) are identified. The true stress-strain data obtain from those material constants are incorporated into the FE simulation and the average strain rate of deformation ($\dot{\bar{\varepsilon}}_0$) near the pole region are identified (Table 6.3). It is further used during curve fitting to MJC model. The range of the variation of the material constants for MJC model are obtained from existing literature (Deng et al., 2019; Song et al., 2019) and defined during curve fitting. The material constants are again utilized to extrapolate true stress for larger stain and incorporated during FE simulation in tabular form (Fig. 6.7). The anisotropic characteristic of AA 5052-H32 FSSW sheet during high-velocity forming is defined by Hill's 1948 yield criterion as mention earlier in Section 2.4.1.

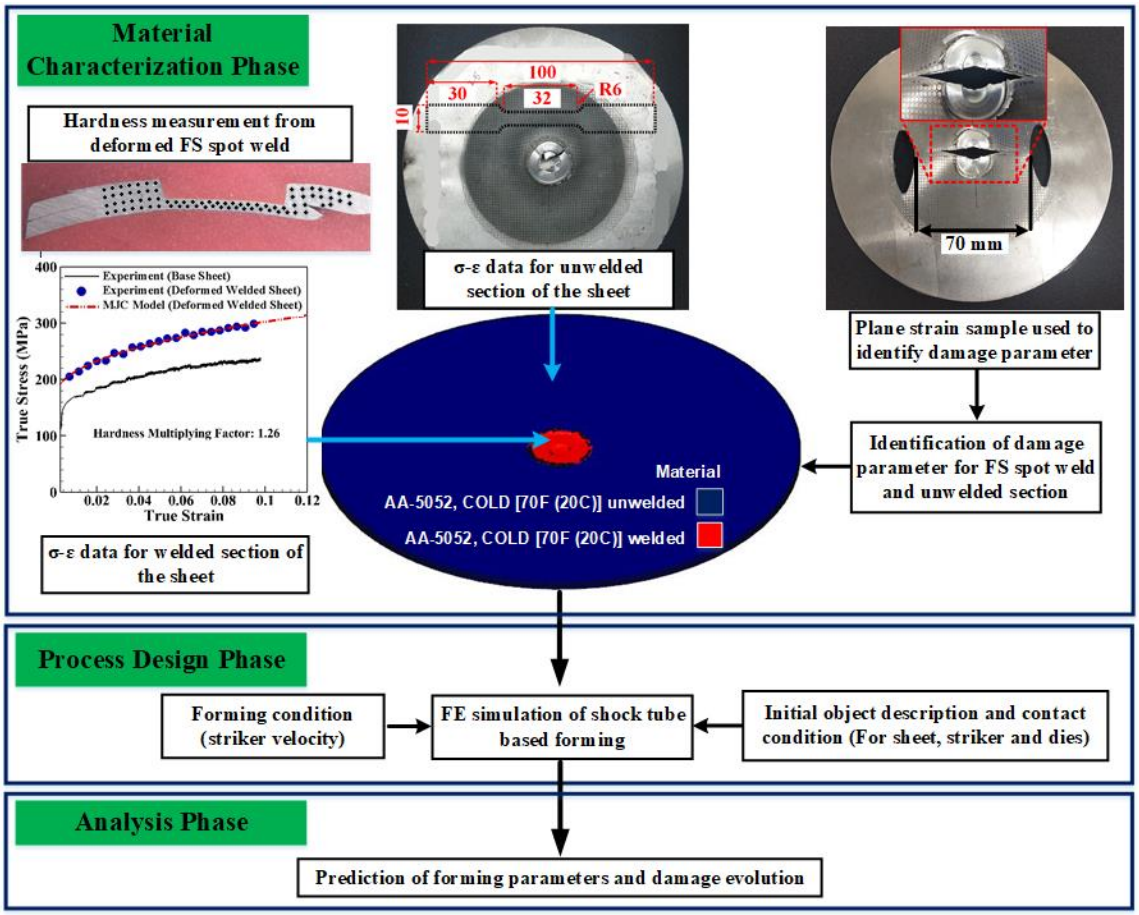

Fig. 6.6: Procedure to identify the rate-dependent mechanical properties for FS spot weld and unwelded section of the FSSW sheet

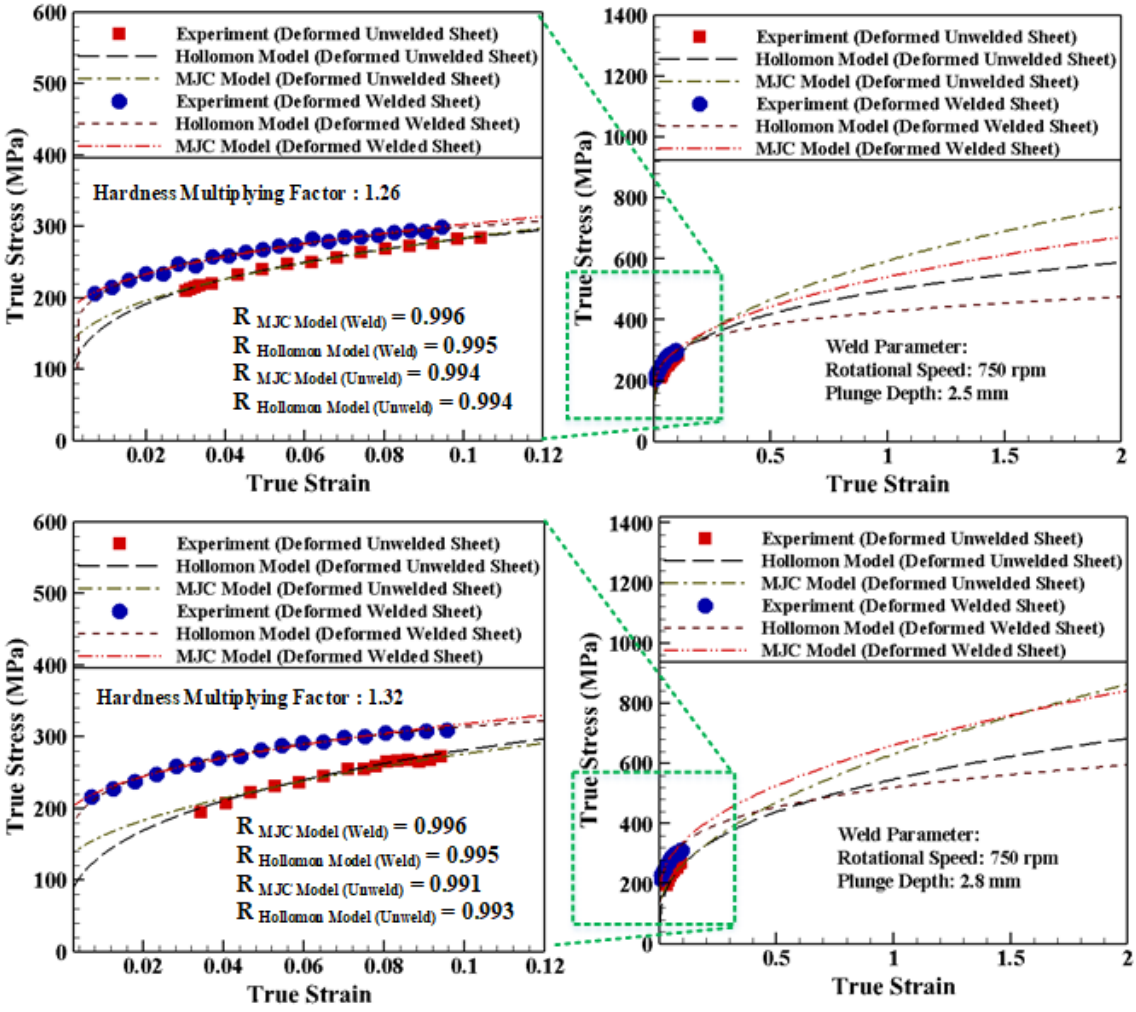

(a)

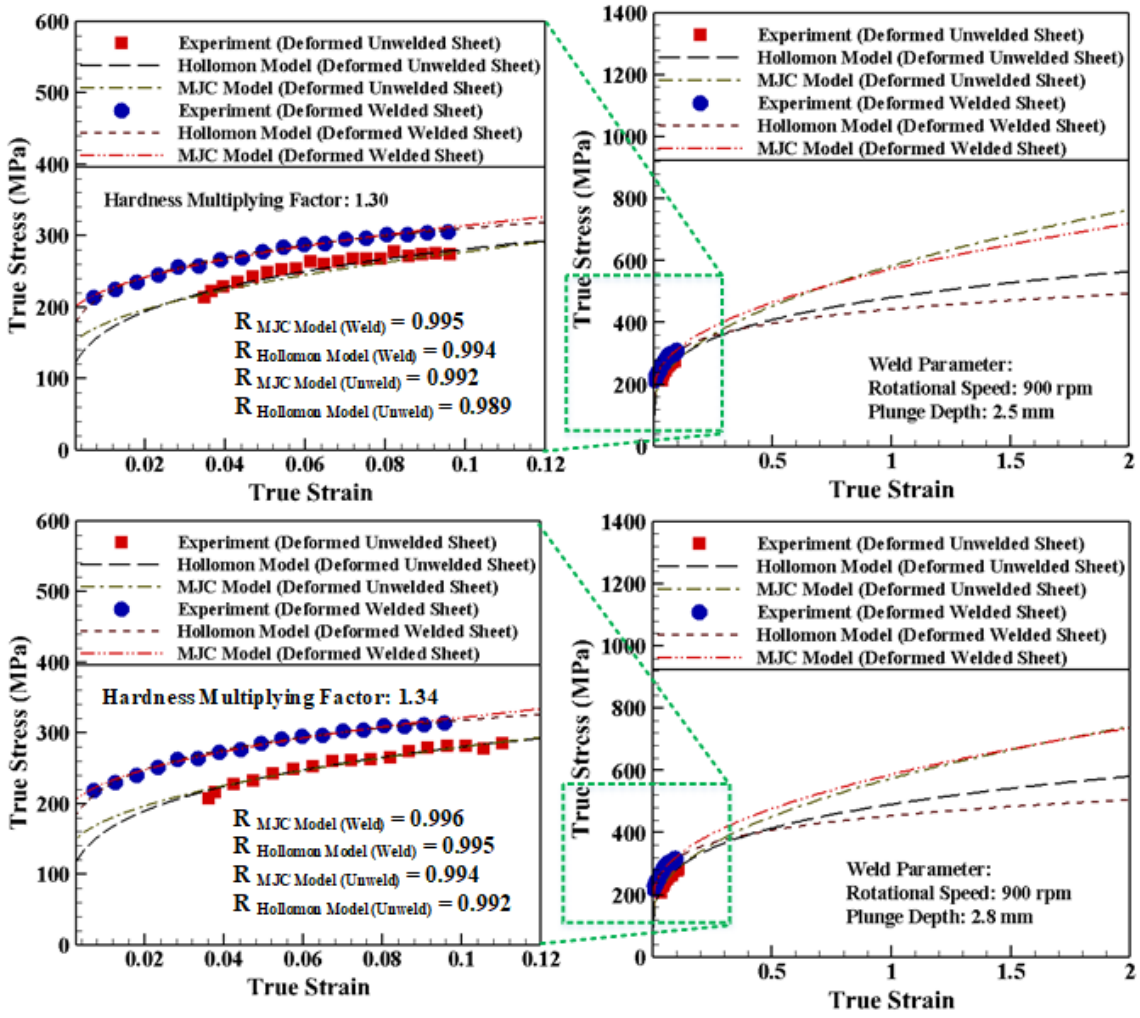

(b)

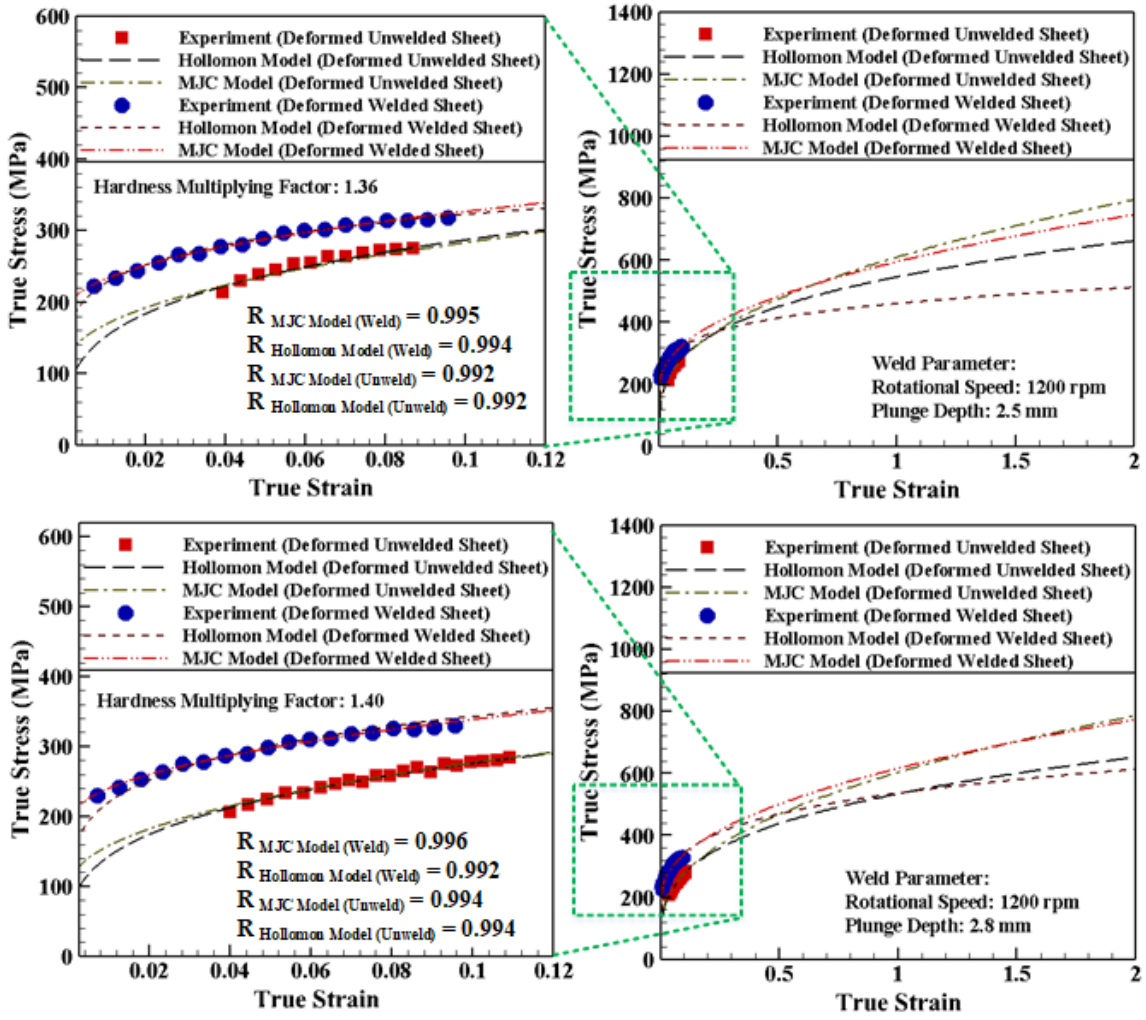

(c)

Fig. 6.7: Rate-dependent stress-strain curves for FS spot weld and unwelded section of the sheets

Table 6.3: Identification of material constants for Hollomon model and MJC model

Hardening Model		Strain rate (s^{-1})	Hardness Multiplying Factor	Hollomon Model		MJC Model				
Material Constants				K (MPa)	n_1	A (MPa)	B (MPa)	n_2	C_1	C_2
FS spot Weld	R.S: 750 rpm P.D: 2.5 mm	2686	1.26	426.32	0.17	142.2	332.4	0.43	- 0.0874	0.0132
	R.S: 750 rpm P.D: 2.8 mm	2651	1.32	447.46	0.17	143.3	331.8	0.45	- 0.0835	0.0143
	R.S: 900 rpm P.D: 2.5 mm	2567	1.30	442.12	0.17	143.2	331.6	0.45	- 0.0865	0.0142
	R.S: 900 rpm P.D: 2.8 mm	2483	1.34	453.45	0.17	140.4	324.7	0.45	- 0.0906	0.0156
	R.S: 1200 rpm P.D: 2.5 mm	2415	1.36	460.18	0.17	143.3	332.9	0.45	- 0.0858	0.0148
	R.S: 1200 rpm P.D: 2.8 mm	2366	1.40	475.81	0.17	144.5	333.6	0.45	- 0.0852	0.0154
Unwelded region	R.S: 750 rpm P.D: 2.5 mm	2686	--	496.08	0.24	135.7	576.9	0.45	- 0.0918	0.0089
	R.S: 750 rpm P.D: 2.8 mm	2651	--	546.92	0.32	137.2	667.9	0.53	- 0.0995	0.0091
	R.S: 900 rpm P.D: 2.5 mm	2567	--	480.03	0.23	137.6	497.5	0.48	- 0.0914	0.0103
	R.S: 900 rpm P.D: 2.8 mm	2483	--	490.27	0.24	137.6	532.2	0.45	- 0.0915	0.0093
	R.S: 1200 rpm P.D: 2.5 mm	2415	--	545.79	0.27	138	668.6	0.46	- 0.0940	0.0081
	R.S: 1200 rpm P.D: 2.8 mm	2366	--	531.63	0.28	136.6	777.5	0.44	- 0.0947	0.0085
R.S: Rotational speed; P.D: Plunge depth										

6.1.3.2 Evaluation of damage parameter in failure model

During the shock tube forming, the sheet metal undergoes plastic deformation at a high strain rate till fracture. Thus, the damage evolution during FE simulation of forming can be obtained by incorporating failure model with accurate damage parameters. In this work, Freudenthal failure model (eq. 3.5) as discussed earlier in Section 3.2.3 is used, because of its better predictability of the failure pattern and fracture strain during the sheet metal forming analysis (Dizaji et al., 2016; Pereira et al., 2020). When the damage parameter (D_1) reaches a critical value, the necking starts and it further leads to crack. The critical damage parameter for both the FS spot weld and unwelded sections are identified separately, and assigned to the respective locations (Fig. 6.6). In order to identify the strain paths during the forming of FSSW sheet, circular grids of 1.5 mm grid diameter are generated on the FSSW sheet before the start of the forming simulation (Fig. 6.8a). The strain paths evolved during the forming of FSSW sheets are represented in Fig. 6.8b. The results clearly depict that the FSSW sheets deform in biaxial mode of deformation at the initial stage. When necking initiates, the strain paths shift towards plane strain condition ($\varepsilon_2 = 0$). Thus, by assuming the deformation behavior of FSSW sheets during failure as plane strain condition, the critical damage parameters of both the FS spot weld and unwelded sections of the sheet for all the cases of FSSW sheets are identified (Table 6.4). The stress ratio and strain ratio required during the calculation of D_1 are derived from Hill's 1948 yield criterion by assuming plane strain condition with no planar anisotropy i.e., $r = r_0 = r_{45} = r_{90} = 0.73$ (discussed in section 3.2.3). The failure strain, $\varepsilon_f = 0.36$, is identified by deforming a plane strain sample during the shock tube impact forming experiment (Fig. 6.6c).

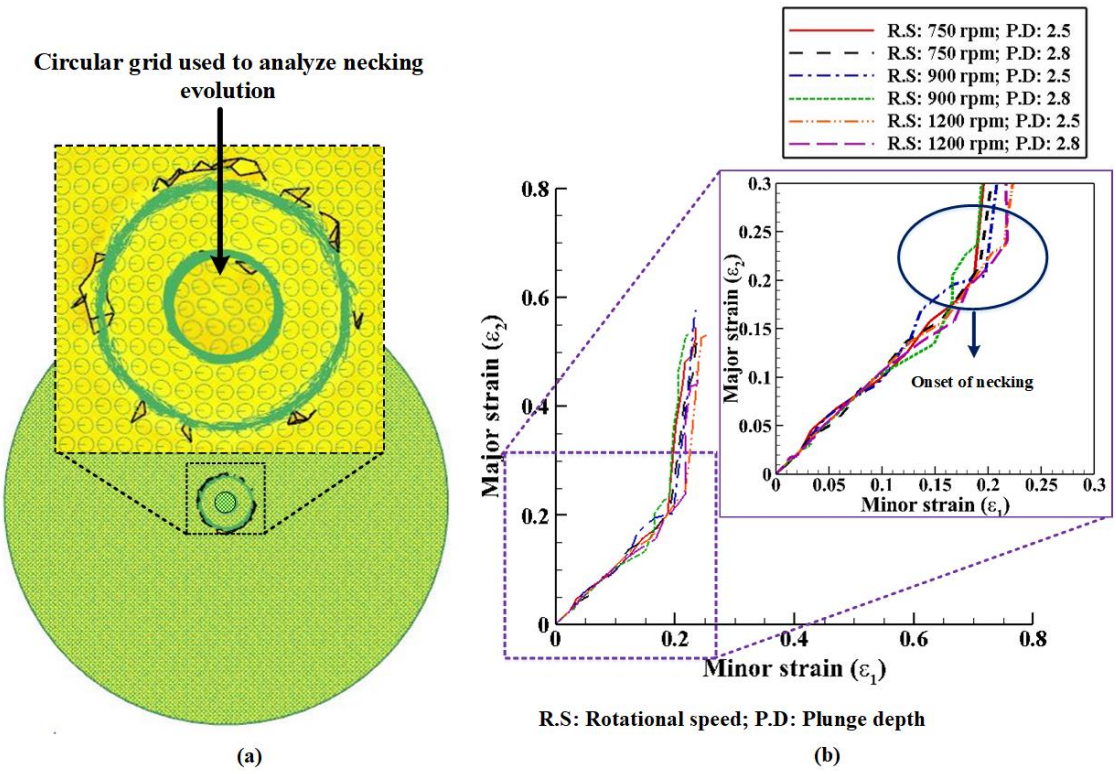

Fig. 6.8: Strain path developed near the necking location of the deformed FSSW sheets

Table 6.4: Critical damage parameter for Freudenthal failure model

Welding Condition		Critical Damage Parameter (MPa)
FS spot weld region	R.S: 750 rpm P.D: 2.5 mm	108.60
	R.S: 750 rpm P.D: 2.8 mm	114.02
	R.S: 900 rpm P.D: 2.5 mm	112.60
	R.S: 900 rpm P.D: 2.8 mm	115.47
	R.S: 1200 rpm P.D: 2.5 mm	117.21
	R.S: 1200 rpm P.D: 2.8 mm	121.23
Unwelded region	R.S: 750 rpm P.D: 2.5 mm	100.76
	R.S: 750 rpm P.D: 2.8 mm	100.86
	R.S: 900 rpm P.D: 2.5 mm	101.33
	R.S: 900 rpm P.D: 2.8 mm	102.86

	R.S: 1200 rpm P.D: 2.5 mm	102.64
	R.S: 1200 rpm P.D: 2.8 mm	104.35

6.1.3.3 Mesh sensitive analysis during impact forming of FSSW sheets

During FE simulation of the shock tube forming, the sheet is clamped between two rigid flanges and a constant blank holding force of 8 kN is provided to the top flange along the loading direction (Fig. 6.1). At the start of FE simulation, the striker touches the FSSW sheets, and it is provided with a velocity with which it deforms the sheet. The striker velocity is assigned by the velocity boundary condition in such a way that it has the velocity, V = 76.85 m/s, at the start of the deformation and becomes zero at the end of the simulation. The procedure to identify the striker velocity from experiment is explained earlier in Section 3.1.2. Furthermore, the final height of deformation measured from experiments are defined as the stopping control for the FE simulation.

In this study, Coulomb's coefficient of friction (μ) is defined as the contact boundary condition between FSSW sheet, striker and the flanges. Sheet failure depends on μ value between the FSSW sheet and the striker. Thus, it is varied between 0.001 to 0.2, and the failure patterns are compared with the experimental results. The results are analyzed for the forming of FSSW sheet made at 750 rpm and 2.5 mm plunge depth. At μ = 0.2, the FS spot welded sheet fails from both the welded joint and the base material (Fig. 6.9), whereas at μ = 0.001, the failure pattern does not match with that from experiment. After several iterations, the failure pattern evolved at μ = 0.05 has a good agreement with the experimental result. Thus, μ = 0.05 is considered as a constant for all the FE simulations.

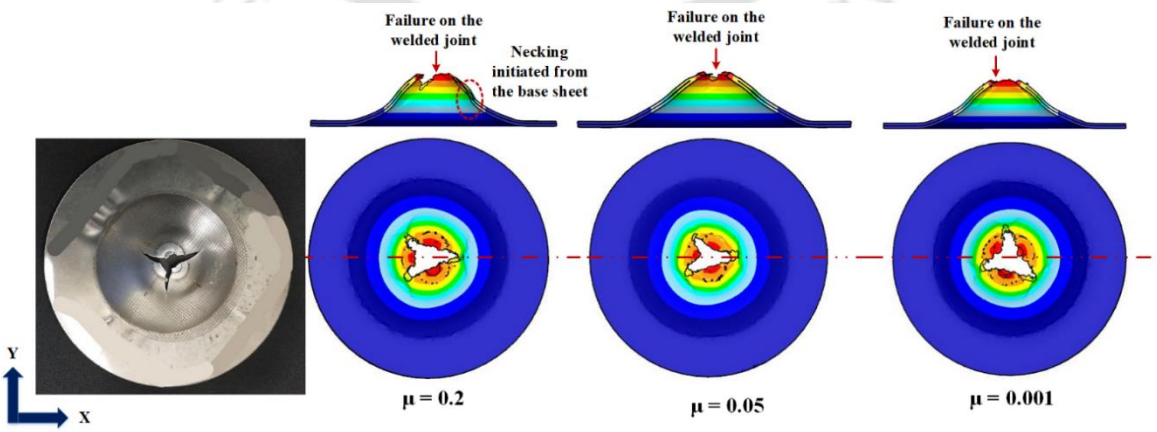

Fig. 6.9: comparison of failure pattern evolved due to variation in Coulomb's coefficient of friction

During this analysis, the element size ratio, which defines the ratio of largest element edge to smallest element edge is considered as 6. The deforming zone of the FSSW sheet is manually re-meshed with fine elements using local mesh density window (Fig. 6.10). The maximum element size inside the mesh density window is kept as 1 mm, whereas the minimum element size is decided by mesh sensitive analysis. Different element sizes such as 0.75 mm, 0.5 mm, 0.375 mm and 0.3 mm are considered during this analysis. The effective strain distribution predicted by different element sizes are compared to the experimental data after forming of the FSSW sheet with the welding condition, 750 rpm and plunge depth 2.5 mm (Fig. 6.10). The results clearly depict a poor correlation with the experimental result for 0.75 mm and 0.5 mm element sizes. On the other hand, the results predicted by 0.375 mm and 0.3 mm element sizes have shown a good agreement with small deviation in the predicted results. In this, minimum element size of 0.375 mm is considered for all the cases of forming simulation because of lesser computational time. Element remeshing is also implemented during impact forming simulation.

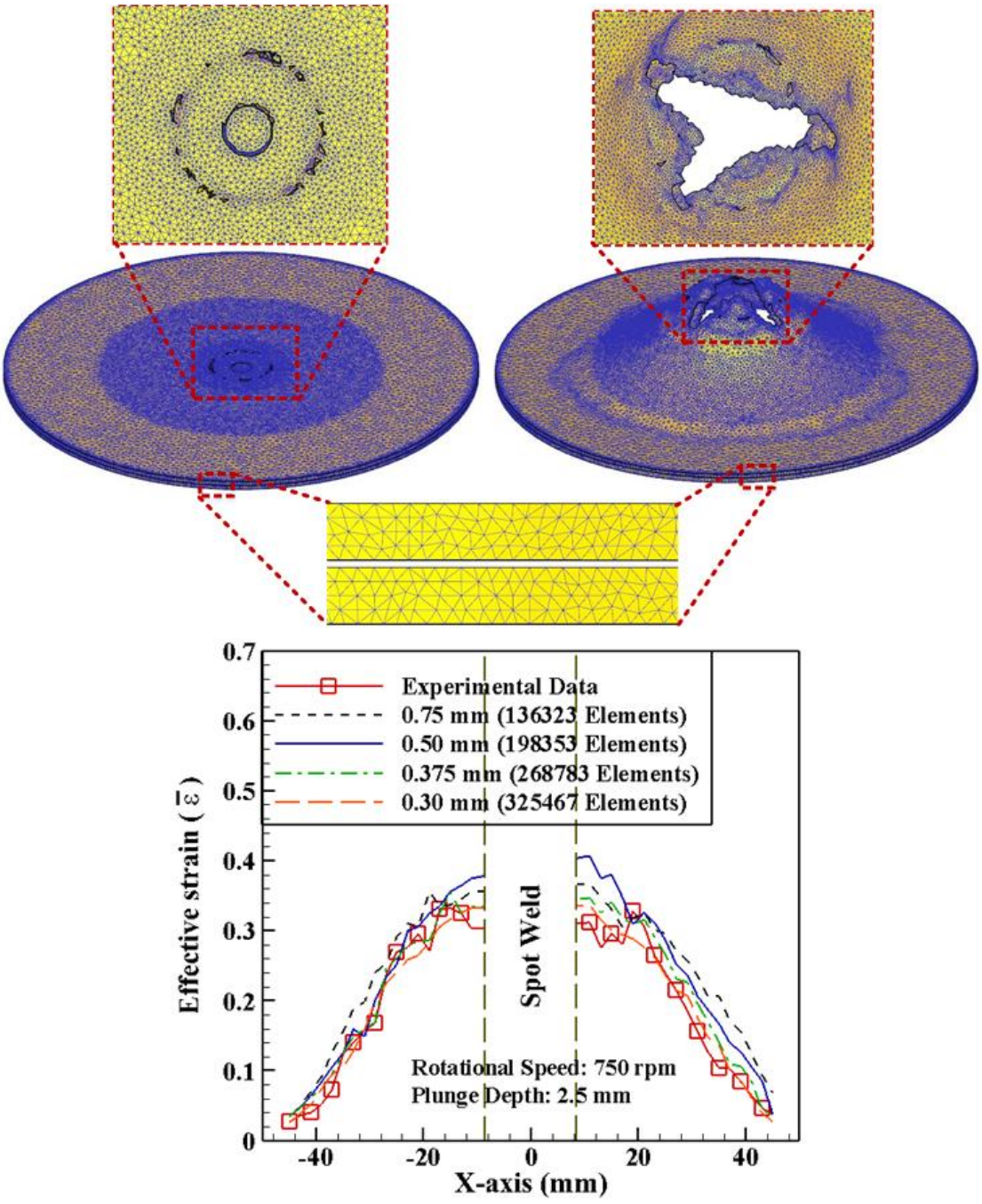

Fig. 6. 10: Mesh sensitive analysis during FE simulation of impact forming of FSSW sheets

6.2 Shock tube impact forming experiments

FSSW experiments are performed on a pair of 1.5 mm thick AA5052-H32 sheets. The welding parameters and dimensions of the tool and the base sheets considered during FSSW experiments are provided in Section 6.1.2.1. Temperature evolution during FSSW experiments are captured by mounting K-type thermocouple on the top sheet at a distance of 10 mm from the shoulder edge. The details about mounting of thermocouple and its circuitry arrangement is highlighted previously in Section 5.1.1. All the FSSW experiments

are performed thrice, out of which two are considered for shock tube forming experiments and one for FS spot weld characterization.

The details about the shock tube facility with instrumentation is discussed earlier in Section 3.1.2. A nylon striker with 95 mm overall length and 54.8 mm diameter is placed in the driven section of the shock tube at a distance of 300 mm from the end of the shock tube. For all the shock tube forming experiments, the bursting pressure is kept constant as 16.82 ± 0.63 bar. The pressure-time graph recorded by two pressure transducers (P_1 and P_2) is shown in Fig. 6.11. The striker velocity is measured with the help of a pair of IR sensors mounted at a distance of 130 mm from the end of the shock tube. The average incident pressure, reflected pressure and striker velocity developed during this experimental condition are 3.2 ± 0.23 bar, 12.64 ± 0.36 bar and 76.85 m/s, respectively.

In order to measure the effective strain ($\bar{\varepsilon}$) developed on the FSSW sheet after deformation, circular grids of diameter 1.83 ± 0.03 mm are printed on the surface of the top sheet. The circular grids deform into elliptical grids after deformation. The major and minor diameters are measured and utilized during the calculation of the effective strain ($\bar{\varepsilon}$) by using Hill's 1948 yield function (refer Section 2.4.1).

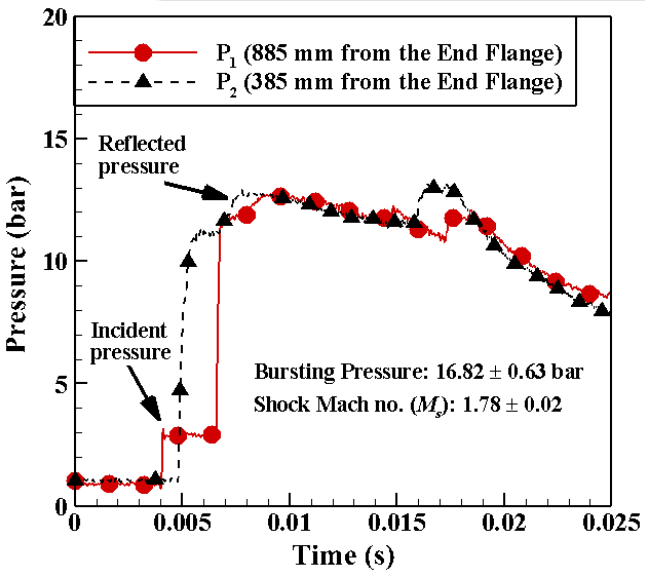

Fig. 6.11: Pressure-time signal recorded by pressure transducers during experiment

6.3 Results and discussion

6.3.1 Temperature evolution validation during FSSW

The temperature evolution predicted during FSSW is compared with the experimental data (Fig. 6.12), and an acceptable agreement is obtained. The results illustrate that during plunging phase, the temperature increases monotonically because of the frictional contact

between the tool and the work piece. The further temperature rise during the dwelling phase is significantly influenced by the frictional heat generated at the interference of the tool shoulder and work-piece. The rate of temperature rises in both the plunging and dwelling stages is significantly dependent on the tool rotational speed. The maximum temperature is observed at 1200 rpm. Furthermore, the tool plunge depth also affects the temperature rise. At higher plunge depth (Z = 2.8 mm), severe plastic deformation at the tool shoulder and work piece interface generates significant amount of frictional heat that helps in further rise in temperature for all the cases of tool rotational speeds (Fig. 6.12).

The FE simulation has been able to predict the trend and the peak temperature accurately for all the FSSW cases. The maximum percentage of error of 8.3 % is observed between the experimental data and FE simulation while predicting the peak temperature in the case of 1200 rpm and 2.8 mm plunge depth. For all other cases of FSSW, the error percentage is lower, and acceptable. The temperature profile predicted along the transverse section of the FSSW sheets are also illustrated in Fig. 6.12. Along the thickness direction, the temperature distribution is in the form of V-shape, i.e., higher temperature on the upper portion of the weld joint than the lower section, which is because of the larger contact area between the tool shoulder and the work-piece. Moreover, the heat dissipation from the bottom surface of the work piece is more compared to the top surface.

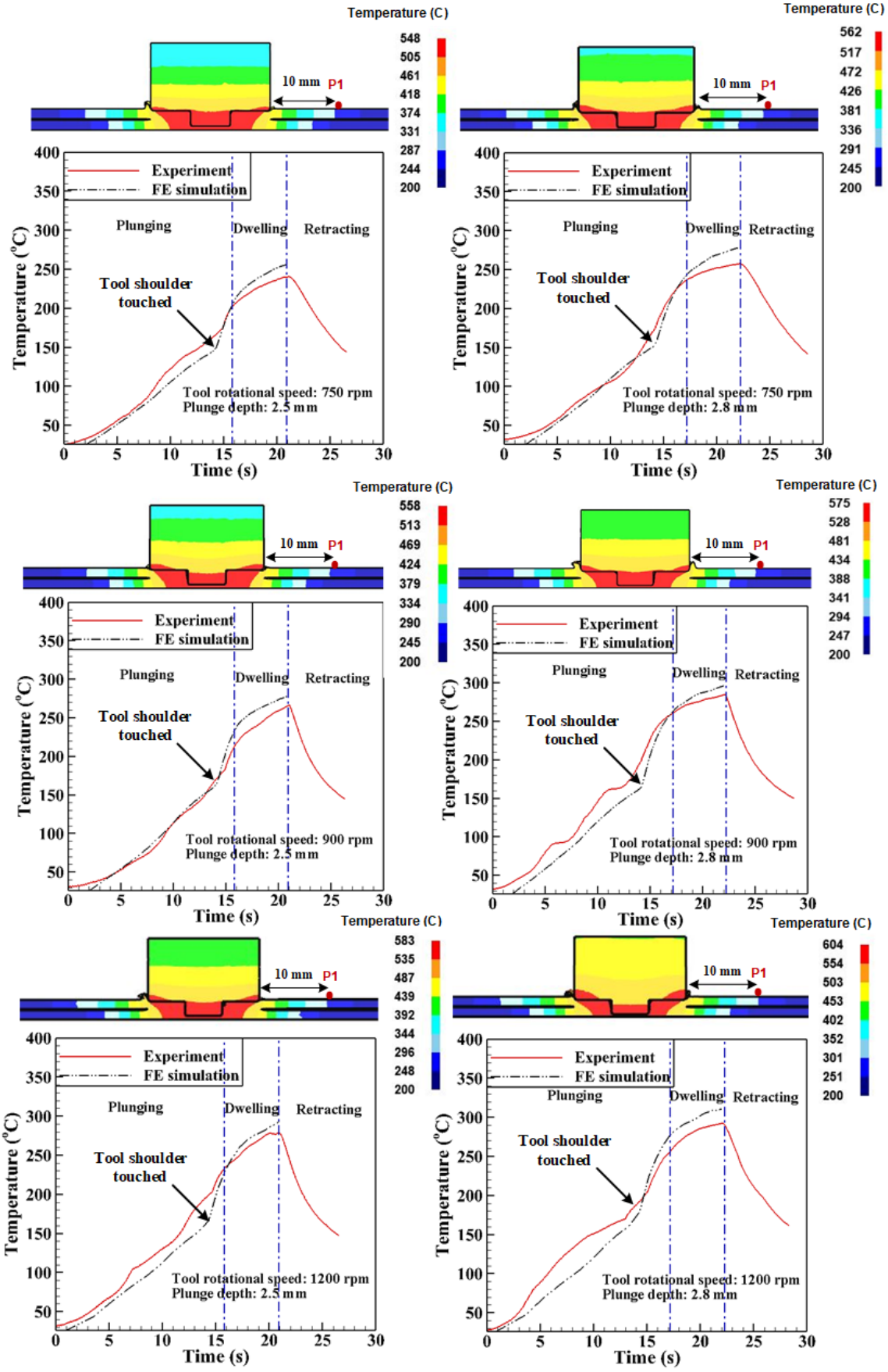

Fig. 6.12: Comparison of the predicted temperature evolution with the experimental data during FSSW

6.3.2 Effect of rotational speed and plunge depth on effective strain and material flow during FSSW

It is known that the plastic deformation of the material plays a vital role during the material mixing and it results in formation of a good quality weld during FSSW. Therefore, the effect of tool rotational speed and plunge depth on the effective strain profile, a quantity describing plastic deformation, is analysed from FE simulation results. Fig. 6.13a clearly depicts that the effective strain developed on the welded region is significantly affected by the tool rotational speed. Effective strain generated in the welded region at 1200 rpm case is larger than in 750 rpm case. Similar observation has been evident in existing literature (Jain et al., 2017a). The effective strain developed in the weld zone decreases from top to bottom because higher stirring of material takes place below the tool shoulder and it is maximum at the SZ formed near the tool pin (Fig. 6.13a). When tool plunge depth is increased, the width of the SZ increases because of the increase in plastic deformation at the tool-work piece interface (Fig. 6.13b). It results in to further rise in strain as depicted in Fig. 6.13a.

The shape of the SZ is also predicted for two different plunge depths, 2.5 mm and 2.8 mm, at tool rotational speed of 750 rpm. Total 133 number of points are defined in the weld spot with 0.5 mm horizontal and vertical spacing before the start of FSSW (Fig. 6.13c) to identify SZ. The results are verified with the experimentally obtained SZ from the macrostructure (Fig. 6.13b), and a good correlation has been observed. The significant rise in plastic deformation due to the increase in plunge depth expands the SZ and it is evident in Fig. 6.13b.

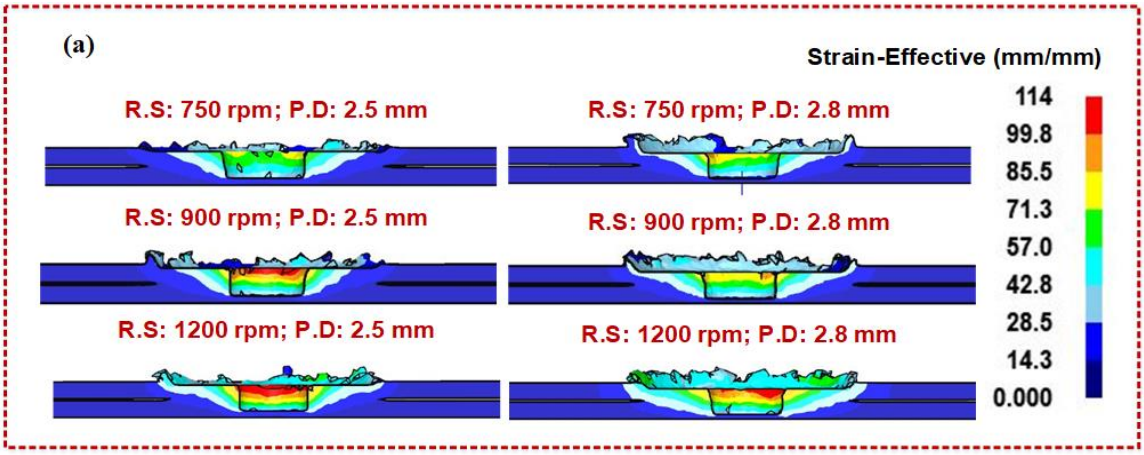

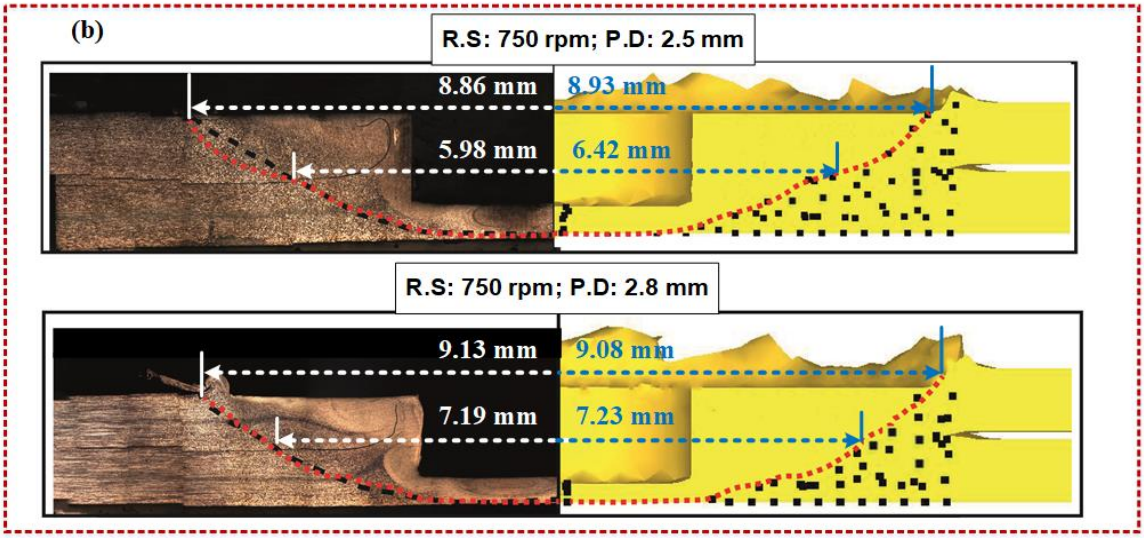

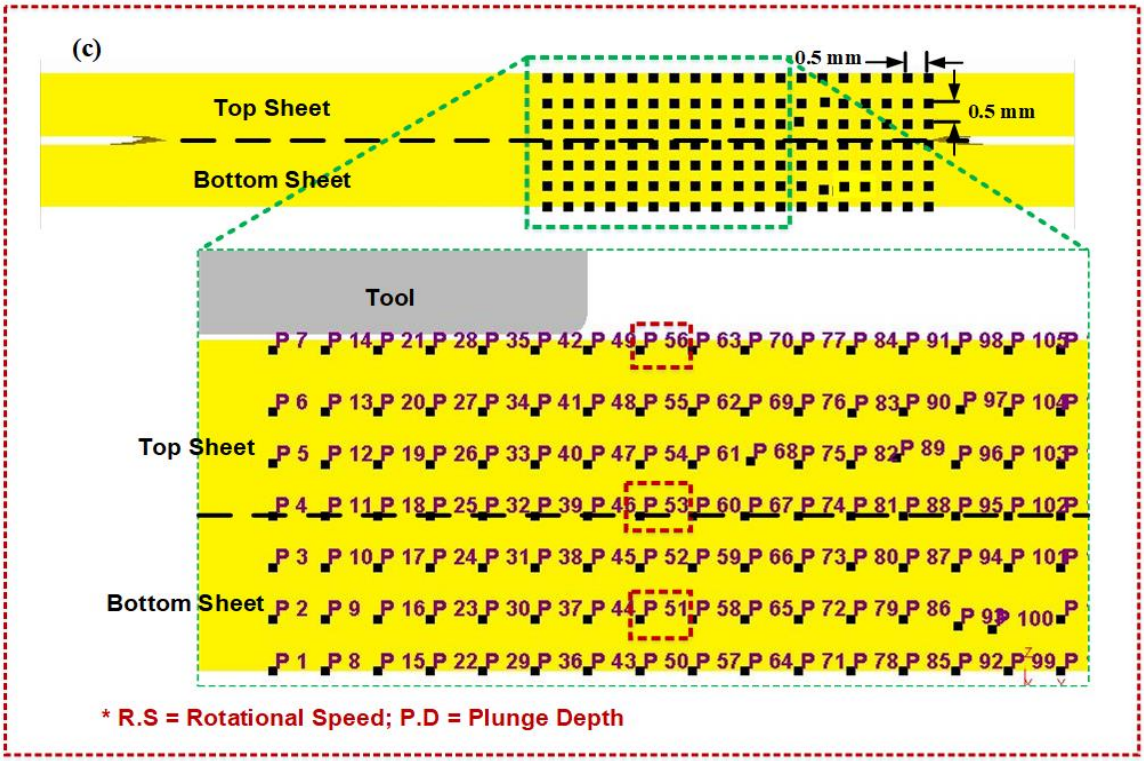

Fig. 6. 13: Influence of rotational speed and plunged depth on effective strain distribution and SZ size determined from FE simulations

To illustrate the material flow during FSSW, three points such as point 56, point 53, and point 51, which are available at the top, middle and bottom regions of the sheet are tracked (Fig. 6.13c). It gives insight about the material mixing phenomenon during FSSW as presented in Fig. 6.14. The choice of defining single block model at the spot weld region helps to understand the material flow phenomenon without any contact instability. The results illustrate that during the plunging phase, the material on the top sheet adjoining to the tool pin (point 56) extrudes upward until the shoulder touches the top sheet. With the progression of the plunging, the rotating tool tries to move the upper region material downward (point 56). At the same time the material in the middle layer (point 53) and bottom layer (point 51) is stirred, and mixed with the top layer material. The material mixing is more intense and uniform at higher rotational speed (1200 rpm). At the same time, higher tool plunge depth (Z = 2.8 mm) assists the bottom region material (point 51) to lift upward and helps the material in uniform mixing. During an experimental investigation, Yang et al. (2010) observed similar phenomenon for the cause of in material flow during FSSW of AZ31 Mg sheets. In an another study, Yuan et al. (2012) examined the material mixing phenomenon at microstructural level during FSSW of AZ31 Mg sheets and reported the better material flow ability at higher tool rotational speed.

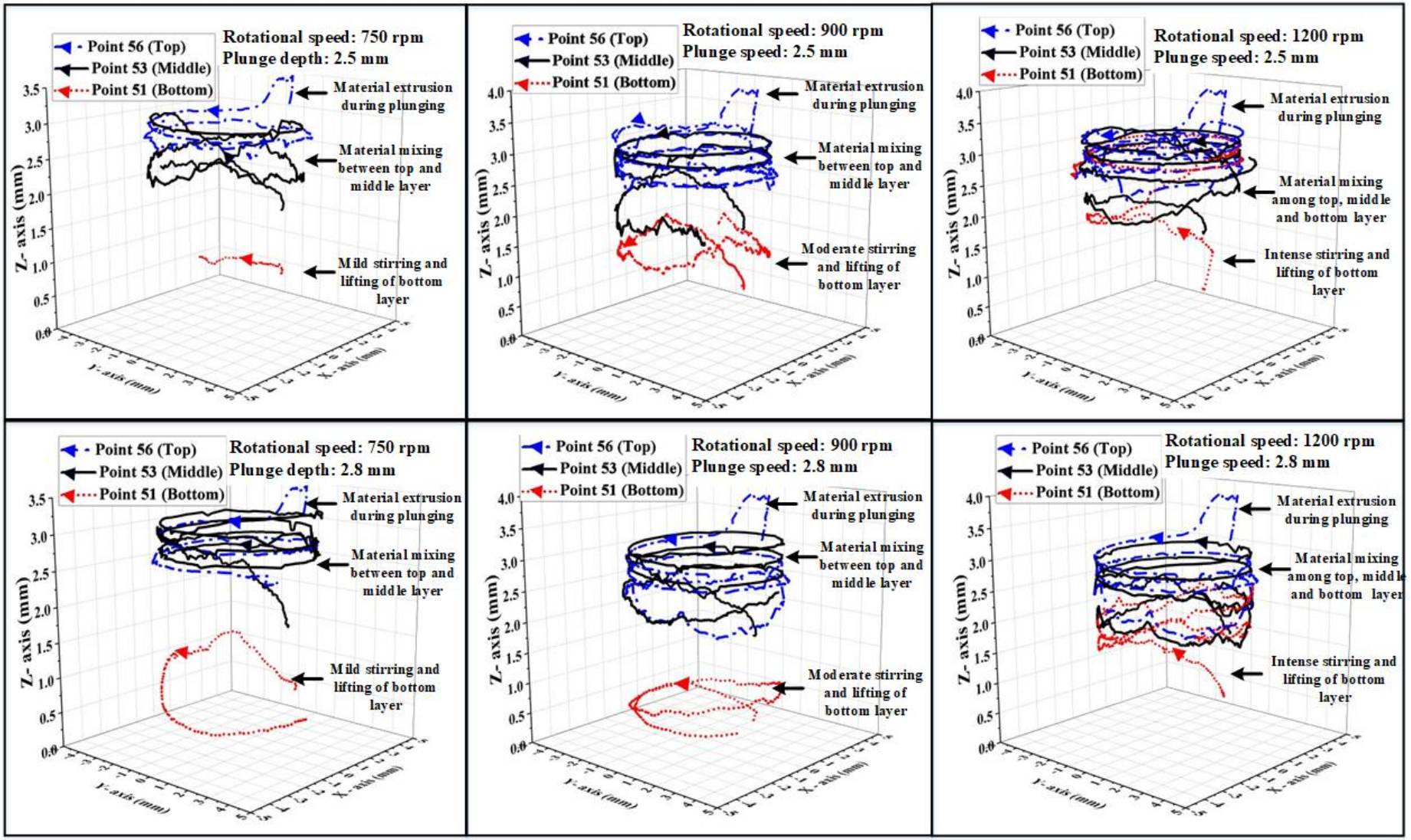

Fig. 6.14: Influence of rotational speed and plunge depth in material flow during FSSW

6.3.3 FSSW joint morphology and hardness distribution

The micrograph of the spot weld in FSSW depicts three distinctive regions such as stir zone (SZ), thermo-mechanically affected zone (TMAZ), and heat affected zone (HAZ) as illustrated in Fig. 6.16. Severe plastic deformation with higher heat input generates fine, recrystallized grains in SZ. TMAZ shows severely deformed, uncrystallised grains and it surrounds the SZ. HAZ experiences a thermal cycle without any plastic deformation.

The macro-structural investigation of the spot weld cross-section reveals the formation of hook (Fig. 6.15). Hook is generally formed in FSSW because of the upward movement of the interface caused due to the penetration of tool pin into the lower sheet during plunging (Yang et al., 2010). Furthermore, the oxide layers present on the surface of the aluminium sheets are trapped at the faying surface and prevent metallurgical bonding of the sheets and assist during hook formation (Yuan et al., 2012). Based on the distribution of oxide particles during the stirring of the material, various regions such as complete metallurgical bonded region, partially metallurgical bonded region and unbonded region are identified from the macrostructure and represented in Fig. 6.15.

It is observed from the existing literature that the hook morphology affects the joint performance significantly (Rana et al., 2018). Thus, in this present study, the effect of tool rotational speed and plunge depth on the hook geometry is analysed. The hook width (horizontal distance from the primary hook to the pin hole periphery) and hook height (vertical distance from the primary hook to the hook initiation point) are quantified for all the FSSW cases and represented in Fig. 6.15. Only one side of the joint cross-section is shown because of the symmetry. Hook width increases and hook height decreases with the rise in tool rotational speed. Similar observation has been reported in literature (Badarinarayan et al., 2009; Rana et al., 2018). It has been observed that at higher tool rotational speed, the size of plastically deformed material increases. It helps in the outward movement of the boundary and merges a portion of hook with the extruded zone and it results in the enlargement of the hook width and reduction on hook height. At the same time, it is also noticed that with the rise in tool plunge depth, the hook width increases further and there is a drastic decrease in the hook height. Badarinarayan et al. (2009) also reported similar observation for the FSSW of AA 5754 sheets, and explained that with the increase in the plunge depth larger volume of the lower sheet material is pushed outward as well as upward towards the upper sheet. When shoulder

contacts the work piece, the material flow increases significantly and it tries to push the hook geometry outward which gives rise to a larger hook width. The effective top sheet thickness reduces with the increase in tool plunge depth and it results in significant decrease in hook height.

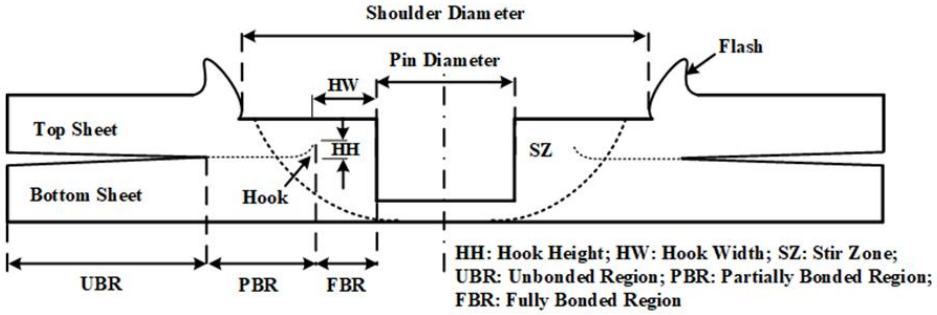

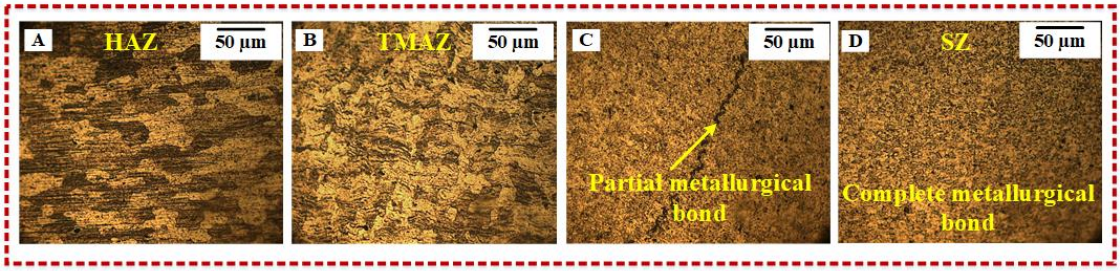

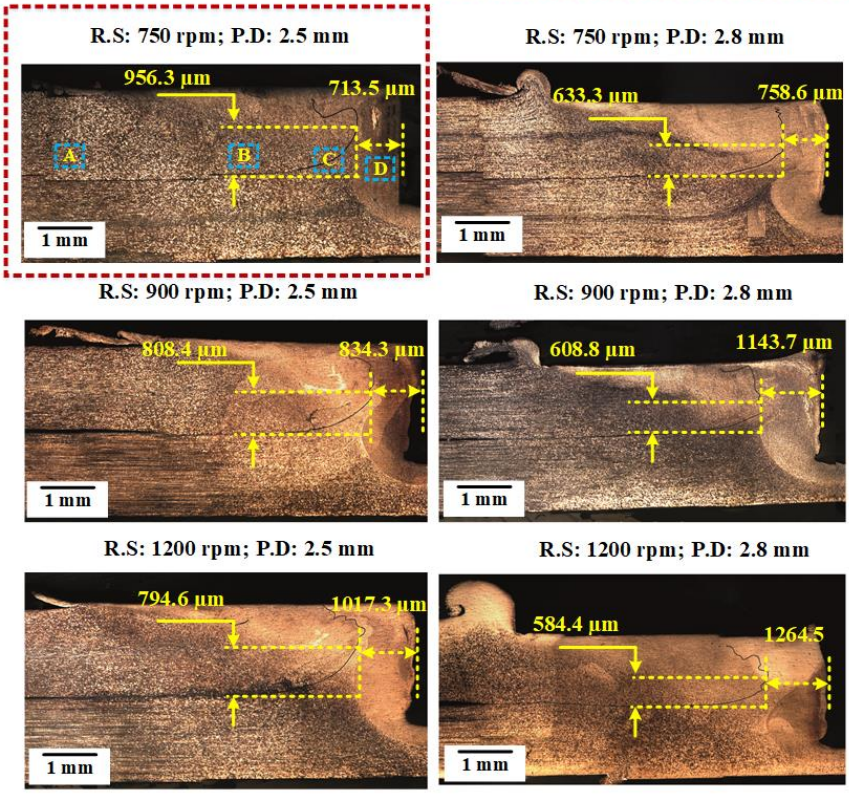

*R.S: Rotational Speed; P.D: Plunge Depth

Fig. 6. 15: Hook morphology and microstructural characterization of spot weld (tool rotational speed: 750 rpm and plunge depth: 2.5 mm)

The hardness variation across the joint cross-section is measured in the mid-thickness of both the top sheet and the bottom sheet (Fig. 6.16). The hardness near the pin hole periphery is larger because of the finer grains developed due to dynamic recrystallization. The localised decrement in the hardness is because of the softening of the material as a result of metallurgical recovery caused due to the thermal cycle (Rana et al., 2018). It is observed from the results that the rise in the tool rotational speed increases the hardness across the joint cross-section. It is because of the dynamic recrystallization occurs due to the severe plastic deformation of the material. Furthermore, Huskins et al. (2010) reported that apart from the grain boundary strengthening, precipitation hardening, solid solution hardening, and increment in dislocation density were also responsible for increase in hardness for AA 5XXX sheets. With the increase in plunge depth, the hardness of the FSSW joint increases further and it is most prominently visible at higher rotational speed (Fig. 6.16).

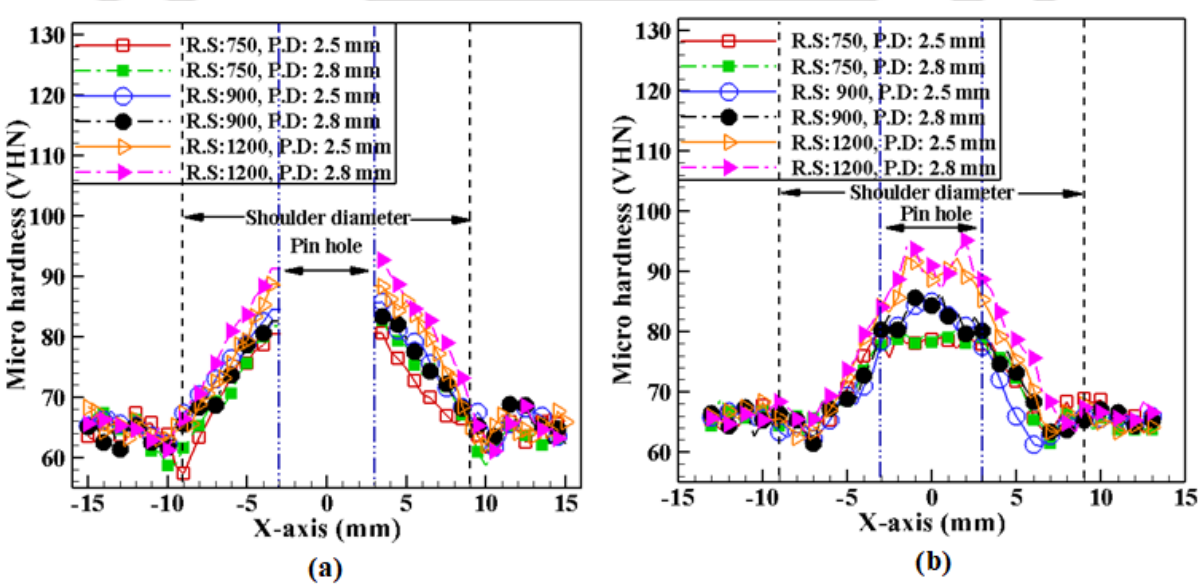

Fig. 6.16: Hardness distribution across the FSSW joint in both (a) top sheet and (b) bottom sheet

6.3.4 Prediction of the deformation profile and failure pattern during impact forming

During this analysis, the FSSW sheets are deformed at a constant striker velocity, V = 76. 85 m/s, during the shock tube impact forming and all the welded sheets fail from the pin hole location after plastic deformation (Fig. 6.17). The results clearly illustrate different height of deformation achieved during the experiment for the same striker velocity. Though necking is initiated from the pin hole, the final height of deformation is controlled by the joint strength. FSSW sheets made at 750 rpm deforms to a larger extent as compared to 1200 rpm case. Welded sheets made at 900 rpm performs in between. Larger hook width and hardness at 1200 rpm increase the joint strength significantly. The weld strength is also affected by the tool plunge depth. It is observed before that larger plunge depth increases hook width (Fig. 6.15) and it has also shown higher hardness (Fig. 6.16). The increment in joint strength at high plunge depth helps to restrict in the crack propagation and there is a decrease in dome height after deformation (Fig. 6.17). Lower dome height is visible for 1200 rpm weld case with larger plunge depth. The deformation profile predicted by FE simulation are also compared with the experimental results (Fig. 6.17), and a good correlation has been found.

Furthermore, the crack pattern is also predicted by FE simulation (Fig. 6.17) and the results have a fair agreement with experimental results. The petal formation during the shock tube impact forming is well predicted by MJC flow stress model in combination with Freudenthal damage model. The results illustrate that lower weld strength in the case of 750 rpm increases crack propagation length. For both 750 rpm and 900 rpm, the crack is initiated from the pin hole and it is propagated towards the unwelded section of the sheet. On the other hand, higher weld strength in both the plunge depths for the case with 1200 rpm, restricts the propagation of the crack within the joint region only (confirmed by visual inspection in Fig. 6.17).

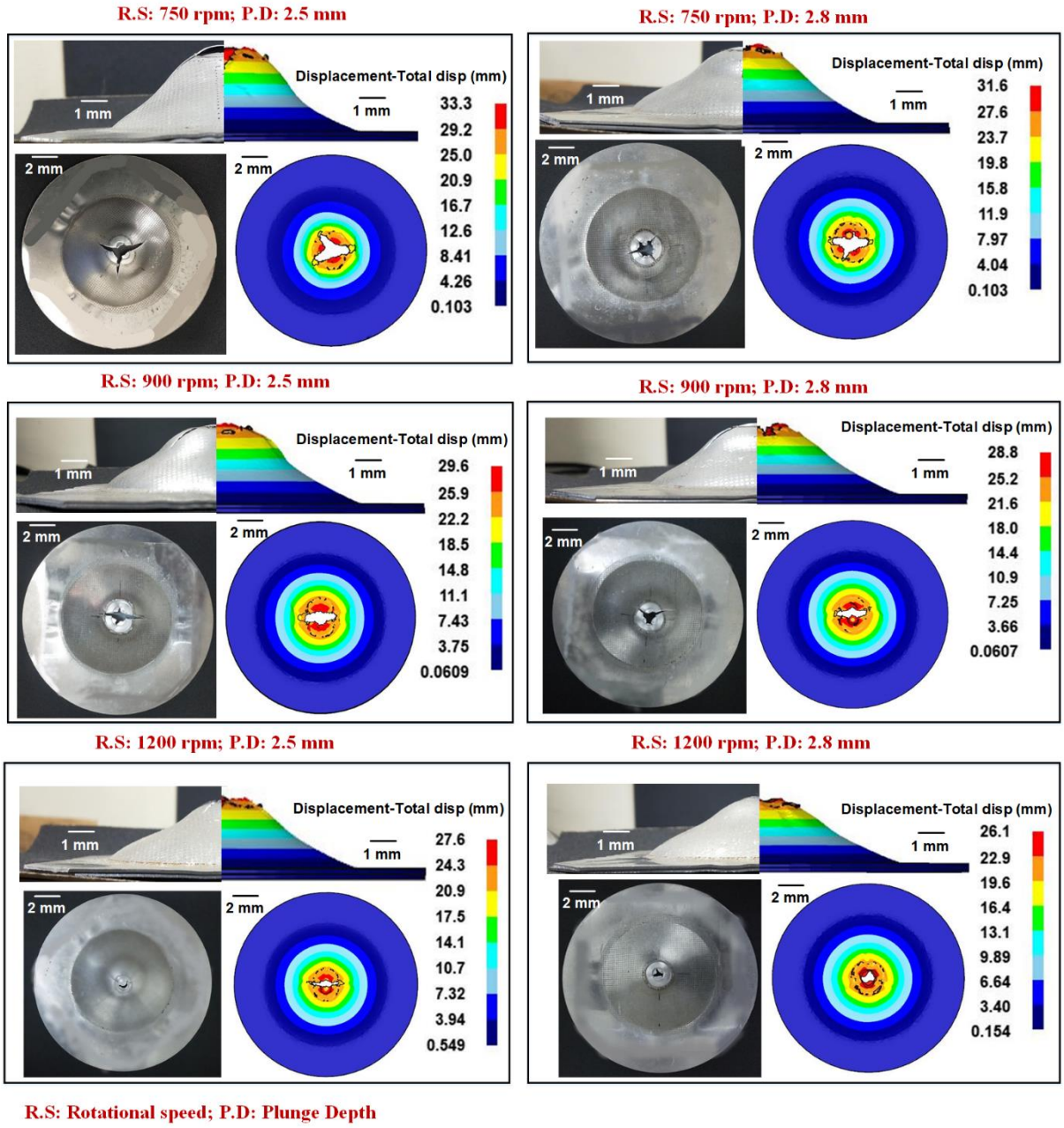

Fig. 6.17: Comparison of the predicted deformation profile and failure pattern with the experimental results

6.3.5 Effective strain distribution during impact forming

Effective strain ($\bar{\varepsilon}$) generated on the top sheet of the FSSW sheets after deformation is compared with the FE simulation results, and a good correlation has been obtained (Fig. 6.18). During impact forming, FSSW sheets deform uniformly and the failure starts from the pin hole for all the cases. The inertial effect developed due to the dynamic loading in the shock tube

helps to stretch the sheet metal uniformly without any strain localization that helps in increase in the formability of the material (Ahmed et al., 2017). Larger deformation in 750 rpm weld cases generates larger effective strain near the pole region, whereas 1200 rpm weld cases develop lesser effective strain. As discussed earlier, larger plunge depth during FSSW generates stronger joint, which restricts deformation and further crack propagation during the shock tube deformation. It results in lower effective strain near the pole region. Furthermore, the results predicted by MJC flow stress model in combination with Freudenthal damage model have a fair agreement with the experimental results.

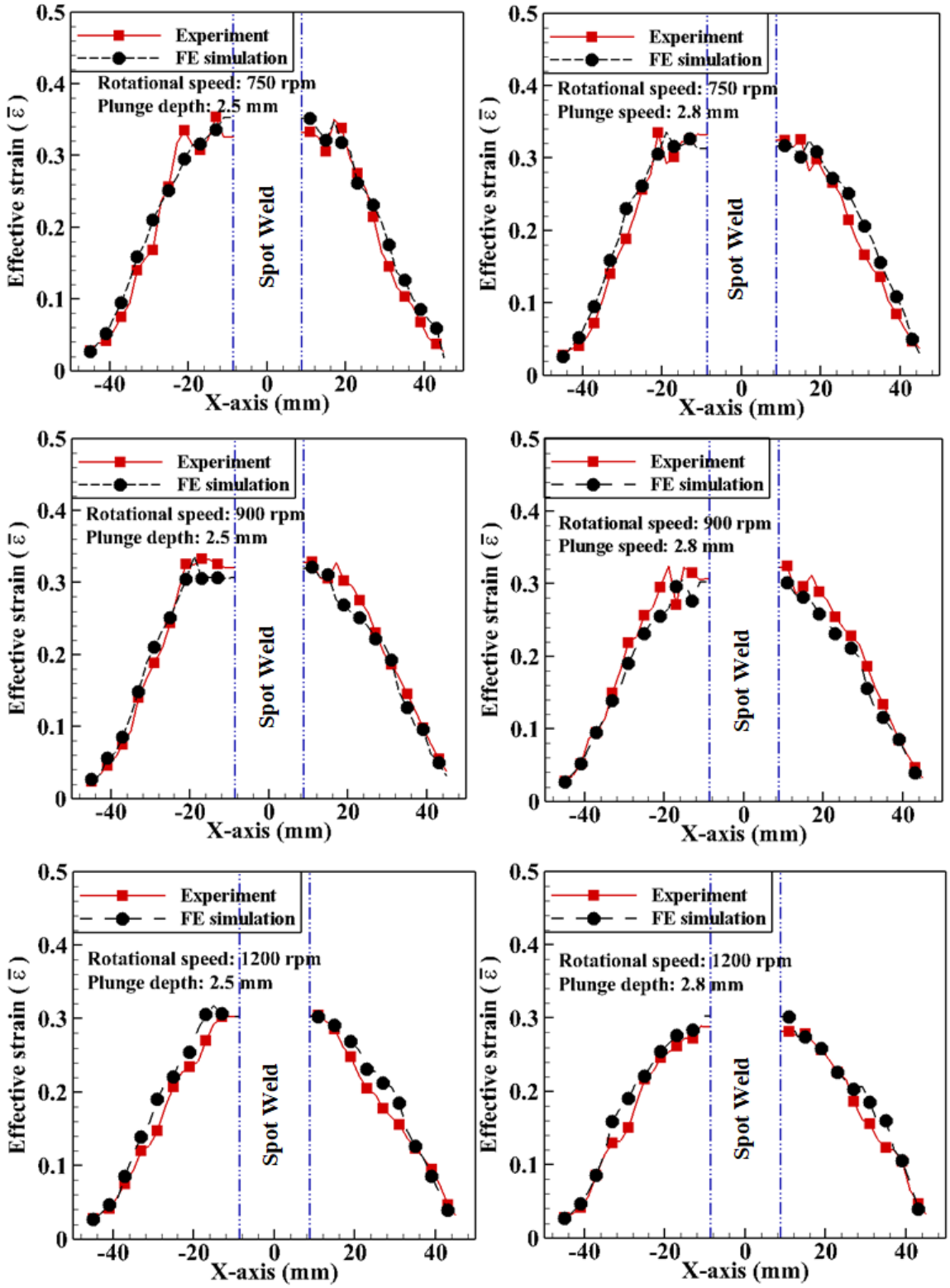

Fig. 6.18: Comparison of the predicted effective strain distribution during impact forming of FSSW sheets with experimental data

6.4 Summary

The present work aims to provide a validated FE model with FSSW and dynamic forming simulated sequentially. Along with this, effect of tool rotational speed and plunge depth during FSSW on the formability of spot welded sheets is studied. Dynamic forming of 1.5 mm thick AA5052-H32 sheets after FSSW is performed using a shock tube. From the results obtained, the following conclusions are drawn.

I. The two-stage manufacturing process consisting of FS spot welding in the first stage and shock tube based forming in the second stage is successfully modelled using DEFORM-3D. The results obtained in both the stages are validated with the experimental data and a good correlation has been found.

II. During FE simulation of shock tube based forming, the rate-dependent material properties of the unwelded section of the FSSW sheets are identified by the tensile test of the sheets deformed using the shock tube. For the FS spot welded region, a hardness increment factor is identified and multiplied to the stress-strain data of the base sheet for this purpose. The predicted forming outputs have a fair agreement with the experimental results. Thus the approach for evaluating the flow stress evolution during high strain rate forming can be followed for predicting the dynamic formability of the welded sheets.

III. The temperature evolution during FSSW confirms that the temperature rise is dependent on the tool rotational speed. Higher plunge depth further increases the temperature in the process.

IV. The material flow phenomenon during FSSW predicted by FE simulations illustrates that the material mixing is more intense at higher tool rotational speed. With the increase in the tool plunge depth, the bottom region material is lifted upward and demonstrated a uniform mixing of the material. The predicted effective strain developed on the FSSW joint also confirms an increase in the SZ width at higher tool rotational speed with larger plunge depth.

V. The hook geometry formed after FSSW confirms that the hook width increases significantly with the increase in tool rotational speed, whereas the hook height shows inverse relationship. At the same time, the rise in tool plunge depth increases the hook width further and there is a drastic decrease in hook height.

VI. During forming of FSSW sheets, the final height of deformation is controlled by the weld joint strength. Larger hook width and higher hardness value at 1200 rpm weld case increase the joint strength significantly and it results into lower height of deformation. FSSW sheets made at 750 rpm deforms more.

VII. The deformation profile, failure pattern and effective strain distribution is well predicted by MJC model in combination with Freudenthal damage model and the results have a fair agreement with the experimental results.

Chapter 7

Conclusions and scope of future work

7.1 Conclusions

In the current work, a detailed analysis is carried out to investigate the dynamic forming behaviour of AA 5052-H32 sheets at different strain rates using a shock tube. The sheets are deformed both in safe limit and beyond the safe limit to have a better understanding about their formability at different loading conditions. Numerical simulations are also carried out for the purpose in DEFORM-3D, FE code. The predicted results are validated with the experimental data obtained from the lab-scale shock tube experiments. The findings are encouraging and can be implemented by the automotive and aerospace industries during the product design. Major conclusions drawn from the present work are as follows.

- The shock tube facility is successfully demonstrated as a dynamic bulge testing device and dynamic Erichsen device to study the rate-dependent formability of the sheets. It can be used in lab scale to characterise the biaxial forming behaviour of the sheets and composites at different ranges of strain rates. Further, the shock tube can be utilized to fabricate a shaped product by mounting a close-end die at the end of the set up.
- A new strategy is followed to evaluate the rate-dependent flow stress-strain data from the tensile test of samples sectioned from the shock tube-based deformed sheet. The stress-strain data are fit to different flow stress models and the material constants are identified. The same material constants are reutilized to obtain the flow stress for larger strain and incorporated during FE simulations. The predicted forming outputs have an acceptable agreement with the experimental data.
- Out of the four flow stress models, the predictability of the MJC model is better because of the inclusion non-linear strain rate sensitivity term during the flow stress calculation.
- The failure strain and the location of necking are well predicted by different failure models in combination with different flow stress models. Out of all, Freudental model and Brozzo model have a good agreement with the experimental results. The failure strain predicted by these failure models has about 8% deviation from the experimental results.

- From the comparison of the failure strain obtained from the quasi-static forming and shock tube-based forming, it is confirmed that a significant rise in failure strain, about 60-70% is observed during the shock tube-based forming. It is because of the inertial forces develop during the high-velocity forming, which deforms the material further at a high strain rate without strain localization.
- The effective strain distribution illustrates that the sheets deform biaxially during the shock tube based forming. SEM analysis also encases deeper and larger parabolic dimples on the fracture surface of the shock tube-based deformed specimen, which confirms that material undergoes larger plastic deformation.
- During the impact forming analysis of the FSSW sheets, the two-stage manufacturing process consisting of FS spot welding in the first stage and shock tube based impact forming in the second stage is successfully demonstrated experimentally in the lab scale and the same has been modelled by establishing an interactive set up during FE simulation. The overall results have a fair agreement with the experimental data. This experimental-modelling strategy can be implemented in industrial product design where the product undergoes multi-stage forming processes.
- The rate-dependent flow strass-strain data for the unwelded section of the FSSW sheets are identified by the tensile test of the sheet deformed by the shock tube, and for the spot weld region, a hardness increment factor is identified and multiplied to the stress-strain data of the base sheet for this purpose. The approaches are simple to implement and sufficiently accurate in predicting the formability of sheets with spot welds.
- The effect of different welding parameters such as tool rotational speed, plunge speed and plunge depth on the welding and forming outputs are analysed during this study. The joint morphology confirms that hook width increases with the increase in tool rotational speed and tool plunge depth. At the same time, lower plunge speed results into larger hook width. The predicted material flow during FSSW illustrates the material mixing phenomenon during the joint formation.
- During the shock tube based forming of FSSW sheets, the final height of deformation is controlled by the weld joint strength. Higher tool rotational speed with larger plunge depth increases the weld strength that restrict the crack propagation during the forming of FSSW

sheets. However, the variation of tool plunge speed has insignificant effect on the dome height and the failure pattern.

7.2 Scope of future work

In this present work, the shock tube facility is successfully demonstrated as a dynamic bulge testing device and dynamic Erichsen device. However, the application of the shock tube facility can be expanded by modifying the existing set up and also by vary some process parameters to meet the specific requirement in the automotive and aerospace industries. The following future works are recommended for further exploration of this field.

- The shock tube is used to study the biaxial forming behavior of the sheets at high strain rates. It can be introduced during the identification of Forming limit curve (FLC) of the sheets.
- The shock tube can be implemented to fabricate a shaped product by mounting a close-end die at the end of the set up.
- In the recent past, the forming limit of the sheets are enhanced by heat treatment, warm forming, and employing high-velocity forming processes. An integration of heating source to the testing chamber of the shock tube will be helpful to study the forming behavior of the sheets at high strain rates with varying temperature conditions.
- Now-a-days, the application of sandwich sheet is increasing in the automotive sectors because of its specific qualities such as light weight, good static and dynamic strength, better thermal and sound insulation. Thus, investigating the dynamic forming behavior and crashworthiness of the sandwich panels using the shock tube will be more interesting.

References

Abd El-Aty, A., Xu, Y., Zhang, S.H., Ha, S., Ma, Y., Chen, D., (2019). Impact of high strain rate deformation on the mechanical behavior, fracture mechanisms and anisotropic response of 2060 Al-Cu-Li alloy. *Journal of advanced research*, 18 , 19–37.

Abedrabbo, N., Pourboghrat, F., Carsley, J., (2007). Forming of AA5182-O and AA5754-O at elevated temperatures using coupled thermo-mechanical finite element models. *International Journal of Plasticity*, 23 , 841–875.

Ahmed, M., Kumar, D.R., Nabi, M., (2017). Enhancement of Formability of AA5052 Alloy Sheets by Electrohydraulic Forming Process. *Journal of Materials Engineering and Performance*, 26 , 439–452.

Ahmed, M., Panthi, S.K., Ramakrishnan, N., Jha, A.K., Yegneswaran, A.H., Dasgupta, R., Ahmed, S., (2011). Alternative flat coil design for electromagnetic forming using FEM. *Transactions of Nonferrous Metals Society of China*, 21, 618–625.

Al-Hassani, S.T.S., Duncan, J.L., Johnson, W., (1974). On the parameters of the magnetic forming process. *Journal of Mechanical Engineering Science*, 16 , 1–9.

Ambriz, R.R., Froustey, C., Mesmacque, G., (2013). Determination of the tensile behavior at middle strain rate of AA6061-T6 aluminum alloy welds. *International Journal of Impact Engineering*, 60 , 107–119.

Babaei, H., Mostofi, T.M., Sadraei, S.H., (2015). Effect of gas detonation on response of circular plate-experimental and theoretical. *Structural Engineering and Mechanics*, 56 , 535–548.

Badarinarayan, H., Shi, Y., Li, X., Okamoto, K., (2009). Effect of tool geometry on hook formation and static strength of friction stir spot welded aluminum 5754-O sheets. *International Journal of Machine Tools and Manufacture*, 49 , 814–823.

Bajpei, T., Chelladurai, H., Ansari, M.Z., (2017). Experimental investigation and numerical analyses of residual stresses and distortions in GMA welding of thin dissimilar AA5052-AA6061 plates. *Journal of Manufacturing Processes*, 25 , 340–350.

Bajpei, T., Chelladurai, H., Ansari, M.Z., (2016). Mitigation of residual stresses and distortions in thin aluminium alloy GMAW plates using different heat sink models. *Journal of Manufacturing Processes*, 22 , 199–210.

Balanethiram, V.S., Daehn, G.S., (1992). Enhanced formability of interstitial free iron at high strain rates. *Scripta metallurgica et materialia*, 27, 1783–1788.

Balanethiram, V.S., Hu, X., Altynova, M., Daehn, G.S., (1994). Hyperplasticity: enhanced

formability at high rates. *Journal of Materials Processing Technology*, 45 , 595–600.

Bisht, A., Kumar, L., Subburaj, J., Jagadeesh, G., Suwas, S., (2019). Effect of stacking fault energy on the evolution of microstructure and texture during blast assisted deformation of FCC materials. *Journal of Materials Processing Technology*, 271, 568–583.

Bisht, A., Ray, N., Jagadeesh, G., Suwas, S., (2017). Microstructural and crystallographic response of shock-loaded pure copper. *Journal of Materials Research*, 32 , 1484–1498.

Black, M., Kishore, S., LeBlanc, J., Lockhart, P., Shukla, A., (2018). Non-destructive imaging and residual strength of composite materials after exposure to blast loading. *Journal of Dynamic Behavior of Materials*, 4 , 408–424.

Bozzi, S., Helbert-Etter, A.L., Baudin, T., Klosek, V., Kerbiguet, J.G., Criqui, B., (2010). Influence of FSSW parameters on fracture mechanisms of 5182 aluminium welds. *Journal of Materials Processing Technology*, 210 , 1429–1435.

Broomhead, P., Grieve, R.J., (1982). The effect of strain rate on the strain to fracture of a sheet steel under biaxial tensile stress conditions. *Journal of Engineering Materials and Technology*, 104 , 102–106.

Buffa, G., Hua, J., Shivpuri, R., Fratini, L., (2006). A continuum based fem model for friction stir welding—model development. *Materials Science and Engineering: A*, 419 , 389–396.

Cai, W., Daehn, G., Vivek, A., Li, J., Khan, H., Mishra, R.S., Komarasamy, M., (2019). A state-of-the-art review on solid-state metal joining. *Journal of Manufacturing Science and Engineering*, 141 , 031012.

Çam, G., İpekoğlu, G., (2017). Recent developments in joining of aluminum alloys. *International Journal of Advanced Manufacturing Technology*, 91 , 1851–1866.

Chen, L., Zhao, G., Yu, J., (2015). Hot deformation behavior and constitutive modeling of homogenized 6026 aluminum alloy. *Materials & Design*, 74 , 25–35.

Chen, M., Lai, Z., Cao, Q., Han, X., Wang, C., Liu, N., Li, L., (2020). Improvement on formability and forming accuracy in electromagnetic forming of deep-cavity sheet metal part using a dual-coil system. *Journal of Manufacturing Processes*, 57 , 209–221.

Chen, Y., Clausen, A.H., Hopperstad, O.S., Langseth, M., (2009). Stress-strain behaviour of aluminium alloys at a wide range of strain rates. *International Journal of Solids and Structures*, 46 , 3825–3835.

Clausen, A.H., Børvik, T., Hopperstad, O.S., Benallal, A., (2004). Flow and fracture characteristics of aluminium alloy AA5083-H116 as function of strain rate, temperature and triaxiality. *Materials Science and Engineering: A*, 364 , 260–272.

Cui, X., Mo, J., Li, J., Xiao, X., Zhou, B., Fang, J., (2016). Large-scale sheet deformation process by electromagnetic incremental forming combined with stretch forming. *Journal of Materials Processing Technology*, 237 , 139–154.

Cui, X., Zhang, Z., Yu, H., Xiao, X., Cheng, Y., (2019). Springback calibration of a U-Shaped electromagnetic impulse forming process. *Metals*, 9 , 603.

Dariani, B.M., Liaghat, G.H., Gerdooei, M., (2009). Experimental investigation of sheet metal formability under various strain rates. *Proceedings of the Institution of Mechanical Engineers, Part B: Journal of Engineering Manufacture*, 223 , 703–712.

Deng, H., Mao, Y., Li, G., Cui, J., (2019). A study of electromagnetic free forming in AA5052 using digital image correlation method and FE analysis. *Journal of Manufacturing Processes*, 37 , 595–605.

Dizaji, S.A., Darendeliler, H., Kaftanoğlu, B., (2016). Effect of hardening models on different ductile fracture criteria in sheet metal forming. *International Journal of Material Forming*, 9 , 261–267.

Doley, J.K., Kore, S.D., (2017). Comparison of electromagnetic forming of friction stir-welded blanks of dissimilar material AA 5052-AA 6061 with conventional forming process. *International Journal of Advanced Manufacturing Technology*, 93 , 3789–3797.

Fengman, H., Zheng, T., Ning, W., Zhiyong, H., (2000). Explosive forming of thin-wall semi-spherical parts. *Materials Letters*, 45 , 133–137.

Fluhrer, J., (2007). DEFORM 3D Version 6.1 User's Manual. Sci. Form. Technol. Corp. Ohio.

Forcellese, A., Simoncini, M., (2020). High-speed deformation of pinless fswed thin sheets in aa6082 alloy. *Metals*, 10 , 15.

Fridlyander, I.N., Sister, V.G., Grushko, O.E., Berstenev, V. V., Sheveleva, L.M., Ivanova, L.A., (2002). Aluminum alloys: Promising materials in the automotive industry. *Metal science and heat treatment*, 44 , 365–370.

Golovashchenko, S.F., (2007). Material formability and coil design in electromagnetic forming. *Journal of Materials Engineering and Performance*, 16 , 314–320.

Golovashchenko, S.F., Gillard, A.J., Mamutov, A. V, (2013). Formability of dual phase steels in electrohydraulic forming. *Journal of Materials Processing Technology*, 213 , 1191–1212.

Grolleau, V., Gary, G., Mohr, D., (2008). Biaxial testing of sheet materials at high strain rates using viscoelastic bars. *Experimental Mechanics*, 48 , 293–306.

Gu, R., Liu, Q., Chen, S., Wang, W., Wei, X., (2019). Study on High-Temperature Mechanical Properties and Forming Limit Diagram of 7075 Aluminum Alloy Sheet in Hot Stamping.

Journal of Materials Engineering and Performance, 28 , 7259–7272.

Gupta, N.K., Iqbal, M.A., Sekhon, G.S., (2008). Effect of projectile nose shape, impact velocity and target thickness on the deformation behavior of layered plates. *International Journal of Impact Engineering*, 35 , 37–60.

Gurson, A.L., (1977). Continuum theory of ductile rupture by void nucleation and growth: Part I—Yield criteria and flow rules for porous ductile media. *Journal of Engineering Materials and Technology*, 99 , 2–15.

Habibi, M., Hashemi, R., Tafti, M.F., Assempour, A., (2018). Experimental investigation of mechanical properties, formability and forming limit diagrams for tailor-welded blanks produced by friction stir welding. *Journal of Manufacturing Processes*, 31 , 310–323.

Habibi, N., Zarei-Hanzaki, A., Abedi, H.R., 2015. An investigation into the fracture mechanisms of twinning-induced-plasticity steel sheets under various strain paths. *Journal of Materials Processing Technology*, 224 , 102–116.

Hadianfard, M.J., Smerd, R., Winkler, S., Worswick, M., (2008). Effects of strain rate on mechanical properties and failure mechanism of structural Al-Mg alloys. *Materials Science and Engineering: A*, 492 , 283–292.

Hambli, R., (2001). Finite element simulation of fine blanking processes using a pressure-dependent damage model. *Journal of Materials Processing Technology*, 116 , 252–264.

Hambli, R., Reszka, M., (2002). Fracture criteria identification using an inverse technique method and blanking experiment. *International journal of mechanical sciences*, 44 , 1349–1361.

Heidari, A., Ghassemi, A., Atrian, A., (2020). A numerical and experimental investigation of temperature effects on the formability of AA6063 sheets using different ductile fracture criteria. *International Journal of Advanced Manufacturing Technology*, 106 , 2595–2611.

Homberg, W., Beerwald, C., Pröbsting, A., (2010). Investigation of the electrohydraulic forming process with respect to the design of sharp edged contours, in: *4th International Conference on High Speed Forming*. pp. 58–64.

Hsu, E., Carsley, J.E., Verma, R., (2008). Development of forming limit diagrams of aluminum and magnesium sheet alloys at elevated temperatures. *Journal of Materials Engineering and Performance*, 17 , 288–296.

Huskins, E. L., Cao, B., Ramesh, K.T., (2010). Strengthening mechanisms in an Al-Mg alloy. *Materials Science and Engineering: A*, 527 , 1292–1298.

Imbert, J., Worswick, M., (2012). Reduction of a pre-formed radius in aluminium sheet using electromagnetic and conventional forming. *Journal of Materials Processing Technology*,

212 , 1963–1972.

Imbert, J.M., Winkler, S.L., Worswick, M.J., Oliveira, D.A., Golovashchenko, S., (2005). The effect of tool-sheet interaction on damage evolution in electromagnetic forming of aluminum alloy sheet. *Journal of Engineering Materials and Technology*, 127 , 145–153.

Iqbal, M.P., Jain, R., Pal, S.K., (2019). Numerical and experimental study on friction stir welding of aluminum alloy pipe. *Journal of Materials Processing Technology*, 274 , 116258.

Jacob, N., Nurick, G.N., Langdon, G.S., (2007). The effect of stand-off distance on the failure of fully clamped circular mild steel plates subjected to blast loads. *Engineering Structures*, 29 , 2723–2736.

Jain, R., Pal, S.K., Singh, S.B., (2017a). Finite element simulation of temperature and strain distribution during friction stir welding of AA2024 aluminum alloy. *Journal of The Institution of Engineers (India): Series C*, 98 , 37–43.

Jain, R., Pal, S.K., Singh, S.B., (2017b). Numerical modeling methodologies for friction stir welding process, in: *Computational Methods and Production Engineering*, pp. 125–169.

Jenab, A., Green, D.E., Alpas, A.T., (2017). Microscopic investigation of failure mechanisms in AA5182-O sheets subjected to electro-hydraulic forming. *Materials Science and Engineering: A*, 691 , 31–41.

Jenab, A., Green, D.E., Alpas, A.T., Golovashchenko, S.F., (2018). Experimental and numerical analyses of formability improvement of AA5182-O sheet during electro-hydraulic forming. *Journal of Materials Processing Technology*, 255 , 914–926.

Jenq, S.T., Sheu, S.L., (1994). An experimental and numerical analysis for high strain rate compressional behavior of 6061-O aluminum alloy. *Computers & structures*, 52 , 27–34.

Jones, N., Uran, T.O., Tekin, S.A., (1970). The dynamic plastic behavior of fully clamped rectangular plates. *International Journal of Solids and Structures*, 6 , 1499–1512.

Joost, W.J., (2012). Reducing vehicle weight and improving US energy efficiency using integrated computational materials engineering. *Jom*, 64 , 1032–1038.

Justusson, B., Pankow, M., Heinrich, C., Rudolph, M., Waas, A.M., (2013). Use of a shock tube to determine the bi-axial yield of an aluminum alloy under high rates. *International Journal of Impact Engineering*, 58 , 55–65.

Kesharwani, R.K., Basak, S., Panda, S.K., Pal, S.K., (2017). Improvement in limiting drawing ratio of aluminum tailored friction stir welded blanks using modified conical tractrix die. *Journal of Manufacturing Processes*, 28 , 137–155.

Khodko, O., Zaytsev, V., Sukaylo, V., Verezub, N., Scicluna, S., (2015). Experimental and

numerical investigation of processes that occur during high velocity hydroforming technologies: An example of tubular blank free bulging during hydrodynamic forming. *Journal of Manufacturing Processes*, 20 , 304–313.

Kiliclar, Y., Demir, O.K., Engelhardt, M., Rozgić, M., Vladimirov, I.N., Wulfinghoff, S., Weddeling, C., Gies, S., Klose, C., Reese, S., Tekkaya A.E., Maier H.J., Stiemer M., (2016). Experimental and numerical investigation of increased formability in combined quasi-static and high-speed forming processes. *Journal of Materials Processing Technology*, 237 , 254–269.

Kim, D., Lee, W., Kim, J., Kim, C., Chung, K., (2010). Formability evaluation of friction stir welded 6111-T4 sheet with respect to joining material direction. *International journal of mechanical sciences*, 52 , 612–625.

Koç, M., Billur, E., Cora, Ö.N., (2011). An experimental study on the comparative assessment of hydraulic bulge test analysis methods. *Materials & Design*, 32 , 272–281.

Koohbor, B., Kidane, A., Lu, W.Y., (2016a). Characterizing the constitutive response and energy absorption of rigid polymeric foams subjected to intermediate-velocity impact. *Polymer Testing*, 54 , 48–58.

Koohbor, B., Kidane, A., Lu, W.Y., Sutton, M.A., (2016b). Investigation of the dynamic stress-strain response of compressible polymeric foam using a non-parametric analysis. *International Journal of Impact Engineering*, 91 , 170–182.

Kosing, O.E., Skews, B.W., (1998). An investigation of high-speed forming of circular plates in a liquid shock tube. *International Journal of Impact Engineering*, 21 , 801–816.

Kpenyigba, K.M., Jankowiak, T., Rusinek, A., Pesci, R., (2013). Influence of projectile shape on dynamic behavior of steel sheet subjected to impact and perforation. *Thin-Walled Structures*, 65 , 93–104.

Kumar, P., LeBlanc, J., Stargel, D.S., Shukla, A., (2012). Effect of plate curvature on blast response of aluminum panels. *International Journal of Impact Engineering*, 46 , 74–85.

Langrand, B., Markiewicz, E., (2010). Strain-rate dependence in spot welds: Non-linear behaviour and failure in pure and combined modes I/II. *International Journal of Impact Engineering*, 37 , 792–805.

Leblanc, J., Shukla, A., (2011). Response of E-glass/vinyl ester composite panels to underwater explosive loading: Effects of laminate modifications. *International Journal of Impact Engineering*, 38 , 796–803.

LeBlanc, J., Shukla, A., (2010). Dynamic response and damage evolution in composite materials subjected to underwater explosive loading: An experimental and computational study. *Composite Structures*, 92 , 2421–2430.

LeBlanc, J., Shukla, A., Rousseau, C., Bogdanovich, A., (2007). Shock loading of three-dimensional woven composite materials. *Composite Structures*, 79 , 344–355.

Lee, J., Park, H., Kim, S.J., Kwon, Y.N., Kim, D., (2018). Numerical investigation into plastic deformation and failure in aluminum alloy sheet rubber-diaphragm forming. *International Journal of Mechanical Sciences*, 142 , 112–120.

Lee, W., Chung, K.H., Kim, D., Kim, J., Kim, C., Okamoto, K., Wagoner, R.H., Chung, K., (2009). Experimental and numerical study on formability of friction stir welded TWB sheets based on hemispherical dome stretch tests. *International Journal of Plasticity*, 25 , 1626–1654.

Li, C., Liu, D., Yu, H., Ji, Z., (2009). Research on formability of 5052 aluminum alloy sheet in a quasi-static–dynamic tensile process. *International Journal of Machine Tools and Manufacture*, 49 , 117–124.

Li, G., Jinn, J.T., Wu, W.T., Oh, S.I., (2001). Recent development and applications of three-dimensional finite element modeling in bulk forming processes. *Journal of Materials Processing Technology*, 113 , 40–45.

Liu, D.H., Li, C.F., Yu, H.P., (2009). Numerical modeling and deformation analysis for electromagnetically assisted deep drawing of AA5052 sheet. *Transactions of Nonferrous Metals Society of China*, 19 , 1294–1302.

Liu, D., Yu, H., Li, C., (2011). Experimental observations of quasi-static-dynamic formability in biaxially strained AA5052-O. *Journal of materials engineering and performance*, 20 , 223–230.

Ma, H., Huang, L., Tian, Y., Li, J., (2014). Effects of strain rate on dynamic mechanical behavior and microstructure evolution of 5A02-O aluminum alloy. *Materials Science and Engineering: A*, 606 , 233–239.

Mahabunphachai, S., Koç, M., (2010). Investigations on forming of aluminum 5052 and 6061 sheet alloys at warm temperatures. *Materials & Design*, 31 , 2422–2434.

Manladan, S.M., Yusof, F., Ramesh, S., Fadzil, M., Luo, Z., Ao, S., (2017). A review on resistance spot welding of aluminum alloys. *International Journal of Advanced Manufacturing Technology*, 90 , 605–634.

Maris, C., Hassannejadasl, A., Green, D.E., Cheng, J., Golovashchenko, S.F., Gillard, A.J., Liang, Y., (2016). Comparison of quasi-static and electrohydraulic free forming limits for DP600 and AA5182 sheets. *Journal of Materials Processing Technology*, 235 , 206–219.

Meng, Z., Huang, S., Hu, J., Huang, W., Xia, Z., (2011). Effects of process parameters on warm and electromagnetic hybrid forming of magnesium alloy sheets. *Journal of Materials Processing Technology*, 211 , 863–867.

Mostofi, T.M., Babaei, H., Alitavoli, M., (2017). The influence of gas mixture detonation loads on large plastic deformation of thin quadrangular plates: Experimental investigation and empirical modelling. *Thin-Walled Structures*. 118, 1–11.

Mousavi, S.A.A.A., Riahi, M., Parast, A.H., (2007). Experimental and numerical analyses of explosive free forming. *Journal of Materials Processing Technology*, 187 , 512–516.

Mynors, D.J., Zhang, B., (2002). Applications and capabilities of explosive forming. *Journal of Materials Processing Technology*, 125 , 1–25.

Nagaraja, S.R., Prasad, J.K., Jagadeesh, G., (2012). Theoretical-experimental study of shock wave-assisted metal forming process using a diaphragmless shock tube. *Proceedings of the Institution of Mechanical Engineers, Part G: Journal of Aerospace Engineering*, 226 , 1534–1543.

Nanda, S. R., Kulkarni, V., & Sahoo, N., (2017). Apt Strain Measurement Technique for Impulsive Loading Applications. *Measurement Science and Technology*, 28 , 037001.

National Instruments, (1998). Strain Gauge Measurement – A Tutorial. Appl. Note 078 1–12.

Neto, D.M., Oliveira, M.C., Alves, J.L., Menezes, L.F., (2014). Influence of the plastic anisotropy modelling in the reverse deep drawing process simulation. *Materials & Design*, 60 , 368–379.

Nishiyama, U., Inoue, T., (1968). A study of the utilization of generated energies in hydro-spark forming and explosive forming. *International Journal of Mechanical Sciences*, 10 , 479–486.

Noh, H.G., Lee, K., Kang, B.S., Kim, J., (2016). Inverse parameter estimation of the Cowper-Symonds material model for electromagnetic free bulge forming. *International Journal of Precision Engineering and Manufacturing*, 17 , 1483–1492.

Noh, H.G., Song, W.J., Kang, B.S., Kim, J., (2015). Two-step electromagnetic forming process using spiral forming coils to deform sheet metal in a middle-block die. *International Journal of Advanced Manufacturing Technology*, 76 , 1691–1703.

Novella, M.F., Ghiotti, A., Bruschi, S., Bariani, P.F., (2015). Ductile damage modeling at elevated temperature applied to the cross wedge rolling of AA6082-T6 bars. *Journal of Materials Processing Technology*, 222 , 259–267.

Nurick, G.N., Shave, G.C., (1996). The deformation and tearing of thin square plates subjected to impulsive loads – an experimental study. *International Journal of Impact Engineering*, 18 , 99–116.

Oliveira, D.A., Worswick, M.J., Finn, M., Newman, D., (2005). Electromagnetic forming of aluminum alloy sheet: Free-form and cavity fill experiments and model. *Journal of*

Materials Processing Technology, 170 , 350–362.

Padmanabhan, M., (1997). Wrinkling and springback in electromagnetic sheet metal forming and electromagnetic ring compression. (Doctoral dissertation,The Ohio State University).

Pankow, M., Justusson, B., Salvi, a., Waas, a. M., Yen, C.F., Ghiorse, S., (2011). Shock response of 3D woven composites: An experimental investigation. *Composite Structures*, 93 , 1337–1346.

Pashazadeh, H., Teimournezhad, J., Masoumi, A., (2014). Numerical investigation on the mechanical, thermal, metallurgical and material flow characteristics in friction stir welding of copper sheets with experimental verification. *Materials & Design*, 55 , 619–632.

Patil, S.P., Fenard, Y., Bailkeri, S., Heufer, K.A., Markert, B., (2019). Investigation of Sheet Metal Forming Using a Rapid Compression Machine. *Materials*, 12 , 3957.

Patil, S.P., Murkute, R., Shirafkan, N., Markert, B., (2018). Deformation of Stacked Metallic Sheets by Shock Wave Loading. *Metals*, 8 , 679.

Percy, J.H., Lim, S.G., (1983). Forming limits for mild steel sheet at high forming rates. *CIRP Annels*, 32 , 177–180.

Pereira, A.F.G., Prates, P.A., Oliveira, M.C., Fernandes, J. V, (2020). Inverse identification of the work hardening law from circular and elliptical bulge tests. *Journal of Materials Processing Technology*, 279 , 116573.

Pham, Q.T., Lee, B.H., Park, K.C., Kim, Y.S., (2018). Influence of the post-necking prediction of hardening law on the theoretical forming limit curve of aluminium sheets. *International Journal of Mechanical Sciences*, 140 , 521–536.

Pickett, A.K., Pyttel, T., Payen, F., Lauro, F., Petrinic, N., Werner, H., Christlein, J., (2004). Failure prediction for advanced crashworthiness of transportation vehicles. *International Journal of Impact Engineering*, 30 , 853–872.

Pothnis, J.R., Perla, Y., Arya, H., Naik, N.K., (2011). High strain rate tensile behavior of aluminum alloy 7075 T651 and IS 2062 mild steel. *Journal of Engineering Materials and Technology*, 133 , 021026

Psyk, V., Risch, D., Kinsey, B.L., Tekkaya, A.E., Kleiner, M., (2011). Electromagnetic forming—a review. *Journal of Materials Processing Technology*, 211 , 787–829.

Rajendran, R., Narasimhan, K., (2001). Damage prediction of clamped circular plates subjected to contact underwater explosion. *International Journal of Impact Engineering*, 25 , 373–386.

Ramezani, M., Ripin, Z.M., (2010). Combined experimental and numerical analysis of bulge

test at high strain rates using split Hopkinson pressure bar apparatus. *Journal of Materials Processing* Technology, 210, 1061–1069.

Ramezani, M., Ripin, Z.M., Ahmad, R., (2010). Plastic bulging of sheet metals at high strain rates. *International Journal of Advanced Manufacturing Technology*, 48 , 847–858.

Rana, P.K., Narayanan, R.G., Kailas, S. V, (2019). Friction stir spot welding of AA5052-H32/HDPE/AA5052-H32 sandwich sheets at varying plunge speeds. *Thin-Walled Structures*, 138 , 415–429.

Rana, P.K., Narayanan, R.G., Kailas, S. V, (2018). Effect of rotational speed on friction stir spot welding of AA5052-H32/HDPE/AA5052-H32 sandwich sheets. *Journal of Materials Processing* Technology, 252, 511–523.

Rao, A.V., Ramakrishnan, N., others, (2003). A comparative evaluation of the theoretical failure criteria for workability in cold forging. *Journal of Materials Processing Technology*, 142 , 29–42.

Ray, N., Jagadeesh, G., Suwas, S., (2015). Response of shock wave deformation in AA5086 aluminum alloy. *Materials Science and Engineering: A*, 622 , 219–227.

Rohatgi, A., Stephens, E. V., Davies, R.W., Smith, M.T., Soulami, A., Ahzi, S., (2012). Electro-hydraulic forming of sheet metals: Free-forming vs. conical-die forming. *Journal of Materials Processing Technology*, 212 , 1070–1079.

Rohatgi, A., Stephens, E. V, Soulami, A., Davies, R.W., Smith, M.T., (2011). Experimental characterization of sheet metal deformation during electro-hydraulic forming. *Journal of Materials Processing Technology*, 211 , 1824–1833.

Romhanji, E., Dudukovska, M., Glišić, D., (2002). The effect of temperature on strain-rate sensitivity in high strength Al--Mg alloy sheet. *Journal of Materials Processing Technology*, 125 , 193–198.

Rusinek, A., Rodríguez-Martínez, J.A., Zaera, R., Klepaczko, J.R., Arias, A., Sauvelet, C., (2009). Experimental and numerical study on the perforation process of mild steel sheets subjected to perpendicular impact by hemispherical projectiles. *International Journal of Impact Engineering*, 36 , 565–587.

Shang, J., Daehn, G., (2011). Electromagnetically assisted sheet metal stamping. Journal of Materials Processing Technology, 211 , 868–874.

Sherwood, J.D., Durban, D., (1996). Squeeze flow of a power-law viscoplastic solid. *Journal of non-newtonian fluid mechanics*, 62 , 35–54.

Shim, J.Y., Kang, B.Y., (2017). Development of electrohydraulic forming process for aluminum sheet with sharp edge. *Advances in Materials Science and Engineering*, 2017,

2715092.

Simoncini, M., Forcellese, A., Mancini, E., Chiappini, G., Sasso, M., (2021). Experimental and numerical investigation on forming limit curves of AA6082 aluminum alloy at high strain rates. *International Journal of Advanced Manufacturing Technology*, 12 , 1973–1991.

Skews, B.W., Kosing, O.E., Hattingh, R.J., (2004). Use of a liquid shock tube as a device for the study of material deformation under impulsive loading conditions. *Proceedings of the Institution of Mechanical Engineers, Part C: Journal of Mechanical Engineering Science*, 218 , 39–51.

Smerd, R., Winkler, S., Salisbury, C., Worswick, M., Lloyd, D., Finn, M., (2006). High strain rate tensile testing of automotive aluminum alloy sheet. *International Journal of Impact Engineering*, 32 , 541–560.

Song, P., Li, W., Wang, X., Xu, W., (2019). Study on mechanical properties and constitutive model of 5052 aluminium alloy. *Materials Science and Technology*, 35 , 916–924.

Soni, M., Ahmed, M., Panthi, S.K., Kumar, S., (2021). Effect of coil design parameters on performance of electromagnetic forming process. *Materials and Manufacturing Processes*. 1–17.

Spranghers, K., Vasilakos, I., Lecompte, D., Sol, H., Vantomme, J., (2012). Full-Field Deformation Measurements of Aluminum Plates Under Free Air Blast Loading. *Experimental mechanics*, 52 , 1371–1384.

Stoffel, M., (2004). Evolution of plastic zones in dynamically loaded plates using different elastic-viscoplastic laws. *International journal of solids and structures*, 41 , 6813–6830.

Stoffel, M., Schmidt, R., Weichert, D., (2001). Shock wave-loaded plates. *International journal of solids and structures*, 38 , 7659–7680.

Su, H., Huang, L., Li, J., Xiao, W., Zhu, H., Feng, F., Li, H., Yan, S., (2021). Formability of AA 2219-O sheet under quasi-static, electromagnetic dynamic, and mechanical dynamic tensile loadings. *Journal of Materials Science & Technology*, 70 , 125–135.

Sun, X., Khaleel, M.A., (2007). Dynamic strength evaluations for self-piercing rivets and resistance spot welds joining similar and dissimilar metals. *International Journal of Impact Engineering*, 34 , 1668–1682.

Suo, T., Chen, Y., Li, Y., Wang, C., Fan, X., (2013). Strain rate sensitivity and deformation kinetics of ECAPed aluminium over a wide range of strain rates. *Materials Science and Engineering: A*, 560 , 545–551.

Takuda, H., Mori, K., Hatta, N., (1999). The application of some criteria for ductile fracture to

the prediction of the forming limit of sheet metals. *Journal of Materials Processing Technology*, 95 , 116–121.

Talebi-Ghadikolaee, H., Naeini, H.M., Mirnia, M.J., Mirzai, M.A., Alexandrov, S., Zeinali, M.S., (2020). Modeling of ductile damage evolution in roll forming of U-channel sections. *Journal of Materials Processing Technology*. 116690.

Tekalur, S.A., Bogdanovich, A.E., Shukla, A., (2009). Shock loading response of sandwich panels with 3-D woven E-glass composite skins and stitched foam core. *Composites Science and Technology*, 69 , 736–753.

Tekalur, S.A., Shivakumar, K., Shukla, A., (2008). Mechanical behavior and damage evolution in E-glass vinyl ester and carbon composites subjected to static and blast loads. *Composites Part B: Engineering*, 39 , 57–65.

Tian, Y., Huang, L., Ma, H., Li, J., (2014). Establishment and comparison of four constitutive models of 5A02 aluminium alloy in high-velocity forming process. *Materials & Design*, 54 , 587–597.

Tiesheng, Z., Zhensheng, L., Changji, G., Zheng, T., (1992). Explosive forming of spherical metal vessels without dies. *Journal of Materials Processing Technology*, 31 , 135–145.

Wagoner, R.H., Chenot, J.L., (1996). Fundamentals of metal forming. John Wiley & Sons Inc, New York.

Wang, D. zhen, Li, N., Han, X. tao, Li, L., Liu, L., (2017). Effect of electromagnetic bulging on fatigue behavior of 5052 aluminum alloy. *Transactions of Nonferrous Metals Society of China*, 27 , 1224–1232.

Wang, E., Wright, J., Shukla, A., (2011). Analytical and experimental study on the fluid structure interaction during air blast loading. *Journal of Applied Physics*, 110 , 114901.

Woo, M.A., Moon, Y.H., Song, W.J., Kang, B.-S., Kim, J., (2019). Acquisition of dynamic material properties in the electrohydraulic forming process using artificial neural network. *Materials*, 12, 3544.

Woo, M.A., Noh, H.G., Song, W.J., Kang, B.S., Kim, J., (2017). Experimental validation of numerical modeling of electrohydraulic forming using an al 5052-H34 sheet. *International Journal of Advanced Manufacturing Technology*, 93 , 1819–1828.

Wright, J., Hebert, R., Maddala, D., Shukla, A., (2014). Experimental study on the response of graded corrugated steel armor to shock loading. *Meccanica*, 50, 479–492.

Xu, J.R., Yu, H.P., Cui, J., Li, C.F., (2013a). Formability of AZ31 magnesium alloy sheets during magnetic pulse bulging. *Materials Science and Engineering: A*, 569 , 150–158.

Xu, J.R., Yu, H.P., Li, C.F., (2013b). Effects of process parameters on electromagnetic forming

of AZ31 magnesium alloy sheets at room temperature. *International Journal of Advanced Manufacturing Technology*, 66 , 1591–1602.

Yacsar, M., Demirci, H.I., Kadi, I., (2006). Detonation forming of aluminium cylindrical cups experimental and theoretical modelling, *Materials & design*, 27, 397–404.

Yan, S.L., Yang, H., Li, H.W., Yao, X., (2016). Variation of strain rate sensitivity of an aluminum alloy in a wide strain rate range: Mechanism analysis and modeling. *Journal of Alloys and Compounds*, 688 , 776–786.

Yan, Z., Du, Z., Cui, X., Huang, C., Meng, Y., (2021). Springback and deformation uniformity of high-strength aluminum alloy sheet using electromagnetic forming. *International Journal of Advanced Manufacturing Technology*, 114 , 1293–1308.

Yang, Q., Mironov, S., Sato, Y.S., Okamoto, K., (2010). Material flow during friction stir spot welding. *Materials Science and Engineering: A*, 527 , 4389–4398.

Yuan, W., Mishra, R.S., Carlson, B., Verma, R., Mishra, R.K., (2012). Material flow and microstructural evolution during friction stir spot welding of AZ31 magnesium alloy. *Materials Science and Engineering: A*, 543 , 200–209.

Zhang, Z., Yang, X., Zhang, J., Zhou, G., Xu, X., Zou, B., (2011). Effect of welding parameters on microstructure and mechanical properties of friction stir spot welded 5052 aluminum alloy. *Materials & Design*, 32 , 4461–4470.

Zhao, Y., Liu, H., Yang, T., Lin, Z., Hu, Y., (2016). Study of temperature and material flow during friction spot welding of 7B04-T74 aluminum alloy. *International Journal of Advanced Manufacturing Technology*, 83 , 1467–1475.

Publications from the present work

Refereed Journals

1. **Barik, S.K.**, Narayanan, R.G., Sahoo, N., (2020). Forming response of AA5052-H32 sheet deformed using a shock tube. *Transactions of Nonferrous Metals Society of China*, 30, 603–618. DOI: https://doi.org/10.1016/S1003-6326(20)65239-6.
2. **Barik, S.K.**, Narayanan, R.G., Sahoo, N., (2020). Prediction of Forming of AA 5052-H32 Sheets under Impact Loading and Experimental Validation. *Journal of Materials Engineering and Performance*, 29 (6), 3941–3960. DOI: https://doi.org/10.1007/s11665-020-04884-w.
3. **Barik, S.K.**, Narayanan, R.G., Sahoo, N., (2021). Failure Strain and Fracture Prediction During Shock Tube Impact Forming of AA 5052-H32 Sheet. *Journal of Engineering Materials and Technology*, 143 (3), 031009. DOI: https://doi.org/10.1115/1.4050703.
4. **Barik, S.K.**, Narayanan, R.G., Sahoo, N., (2022). Assessment of stress-strain constitutive models and failure models on the shock tube based impact forming of AA 5052-H32 sheet. *Journal of Manufacturing Processes*, 74, 573–591. DOI: https://doi.org/10.1016/j. jmapro.2021.12.047.
5. **Barik, S.K.**, Narayanan, R.G., Sahoo, N., (2022). Formability and failure response of AA5052-H32 thin sheets with friction stir spot welds during the shock tube-based impact forming. *International Journal of Advanced Manufacturing Technology*, 13 (3), 1−25. DOI: https://doi.org/10.1007/s00170 -021-08566-2.
6. **Barik, S.K.**, Narayanan, R.G., Sahoo, N., (2022). Impact forming of AA5052-H32 sheets with friction stir spot welds using a shock tube and failure assessment. *Journal of Engineering Materials and Technology*, 1−39. DOI: https://doi.org/10.1115/ 1.4053894.

Book Chapters

1. **Barik, S.K.**, Narayanan, R.G., Sahoo, N., (2019). Experimental Investigation on the Forming of AA 5052-H32 Sheet Using a Rigid-Body-Based Impact in a Shock Tube, in: Advances in Forming, Machining and Automation. Springer, pp. 79–90. DOI: https://doi.org/10.1007/978-981-32-9417-2_6.

2. **Barik, S.K.**, Narayanan, R.G., Sahoo, N. Shock tube based forming of sheets, in: Metal forming processes: Developments in experimental and numerical approaches. Taylor & Francis. (Accepted for publication)

Refereed Conferences

1. **Barik, S.K.**, Sahoo, N., Narayanan, R.G., (2016). High strain rate deformation study on sheet and composites, Proceedings of 4th National Symposium on Shock Waves (NSSW), Karunya University, Coimbatore, February 25-26.
2. **Barik, S.K.**, Sahoo, N., Narayanan, R.G., (2016). Experimental investigation on the forming behavior of stainless steel sheet using shock tube, Proceedings of Conference on Sheet Metal Forming, 2016 (SMF'16), IIT Bombay, Mumbai, December 08-09.
3. **Barik, S.K.**, Sahoo, N., Narayanan, R.G., (2016). Experimental study on the forming response of stainless steel sheet using shock tube, Proceedings of 6th international & 27th All India Manufacturing Technology, Design and Research Conference (AIMTDR 2016), College of Engineering Pune, Pune, December 16-18.
4. **Barik, S.K.**, Narayanan, R.G., Sahoo, N., (2018). Experimental investigation on the forming of AA 5052-H32 sheet using a rigid body based impact in a shock tube, Proceedings of 7th International & 28th All India Manufacturing Technology, Design and Research Conference (AIMTDR2018), College of Engineering Guindy, Anna University, Chennai, December 13-15.
5. **Barik, S.K.**, Narayanan, R.G., Sahoo, N., (2019). Prediction of high-velocity forming behavior of AA 5052-H32 pre-strained sheet, Proceedings of 64th Congress of the Indian Society of Theoretical and Applied Mechanics (ISTAM 2019), IIT Bhubaneswar, Bhubaneswar, December 10-12.